CONCURRENT DIFFUSE OPTICAL TOMOGRAPHY, SPECTROSCOPY AND MAGNETIC RESONANCE IMAGING OF BREAST CANCER.

A dissertation in BioEngineering

Vasilis Ntziachristos

2000

CONCURRENT DIFFUSE OPTICAL TOMOGRAPHY, SPECTROSCOPY AND MAGNETIC RESONANCE IMAGING OF BREAST CANCER.

Vasilis Ntziachristos

A DISSERTATION

in

Bioengineering

Presented to the Faculties of the University of Pennsylvania in Partial Fulfillment of the Requirements for the degree of Doctor of Philosophy.

2000

_____	_____
Britton Chance	**ArjunYodh**
Supervisor of dissertation	Supervisor of dissertation

_____

David Meaney

Graduate Group Chairperson

ABSTRACT

CONCURRENT DIFFUSE OPTICAL TOMOGRAPHY, SPECTROSCOPY AND MAGNETIC RESONANCE IMAGING OF BREAST CANCER.

Vasilis Ntziachristos

Britton Chance & Arjun Yodh

Diffuse Optical Tomography (DOT) in the Near Infrared (NIR) offers the potential to perform non-invasive three-dimensional quantified imaging of large-organs in vivo. The technique targets tissue intrinsic chromophores such as oxy- and deoxy- hemoglobin and the uptake of optical contrast agents.

This work considers the DOT application in studying the vascularization, hemoglobin saturation and Indocyanine Green (ICG) uptake of breast tumors in-vivo as measures of angiogenesis, blood vessel permeability and oxygen delivery and consumption. To realize this work an optical tomographer based on the single-photon-counting time-correlated technique was coupled to a Magnetic Resonance Imaging (MRI) scanner. All patients entered the study were also scheduled for biopsy; hence histopathological information was also available as the "Gold Standard" for the diagnostic performance.

The feasibility of Diffuse Optical Tomography to image tissue in-vivo is demonstrated by directly comparing contrast-enhanced MR and DOT images obtained from the same breast under identical geometrical and physiological conditions. The effect of tissue optical background heterogeneity on imaging performance is also studied using simulations. Additionally, optimization schemes are presented that yield superior reconstruction and spectroscopic capacity when probing the intrinsic and extrinsic contrast of highly heterogeneous optical media.

The simultaneous examination also pioneers a hybrid diagnostic modality where MRI and image-guided localized diffuse optical spectroscopy (DOS) information are concurrently

available. The approach employs the MR structural and functional information as a-priori knowledge and thus improves the quantification ability of the optical method. We have employed DOS and localized DOS to quantify optical properties of tissue in two and three wavelengths and obtain functional properties of malignant, benign and normal breast lesions. Generally, cancers exhibited higher hemoglobin concentration, lower hemoglobin saturation and higher ICG uptake than normal and benign lesions.

The use of DOT and localized DOS is found to be a valuable clinical tool to study tissue function. The potential to use DOT for early breast cancer detection by employing emerging classes of optical contrast agents that target highly specific biochemical cancer properties in the cellular level has also been demonstrated.

AKNOWLEDGEMENTS

In retrospect, I cannot think of myself doing something different these past four years than a thesis with Britton Chance and Arjun Yodh. I certainly have not reached Ithaka yet, but certainly this was the most probable path there. The years that led to the completion of this thesis have been really remarkable for me and I am truly grateful to the many people I mention here for this experience.

It is not often that you have the opportunity to relate with a champion in life. From driving through Monaco and sharing his past ventures with Royals of Philadelphian descent, to sailing under the stars in the Keys, my graduate years with Britton Chance were nothing limited to only a laboratory experience. It was rather a life adventure. Britton Chance has affected me in many ways. If I had to single out one aspect of the interaction it would certainly be the trust with which he embraced me. I later realized that on the personal level, there is something more than the intelligence, the innovation or the many awards and medals that make you truly exceptional. It is the grace of believing in people and sanctioning them to create unconditionally. It was this trust that allowed me to grow in knowledge and experience and obtain a wider perspective in science and research. But in the daily laboratory life it was a thrill to work with him. He was always available to discuss results and ideas and was ceaselessly enthusiastic on progress. With the same eagerness he would argue on the permeability of tumor vessels to ICG or join me next to the oscilloscope for measuring the output pulse height of a new Photo-Multiplier Tube. His renowned experience with so many different scientific areas, emanating from a life of pioneering research, was overwhelming and a constant example that there are no limits to what can be accomplished. When writing grants, he would impart so many different perspectives to wake the mind and keep vibrant late evening discussions. And when help was in need, he was never to deny it. I could not but be deeply grateful to my mentor for my thesis years.

My experience at Penn would not be accomplished without having worked with Dr. Arjun Yodh. Having a superb scientific talent and perception, Arjun was illuminating problems and approaches with light that was certainly non-diffuse. His critical mind and

methodology was a sanctuary when the walk was becoming random. Arjun taught me to look into a problem and search not only for the apparent solution but also for all its implications that expand it and reconstitute it and connect it with other problems. Thus the thought process becomes clear and precise and therefore can be easily explained and transferred to others. His unconditional advice on scientific and personal issues was inspirational and faithful and it had a great impact on my decisions. I am sincerely indebted to his help and faith.

Certainly a great virtue of my two advisors was their collaboration and interaction with many top, highly acclaimed scientists and thinkers and their ability to draw from the best of students and researchers to work with. In this environment I was effortlessly exposed to superb and talented minds and many times developed personal relationships and interactions that inspired me.

I should begin by acknowledging Dr. Mitch Schnall as it was his liberal interest in scientific progress and his unique perspective on the interaction of technology and clinical research that allowed the clinical part of this work to be achieved. I am grateful to Dr. Less Dutton and Dr. John S. Leigh for providing working and computing facilities when they were mostly needed and Dr. John Schotland for prodigious conversations and collaboration. I am thankful to Dr. Andreas Hielscher for his help with time-domain simulations and useful discussions. I am indebted to Dr. Bruce Tromberg for his insightful outlook on BioOptics, his critical comments and support on this work and for being an enthusiastic mentor.

I want to thank the people that thrust me in the field: Dr. Maureen O'Leary for initiating me with the principles of Diffuse Optical Tomography, Dr. David Boas for his stimulation and friendship and Mitsuharu Miwa and Hanli Liu for great conversations on time-resolved spectroscopy. My further education in the research ways would not have been imaginative and enthralling without having the fortune to work with Dr. Joe Culver, Dr. Nirmala Ramanujam and Dr. Robert Danen. I thank them for sharing scientific and social excitements, and for their friendship.

I am also grateful to Thomas Connick for the long hours we spent designing the coupling of the optical system into the MRI scanner and for his invaluable help with constructing and testing the RF coils to Mike Carmen, William Penney and Gabor Mizsei for

their technical support and to Norman Butler, Tanya Kurtz, Doris Cain, Jean Mc Dermott and Lori Pfaff for their vital assistance with patient scheduling, management and consent.

I wish to thank all the people in the laboratories of BC and Arjun and affiliated laboratories with whom we shared scientific and everyday experiences. In particular XuHui Ma for his devotion and help with the experimental approaches, Dr. Xavier Intes for making it more interesting, Dr. Lori Arakaki for a beautiful collaboration and very interesting results on the muscle experiments, Monica Holboke and Turgut Durduran for always being there when emergencies with simulations arose, Shuoming Zhu, Honyan Ma, Yu Chen, Cecil Cheung and Regine Choe for their help with instrumentation experiments and Chilton Alter who unconditionally donated his mind activity to science. Life in the laboratory and outside of it would not be as easy and as enjoyable without Dorothea McGovern Coleman and Mary Leonard to understand the needs and provide unrestricted help. Last but not least Dr. Shoko Nioka for providing not only help with the clinical examinations but also for being such a generous and enthusiastic host, always affording me with a feeling of belonging to a family.

I would like to thank Dr. Manuel Nieto-Vesperinas for his hospitality and scientific advice in my visits to his laboratory in Madrid and Jorge Ripoll Lorenzo for being a brilliant collaborator and friend.

I would like to thank the faculty of the Department of Bioengineering for giving me an interdisciplinary education in Engineering and Medicine. In particular Dr. Kenneth Foster who introduced me to Bioengineering approaches in clinical research for his hospitality and his advice, Dr. Gabor Herman and Dr. Zair Censor for their expert advice on the inverse ways and Dr. David Meaney for his help with the graduate affairs. Lisa Halterman has been precious throughout departmental functions and a courteous host that was uniting such a scientifically diverse graduate group.

I am grateful to Dr. Bjørn Quistorff who prompted my graduate vocation with his support and encouragement and Dr. George Segiadis for fascinating me with the application of engineering to serve medicine.

I could not have been fulfilled in pursuing this work without the support of Katerina Ivanova, Manos Chajakis, Edgar Garduño, my brother Leonidas and good friends that surrounded me with their love and understanding all these years.

Finally I would not have reached the point of writing this thesis without the encouragement of my mother Venetia and my father Dimitri that inspirited me with the joy for progress and taught me to aim high and pursue my goals without hesitation. I am ultimately grateful to their unconditional support of my decisions and for their love.

TABLE OF CONTENTS

LIST OF TABLES

LIST OF FIGURES

1 Introduction

This work occurred at a truly exciting period for diffuse photons. It started at the beginning of 1996 where many theoretical advances and laboratory devices had demonstrated potential to use diffuse photons clinically. It was postulated that diffuse photons would aid our study of the human body in-vivo and would supplement X-ray photons, tissue proton and phosphorus resonances in magnetic fields, ultrasonic waves and simultaneous emissions of radioisotopes amongst other technologies. There was a compelling reason to pursue this work. Light is probably the "best surviving tool" in the Bio-field [1]. And that of course is not accidental. Light offers unique interactions with tissue elements to allow the study of biochemical and pathophysiological functions by probing tissue elements and given the correct mathematical tools by quantifying them. Although light has been used to image surface structures for the last 100 years, its use to measuring large organs and probe internal structures has been limited mainly due to the high scattering that tissue exhibits in the visible and Near Infrared region. In the late 1980's photon propagation in tissue was modeled with a simple differential equation, the diffusion equation. This led to

a small revolution that fueled the "photon diffusion" field. The field flourished in the 1990's because the use of rigorous light propagation models in tissue opened up new ways to perform quantitative spectroscopy and tomography of deep tissue. Furthermore several technological advances have made the manipulation of light a more cost-effective and clinically feasible process. The enthusiast of optical and electronic technology can delve in a plethora of technologies such as laser diodes, miniaturized photo-multiplier tubes and CCD cameras to construct instruments that exploit light. From single photon counting to the use of polarized light and fluorescence, the field is now expanding rapidly in many fascinating biomedical applications.

The present work attempted to link theory with clinical application and has targeted the leading contributor to cancer mortality in women aged 15-54: breast cancer. The purpose was two fold: First the theory had to be validated clinically and its performance should be evaluated. Second the contrast and physiology of breast tumors would be studied by resolving the hemoglobin concentration and saturation as well as the contrast agent uptake. In order to pursue this venue a diffuse optical tomographer based on the single-photon counting time correlated technique was developed and coupled to a Magnetic Resonance scanner to obtain simultaneous DOT-MRI examinations of the same breast under the same geometry and physiological conditions. Imaging of intrinsic contrast and of the distribution of contrast agents was performed with both modalities. The scheme offered the opportunity for a highly correlated study where the DOT findings could be compared against an established clinical imaging modality. Since all patients entered the study were also scheduled for biopsy, histopathological information was also available as the "Gold Standard" for the diagnostic performance. Besides the validation of DOT as a stand-alone imaging modality, the simultaneous examination pioneers a hybrid diagnostic modality where MR information and image-guided localized diffuse optical spectroscopy (DOS) information are concurrently available. In the present application the MR information is used to simplify the DOT problem and thus make possible the spectral quantification of selected structures in the tissue.

In the chapters that follow theory fundamentals, instrumentation and experimental specifics and clinical results are presented. Special attention has been given to imaging highly heterogeneous structures such as tissue with and without contrast agents. Issues pertaining to the experimental optimization of Diffuse Optical Tomography are presented. Furthermore the theory and experimental methodology for performing spectroscopy and image guided localized spectroscopy are presented. **Chapter 2** presents the general motivation for developing alternative imaging methods for breast cancer detection and outlines the role and feasibility of the optical method. **Chapter 3** reviews the fundamentals of photon propagation in tissue and describes analytical solutions for performing spectroscopy and tomography. **Chapter 4** presents methodologies for performing diffuse optical spectroscopy in tissues in the three light-source domains, namely the constant-intensity domain, the modulated-intensity domain (frequency domain) and the pulsed-intensity domain (time-domain). A sensitivity analysis employing realistic experimental uncertainties is given and robust fitting alternatives are presented. **Chapter 5** presents the methodology for performing tomography and image-guided localized spectroscopy. **Chapter 6** describes practical and experimental issues in performing tomography of tissue. The consequences arising from imaging optically heterogeneous structures such as the breast is outlined and algorithms for improving the performance of DOT are given. The work in this chapter was initiated when seeking an understanding of the original clinical results and ignited a better insight of the performance of DOT clinically, by verifying the findings and hypotheses with simulated data, and developing DOT improvements in an iterative manner. **Chapter 7** reports on the development of the time-domain tomographer/spectrometer and gives the spectroscopic and tomographic performance evaluation of the instrument with laboratory measurements of breast like phantoms. **Chapter 8** describes the clinical examination protocol and the tools developed for MR-DOT image coregistration and for coupling MRI and DOT in a hybrid modality. **Chapter 9** describes and discusses the clinical results. Finally **Chapter 10** concludes the findings and the experience of this work and points to future directions.

2 Breast cancer and the optical method

This chapter briefly outlines the severity of breast cancer in our society, the need for alternative breast cancer diagnostic methods and the role that the optical method can play in preventing breast cancer.

2.1 Increasing Sensitivity and Specificity in Breast Cancer Detection.

It has been estimated that 1 out of every 9 women will develop breast cancer during her lifetime and approximately 30% of them will die of the disease [2,3].

The beneficial effect of screening mammography has been shown in several studies world-wide where 20%-50% reduction in breast cancer mortality with screening has been demonstrated [4,5,6,7,8,9,10]. In general, the smaller the lesion at the time of detection, the better the treatment efficiency [11,12]. Conversely, while mammography has clearly become the method of choice in the detection of early, clinically occult breast cancer, it has

limitations. First, of all the breast cancers, only an average of 88% are seen on mammography [13]. Secondly the positive predictive value PPV for mammographic screening ranges from 3% to 38%. The variability of PPV values reported in the literature depends on the patient age, on issues pertaining to how the study was performed and on the systematic screening follow-up of selected low suspicious lesions [14,15]. For an estimated 150,000 new cases of breast cancer diagnosed employing biopsy each year and an average of 20% true positive rate, approximately 750,000 breast biopsies will be performed to make these diagnoses. The lack of mammographic specificity subjects many women with benign breast disease to unnecessary biopsy. In fact, it has been estimated that the expense of biopsies is the major cost of screening mammography programs, accounting for 32.2%, slightly more than the cost of the mammograms themselves [16].

Based on the mammographic performance it would be very advantageous to develop ways to decrease the number of benign breast biopsies, without compromising the ability to effectively screen for breast cancer. The introduction of needle biopsy in the form of stereotactic fine needle aspiration biopsy (FNAB) [17,18,19,20] and stereotactic core-needle biopsy (SCNB) [21,22] have received attention lately as alternatives to surgical biopsy. The techniques are less invasive than surgical biopsy, cost effective and especially SCNB has an average reported false negative rate close to that of surgical biopsy (~5%) [23,24]. Nevertheless they remain invasive procedures requiring a skilled cyto-pathologist and lesion localization expertise. High-resolution ultrasound has gained interest during the last few years because it has shown ability to characterize some mammographically detected abnormalities by differentiating cysts from solid lesions. However, it is not generally considered a technique to characterize solid breast masses. CT scanning has not demonstrated any significant role in the evaluation of patients with suspicious breast lesions [25]. Magnetic Resonance Imaging (MRI) offers exciting potential for increased tissue characterization compared to other imaging modalities [26, 27, 28]. In this case cancers are differentiated mainly based on features extracted after the intravenous administration of Gadolinium chelates. Such features include architectural characteristics of the enhancement [29,30,31,32], the kinetics of the uptake and release of the contrast agent [33] and the relative

enhancement of lesions compared to background and other structures [29,31]. Reported sensitivity and specificity values average to 91% and 78% respectively [26,27]. Furthermore certain biochemical and physiological parameters, as investigated by Magnetic Resonance Spectroscopy (MRS), have shown the potential to add specificity in cancer characterization. Specifically the phosphocreatine / phospho-ethan-olamine peak in ^{31}P-MRS [34,35,36,37] and the choline peak in ^{1}H-MRS [37, 38] are generally increased in malignant lesions.

This plethora of imaging and spectroscopic methods, offers the exciting potential to follow up the initial mammographic finding with a second diagnostic technique. The combination of different diagnostic modalities is necessary because so far, the reported ROC curves for the different non-invasive diagnostic techniques indicate that no single method would suffice alone to perform satisfactory breast cancer detection. It is anticipated that the combined results of multi-modality examinations would result in increased specificity. In that respect it would be beneficial to combine modalities that yield features that are disease-predictive but not correlated to each other, since high correlation would indicate data redundancy.

2.2 The role of the optical method in breast cancer detection.

NIR methods offer novel criteria for cancer differentiation with the ability to in-vivo measure oxygenation and vascularization state, the uptake and release of contrast agents and organelle concentration in an economical and portable package. These properties are believed to be malignancy specific and may significantly contribute to increased specificity.

Breast cancer, above a few millimeters in diameter, initiate very active angiogenesis, believed to be characteristic of all rapidly growing tumors [39,40]. The increase of blood vessels does nevertheless fail to deliver adequate oxygen to the tumor and thus most tumors are hypoxic [41]. Therefore the optical technique, with its unique ability to measure oxygenation state and blood volume content represents an excellent candidate for cancer diagnosis. The optical method, being a functional probe, offers a new dimension for tumor

differentiation that promises to offer enhanced detection specificity, especially when combined with the sensitivity and high resolution of existing imaging methods.

Furthermore, the optical method affords access to "colorimetric" contrast agents where the organic chemistry and the feasibility of effective tailoring of substituents to afford high specificity can ultimately be studied. It has been pointed out [39, 42, 43] that neovascularization leads to leaky blood vessels that allows penetration of NIR contrast agents into the extravascular space and is expected to yield additional contrast between malignancy and other types of tissue. Indocyanine green (ICG) is the only known NIR-absorbing dye with a high extinction coefficient that has been approved for human use, e.g. for studies of liver and cardiac function and angiography. There are however, many opportunities to develop better optical contrast agents that show high absorption and fluorescence and target functional features of tumors. Companies that are interested in NIR contrast agents are numerous, for example, Optimedx of Seattle, WA, Fuji Color of Japan, Malinckrodt Medical Products, Molecular Devices, Schering Berlin etc. It is expected that it will be an intense effort to convert many of the fluorescent probes used for cell and molecular biological studies to the NIR "window" to enable their use in tissues. Increased sensitivity and specificity may be achieved by the use of the old or new generation of probes.

Recently a new class of biocompatible, optically quenched near infrared fluorescence (NIRF) imaging probes has been developed [44]. The NIRF probes are activated by proteolytic enzymes, which are usually at elevated levels in several tumors, presumably in adaptation to rapid cell cycling; removal of unnecessary regulatory proteins and for secretion to sustain invasion, metastasis formulation and angiogenesis. Recent studies [45] using the NIRF probes in cell cultures and mammary tumors implanted into nude mice, close to the surface, have demonstrated a 12-fold increase in tumor contrast, allowing the detection of sub-millimeter tumors. These probes overcome the limitations of traditional fluorescent contrast agents that may accentuate non-specific differences and yield a contrast that is typically less than 4:1. Advanced DOT technology and low noise detection systems can be used to reconstruct the accumulated NIRF probes in deep-seated sub-millimeter cancers and

yield highly sensitive early cancer detection modality. It is envisaged that molecular-level probing will lower the limits of early cancer detection since detection can occur before anatomic changes, usually detected by common radiologic techniques become apparent.

3 Theory of photon diffusion

This chapter reviews the key points in the derivation of the diffusion equation and outlines the analytical solutions developed for homogeneous and heterogeneous media with simple boundary conditions. The purpose of this chapter is to serve as a reference for the developments described in Chapters 3-8. The review is primarily based on the publications by Haskel et. al.[53] , Patterson et.al.[50] on solutions of the diffusion equation in the presence of boundaries, on the theses of Maureen O'Leary [55] and David Boas [46] who studied and concisely described aspects of the propagation of diffuse photon density waves and tomographic principles for Diffuse Optical Tomography and on the book "Principles of Computerized Tomography" by Kak and Slaney. These theoretical treatments constitute the starting point for the work presented in this thesis and for this reason they received my main focus. Many other scientists have significantly contributed to the developments of the BioMedical Photon Diffusion field and some of their work is referenced in this and subsequent chapters.

Section 3.1 links the radiance with the photon fluence rate and flux in a diffuse homogeneous medium and illuminates the key steps and approximations that lead to the diffusion equation. **Section 3.2** describes solutions derived for the homogeneous diffusion equation in the time and frequency domain. **Section 3.3** outlines the effect of a diffuse non-diffuse planar boundary on the propagation of diffuse photon density waves and discusses the partial current and extrapolated boundary condition and the corresponding solutions. **Section 3.4** gives solutions for the homogeneous diffusion equation in the presence of boundaries. **Section 3.5** assess the Born and Rytov solutions of the heterogeneous diffusion equation for diffuse media with spatially varying absorption, scattering or fluorescence properties. Finally **section 3.6** indicates practical differences between the Born and Rytov approximation.

3.1 From transport to diffusion

The propagation of incoherent photons in a scattering and absorbing medium is described by the Boltzmann transport equation, i.e.,

$$\frac{1}{c}\frac{\partial L(\vec{r},\hat{s},t)}{\partial t}+\nabla\cdot L(\vec{r},\hat{s},t)\hat{s}=-(\mu_a+\mu_s)L(\vec{r},\hat{s},t)+\mu_s\iint_{4\pi}L(\vec{r},\hat{s},t)f(\hat{s}\cdot\hat{s}')d\hat{s}'+Q(\vec{r},\hat{s},t)\,, \qquad \textbf{(3-1)}$$

where $L(\vec{r},\hat{s},t)$ is the radiance [W/(m^2 sr)] at position $\vec{r}$, at time *t*, propagating along the unit vector $\hat{s}$. The absorption coefficient μ_a [cm^{-1}] and the scattering coefficient μ_s [cm^{-1}] are the inverses of the absorption and scattering mean free paths respectively and c [cm/sec] is the speed of light in the medium. The function $f(\hat{s}\cdot\hat{s}')$ is the probability density function (pdf) over all solid angles of the change in photon propagation direction from $\hat{s}$ to $\hat{s}'$ due to an elastic scattering event. We have for any pdf, $\iint_{4\pi}f(\hat{s}\cdot\hat{s}')d\hat{s}'=1$. $Q(\vec{r},\hat{s},t)$ [W/(m^3 sr)] is the photon power injected per unit volume at position $\vec{r}$ along $\hat{s}$.

Integration over all solid angles converts Eq.(3-1) to a simpler form, i.e.:

$$\frac{1}{c}\frac{\partial \phi(\vec{r},t)}{\partial t} + \nabla \cdot \vec{j}(\vec{r},t) = -\mu_a \phi(\vec{r},t) + S(\vec{r},t), \quad \textbf{(3-2)}$$

where

$$\phi(\vec{r},t) = \iint_{4\pi} L(\vec{r},\hat{s},t)d\Omega, \quad \textbf{(3-3)}$$

is the photon fluence rate [W/cm^2],

$$\vec{j}(\vec{r},t) = \iint_{4\pi} L(\vec{r},\hat{s},t)\hat{s}d\Omega, \quad \textbf{(3-4)}$$

is the photon flux [W/cm^2] and

$$S(\vec{r},t) = \iint_{4\pi} Q(\vec{r},\hat{s},t)d\Omega, \quad \textbf{(3-5)}$$

is the integrated source term [W/cm^3].

Eq.(3-1) and subsequently Eq.(3-2) reflect energy conservation in the system. Mathematically, the use of this equation for tissue measurements imposes several practical limitations due to its integral-differential nature. Therefore approximations have been developed to convert the transport equation to more manageable but functional forms. A standard approach expands the radiance and source term in a series of spherical harmonics. Truncation of the series at N terms can simplify the transport equation and is denoted as the P_N approximation. The simplest and most commonly used approximation is the first order P_1 approximation where N=1. This approximation further reduces to the diffusion equation in a step-wise simplification sequence. This reduction effectively describes the limits of the diffusion approximation. Often, when some approximations do not hold, one has to backtrack in the derivation and retrieve a formulation that better describes his specific

problem. The relations between radiance, fluence rate and flux are fundamental in describing appropriate boundary conditions for realistic measurements. Here I outline the key steps within the P_1 approximation that yield the diffusion equation.

In the P_1 approximation, the expansion of the radiance can be written as [53]

$$L(\vec{r},\hat{s},t)=\frac{1}{4\pi}\phi(\vec{r},t)+\frac{3}{4\pi}\vec{j}(\vec{r},t)\cdot\hat{s}\,. \qquad \textbf{(3-6)}$$

This approximation works well when scattering is much stronger than absorption. Eq.(3-6) expresses the radiance as the summation of the isotropic fluence rate $\phi(\vec{r},t)$ and a small directional photon flux. Additionally, in order to obtain the diffusion equation the source is assumed isotropic. Under the P1 and diffusion approximations, the substitution of Eq.(3-6) into Eq.(3-1), subsequent multiplication by $\hat{s}$, and integration over all solid angles yields

$$\frac{3}{c}\frac{\partial\vec{j}(\vec{r},t)}{\partial t}=-\vec{\nabla}\phi(\vec{r},t)-\frac{1}{D}\vec{j}(\vec{r},t)\,, \qquad \textbf{(3-7)}$$

where

$$D=\frac{1}{3[(1-g)\mu_s+\mu_a]}=\frac{1}{3[\mu_s'+\mu_a]} \qquad \textbf{(3-8)}$$

is the diffusion coefficient, g is the anisotropy coefficient and expresses the average cosine of the scattering angle. For biological tissues g≈0.9, which indicates scattering in the forward direction. For isotropic scattering g=0. The reduced scattering coefficient μ_s' is a construction that approximates the diffusion of photons as an isotropic scattering phenomenon, even though each individual scattering event is primarily towards the forward direction. The reduced scattering coefficient is the reciprocal of the mean random-walk step, (i.e. the average distance a photon travels in tissue before its initial direction is randomized). Since Eq.(3-6) and subsequent derivations are valid under the assumption that $\mu_s' >> \mu_a$ the

dependence of the diffusion coefficient on the absorption coefficient is often dropped i.e., $D = 1/3\mu_s'$.

The Fourier Transform of Eq.(3-7) after rearrangement yields

$$\vec{j}(\vec{r}) = -\frac{cD}{c - 3i\omega D}\vec{\nabla}\phi(\vec{r}) . \qquad \textbf{(3-9)}$$

For most biological applications $c >> 3\omega D$ for $\omega < 2\pi$ GHz, so that

$$\vec{j}(\vec{r}) \approx -D\vec{\nabla}\phi(\vec{r}) . \qquad \textbf{(3-10)}$$

Combining Eq.(3-10) with the Fourier transform of Eq.(3-2) yields the frequency domain diffusion equation

$$-\frac{i\omega}{c}\phi(\vec{r}) - D\vec{\nabla}^2\phi(\vec{r}) + \mu_a\phi(\vec{r}) = S(\vec{r}) . \qquad \textbf{(3-11)}$$

Direct substitution of Eq.(3-10) in Eq.(3-2) yields the time-domain equivalent, i.e.:

$$\frac{1}{c}\frac{\partial\phi(\vec{r},t)}{\partial t} - D\vec{\nabla}^2\phi(\vec{r},t) + \mu_a\phi(\vec{r},t) = S(\vec{r},t) . \qquad \textbf{(3-12)}$$

Eq.(3-11) and Eq.(3-12) have been derived for the fluence rate established in a homogeneous infinite medium with a spatially invariant diffusion coefficient *D* and absorption coefficient μ_a due to the disturbance of the photon source. It is also valid in the domains of any piecewise homogeneous media.

3.2 Solutions of the diffusion equation for homogeneous media.

Solutions are easily derived for the diffusion equation in the time and frequency domain for a delta driving function in Eq.(3-12) and Eq.(3-11) respectively. The impulse response of an infinite diffuse medium has been given by Patterson et. al. [50]. i.e.:

$$\phi(|r-r_s|,t)=\frac{c}{(4\pi cDt)^{-3/2}}\exp(-\frac{|r-r_s|^2}{4Dct}-\mu_a ct)\,. \qquad \textbf{(3-13)}$$

In the frequency domain the diffusion equation can be written as a Helmholtz equation. If we further assume an intensity modulated point source $\delta(\vec{r}_s)$ with gain A at position $\vec{r}_s$ Eq.(3-11) can be rewritten as

$$[\vec{\nabla}^2+k^2]\phi(\vec{r},\vec{r}_s)=-A\frac{\delta(\vec{r}_s)}{D}\,, \qquad \textbf{(3-14)}$$

where

$$k^2=\frac{-c\mu_a+i\omega}{cD}\,. \qquad \textbf{(3-15)}$$

The solution of the Helmholtz equation (Eq.(3-14)) is

$$\phi(|\vec{r}-\vec{r}_s|)=\frac{A}{4\pi D|\vec{r}-\vec{r}_s|}\exp(-ik|\vec{r}-\vec{r}_s|)\,, \qquad \textbf{(3-16)}$$

and describes a scalar, damped propagating wave, called the diffuse photon density wave at modulation frequency ω. The wave described by Eq.(3-16) is an "alternating intensity" wave, "carried" on a constant intensity photon distribution in the medium i.e. a constant intensity (zero-frequency) diffuse photon density wave. The two waves can be assumed linearly superimposed and practically separated by simple filtering. For ω=0 Eq.(3-16) yields the solution for a photon source of constant intensity. Use of photon waves at zero frequency (constant intensity) constitute the Constant Wave (CW) domain.

The solutions given by Eq.(3-13) and Eq.(3-16) describe the propagation of diffuse photon density waves in infinite homogeneous media and since they are derived for delta forcing functions they are usually referred to as the "Green's functions" or "Green's function solutions" for the diffusion equation in each corresponding domain. Solutions for more complicated photon sources can be derived by convolution of the photon source function and the corresponding Green's function solution. These solutions however have restricted practical application in tissue measurements since tissue is hardly an infinite medium. In the following two sections the effect of boundaries on diffuse photon density wave propagation is examined and some common solutions in the presence of boundaries are given.

3.3 Boundary effects.

For non-invasive tissue measurements, we need solutions that account for the effect of the boundaries. Here the derivation of boundary conditions for a diffuse/non-diffuse planar boundary (semi-infinite diffuse medium) such as a geometrically simplified air-tissue interface is reviewed. This fundamental formulation can be then applied to more complicated geometries either analytically or numerically.

Photons that impinge on a boundary will be transmitted and reflected in a manner that depends on the properties of this interface (i.e. the optical properties of the media on both sides of the interface). The radiance L_b that will be reflected back from the boundary to the medium due to an incident radiance L is given by [47,48,49]:

$$L_b = \iint_{\hat{s}\cdot\hat{z}>0} R_{Fresnel}(\hat{s}) L(\hat{s}) \hat{s}\cdot\hat{z} d\hat{s}\,, \qquad \textbf{(3-17)}$$

where $\hat{z}$ is the unit vector normal to the boundary pointing outwards from the medium of interest as shown in Figure 3-1 and $R_{Fresnel}(\hat{s})$ is the Fresnel reflection coefficient for light incident upon the boundary in a direction $\hat{s}$ from within the medium[53].

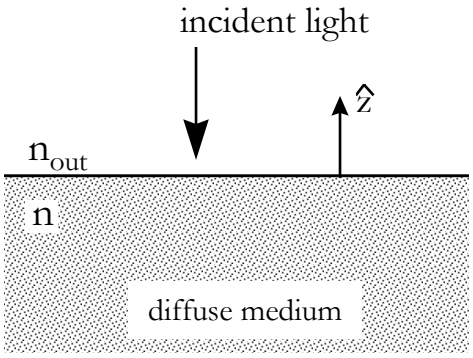

Figure 3-1: Configuration assumed in the calculation of the photon field detected from a diffuse non-diffuse interface

If $\theta_c = \sin^{-1}(n_{out}/n)$ is the critical angle for total internal reflection, θ is the angle of incidence from within the medium, (i.e. $\cos\theta = \hat{s}\cdot\hat{z}$), and θ' is the refracted angle outside the medium (i.e. $n\sin\theta = n_{out}\sin\theta'$), then the Fresnel reflection coefficient for unpolarized light is

$$R_{Fresnel}(\hat{s}) = 1 \text{ for } \theta_c \le \theta < \pi/2$$

$$R_{Fresnel}(\theta) = \frac{1}{2}\left(\frac{n\cos\theta' - n_{out}\cos\theta}{n\cos\theta' + n_{out}\cos\theta}\right)^2 + \frac{1}{2}\left(\frac{n\cos\theta - n_{out}\cos\theta'}{n\cos\theta + n_{out}\cos\theta'}\right)^2 \qquad \textbf{(3-18)}$$

$$\text{for } 0 \le \theta < \theta_c .$$

Eq.(3-16) can be simplified then as

$$L_b = \iint_{\hat{s}\cdot\hat{z}>0} R_{Fresnel}(\hat{s})L(\hat{s})\hat{s}\cdot\hat{z}d\hat{s} = R_\phi\frac{\phi}{4} - R_j\frac{j_z}{2}, \qquad \textbf{(3-19)}$$

where

$$R_\phi = \int_0^{\pi/2} 2\sin\theta\ \cos\theta\ R_{Fresnel}(\theta)d\theta,$$

$$R_j = \int_0^{\pi/2} 3\sin\theta\ \cos^2\theta\ R_{Fresnel}(\theta)d\theta. \qquad \textbf{(3-20)}$$

The back reflected radiance L_b should be also given by integrating the radiance for all angles that $\hat{s}\cdot\hat{z}<0$, using Eq.(**3-6),** i.e.

$$L_b=\iint_{\hat{s}\cdot\hat{z}<0} L(\hat{s})\hat{s}\cdot(-\hat{z})d\hat{s}=\frac{\phi}{4}+\frac{j_z}{2}. \qquad \textbf{(3-21)}$$

By combining Eq.(3-18) with Eq.(3-20) we obtain:

$$R_\phi\frac{\phi}{4}-R_j\frac{j_z}{2}=\frac{\phi}{4}+\frac{j_z}{2}, \qquad \textbf{(3-22)}$$

or

$$\phi=-2\frac{1+R_j}{1-R_\phi}j_z. \qquad \textbf{(3-23)}$$

Eq.(3-22) gives a relation between the flux and fluence rate in the boundary. Haskel et.al. [53] has noted that $|j_z|/|\phi|\approx 0.2$ for the expected index of refraction mismatch at the boundary of tissue measurements the ratio. This relation is hardly in agreement with the diffusion approximation that requires $|j_z|<<|\phi|$ and its effect should be considered in the evaluation of results. Under this condition however the back-reflected radiance can be defined by means of a reflection coefficient R_{eff} i.e.

$$L_b=R_{eff}\iint_{\hat{s}\cdot\hat{z}>0} L(\hat{s})\hat{s}\cdot\hat{z}d\hat{s}=R_{eff}\left(\frac{\phi}{4}-\frac{j_z}{2}\right), \qquad \textbf{(3-24)}$$

where

$$R_{eff}=\frac{R_\phi+R_j}{2-R_\phi+R_j}. \qquad \textbf{(3-25)}$$

3.4 Solutions of the diffusion equation in the presence of boundaries.

Eq.(3-23) gives a relation between the photon fluence rate and photon flux at the boundary and it is commonly referred to as the partial-current boundary condition. Using Eq.(3-10) we can find the equivalent of the partial boundary condition expressed for fluence rate only, i.e.,

$$\phi = -2D\frac{1+R_j}{1-R_\phi}\frac{\partial\phi}{\partial z} = 2D\frac{1+R_{eff}}{1-R_{eff}}\frac{\partial\phi}{\partial z} \text{ at } z=0. \qquad \textbf{(3-26)}$$

This is a mixed Dirichlet-Neuman boundary condition that can be applied directly to a numerical solution of the diffusion equation.

For obtaining analytical solutions of the diffusion equation in the presence of a planar boundary a different approach is followed. The general strategy is to approximate the source term with a sum of isotropic point sources, using appropriate image sources and sinks to satisfy Eq.(3-22) or Eq.(3-26) in the medium of interest using the principle of superposition. Two approaches have been reported yielding similar and most accurate results. The first approach assumes that the photons injected in the surface of a diffuse medium are effectively equivalent to an isotropic point source at a depth $z_0=1/\mu_s'$ ($z=z_0$, $\rho=0$), i.e. at one mean random walk step under the surface, an image source located at z_b above the boundary ($z=-z_0$, $\rho=0$) and an exponentially decaying photon sink along z at $z=-z_0$, $\rho=0$, decaying exponentially away from the boundary at a rate $\exp(-|z|-z_0/z_b)$, $|z|>z_0$ as shown in Figure 3-2. The total strength of the photon sink equals the strength of the real and image source.

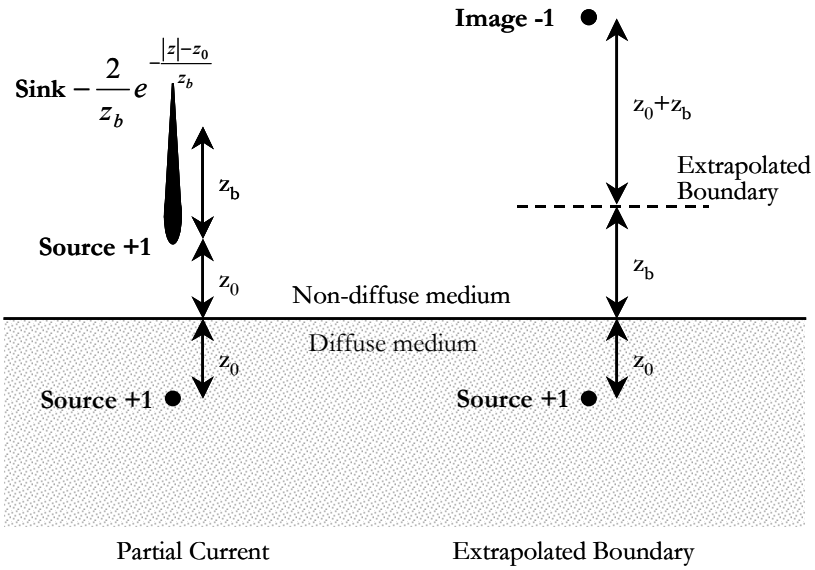

Figure 3-2: Partial boundary condition configuration (left) and extrapolated boundary condition configuration (right)

This approach most closely matches the partial current boundary condition. However a simpler construction, the extrapolated boundary condition [50,51,52] offers implementation simplicity and reasonable accuracy. This second method assumes an isotropic point source at $z=z_0$, $\rho=0$, and a point sink at $z=-z_0-2z_b$, $\rho=0$ (as also shown in Figure 3-2) where z_b is given by

$$z_b = \frac{2}{3\mu_s'} \frac{1+R_{eff}}{1-R_{eff}}. \qquad \textbf{(3-27)}$$

Haskel et. al. [53] have shown that the partial-current and the extrapolated boundary conditions give solutions that are equal to within 3% at source detector distances larger than

~5 mm for tissue optical properties. Since the results between the two boundary conditions are very similar we will focus on solutions obtained using the extrapolated boundary condition because it results in simpler analytical expressions. The extrapolated boundary condition sets the fluence rate to zero at the extrapolated boundary, i.e. at $z=-z_b$. This extrapolated boundary obviously depends on the scattering properties of the medium and the index of mismatch at the interface. Table 3-1 tabulates the extrapolated length for a physiological range of scattering coefficients and for an 1) air-tissue, 2) water-tissue and 3) resin-tissue interfaces.

Table 3-1: Extrapolated depth (in cm) for combinations of index of refraction and reduced scattering coefficients.

μ_s' (cm^{-1})	3	5	7	9	11	13	15
$n/n_0=1.00$	0.222	0.133	0.095	0.074	0.060	0.051	0.044
$n/n_0=1.333$	0.559	0.335	0.239	0.186	0.152	0.129	0.112
$n/n_0=1.400$	0.570	0.342	0.244	0.190	0.155	0.131	0.114

Using the diffuse photon density wave solution for the infinite case and applying the principle of superposition for the real and image sources we can reach simple analytical expressions for a planar boundary interface (reflectance geometry). For the coordinate system shown in Figure 2, and assuming a distance $z_c = 2z_b + z_0$, the time domain solution can be derived as a superposition of Eq.(3-13) for the real and image sources, i.e.,

$$\phi(\rho,z,t)=\frac{Ac}{(4\pi cDt)^{-3/2}}\exp(-\mu_a ct)\left(\exp\left(-\frac{r_0^2}{4cDt}\right)-\exp\left(-\frac{r_c^2}{4cDt}\right)\right), \qquad \textbf{(3-28)}$$

where

$$r_0=\sqrt{|z-z_0|^2+\rho^2}\ , \qquad \textbf{(3-29)}$$

$$r_c=\sqrt{|z+z_c|^2+\rho^2}\ . \qquad \textbf{(3-30)}$$

Using Eq.(3-16) for the same coordinate system of Figure 2 we obtain the frequency domain reflectance solution, i.e.

$$\phi(\rho,z)=\frac{A}{4\pi cD}\left(\frac{\exp(-ikr_0)}{r_0}-\frac{\exp(-ikr_c)}{r_c}\right). \qquad \textbf{(3-31)}$$

The use of image sources can be used to describe analytically more complicated geometries. For example Patterson et. al. [50] have used the method of image sources to provide analytical solutions for the infinite slab, namely a diffuse medium that is confined between two infinite slabs as shown in Figure 3 (transmittance geometry). The methodology, as further described by Farell. et. al. [51] and others is to employ a series of dipoles (pairs of a positive and a negative source) that effectively set the flux to zero at the two extrapolated boundaries assumed for the two planar interfaces. For M number of dipoles (pairs of a positive and negative source) and a slab of thickness *d*, the analytical solution for transmittance geometry in the time domain is

$$\phi(\rho,z,t)=\frac{Ac}{(4\pi cDt)^{-3/2}}\exp(-\mu_a ct)\sum_{m=1}^{M}\left(\exp\left(-\frac{R_0^2(m)}{4cDt}\right)-\exp\left(-\frac{R_c^2(m)}{4cDt}\right)\right), \qquad \textbf{(3-32)}$$

where

$$R_0(m)=\left(\left(2\cdot floor\left(\frac{m}{2}\right)d'+(-1)^{m-1}(z-z_0)\right)^2+\rho^2\right)^{1/2}, \qquad \textbf{(3-33)}$$

$$R_c(m)=\left(\left(2\cdot floor\left(\frac{m}{2}\right)d'+(-1)^{m-1}(z+z_c)\right)^2+\rho^2\right)^{1/2}, \qquad \textbf{(3-34)}$$

$$d'=d+2z_b, \qquad \textbf{(3-35)}$$

floor(x) is the nearest integer of x towards minus infinity and $0 < z < d$. For M=1 Eq.(3-32) yields the solution derived for reflectance, namely Eq.(3-28). Similarly in the frequency domain the transmittance solution is

$$\phi(\rho, z) = \frac{1}{4\pi c} \sum_{m=1}^{M} \left(\frac{\exp(-ikR_0(m))}{R_0(m)} - \frac{\exp(-ikR_c(m))}{R_c(m)} \right), \qquad \textbf{(3-36)}$$

which for N=1 also reduces to Eq.(3-31).

Usually retaining only 4 pairs dipoles suffices to satisfy the boundary conditions for practical implementations [50], since the contributions of additional dipoles become very small. The thicker the slab, the better this approximation performs. For thin slabs (of the order of 1cm or thinner) keeping additional dipoles may be necessary for improved accuracy. For media bounded by additional perpendicular planar interfaces, one could use the method of image sources to satisfy the boundary conditions. However for increased boundary complexity, numerical methods become the method of choice due to their ability to effectively model irregular boundaries.

The solutions given for reflectance and transmittance, describe the photon fluence rate in the bounded media. For experimental measurements the component detected by a lens system or a fiber placed on the surface, is the radiance (Eq.(3-6)) emitted from the diffuse medium and integrated over the numerical aperture. Haskel et. al. [53] have shown that the detected signal for the extrapolated boundary condition is approximately proportional to the fluence rate. On the other hand, Kienle et.al. [54] has found that using both the fluence rate and the flux terms to model the detected signal gave better boundary models in the time domain and CW domain. He also noted that the extrapolated boundary formulation that retains the fluence rate and flux terms predicts better time-resolved profiles at early times (100-200 picoseconds) than the partial current boundary. Farell et.al. [51] has compared the extrapolated boundary condition with a boundary model that used an extended source, similar but not identical to the requirements of a partial current boundary

condition. Monte Carlo and experimental measurements demonstrated in that study that both models were predicting accurately the photon intensity of steady state diffuse reflectance for source-detector separations larger than 1 mean free path. The extrapolated boundary condition was found to outperform the extended source model even at source detector separations smaller than 1 mean free path.

Generally, investigators agree that most boundary model differences occur close to the limits of the diffusion approximation, namely for source detector separations close or under a mean free path. In the time domain this also reflects to times shorter than ~100-200 picoseconds where the photons considered have not had time to become diffuse. The present work is mainly concerned with human tissue measurements where these diffusion approximations limits are generally reached. Therefore it assumes the simpler of the solutions, namely the one suggested by Haskel et.al.[53] in considering the detected signal proportional to the fluence rate and the extrapolated boundary condition including corrections for index of refraction mismatch at the boundary. The discussion and the expressions derived in the following chapters implicitly carry this boundary model. However it is straightforward in most cases to adapt the methodology of the following chapters in smaller dimension problems by deriving Greens functions for the most appropriate boundary models given the geometrical constrictions of the specific problem.

3.5 Solutions of the diffusion equation for heterogeneous media

The discussion in sections 3.1-3.4 focused on homogeneous diffuse media, namely media where the diffusion coefficient was spatially invariant. Here we will focus on analytical solutions derived on the premise of heterogeneous media where the diffusion coefficient is spatially varying. The analysis will be performed in the frequency domain since the frequency decomposition leads to simpler analytical expressions. Data obtained in the time-domain can be effectively converted to the frequency domain using the Fourier Transform. We will

begin by noticing that if the diffusion coefficient has a spatial dependence, i.e. $D = D(\vec{r})$, the substitution of Eq.(3-10) to Eq.(3-2) (after taking the Fourier transform) yields:

$$-\frac{i\omega}{c}\phi(\vec{r}) - \vec{\nabla}D(\vec{r})\vec{\nabla}\phi(\vec{r}) + \mu_a\phi(\vec{r}) = S(\vec{r}) . \qquad \textbf{(3-37)}$$

In general it is very difficult to derive analytical solutions for the general case of Eq.(3-37). The most common approach to solve the heterogeneous case is the perturbation method, which makes Eq.(3-37) linear by assuming that the medium's heterogeneity can be described as small variations around a homogeneous background. The solutions further simplify in media where only the absorption or only the reduced scattering coefficient varies [55]. In the following we will outline the solutions for heterogeneous absorption, scattering and fluorescence.

3.5.1 Solutions derived for absorptive heterogeneity

The diffuse regime assumes that $\mu_s' >> \mu_a$. When only absorption heterogeneity exists, μ_s' is constant, $\mu_a = \mu_a(\vec{r})$, and $\mu_s' >> \mu_a(\vec{r})$ so that $D \approx 1/3\mu_s'$. Then Eq.(3-37) reduces to Eq.(3-11).

Using perturbation theory, the absorption coefficient is divided into a background average component and a spatially varying component, i.e.,

$$\mu_a(\vec{r}) = \mu_{a0} + \delta\mu_a(\vec{r}) . \qquad \textbf{(3-38)}$$

We will assume that the driving function of Eq.(3-37) is an intensity-modulated point source at position $\vec{r}_s$ with gain A, i.e. $S(\vec{r}) = A\delta(\vec{r}_s)$. Then substitution of Eq.(3-38) to Eq.(3-37) yields the heterogeneous diffusion equation for absorption variations, i.e.

$$[\vec{\nabla}^2 + k^2 + O(\vec{r})]\phi(\vec{r},\vec{r}_s) = A\frac{\delta(\vec{r}_s)}{cD_0}, \quad \textbf{(3-39)}$$

where

$$O(\vec{r}) = \frac{\delta\mu_a(\vec{r})}{D_0}, \quad \textbf{(3-40)}$$

and D_0 denotes the background, spatially invariant diffusion coefficient.

The fluence rate $\phi(\vec{r})$ in Eq.(3-39) contains contributions from both the homogeneous background medium with absorption coefficient μ_{a0} and from the distributed heterogeneity $\delta\mu_a(\vec{r})$. This field can be expanded appropriately as a superposition of the 0^{th} order fluence rate due to μ_{a0} and higher order terms due to the heterogeneous distribution $\delta\mu_a(\vec{r})$. By keeping only the 0^{th} and 1^{st} order terms the problem effectively becomes linear and thus easy to solve. There are two common ways to perform this expansion; the Born and the Rytov expansions.

The Born expansion. The Born expansion writes the total fluence rate or <u>total field</u> $\phi(\vec{r},\vec{r}_s)$ as

$$\phi(\vec{r},\vec{r}_s) = \phi_0(\vec{r},\vec{r}_s) + \phi_{sc}(\vec{r},\vec{r}_s), \quad \textbf{(3-41)}$$

where $\phi_0(\vec{r},\vec{r}_s)$, the <u>incident field</u>, is the field that would have been detected if no optical heterogeneity was present and $\phi_{sc}(\vec{r},\vec{r}_s)$, the <u>scattered field</u>, is the field attributed only to the heterogeneous optical distribution. Substitution of Eq.(3-41) into Eq.(3-39) and subtraction of the homogeneous Helmholtz equation (Eq.(3-14)) yields

$$[\vec{\nabla}^2 + k^2]\phi_{sc}(\vec{r},\vec{r}_s) = -O(\vec{r})\phi(\vec{r},\vec{r}_s). \quad \textbf{(3-42)}$$

This scalar Helmholtz equation can not be solved for $\phi_{sc}(\vec{r},\vec{r}_s)$ directly but a solution can be derived as a convolution of the driving function $-O(\vec{r})\phi(\vec{r},\vec{r}_s)$ with the Green's

function solution (Eq. (3-16)) for the homogeneous Helmholtz equation. It can be shown that for the scattered field $\phi_{sc}(\vec{r}_d, \vec{r}_s)$ detected at position $\vec{r}_d$ this convolution yields

$$\phi_{sc}(\vec{r}_d, \vec{r}_s) = -\int_V g(\vec{r}_s - \vec{r}_d) O(\vec{r}) \phi(\vec{r}, \vec{r}_s) d\vec{r} \,. \qquad \textbf{(3-43)}$$

Eq.(3-43) expresses the scattered field $\phi_{sc}(\vec{r}_d, \vec{r}_s)$ as a function of the total field (i.e. $\phi_0(\vec{r}, \vec{r}_s) + \phi_{sc}(\vec{r}, \vec{r}_s)$) and therefore it still needs to be solved for $\phi_{sc}(\vec{r}_d, \vec{r}_s)$. The Born approximation simplifies Eq.(3-43) when the scattered field is weak compared to the incident field, i.e.

Born approximation : $\phi_{sc}(\vec{r}, \vec{r}_s) << \phi_0(\vec{r}, \vec{r}_s)$. **(3-44)**

This is true in the case of weak perturbations. Then

$$\phi\ (\vec{r}, \vec{r}_s) \approx \phi_0(\vec{r}, \vec{r}_s) \,. \qquad \textbf{(3-45)}$$

In the Born approximation Eq.(3-43) thus simplifies to

$$\phi_{sc}(\vec{r}_d, \vec{r}_s) = -\int_V g(\vec{r} - \vec{r}_d) O(\vec{r}) \phi_0(\vec{r}, \vec{r}_s) d\vec{r} \,. \qquad \textbf{(3-46)}$$

The Born approximation is a straightforward way to obtain a solution to the heterogeneous diffusion approximation. However it imposes many limitations both theoretically and experimentally. These limitations will be outlined in § 5.3.

The Rytov expansion. A more effective solution is obtained using the Rytov expansion which write the total field as the sum of a homogeneous $\Phi_0(\vec{r}, \vec{r}_s)$ and heterogeneous or scattered $\Phi_{sc}(\vec{r}, \vec{r}_s)$ exponential complex phase respectively, i.e

$$\phi(\vec{r},\vec{r}_s) = \exp[\Phi_0(\vec{r},\vec{r}_s) + \Phi_{sc}(\vec{r},\vec{r}_s)], \quad \textbf{(3-47)}$$

where the incident field is

$$\phi_0(\vec{r},\vec{r}_s) = \exp[\Phi_0(\vec{r},\vec{r}_s)], \quad \textbf{(3-48)}$$

and the scattered field is

$$\phi_{sc}(\vec{r},\vec{r}_s) = \exp[\Phi_{sc}(\vec{r},\vec{r}_s)]. \quad \textbf{(3-49)}$$

The analysis to derive a solution similar to the Born solution has been described [56]. Substitution of Eq.(3-47) into Eq.(3-39) and subtraction of the homogeneous Helmholtz equation for the homogeneous field in Eq.(3-48) yields the heterogeneous Helmholtz equation for the Rytov expansion, i.e.

$$[\vec{\nabla}^2 + k^2]\phi_0(\vec{r},\vec{r}_s)\Phi_{sc}(\vec{r},\vec{r}_s) = -\phi_0(\vec{r},\vec{r}_s)\left((\vec{\nabla}\Phi_{sc}(\vec{r},\vec{r}_s))^2 + O(\vec{r})\right). \quad \textbf{(3-50)}$$

Eq.(3-50) can be solved for $\Phi_{sc}(\vec{r}_d,\vec{r}_s)$, which is the scattered complex phase detected at position $\vec{r}_d$, using again the Green's function decomposition, i.e.

$$\Phi_{sc}(\vec{r}_d,\vec{r}_s) = -\frac{1}{\phi_0(\vec{r}_d,\vec{r}_s)}\int_V g(\vec{r}-\vec{r}_d)\left((\vec{\nabla}\Phi_{sc}(\vec{r},\vec{r}_s))^2 + O(\vec{r})\right)\phi_0(\vec{r},\vec{r}_s)d\vec{r}\,. \quad \textbf{(3-51)}$$

Similarly to the Born derivation, Eq.(3-51) expresses the scattered complex phase $\Phi_{sc}(\vec{r},\vec{r}_s)$ as a function of the heterogeneous distribution and the divergence of the scattered complex phase. The Rytov approximation simplifies Eq.(3-51) when the scattered complex phase is slowly varying. In this case we can assume that

Rytov approximation : $(\nabla \phi_{sc}(\vec{r},\vec{r}_s))^2 << O(\vec{r})$. **(3-52)**

Then the Rytov solution is

$$\Phi_{sc}(\vec{r}_d,\vec{r}_s) = -\frac{1}{\phi_0(\vec{r}_d,\vec{r}_s)}\int_V g(\vec{r}-\vec{r}_d)O(\vec{r})\phi_0(\vec{r},\vec{r}_s)d\vec{r}\,. \quad \textbf{(3-53)}$$

3.5.2 Solutions derived for scattering heterogeneity

The derivation of solutions for heterogeneous scattering is similar to the derivation of solutions for absorbing heterogeneity. One of the implications however is that Eq.(3-37) cannot be decomposed in a similar manner to the absorption heterogeneous case since scattering dominates the diffusion coefficient. Instead we assume that since $\mu_s' >> \mu_a$ it will also be that $\mu_s'(\vec{r}) >> \mu_a$ so that

$$D = D(\vec{r}) \approx \frac{1}{3\mu_s'(\vec{r})} = D_0 + \delta D(\vec{r})\,, \quad \textbf{(3-54)}$$

where D_0 is the average background diffusion coefficient and $\delta D(\vec{r})$ is the heterogeneous distribution or perturbation around D_0. Again, the driving function of Eq.(3-37) is assumed to be an intensity modulated point source at position $\vec{r}_s$ with gain A, i.e. $S(\vec{r}) = A\delta(\vec{r}_s)$. Substituting Eq.(3-54) into Eq.(3-37) and rearranging the terms yields:

$$D_0[\vec{\nabla}^2 + k^2]\phi(\vec{r},\vec{r}_s) + \vec{\nabla}\delta D(\vec{r})\cdot\nabla\phi(\vec{r},\vec{r}_s) + \delta D(\vec{r})\nabla^2\phi(\vec{r},\vec{r}_s) = -A\delta(\vec{r}_s)\,. \quad \textbf{(3-55)}$$

In the Born regime the total field is similarly written as $\phi(\vec{r},\vec{r}_s) = \phi_0(\vec{r},\vec{r}_s) + \phi_{sc}(\vec{r},\vec{r}_s)$. Then substitution of the total field in Eq.(3-55) and subtraction of the homogeneous Helmholtz equation yields:

$$D_0[\vec{\nabla}^2 + k^2]\phi_{sc}(\vec{r},\vec{r}_s) = -\vec{\nabla}\delta D(\vec{r})\cdot\vec{\nabla}\phi(\vec{r},\vec{r}_s) - \delta D(\vec{r})\vec{\nabla}^2\phi(\vec{r},\vec{r}_s). \quad \textbf{(3-56)}$$

O'Leary has shown in her thesis [55] (Chapter 5 pp. 118-119) that the solution for the scattered field detected at $\vec{r}_d$ can be written as

$$\phi_{sc}(\vec{r}_d,\vec{r}_s) = \int_V \vec{\nabla}g(\vec{r}-\vec{r}_d)\cdot\vec{\nabla}\phi_0(\vec{r},\vec{r}_s)\frac{\delta D(\vec{r})}{D_0}d\vec{r}\,. \quad \textbf{(3-57)}$$

This solution is found using the Green's decomposition for the driving function of Eq.(3-56) and then the Green's first identity followed by the Born approximation,

In the Rytov approximation the total field is described by Eq.(3-47). Then the solution for the scattered phase is given (O'Leary thesis, Chapter 5 pp.119-123) by:

$$\Phi_{sc}(\vec{r}_d,\vec{r}_s) = \frac{1}{\phi_0(\vec{r}_d,\vec{r}_s)}\int_V \vec{\nabla}g(\vec{r}-\vec{r}_d)\cdot\vec{\nabla}\phi_0(\vec{r},\vec{r}_s)\frac{\delta D(\vec{r})}{D_0}d\vec{r}\,. \quad \textbf{(3-58)}$$

Linear superposition of Eq.(3-46) and Eq.(3-57) under the Born approximation or Eq.(3-53) and Eq.(3-58) under the Rytov approximations can be used as solutions for media where both the absorption coefficient and the reduced scattering coefficient are varying.

3.5.3 Solution derived for fluorescence heterogeneity.

This subsection reviews the solution obtained for fluorophores of a single lifetime to complete the discussion of analytical perturbative solutions in diffuse media even though fluorescence has not been the main focus of this work. Several investigators have studied fluorescence imaging and tomography in the diffuse regime. The discussion here is based on the analysis by Li[57] and O'Leary [55] who have used the perturbation approach of the

diffusion equation for florescence waves to derive an analytical solution similar to those derived for absorption perturbations. In this analysis the fluorescent radiation is assumed to be well separated in energy from that of incident photons so we can safely ignore the possibility of the excitation of fluorophores by the fluorescent re-emission. Fluorophore and chromophore absorptions are treated separately and fluorophore–induced scattering changed are assumed negligible for notational simplicity (although the scattering effect can be easily incorporated). Absorption due to fluorophores can be treated as the sum of the chromophore absorption coefficient plus the fluorophore absorption coefficient.

Let $\phi(\vec{r},t)$ be the established photon fluence rate in a homogeneous medium containing a weakly absorbing distribution of fluorophores. The fluorophores are going to be excited by this photon distribution and act as a secondary point source of fluorescent light. Treating fluorophores as two level quantum systems and ignoring saturation effects yields that the number of excited fluorophores $N(\vec{r},t)$, at position $\vec{r}$, obeys the following linear diffusion equation[57],

$$\frac{\partial N(\vec{r},t)}{\partial t} = -\Gamma \cdot N(\vec{r},t) + \sigma \cdot c \cdot \phi(\vec{r},t) N_t(\vec{r}), \qquad \textbf{(3-59)}$$

where Γ is the excited dye decay rate, $N_t(\vec{r}) = [F] \cdot \gamma$, is the concentration of the fluorophore F multiplied by the fluorescent yield γ at a position $\vec{r}$ and σ is the absorption cross section of the dye. We have also assumed that $N_t(\vec{r}) >> N(\vec{r})$. For an intensity modulated point source at position $\vec{r}_s$, the Fourier Transform of Eq. (3-59) yields

$$-i\omega N(\vec{r}) = -\Gamma \cdot N(\vec{r}) + \sigma \cdot c \cdot \phi(\vec{r},\vec{r}_S) \cdot N_t(\vec{r}). \qquad \textbf{(3-60)}$$

Eq.(3-60) can be solved for the rate of production of fluorescent photons $\Gamma \cdot N(\vec{r})$, i.e.,

$$\Gamma \cdot N(\vec{r}) = \frac{\sigma \cdot c \cdot \phi(\vec{r}, \vec{r}_s) \cdot N_t(\vec{r})}{1 - i\omega\tau}, \qquad \textbf{(3-61)}$$

where $\tau = 1/\Gamma$ is the fluorescent lifetime. Eq.(3-61) is the strength of the fluorescence at position $\vec{r}$. Typically the fluorescence lifetime may also be spatially dependent but it is assumed otherwise here for simplicity. This secondary photon source will create fluorescence diffuse photon density waves that are propagating according to Eq.(3-16) for the infinite medium case and subsequent solutions developed for the appropriate geometry. The detected fluorescence fluence rate at position $\vec{r}_d$ will then be

$$\phi_{fl}(\vec{r}_d) = \Gamma \cdot N(\vec{r}) \cdot g^{fl}(\vec{r}_d, \vec{r}), \qquad \textbf{(3-62)}$$

where the greens function superscript '*fl*' denotes that the properties of the fluorescent diffuse waves are governed by the optical properties of the medium at the fluorescent wavelength. To calculate the total fluorescent signal from a homogeneous distribution of fluorophore, we integrate over all fluorophores, i.e.,

$$\phi_{fl}(\vec{r}_d, \vec{r}_s) = \int_V g_{fl}(\vec{r} - \vec{r}_d) \frac{\sigma c N_t(\vec{r})}{1 - i\omega\tau} \phi_0(\vec{r}, \vec{r}_s) d\vec{r}\,. \qquad \textbf{(3-63)}$$

Eq.(3-63) is very similar to Eq.(3-46). Therefore fluorescence tomography can be treated virtually identically to absorption and scattering tomography described Chapter 5.

3.6 A personal perspective on the Rytov and Born approximation

The performance of the Born and Rytov approximation has been studied and compared in the past. Theoretically, the Born approximation requires that the scattered field is small compared to the incident field. The Rytov approximation on the other hand assumes

a slowly varying scattered field. For biomedical applications it is not intuitive to argue in favor of a specific approximation. Biological structures may exhibit a high absorption and scattering resulting in large magnitude scattered field or may have well defined borders resulting in large scattered-field spatial variations.

Kak and Slaney [56] have addressed the issue of Rytov vs. Born and have shown that both approximations are valid for small objects and produce similar errors. For distributed or large heterogeneities the performance of the two approaches depends on the size, magnitude and spatial variation of the heterogeneity. However the Rytov approximation attains several experimental advantages as will be analytically described in §5.3. In this subsection I will elaborate on the similarity of the Born and Rytov solutions and the practical limit in which they are equivalent.

Let us consider the Born and Rytov solutions obtained for absorptive perturbations, but the analysis in the following is independent of the type of heterogeneity and therefore is equally applied for any first order perturbative solution. Dividing the Born solution (Eq.(3-46)) by the incident field $\phi_0(\vec{r}_d,\vec{r}_s)$ it yields the normalized Born solution

$$\frac{\phi_{sc}(\vec{r}_d,\vec{r}_s)}{\phi_0(\vec{r}_d,\vec{r}_s)} = -\frac{1}{\phi_0(\vec{r}_d,\vec{r}_s)}\int_V g(\vec{r}-\vec{r}_d)O(\vec{r})\phi_0(\vec{r},\vec{r}_s)d\vec{r}\,. \qquad \textbf{(3-64)}$$

Using Eq.(3-41), the left-hand side of Eq.(3-64) can be written as the normalized Born scattered field ϕ_{sc}^{nB}, i.e.

$$\phi_{sc}^{nB}(\vec{r}_d,\vec{r}_s) = \frac{\phi(\vec{r}_d,\vec{r}_s)-\phi_0(\vec{r}_d,\vec{r}_s)}{\phi_0(\vec{r}_d,\vec{r}_s)}\,. \qquad \textbf{(3-65)}$$

I rewrite now the solution obtained for the Rytov field (Eq.(3-53))

$$\Phi_{sc}(\vec{r}_d,\vec{r}_s) = -\frac{1}{\phi_0(\vec{r}_d,\vec{r}_s)}\int_V g(\vec{r}-\vec{r}_d)O(\vec{r})\phi_0(\vec{r},\vec{r}_s)d\vec{r}\,. \qquad \textbf{(3-66)}$$

Combing Eq.(3-47) and Eq.(3-48) the Rytov scattered field can be written as

$$\Phi_{sc}(\vec{r}_d,\vec{r}_s)=\ln\frac{\phi(\vec{r}_d,\vec{r}_s)}{\phi_0(\vec{r}_d,\vec{r}_s)}. \qquad \textbf{(3-67)}$$

The right hand side of the normalized Born and the Rytov solutions are identical. Therefore the scattered field predicted given a known heterogeneous distribution is exactly the same for both approximations!

The left hand-side of the normalized Born and Rytov solutions are independent of the approximation used because it is the experimental measurement. The total field $\phi(\vec{r}_d,\vec{r}_s)$ is the field measured from the heterogeneous medium. The homogeneous field $\phi_0(\vec{r}_d,\vec{r}_s)$ is the field that would have been measured from the same medium if no heterogeneity was present and it is also determined using experimental measurements (either a direct measurement on a calibration medium or a similar experimental determination).

For weak scattered fields ($\phi(\vec{r}_d,\vec{r}_s)\approx\phi_0(\vec{r}_d,\vec{r}_s)$) the fields $\phi_{sc}^{nB}(\vec{r}_d,\vec{r}_s)$ and $\Phi_{sc}(\vec{r}_d,\vec{r}_s)$ are virtually equal. This can be seen by noting that for any small number ε, such that $\varepsilon\approx 0$ and any number a, such that $a>>\varepsilon$, it holds that

$$\ln\left(\frac{a-\varepsilon}{a}\right)\approx\frac{-\varepsilon}{a}=\frac{(a-\varepsilon)-a}{a}\ \text{ for } \varepsilon<<a. \qquad \textbf{(3-68)}$$

Obviously the left-most part of Eq.(3-68) corresponds to the Rytov formulation (Eq.(3-67)) and the right-most part of Eq.(3-68) corresponds to the normalized Born formulation (Eq.(3-65)). Figure 3-3 plots the values $\ln((a-\varepsilon)/a)$ and ε/a as a function of ε assuming a=1. For ε values less than 0.1 very small differences can be observed between the two expressions plotted. Therefore the Rytov and the normalized Born solutions (and by extension the Born solution as well) are equivalent in this limit. As the scattered field increases (and so does ε) the left part of Eq.(3-68) grows faster than the right part of Eq.(3-68). Therefore for a total field that deviates more than 10% from the homogeneous field

detected, an inverse solution based on the Rytov approximation is expected to produce a "higher" reconstructed value since it divides a larger number than the Born solution (normalized or not).

Therefore the difference in performance between the Rytov and Born solutions is not related with the approximations employed per se, namely with the physics of the problem, but with the way each of the solutions treats (normalizes) the experimental measurements. The approximations in the physics, assumed in the derivation of each of the solutions, are included in the integral of Eq.(3-64) and Eq.(3-66) and further affect the accuracy of the results obtained as described by Kak and Slaney [56] and briefly in the beginning of this subsection.

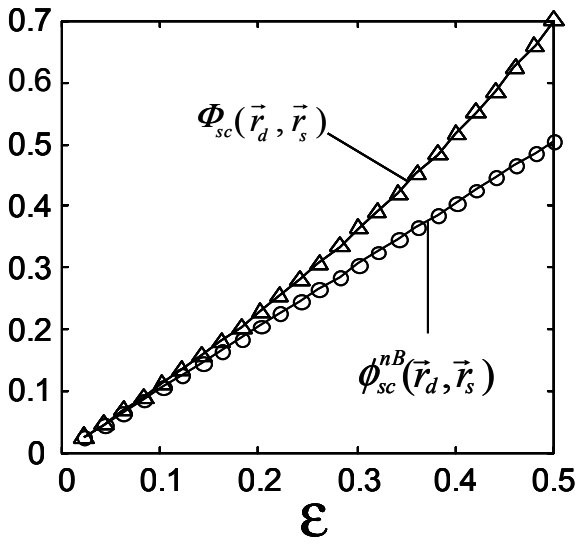

Figure 3-3: Rytov vs. normalized Born vector as a function of the field perturbation. (see text above for details)

4 Diffuse Optical Spectroscopy.

Optical spectroscopy of non-diffuse media is a fundamental tool of the medical sciences and has been used for more than a century to study suspensions of cells, organelles and tissue elements in general [1]. The technique measures the attenuation of constant intensity light as a function of wavelength and relates it to the presence and concentration of absorbers with known absorption spectra. On the other hand, the use of light attenuation measurements to study tissue *in vitro* or *in-vivo* is limited by the highly scattering nature of the cellular structures. The direct relation between chromophore concentration and light attenuation that is used in the typical photospectrometer (via the Beer-Lambert's law) cannot apply in the study of diffuse media: both scattering and absorption attenuates light. Therefore light attenuation cannot characterize tissue absorption and scattering independently.

Diffuse Optical Spectroscopy (DOS) was developed at the end of the 80's to address the implications arising from the high scattering tissue nature and relied on two breakthroughs:

The first was the development of photon diffusion theory. Solutions of the diffusion equation for the appropriate geometry provided the tools to quantitatively describe the photon propagation in tissues. These solutions can be inverted or fitted to the experimental data to obtain tissue optical properties.

The second was the use of advanced source and detection technology to overcome the limitations of intensity attenuation measurements, which provide one piece of information for a problem that has (at least) two unknowns: the absorption coefficient and the reduced scattering coefficient. Intensity modulation light or picosecond or femtosecond photon pulses were employed and offered higher information content. The intensity modulation technique provides at least two pieces of information (amplitude attenuation and phase delay) when performed at a single frequency. The photon pulse technique is equivalent to intensity modulation measurements at multiple frequencies via the Fourier transform and yields superior information content. Other approaches to achieve higher information content or more accurate instrument calibration rely on light measurements as a function of position [79]. Instrument complexity generally scales with the source information content.

In general, spectroscopic techniques assume that the medium of interest is homogeneous and therefore they measure optical properties averaged over the whole tissue volume. Hence, in general, spectroscopy requires simpler instrumentation and mathematical tools than tomography. For this reason, spectroscopy propagates in clinical applications much faster than imaging. This was certainly true for Diffuse Optical Spectroscopy (DOS) in the NIR. Diffuse Optical Spectroscopy is the most widely used technology that employs diffuse photons in clinical applications [58,59]. The technique has primarily targeted oxy- and deoxy-hemoglobin [60,61] to provide a quantitative assessment of tissue oxygenation (oximetry) and hemoglobin concentration [62,63]. In contrast to the pulse oximeter, DOS probes blood in the vascular bed, primarily in the capillaries, arterioles and venules.

Therefore it directly relates to tissue function [64, 65]. Furthermore it provides quantitative measures of oxy- and deoxy- hemoglobin independently. Applied to muscle the technique also probes myoglobin concentrations [66]. Several other tissue pigments or components have been considered as targets including cytochrome oxidase states [67] and glucose [68].

An inherent characteristic of spectroscopy in general and Diffuse Optical Spectroscopy in particular, is that it uses the "bulk" measurement to derive average tissue optical properties. By contrast, imaging with Diffuse Optical Tomography uses "differences" or "perturbations" carried on this bulk photon information. Therefore DOS by construction operates on a much higher signal-to-noise ratio than DOT. Hence it is virtually impossible to make a tomographic system work reliably if any single source-detector pair of this system cannot perform accurate spectroscopic measurements of the tissue average optical properties. Validating the spectroscopic performance of a system is a basic check that the hardware works and that there is cogency between the theoretical model used and the experimental set-up. Of course I can think of experimental uncertainties that affect the absolute DOS measurements more than the relative DOT measurements and I will discuss this issue in this chapter. But there is another fundamental reason to validate the spectroscopic capacity of any imager. The average optical properties of the diffuse medium are an integral part of the tomographic problem as will be discussed in detail in Chapter 5. Hence, accurate determination of the tissue absorption and reduced scattering coefficient is important; it enables one to calculate the photon propagation paths in that particular medium and thus improve the accuracy of the tomographic analysis. Therefore although the work in this thesis has a focus on Tomography, DOS was an integral part of DOT.

In this chapter the basic DOS principles are discussed and methodologies developed to quantify the absorption coefficient the reduced scattering coefficient and the absorption coefficient changes are presented. Although the instrument used in this work was a time-domain instrument (see Chapter 7), all three major experimental techniques, namely the continuous intensity DOS, the intensity modulated (frequency domain) DOS and the pulsed intensity (time-domain) DOS are presented, with the latter receiving the higher attention.

Section 4.1 focuses on intensity modulated DOS and presents the basic principles for quantifying tissue optical properties. Experimental issues regarding instrument and technique calibration are discussed. A method for self-calibration based on intensity and phase is presented and a sensitivity analysis for deriving the hemoglobin concentration and saturation using the self-calibrated method is performed. **Section 4.2** presents the constant intensity DOS as a subcategory of the intensity modulated DOS where the modulation frequency is zero. **Section 4.3** presents the basic principles of time-domain DOS and deals with the time-domain data deconvolution and fitting in order to extract the optical properties of diffuse media. **Section 4.4** presents a sensitivity analysis of time-domain DOS with respect to common experimental uncertainties. Finally **Section 4.5** presents a method that can very accurately quantify absorption changes, based on the integration of time-resolved data. This technique was used to measure the average absorption increase of the breast as a function of time due to the administration of the NIR contrast agent Indocyanine Green (see Chapter 9). The method yielded a quantification accuracy of differential absorption coefficient measurements of the order of 10^{-3} cm^{-2}.

4.1 Intensity-modulated DOS and experimental calibration.

Here I discuss issues pertaining to applying diffusion theory to experimental measurements of diffuse photon density waves for obtaining quantified measurements of tissue optical properties. It will become apparent that instrument calibration is a very important factor in quantification. A method to obtain the absorption coefficient without instrument calibration is presented, as it may lead to practical clinical instruments in certain applications.

4.1.1 Calculation of optical properties

Intensity modulation NIR spectroscopy lies in a balanced position between instrumentation complexity and information content. Therefore it has been selected by several investigators to extract tissue chromophore concentrations [69] and to correlate them

with physiological parameters [70,71]. The technique measures the amplitude attenuation and phase shift of a diffuse photon density wave propagating into the highly scattering medium, relative to the amplitude and phase of the photon field injected into the medium. This measurement derives the medium optical properties using a solution of the diffusion equation with the appropriate boundary conditions [72,73,74,75,76] as outlined in chapter 3. These solutions predict the amplitude and phase of the photon wave at the detection site and depend on the initial parameters of the photon source, on the source-detector separation, the frequency of the wave, the absorption and reduced scattering coefficients of the medium and its index of refraction.

Let $\phi(\mu_a, \mu_s', c_n, \rho, f)$ be the photon fluence rate measured at a site of distance ρ away from a photon source modulated at frequency f (see Eq.(3-16) for infinite medium and subsequent solutions in the presence of boundaries in §3.4). We use the fluence rate since it is proportional to the detected signal for the applications considered in this work as outlined in §3.3 and §3.4. However the following discussion applies to other boundary formulations as well, for example when a combination of both the fluence rate and the flux are considered. For a medium with an absorption coefficient μ_a, a reduced scattering coefficient μ_s' and a refractive index n (so that the speed of light propagation is c_n) the photon fluence rate can be decomposed in a logarithmic amplitude $A(u)$ and a phase $P(u)$ measurement, i.e

$$A(u) = \log\left(A_0 \cdot \sqrt{(\mathrm{Re}[\phi(u)])^2 + (\mathrm{Im}[\phi(u)])^2} \right), \qquad \textbf{(4-1)}$$

and

$$P(u) = \frac{180^0}{\pi} \cdot \arctan \frac{\mathrm{Im}[\phi(u)]}{\mathrm{Re}[\phi(u)]} + P_0 , \qquad \textbf{(4-2)}$$

where $u \equiv [\mu_a, \mu_s', c_n, \rho, f]$ is the vector of parameters, A_0 is the amplitude gain factor and P_0 is the initial phase. A_0 incorporates the amplitude of the photon field injected into the medium and the instrument gain. P_0 is the summation of the initial phase of the photon field injected into the medium and the phase delay introduced by instrument fibers and electronic

components of the detection system. If the light source-detector separation, modulation frequency and index of refraction of the tissue are known, and assuming that the instrument-specific parameters A_0, P_0 can be determined, a system of two equations for phase and amplitude and two unknowns (μ_a, μ_s') can be constructed and solved numerically for determination of the medium optical properties.

4.1.2 Experimental calibration

In practice, the direct measurement of the amplitude of the incident wave, by abutting the source and detector fibers using appropriate attenuation, imposes experimental complexity. Furthermore the uncertainty on the exact gain used and signal loss due to the abutting, may affect the accuracy of the calculation. Similarly, measurement of the incident wave phase by abutting the source and detector fibers after light attenuation introduces experimental uncertainties such as amplitude-phase cross-talk errors [77,78]. In order to avoid measurement of the absolute initial amplitude and phase, many investigators have described methods to account for the instrument induced phase delay. Fantini et. al.[79,80] have devised a multi-separation measurement to cancel out the instrument initial phase and calculate the optical properties of the volume under investigation from the slope of amplitude and phase with varying source-detector distance. Sevick et. al. have proposed phase calibration on a phantom with known optical properties [60]. For example if u' is the medium of known optical properties (calibration medium), we can obtain a differential measurement of amplitude and phase, i.e.

$$\Delta A(u,u') = A(u) - A(u') = \log\left(\frac{\sqrt{(\mathrm{Re}[\phi(u)])^2 + (\mathrm{Im}[\phi(u)])^2}}{\sqrt{(\mathrm{Re}[\phi(u')])^2 + (\mathrm{Im}[\phi(u')])^2}}\right), \qquad \textbf{(4-3)}$$

and

$$\Delta P(u,u') = P(u) - P(u') = \frac{180^0}{\pi}\cdot\left(\arctan\frac{\mathrm{Im}[\phi(u)]}{\mathrm{Re}[\phi(u)]} - \arctan\frac{\mathrm{Im}[\phi(u')]}{\mathrm{Re}[\phi(u')]}\right). \qquad \textbf{(4-4)}$$

The factors A_0, P_0 have been eliminated from Eq.(4-1) and Eq.(4-2). Assuming that the source-detector separation, the modulation frequency and the index of refraction are known, Eq.(4-3) and Eq.(4-4) can be again fitted for the unknown optical properties of medium *u*.

4.1.3 Self-calibration with diffuse photon density wave differentials

More recently, Kohl et. al [81,82] have reported an adept way to calculate the absorption coefficient when there are physiological or induced changes in light absorption, for continuous light and for modulation-depth and phase measurements. The technique is independent of the initial instrument gain and phase (A_0, P_0) and of a background "calibration" medium u'. The technique requires premise of the background reduced scattering coefficient but is quite insensitive to the actual value of this coefficient. Moreover, one single light source and a single detector are sufficient. Conversely the technique is sensitive to measurement noise. Here I discuss a variation of the method suggested by Kohl et. al. that uses the intensity and phase of diffuse photon density-waves. I will discuss the theory and show a sensitivity analysis for determining the hemoglobin concentration and saturation.

Under certain physiological assumptions the determination of u' can be significantly simplified. Let us assume tissue measurements at a known modulation frequency and source detector separation. We also assume that the index of refraction and the reduced scattering coefficient of the medium are assumed constant and known. Under these premises the problem depends only on the absorption coefficient. For an absorption coefficient change from μ_{a1} to $\mu_{a2} = \mu_{a1} + \Delta\mu_a$, the amplitude difference $\Delta A(u,u')$ can be simply written as $\Delta A(\mu_{a1},\mu_{a2}) = A(\mu_{a1}) - A(\mu_{a2})$ and similarly the phase difference $\Delta P(u,u')$ as $\Delta P(\mu_{a1},\mu_{a2}) = P(\mu_{a1}) - P(\mu_{a2})$. Assuming that $\Delta\mu_a \to 0$, these differences become differentials. The ratio of the amplitude differential dA to the phase differential dP, namely

$$Q_{ac} = \frac{dA(\mu_{a1}, \mu_{a1} + d\mu_a)}{dP(\mu_{a1}, \mu_{a1} + d\mu_a)}, \qquad \textbf{(4-5)}$$

can be used to derive the absolute absorption coefficient of the medium. Figure 4-1 depicts the Q_{ac} for reflectance geometry, as a function of a physiologically relevant μ_a range in the NIR, plotted for different μ_s' values. The plot has been constructed for a source-detector separation of 3 cm, index of refraction n=1.333 and a $d\mu_a$ value arbitrarily chosen to be 10^{-4} cm^{-1}. Q_{ac} is continuous and is monotonously increasing with μ_a in a virtually linear trend. This illustrates that for every small absorption change around a background μ_a there is always a Q_{ac} value that uniquely identifies this μ_a given the background μ_s'. Moreover Figure 4-1 depicts that this μ_a identification is relatively insensitive to the exact value of the background μ_s' value. For a μ_s' uncertainty of ± 5 cm^{-1} the expected error in μ_a does not exceed ± 0.005 cm^{-1}.

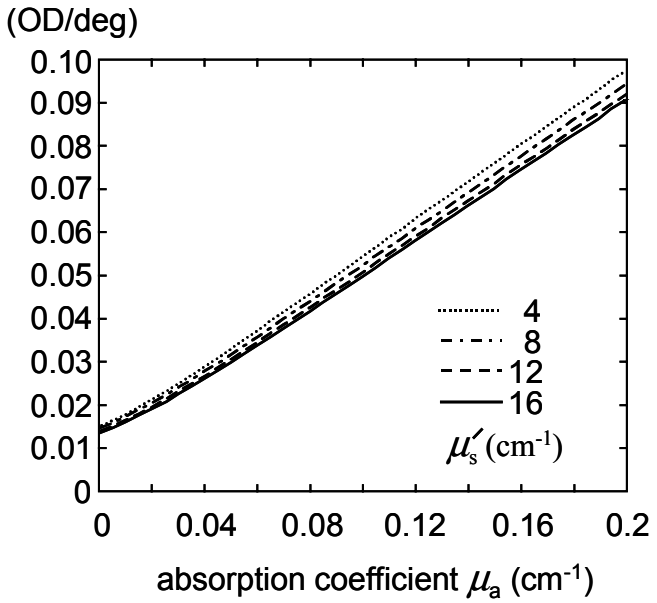

Figure 4-1: The Q_{ac} ratio as a function of the absorption coefficient for four different scattering backgrounds and a source-detector distance of 3 cm.

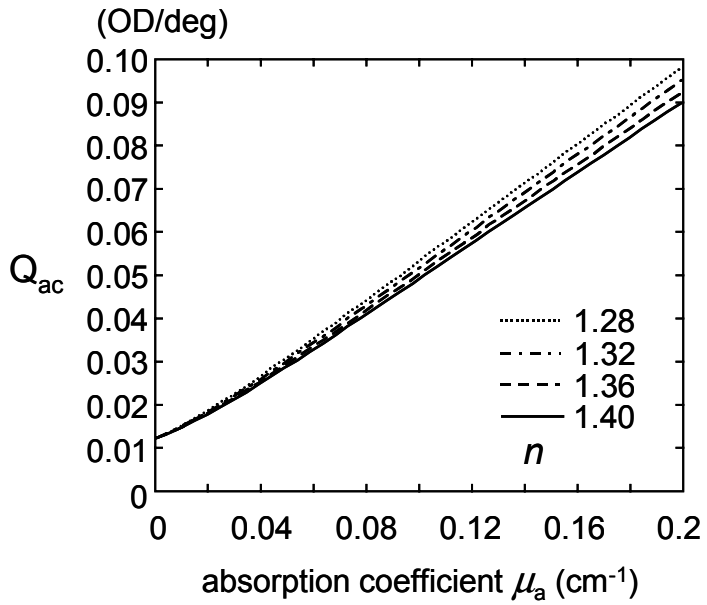

Figure 4-2: The Q_{ac} ratio as a function of the index of refraction for four different indices of refraction.

Similarly, figure 4-2 depicts even lower sensitivity to index of refraction uncertainty. The resulting μ_a error due to the μ_s' assumption error is approximately 10^3 times lower than the μ_s' deviation from its actual value.

The Q_{ac} versus μ_a relationship described by Eq.(4-5) may be employed to construct a lookup table or can be approximated with a polynomial, and subsequently used to calculate μ_a values during absorption changes, using μ_s' estimates. Besides its independence on A_0 and P_0, Q_{ac} is also insensitive to amplitude and phase instrument drift during long experiments since it depends only on virtually instantaneous temporal events. Conversely, since it is a ratio of two quantities, Q_{ac} is unstable when the denominator (i.e. the phase difference) becomes so small that is comparable to, or significantly affected by background noise.

For measurements that extend over a period of time, the method presented above can be used to estimate the absorption coefficient at selected points where maximum signal changes occur and favorable signal-to-noise conditions exist. Then the calculated μ_a and assumed μ_s' and c_n values can be used, in conjunction with the known ρ and f parameters, to determine u' in Eq.(4-3) and Eq.(4-4) at the selected time points. Consecutively the corresponding optical properties of the tissue during the measurement period can be obtained employing a numerical solution of Eq.(4-3) and Eq.(4-4). These calculated optical properties carry the errors, introduced by the assumption of μ_s', c_n and the calculation of μ_a used in the determination of vector u'. As will be shown in the following sub-section, the use of the method in the clinical environment is justified since blood saturation and hemoglobin concentration calculations are fairly insensitive to assumptions of μ_s' and c_n.

4.1.4 Sensitivity analysis

The method presented in the previous sub-section offers a great experimental simplification since it is independent of initial phase and amplitude calibration. However it requires the assumption of the background reduced scattering coefficient μ_s'. In this sub-section, the error introduced in the calculation of saturation and hemoglobin concentration is assessed as a function of the deviation of the assumed μ_s' from the real background value. A semi-infinite homogeneous medium is assumed. The medium undergoes a linear increase of blood oxygen saturation (Y) from 5% to 100% and a corresponding arbitrary linear hemoglobin concentration (H) change from 60 to 100 μM, as shown in Figure 4-3b and Figure 4-3 a respectively. A set of 20 equally spaced Y and H values is employed, to cover the range under investigation. For each point of the set the absorption coefficient of the medium was calculated assuming only two chromophores, i.e.

$$\mu_a^{\lambda} = \varepsilon_{HB}^{\lambda} \cdot [HB] + \varepsilon_{HB02}^{\lambda} [HBO_2], \qquad \textbf{(4-6)}$$

where [HB]=H·(1-Y) and [HBO2]= H·Y are the concentrations of deoxy- and oxy-hemoglobin respectively and $\varepsilon_{HB}^{\lambda}, \varepsilon_{HB02}^{\lambda}$ are the extinction coefficients of deoxy- and oxy hemoglobin at wavelength λ. The absorption coefficient was calculated at two wavelengths λ_1=750nm and λ_2=780nm. Eq.(3-31) was used with the calculated $\mu_a^{\lambda_1}, \mu_a^{\lambda_2}$ values to simulate the corresponding amplitude and phase values assuming μ_s'=10cm^{-1}, n=1.333, f=200MHz and ρ=3 cm. Also in order to incorporate Eq.(4-5) into the analysis a small absorption change was induced around the middle point of the Y-H set ($\Delta\mu_a$=10^{-4} cm^{-1}). Eq.(3-31) was again employed to assess the corresponding amplitude and phase changes.

After the calculation of the forward problem, namely the calculation of the amplitude and the phase for the different points of the Y-H set, Eq.(4-3), Eq.(4-4) and Eq.(4-5) were employed to back-calculate $\mu_a^{\lambda_1}, \mu_a^{\lambda_2}$ assuming μ_s' values ranging between 5 cm^{-1} and 15 cm^{-1}. For each μ_s' value a look-up table was constructed based on the Q_{ac} ratio and estimated the absorption coefficient of the middle point of the Y-H set, for the data obtained due to the small absorption change. This point was subsequently used to normalize the measurement as in Eq.(4-3) and Eq.(4-4). Minimization was based on the Nelder-Mead simplex search [83], provided within the Matlab software package (MathWorks, MA USA) to minimize Eq.(4-3) and Eq.(4-4) in the least squares sense, for the different μ_s' estimates. The back-calculated $\mu_a^{\lambda_1}, \mu_a^{\lambda_2}$ values were substituted in a system created using Eq.(4-6) at λ_1, λ_2 which after being solved analytically provided [HB]c and [HbO2]c and hence Yc and Hc values. The subscript 'c' denotes that these are back-calculated values. Figure 4-3a and b also plot Hc and Yc calculated for an overestimation of μ_s' by 3 cm^{-1}. The error of the calculation increases away from the calibration point.

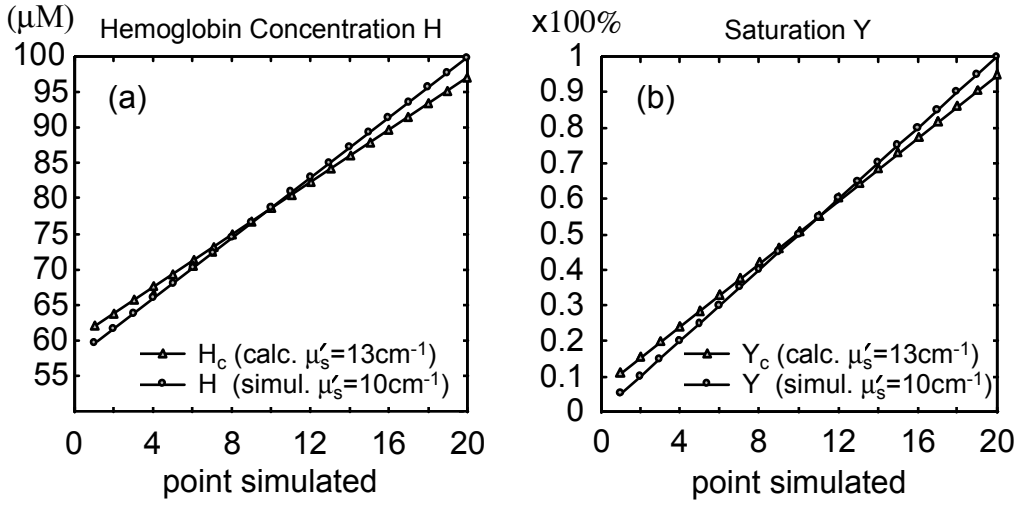

Figure 4-3: Hemoglobin concentration (H) and blood saturation (Y) for 20 selected values used in the forward problem for μ_s' = 10cm^{-1} and the corresponding back-calculated values (H_c, Y_c) for an overestimation of the reduced scattering coefficient by 3cm^{-1}.

Figure 4-4a depicts the average normalized error E_H between H and H_c and Figure 4-4b depicts the average normalized error E_Y between Y and Y_c, as a function of μ_s' deviation from the value used to simulate the forward problem (μ_s'=10cm^{-1}). The E_H and E_Y values are calculated for all points of the set as

$$E_H = \frac{1}{20 \cdot (H_{\max} - H_{\min})} \cdot \sum_{m=1}^{20} |H - H_c|, \qquad \textbf{(4-7)}$$

$$E_Y = \frac{1}{20} \cdot \sum_{m=1}^{20} |Y - Y_c|, \qquad \textbf{(4-8)}$$

where $H_{\max}$, $H_{\min}$ is the maximum and minimum values of the H range , namely 100mM and 60mM. There is no need to normalize the E_Y since the full Y range was included in the calculation. Generally, an overestimation of the reduced scattering coefficient results in smaller errors than an underestimation by the same amount. Moreover the hemoglobin

concentration calculation appears more sensitive to the approximations of the method than the saturation calculation. For μ_s' overestimation, E_Y scales approximately as 1%/cm^{-1}. The corresponding rate for E_H is ~2%/cm^{-1}. Since E_Y and E_H are average values for the full saturation range (5-100%), the rates estimated are expected to be the upper limit of the expected errors in real measurements where saturation variations rarely exceed half of this range. Therefore sensible accuracy in calculating blood saturation is predicted and reasonable hemoglobin concentration quantification is expected when using the Q_{ac} method.

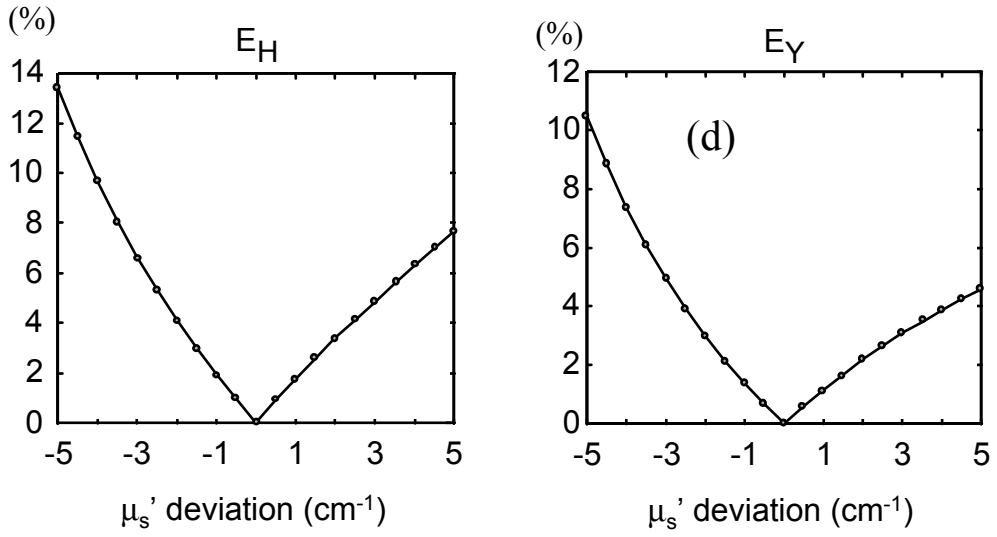

Figure 4-4: Sensitivity of the hemoglobin concentration and blood saturation calculation to the assumption of the background reduced scattering coefficient. c) average error in back-calculating hemoglobin concentration and d) blood saturation as a function of the difference of the reduced scattering coefficient used in the forward problem and the one assumed during the inversion.

We note that the relative insensitivity of the saturation to the method is because the method introduces systematic errors, namely a bias of the calculated absorption coefficient.

In Chapter 6 we will show that the saturation calculation is more sensitive to random noise, therefore this sensitivity analysis is not valid for low signal-to-noise measurements.

We could further apply a methodology to estimate the goodness of the reduced scattering coefficient guess and consequently improve it by iteration. This methodology is based on the fact that the saturation calculation error does not depend linearly on the deviation of the assumed reduced scattering coefficient from the real value. Therefore when a blind guess of scattering coefficient is required, the saturation calculation can be done twice, using two adjacent μ_s' estimates. If the resulting difference between the calculated saturation at the two different μ_s' values has a rate that deviates from the predicted $1\%/\text{cm}^{-1}$, shown in the sensitivity analysis, it means that the calculation has not been done at optimum background μ_s' selection. The procedure can be repeated until this theoretical rate is reached (within the region of physiologically relevant reduced scattering coefficients).

4.2 Constant Wave DOS and experimental calibration.

The simplest form of Diffuse Optical Spectroscopy is the CW-DOS. Here light of constant intensity is injected into the medium, and its attenuation through the medium is measured at a distance ρ. The limitation of this technique was outlined in the introduction of this chapter. Since only one piece of information is available, one can at most solve for one unknown, therefore the method is not well suited for resolving both the absorption and the scattering properties of diffuse media. Experimentally however the technique is technologically simple so that it still becomes attractive for specific applications, for example when only the absorption coefficient is to be measured, in a medium with known and invariant reduced scattering coefficient. This could be true when measuring the concentration of injected contrast agents into tissue.

The methodology and calibration issues that were outlined in the previous section are similarly applied here. Since no phase measurement exists, only amplitude calibration is required. A differential measurement using two media u and u' can now be written

$$\Delta A(u,u') = A(u) - A(u') = \log\left(\frac{\phi(u)}{\phi(u')}\right). \qquad \textbf{(4-9)}$$

Here $\phi(u)$ is the photon fluence rate measured at a distance ρ away from a photon source, for photons that have propagated in a medium with an absorption coefficient μ_a, a reduced scattering coefficient μ_s' and a refractive index n so that the speed of light propagation is c_n. According to Eq.(3-15) the wave propagation vector for zero modulation frequency is

$$k^2 = \frac{-\mu_a}{D} = -3\mu_a\mu_s'. \qquad \textbf{(4-10)}$$

If μ_s' in both media is known, then Eq.(4-9) can be solved for μ_a and vice-versa.

Nichols et. al. [84] have shown that in certain cases where measurements are performed as a function of distance, starting very close to the source position (less than a mean free path), the amplitude measurement at multiple distances can be fitted for both the absorption and reduced scattering coefficient. This method is based on the fact that close to the source, the detected field becomes sensitive to the depth at which photons initially become diffuse. This depth is a function of the scattering coefficient only. Therefore the absorption and reduced scattering coefficient become independent.

4.3 Time-domain DOS.

Time resolved spectroscopy was the main focus of this work and will be discussed in more detail. In this section I present the general methodology of extracting tissue optical properties based on fits of the time-resolved data and discuss several experimental factors that affect the quantification accuracy. In the following sections I will present a sensitivity analysis relevant to the most common experimental uncertainties and a new method to

quantify absorption changes with much higher accuracy than the one achieved by fitting time-resolved curves.

4.3.1 Calculation of optical properties

Figure 4-5 shows a typical time resolved measurement through a diffuse medium. The pulse with a center at $t=t_0$ was the incident photon pulse. The parameters of the measurement were ρ=5cm, μ_s'=5cm^{-1} and μ_a=0.05cm^{-1}. The time resolved curve is a histogram of photon pathlengths into tissue. Data analysis methods commonly used to quantify absolute optical properties include fitting the shape of time-resolved experimental curves, or selected parts of them to appropriate solutions of the diffusion equation. Another measure related to optical properties is the integrated photon fluence rate. This measure is equivalent to a CW measurement, offering low information content. In principle this measurement could be combined with the general curve fitting to restrict the fitting process. It is not usually considered in calculations however, due to the experimental difficulty of accurately determining the number of incident photons injected into the medium during the measurement.

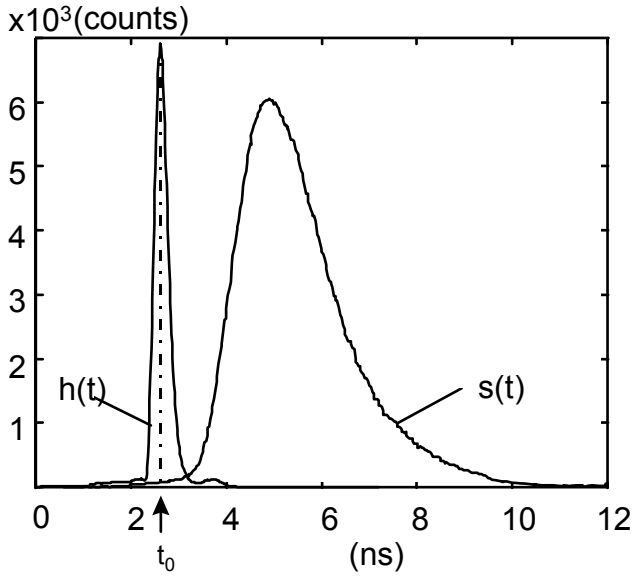

Figure 4-5. Typical time resolved measurement *s(t)* and instrument impulse response h(t).

4.3.2 Deconvolution and Data fitting

As a result of the finite duration of the laser photon pulses, the photon dispersion along the fibers and the photo-electron spreading in the detector, the measured signal *s(t)* is a convolution of a "real" signal *r(t)* and the finite impulse response of the instrument *h(t), i.e.*

$$s(t) = h(t) \otimes r(t) = \int_{-\infty}^{\infty} h(t-v)r(v)dv\,. \qquad \textbf{(4-11)}$$

In order to obtain absolute tissue optical properties we need to correct for instrumental response. The simplest deconvolution operation is the linear frequency domain method that takes advantage of the simplicity of the convolution theorem:

$$R(f) = \frac{S(f)}{H(f)}\,, \qquad \textbf{(4-12)}$$

where *R(f), S(f), H(f)* are the Fourier Transforms of the signals *r(t), s(t)* and *h(t)* respectively. The inverse Fourier Transform of *R(f)* yields the desired *r(t)* signal. Unfortunately, except in certain cases where extremely favorable signal-to-noise ratios are available, the Inverse Fourier Transform of Eq.(4-12) is severely degraded by measurement noise even when matched filtering is performed [85].

Under these circumstances improved behavior can be obtained by numerical methods in the time domain. Jannson [85] has suggested an efficient and accurate iterative technique, which is a modification on an original suggestion by Van Gitter given by

$$r_n = r_{n-1} + a(r_{n-1})(s - r_{n-1} \otimes h), \qquad \textbf{(4-13)}$$

where the subscript *n* denotes the iteration step. The time dependence *r(t), s(t)* and *h(t)* is implied but not explicitly written. The first guess for r is typically *s*. Both conversion time and accuracy depend on the selection of the quantity *a,* which depends on the amplitude of r_{n-1}, and it is assigned empirically [85] for specific applications. Proper *a* structure helps

eliminate non-physical solutions produced by the linear Van Gitter method (where *a* equals 1). One of the great advantages of these linear and non-linear numerical methods is that they convert a deconvolution to a convolution operation. Convolution is an easily manipulated operation, and in the case of the linear methods it acts as a low pass filter reducing noise. Eq.(4-13) however requires careful implementation to ensure convergence and optimum results. The deconvolved result, after n iterations, can be fitted with the solution of the diffusion equation that best represents the boundary conditions of the measurement. Other deconvolution methods based on the maximum likelihood estimates of the spectra have also been proposed [86]. The existence of a large number of deconvolution methods exemplifies the complexity of the operation and the need for application specific algorithms to ensure best performance.

When the quantification of absolute optical properties is in quest, there is no need to independently deconvolve and then fit the time-resolved curve. For fitting purposes a standard non-linear fitting procedure (such as the Levenberg-Marquardt method) can be employed to fit the data to the appropriate solution of the diffusion equation in the least squares sense. In practice efficient calculations are achieved by directly fitting the measurements to the convolution of the appropriate diffusion equation solution with the instrument's impulse response, namely minimizing the function

$$\chi^2 = \sum_{k=K1}^{K2} \left(\frac{s(k,u) - A_0 y^*(k,u)}{\sigma_k} \right)^2 , \qquad \textbf{(4-14)}$$

where $u \equiv [\mu_a, \mu_s', c_n, \rho, t_0]$ is the vector of free parameters, A_0 is the gain factor, y*=h⊗y is the convolution of the instrument impulse response h=h(t) with the solution of the diffusion equation solution $\phi=\phi$(t,u) calculated for the appropriate boundary condition and the vector *u*. The parameter k is the discrete time variable, [K1,K2] is the time interval of the fit, s(k,u) is the measured time-resolved curve and σ_k=[s(k)]$^{1/2}$ is the measurement error (standard deviation) of the kth data point. This procedure is theoretically equivalent to performing a deconvolution step followed by data fitting, but offers implementation and performance

advantages. Nevertheless in order to decompose the effect of various experimental uncertainties and help the discussion, it may prove useful in the following sections to consider the deconvolution and data fitting as two independent steps.

4.3.3 Data fitting considerations

The selection of the time interval [K1,K2] plays an important role in the quantification of optical properties. It is demonstrated in the sensitivity analysis at the following sub-section that the selection of this interval has a prominent effect on the quantification accuracy. Additionally the selection of the free parameters plays an important role in the quantification accuracy. In principle the parameters A_0, ρ and t_0 can be assumed a-priori knowledge and not included in the fitting process to restrict the fitting process. However if there is evidence that certain experimental uncertainties exist, such as A_0 and t_0 fluctuations or ρ uncertainties, these parameters can be selectively left free to compensate for such effects under good signal to noise conditions. For example A_0 is customarily allowed to be a free parameters due to difficulties to calculate or experimentally determine the instrument gain factor (e.g. to account for the laser power, detector gain and optics' coupling to each-other and to tissue).

One additional complication derives from the nature of t_0, which in contrast to the rest of the parameters is a discrete variable. For the cases that t_0, is taken as a free parameter, the algorithm can fit the time-resolved curves for a selected interval, for example $t \in [\ t_0 - 100\text{ps},\ t_0 + 100\text{ps}\ ]$. Then the fit of the minimum χ^2 obviously yields. Obviously the t_0 time step equals the instrument's time resolution δt and hence the number of fits executed for each time resolved curve equals $200\text{ps}/\delta t$.

4.4 Time domain DOS sensitivity.

In this section I outline common experimental errors that are introduced in measurements of time-resolved photons and investigate their influence rate on the

quantification accuracy. I also demonstrate that DOS quantification depends on the medium's optical properties, independently of signal to noise considerations. To perform the sensitivity analysis the solution for reflectance geometry in the time domain (Eq.(3-28)) has been used to simulate time-resolved curves measured from a semi-infinite medium with optical properties μ_a and μ_s' at a source detector separation ρ. Then an assumed experimental error is induced in the time-resolved curve, for example a time shift. The modified time-resolved curve is then fitted to Eq.(3-28) for reflectance and the resulting optical properties are compared with the ones used for the simulation to produce the relative quantification error, ε, which is simply defined as

$$\varepsilon = \frac{\mu_{fitted} - \mu_{real}}{\mu_{real}} \times 100\% , \qquad \textbf{(4-15)}$$

where μ_{fitted} is a parameter that is fitted for and μ_{real} is the value of this parameter that was used in the simulation. Therefore ε_s denotes the relative quantification error in estimating the reduced scattering coefficient and ε_a is the relative quantification error in estimating the absorption coefficient.

4.4.1 Impulse response measurement induced errors

The most significant calibration of a time-resolved instrument is the measurement of its impulse response, also known as instrument function measurement. This measurement describes the instrument operation and conveys three important pieces of information, i.e. the incident photon pulse power, the incident pulse launch time and the overall photon dispersion and electronic fluctuations of the instrument. The instrument impulse response can be measured by abutting the source and detector fibers using the proper optical signal attenuation.

Incident photon-pulse finite width.

The deviation of the impulse response from an ideal delta function is associated with both photonic and electronic phenomena. Photonic phenomena include the finite-width incident photon-pulse, due to the laser characteristics, and the photon-dispersion along optical fibers, which may be used to guide photons to and from the medium under investigation. Electronic phenomena include the transient time spread [87] (TTS) of the electrons during amplification in the photo-multiplier tube and the trigger-signal time uncertainty between the laser and the TAC. Although these are the dominant factors determining the instrument impulse response, any other time-uncertainty associated with the propagation of photons or electrons along the instrument will contribute to pulse broadening.

The detected time-resolved curve can be considered as the convolution of the finite-width instrument impulse response with the time-resolved photon response from the diffuse medium as discussed earlier. In order to investigate the effect of this convolution operation to the quantification accuracy of the time-resolved method, four time-resolved curves were convoluted with impulse responses of increasing full-width-at-half-maximum (FWHM), and fitted without correcting for the convolution effect. The time resolved curves were produced again using Eq.(3-28) at four combinations of absorption and reduced scattering coefficients. The optical properties were selected from the physiological range to study low and high absorbing and low and high scattering media, in the four possible combinations. The different full-width at half maximum (FWHM) of the impulse responses were created by changing the time-scale of an experimentally measured impulse response.

Figure 4-6 depicts the relative quantification errors, ε_a and ε_s of the fitting result, as a function of the varying impulse response (FWHM), for the four combinations of medium optical properties. The results clearly demonstrate that even a small impulse-response full FWHM can have a significant effect in the accuracy of quantification if it is left unaccounted. Generally the error introduced in the μ_s' calculation is higher than in the μ_a calculation. Additionally the dependence of the quantification performance on the optical

properties is evident. High scattering and low absorbing media can be quantified more accurately than media with other optical property combinations.

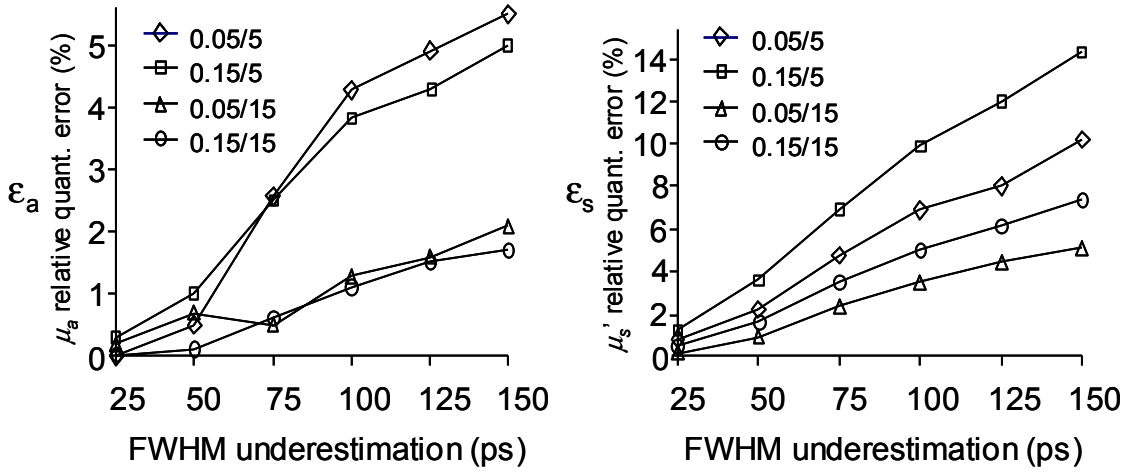

Figure 4-6. Relative quantification errors of time-resolved NIR spectroscopy as a function of the impulse response FWHM variation.

Incident photon-pulse launch time uncertainty

The incident pulse-launch time t_0, can be obtained from the impulse response measurement. Assuming that deconvolution is performed, t_0 can be assigned as the time point when the impulse response maximum occurs. However since the impulse response measurement cannot occur simultaneously with the data measurement, errors in determining t_0, associated with the stability of the time position of this maximum point over a period of time, may lead to quantification errors.

The incident photon-pulse launch time uncertainty can be attributed to two effects, namely drift and jitter. Drift is generally caused by laser or environmental temperature changes during the measurement and is manifested as a gradual t_0 change over time. Jitter is

a random t_0 fluctuation due to electrical, electronic and photo-electronic uncertainties and the quantization operation of the multi-channel analyzer.

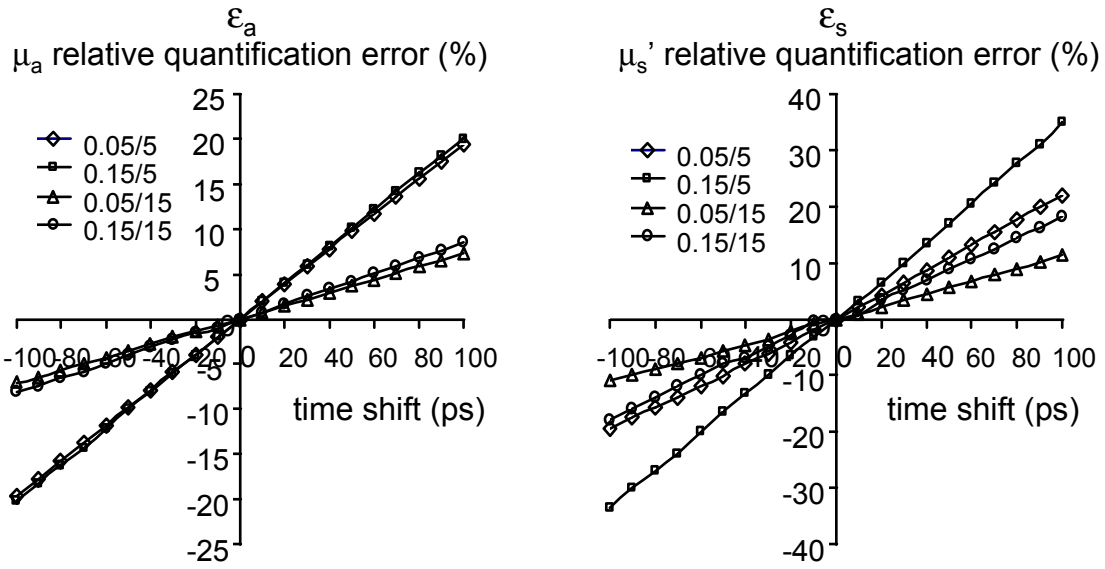

Figure 4-7 Quantification error of NIR time-resolved spectroscopy as a function of time shift of the instrument impulse response relatively to the measured curve.

The influence of time-drift and jitter on quantification errors can be studied collectively as a time shift. The time-resolved curves were created employing a delta-function impulse response at time $t = t_0$. Time uncertainties were then introduced by fitting the time resolved-curves assuming that the impulse response was shifted towards earlier (positive) or later (negative) times compared to t_0. Figure 4-7 depicts the relative quantification errors ε_a and ε_s as a function of this impulse response time shift. Four optical property combinations were studied again. The quantification of μ_s' is shown in general to be more sensitive to time uncertainties, compared to the μ_a quantification. Furthermore the dependence of ε_a and ε_s on the medium optical properties is evident, with quantification of lower scattering and higher absorption media demonstrating more sensitivity to time-shifts.

Selective waveguide mode excitation and fiber length variability

Optical fibers are often used for NIR spectroscopy of tissue due to the convenience they offer to obtain measurements in various geometries. It is also a common practice to use multi-mode fibers in the detection part, to increase the photon collection efficiency. An important source of error, and maybe the most complicated and difficult to account for, is the uncertainty associated with selective excitation of wave-guide modes in the detection fibers. This effect is further complicated by possible length variability between fibers constituting a fiber bundle, especially when long fiber bundles are employed.

When a fiber collects light from a diffuse medium all wave-guide modes are excited since photons are collected from all the angles accepted by the fiber's numerical aperture. Conversely an impulse response measurement employs collimated light. Therefore it is possible to excite a smaller number of wave-guide modes than the theoretical limit of the fiber, resulting in an underestimation of the actual impulse response FWHM. This phenomenon is also manifested when the source and detector fibers are not exactly parallel to each other when abutting them. In this case repeating the impulse response measurement by rotating the source tip relative to the detection tip, may excite different modes resulting in changes of pulse width, pulse amplitude, time-position of the maximum and shape. The phenomenon becomes more evident when the fiber guide numerical aperture and length increases leading to higher expected dispersion [112]. Experimental verification of such error sources has been reported [88]. The sensitivity to FWHM and t_0 uncertainty has been studied in Figure 4-6. and Figure 4-7 independently and the superposition of the two may be used to estimate the upper limits of the combined error.

4.4.2 Positional blurring

Increased photon collection requirements directs the use of fiber bundles, as discussed earlier, with a diameter that can extend up to several millimeters. Therefore a measurement can be seen as the integration of photons collected over the extended area that the tip of the fiber bundle covered when coupled to the medium under measurement. This will be equivalent to a simultaneous multi-separation measurement. Obviously this effect will be more evident as the fiber bundle collection area increases. Figure 4-8a depicts the relative

quantification error as a function of the fiber bundle tip radius for source-detector separation of 5 cm. The forward model that simulated the time-resolved curves performed numerical integration of all the photons over the entire detector area, predicted using Eq.(3-28) for every time-bin. Figure 4-8b depicts the same calculation for a source detector separation of 3cm. Again we observe that the reduced scattering coefficient is more sensitive than the absorption coefficient and as expected the accuracy deteriorates for smaller source detector separation.

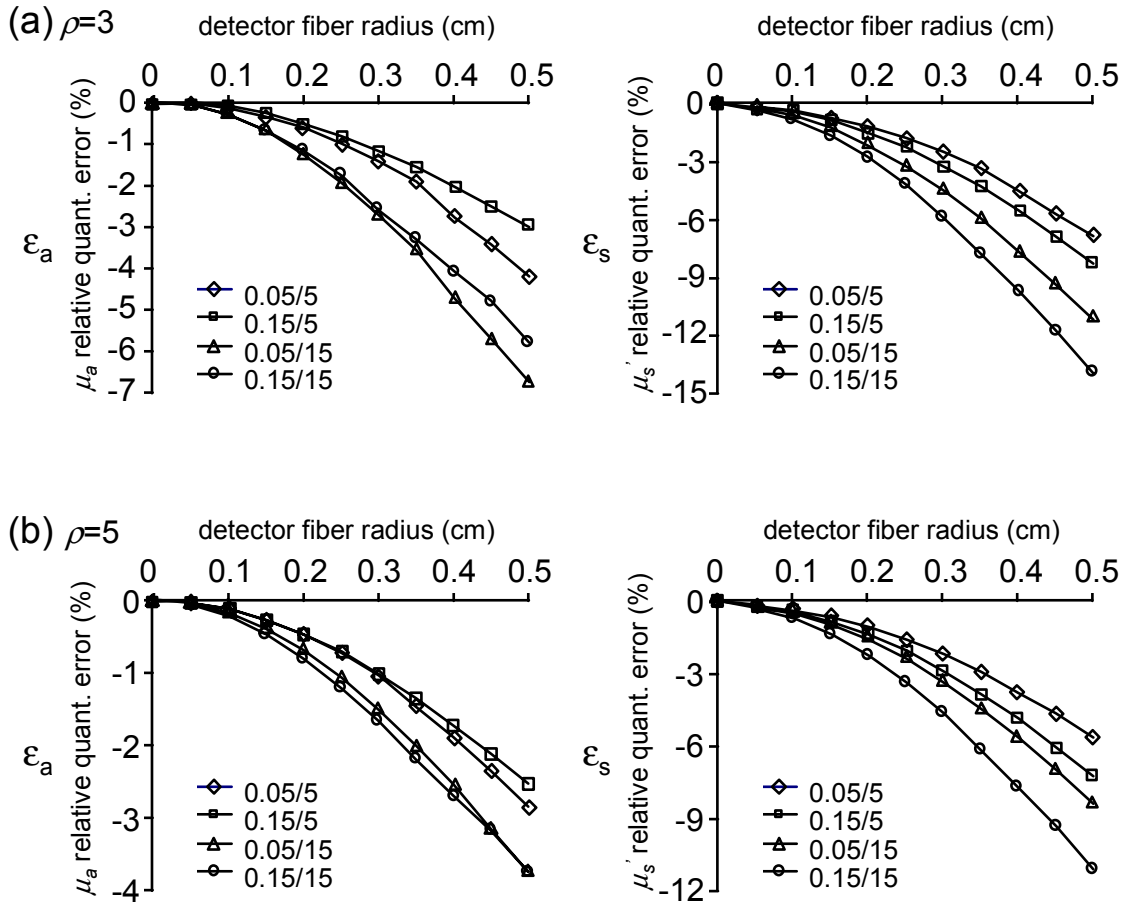

Figure 4-8 Quantification error of NIR time-resolved spectroscopy as a function of detection fiber radius.

4.4.3 Influence of optical properties on time-domain DOS quantification.

Figure 4-6., Figure 4-7 and Figure 4-8 have already demonstrated the quantification dependence on the optical properties of the measured medium. The effect is easily explained by observing time-resolved curves for different absorption and scattering backgrounds. Figure 4-9a. depicts normalized time-resolved curves corresponding to source-detector separation r=5cm, reduced scattering coefficient μ_s'=15cm^{-1}, and varying absorption coefficient in the range 0.04-0.2 cm^{-1} increasing with steps of μ_a =0.04cm^{-1}. It is easily seen that the contrast in the curve shape between 0.04 cm^{-1} and 0.08 cm^{-1} is significantly pronounced compared to the contrast for the same absorption change from 0.16 cm^{-1} to 0.20 cm^{-1}. Another characteristic feature is the reduced FWHM of the time-resolved curve in the higher absorption regime. Figure 4-1b shows similar normalized time-resolved curves, for the same source detector separation, plotted for background μ_s'=5cm^{-1}. It is evident that the contrast and the overall width of the curves further decrease in the low scattering regime.

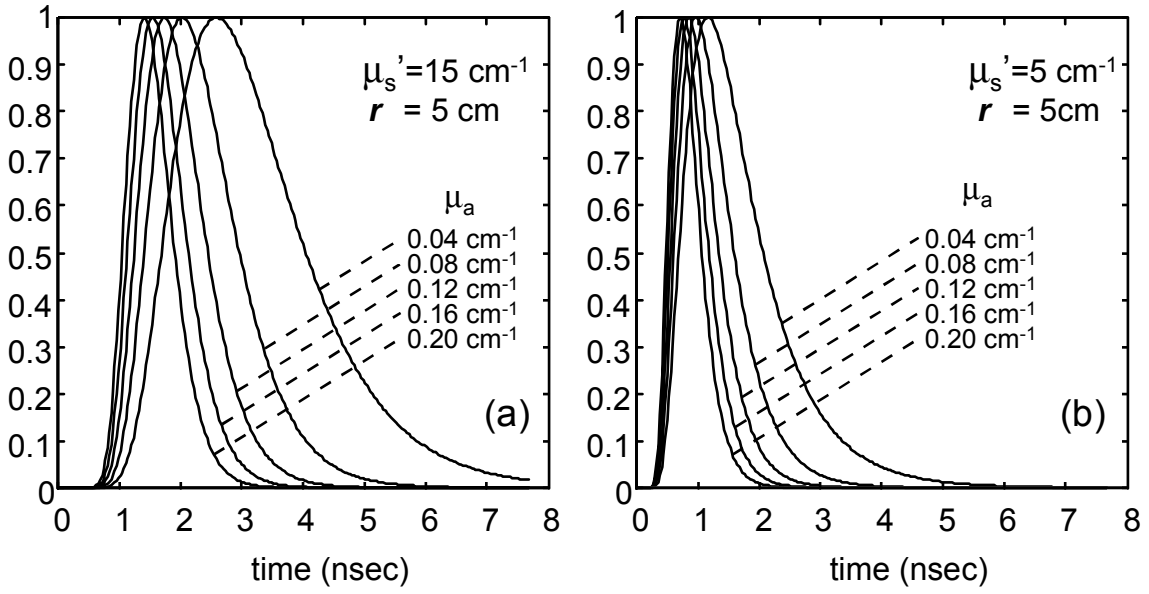

Figure 4-9: Dependence of time-resolved curve shape on the underlying optical properties. a) Time resolved curves plotted for μ_s'=15cm^{-1} r=5cm and different absorption coefficients b) same plot for μ_s'=5cm^{-1}

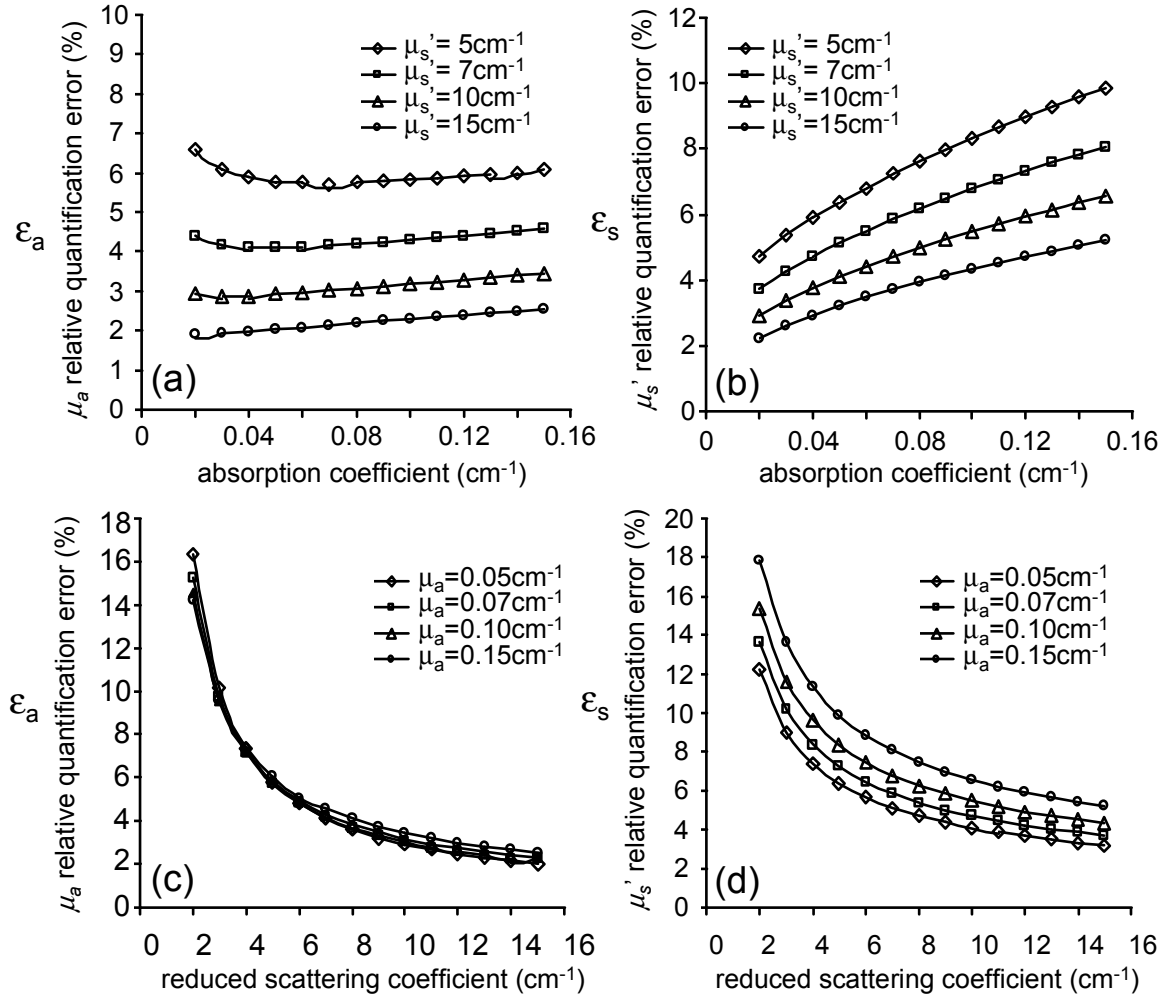

Figure 4-10 Quantification errors of NIR time-resolved spectroscopy induced due a 30 ps time shift of the impulse response, as a function of the optical properties of the medium measured.

It is straightforward now to describe the dependence of the quantification error on the value of the optical properties to be measured. For a certain instrument we can logically derive that the influence of the impulse response uncertainties will have a higher impact on quantification error for media with higher absorbing and lower scattering values due to the

narrower FWHM of the time-resolved curve. Furthermore it is expected that the quantification accuracy will deteriorate at the higher absorption regime due to the decrease in contrast between the curve shapes. Conversely positional blurring will favor narrower curves by inducing less overall time spread as compared to higher FWHM curves.

In order to demonstrate the non-linear behavior of the dependence as a function of the optical property we have focused on time uncertainties that induce the higher errors. Simulated curves were produced by varying the absorption or the scattering coefficient and fitted with an impulse response that had an induced time uncertainty of 30ps. Figure 4-10a and b depict the relative quantification errors ε_a and ε_s respectively for a medium with varying absorption coefficient for three different scattering backgrounds. Similarly Figure 4-10c and d show the relative quantification errors ε_a and ε_s as a function of reduced scattering coefficient variation for three different absorbing backgrounds. The relative quantification error ε_a has a non-linear dependence on absorption changes being relatively stable in the low absorption regime but increasing for higher absorption. On the contrary the dependence of ε_s is linear and increases for increasing scattering. Furthermore it is shown that ε_s is always larger than the corresponding ε_a.

4.4.4 Absolute accuracy limits.

During the previous sections, several experimental error sources and their influence on the quantification accuracy were discussed. The effect of these error sources can either be completely eliminated with appropriate data analysis procedures or minimized but not totally expunged with appropriate instrumentation design and appropriate algorithmic selection. The latter error sources ultimately determine the quantification accuracy of a time-resolved measurement.

Errors associated with the convolution process of the measurement with the finite-width impulse response can be eliminated by a deconvolution process. An efficient deconvolution procedure is suggested in Eq.(4-14). Instrument drift can be reduced by

allowing warming up of the instrument components before the measurement and by employing active electronic temperature compensation, which is a technique offered by several manufacturers to reduce the sensitivity of laser diode performance to surrounding temperature variations. The remnant drift and jitter can be monitored throughout the experiment using a reference fiber to collect a small portion of the incident pulse and directed to the detector with an appropriate time delay so that it does not interfere with the time-resolved curve obtained from the measurement. The reference fiber does not provide the impulse response measurement but can be used for post-processing retrieval of laser amplitude and temporal variations that could be used to correct the time axis of the measurement. The efficiency of this approach to eliminate time uncertainties is restricted by two factors. The first is that the selective excitation of a small portion of the photocathode area by the reference fiber may not reflect the overall TTS of the detector resulting in different time error statistics than the actual measurement and the effect will be more prominent for higher diameter detectors. The second is that since the time resolved detection has a discrete time step, the time resolution of the acquisition will be a definite upper limit of the accuracy of the correction and consequently of the quantification.

Another alternative is to allow the parameter t_0 to be a free parameter of the fit. This approach is equivalent to fitting only the amplitude information data in the frequency domain. Again due to the discrete nature of the detection, the instrument resolution will impose an upper limit on the quantification accuracy. Additionally this approach is more sensitive to incomplete modeling of the boundary conditions, which may lead to alterations of the time resolved curve shape.

Phenomena associated with the dispersion and length variability of the fiber bundles can be minimized by using low dispersion fibers and wide laser pulses to excite as many waveguide modes as possible. However it is difficult to correct for such effects. Therefore the uncertainties in the impulse response FWHM that are introduced by this error source may propagate unaccounted to the quantification calculation. The uncertainties introduced

by fiber dispersion and length variability on the t_0 can be partly accounted for by allowing t_0 to be a free fit parameter.

Finally errors induced by the finite diameter of the detection fiber bundles can be accounted by employing an integrated photon current for the area that the detection fiber occupies. If S is this area then the modified solution can be simply written as

$$y = \int_S \phi(u,r)dr \,. \qquad \textbf{(4-16)}$$

This approach accounts for positional blurring under the assumption of equal detection gain for all single fibers constituting a fiber bundle. The quantification of time-resolved spectroscopy can be further improved when selected parts of the curve are fitted for as will be discussed in the following section.

4.4.5 Selective fit of the time-resolved curve.

Under several circumstances fitting selected parts of the curve can improve the sensitivity of the fit to experimental errors or simplify the calculation process. Chance et. al. have suggested that the slope of the time resolved curve can be used to estimate the absorption coefficient assuming that the instrument impulse response has small FWHM so that it does not blur the time-resolved curve significantly [89]. A more general approach is to fit the time resolved curve for different values of the interval [K1,K2] in Eq.(4-14). Here I demonstrate that the fitting process becomes less sensitive to time uncertainties if the last part of the time resolved curve is fitted for both the absorption and reduced scattering coefficient. Let us consider the fitting scheme of Figure 4-11 where the time-resolved curve is fitted from its maximum to the later times.

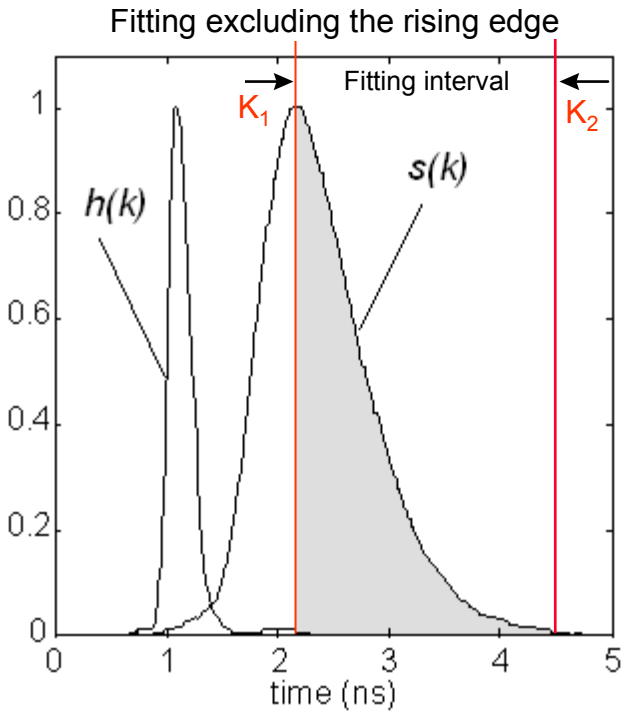

Figure 4-11. Fitting scheme that increases the accuracy of NIR time-resolved spectroscopy by fitting only the curve shape at later times.

Figure 4-12 plots the results of applying the fit suggested in Figure 4-11 for the case demonstrated in Figure 4-10, namely an instrument response shift by 30ps. The improvement when using only the falling part of the curve in the fitting is remarkable. The relative absorption error ε_a is improved by more than 100% and the relative scattering error ε_a by more than 30%. The calculation is made in the absence of noise.

Kienle et.al [54] have also noted that the diffuse model and boundary conditions used are not valid for early arriving photons that are not completely diffuse. This is especially true when short source-detector separations are used. We can therefore conclude that the rising part of the time resolved curve is very sensitive to time uncertainties, either theoretical

or experimental. By excluding the rising edge both the absorption and the reduced scattering coefficient can be quantified with higher accuracy.

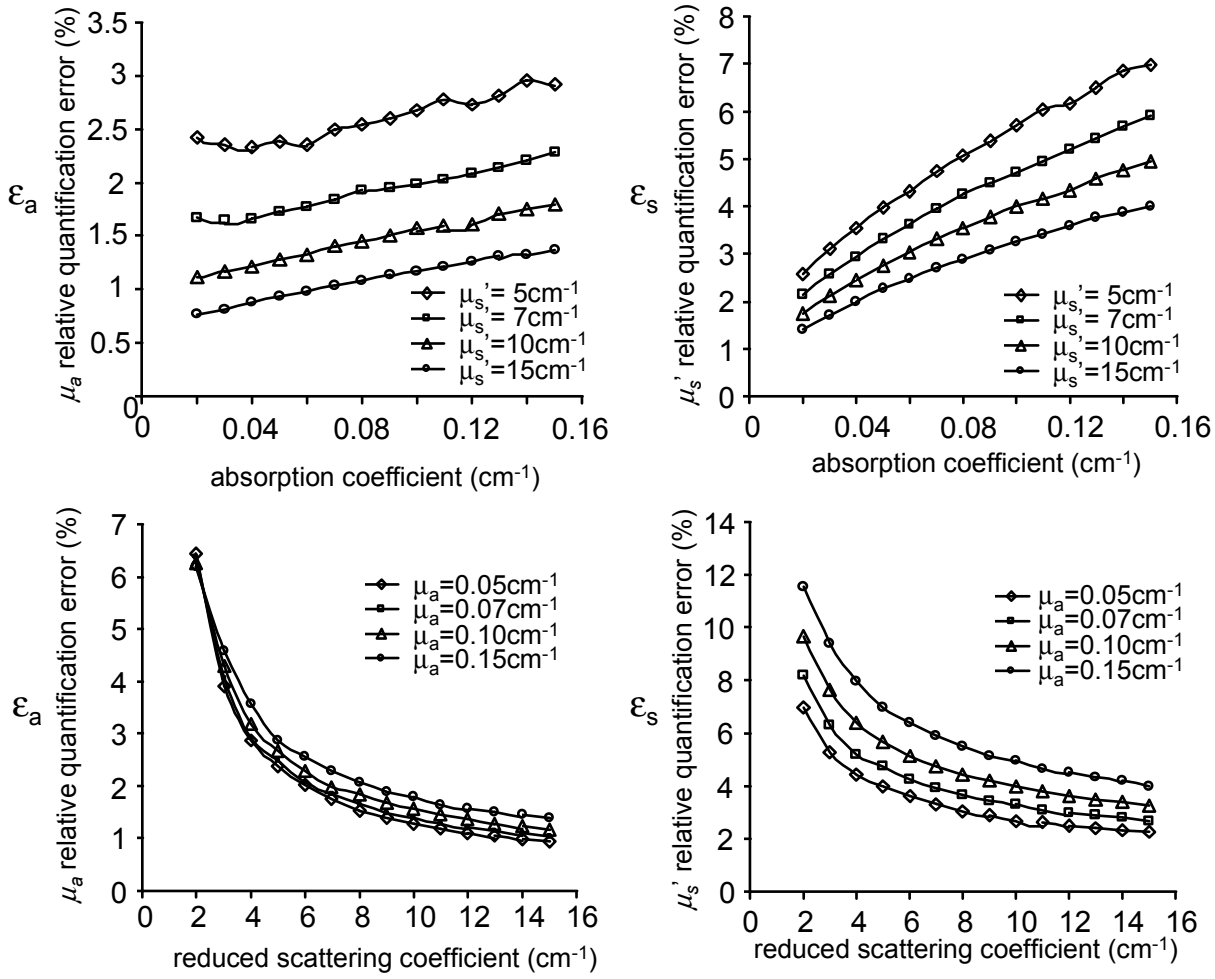

Figure 4-12. The quantification errors of NIR time-resolved spectroscopy induced due a 30ps impulse response shift observed when fitting only the falling part of the time-resolved curve, for different combinations of optical properties.

4.4.6 Discussion.

The investigation of the effect of experimental errors on the quantification accuracy of time resolved measurements, using curve shape fitting, has revealed that significant inaccuracies can arise if appropriate correction schemes are not employed. The method is generally most sensitive to temporal uncertainties of the impulse response, followed by uncertainties in the impulse response finite width and positional blurring. It has been also shown that the calculation of the reduced scattering coefficient is generally more susceptible to errors than the absorption coefficient.

Furthermore the quantification accuracy depends on the medium optical properties. Impulse response time and FWHM uncertainties induce higher quantification errors in media with higher absorption and lower scattering. It has to be noted that this observation is not associated with violating the assumption of the diffusion approximation, which requires that $\mu_s' >> \mu_a$, or signal-to-noise considerations, but it is a direct effect of the narrow FWHM that the time resolve curve attains in this optical property regime. Conversely an inverse dependence is observed for positional blurring.

Additionally experimental uncertainties induce an absorption-scattering cross-talk. This cross-talk is expected to deteriorate under non-favorable signal-to-noise conditions

When absolute quantification of optical properties is required, curve-shape fitting yields a convenient way to characterize the media. However when relative changes are monitored, the quantification accuracy can significantly improve when the amplitude information is included. Specifically curve-shape fitting can be applied to fit the most accuracy-favorable measurement and all subsequent calculations can fit only for the absorption and scattering coefficient, using the amplitude calculated from the curve-shape fitting as a fixed parameter. Additionally the difference of the number of photons detected between measurements has been shown to be a very accurate measure when absorption changes are considered. In this case an additional experimental factor, namely the amplitude stability of the laser source must be considered in determining the quantification accuracy.

4.5 Time domain differential measurements.

Eq.(4-14) is generally used for calculating absolute absorption and scattering coefficients. However when considering absorption *differential changes* that might arise as a function of time, I present a technique, which significantly outperforms in accuracy and sensitivity the methods presented in the preceding sections. Let us consider a small absorption change of the tissue volume from μ_{a1} to μ_{a2}, assuming constant scattering coefficient μ_s'. Then the photon fluence rate will in general change from ϕ_1 to ϕ_2 respectively. For example, according to Eq.(3-13) for a homogeneous and infinite medium:

$$\frac{\phi_2(\rho,t)}{\phi_1(\rho,t)} = \exp(-(\mu_{a2}-\mu_{a1})ct) = \exp(-\Delta\mu_a ct), \qquad \textbf{(4-17)}$$

where ρ is the source detector separation.

Taking the natural logarithm of Eq.(4-17) and integrating over time retrieves the absorption change

$$\Delta\mu_a = -\frac{2}{c(t_2^2-t_1^2)}\int_{t_1}^{t_2}\ln\frac{\phi_2(r,t)}{\phi_1(r,t)}dt. \qquad \textbf{(4-18)}$$

Here t_1, t_2 can be any time interval within the time-resolved curve. It is straightforward to show that even in more complex formulations, such as in reflectance using the extrapolated boundary condition (Eq.(3-36)) in transmittance with finite slab geometry, Eq.(4-18) still holds.

According to Eq.(3-32) the photon fluence rate for reflectance or transmittance geometry is

$$\phi(\rho,z,t)=\frac{Ac}{(4\pi cDt)^{-3/2}}\sum_{m=1}^{M}\left(\exp\left(-\frac{R_0^2(m)}{4cDt}\right)-\exp\left(-\frac{R_c^2(m)}{4cDt}\right)\right)\exp(-\mu_a ct)\,, \qquad \textbf{(4-19)}$$

where $R_0(m)$ and $R_c(m)$ are the distances given by Eq.(3-33) and Eq.(3-34). The ratio of reflected or transmitted fluence rates ϕ_1 and ϕ_2 gives again

$$\Delta\mu_a=-\frac{2}{c(t_2^2-t_1^2)}\int_{t_1}^{t_2}\ln\frac{\phi_2(r,t)}{\phi_1(r,t)}dt \qquad \textbf{(4-20)}$$

Eq.(4-18) and Eq.(4-20) integrate the area between the time-resolved baseline curve and the time-resolved curve after the absorption change as indicated in Figure 4-13.

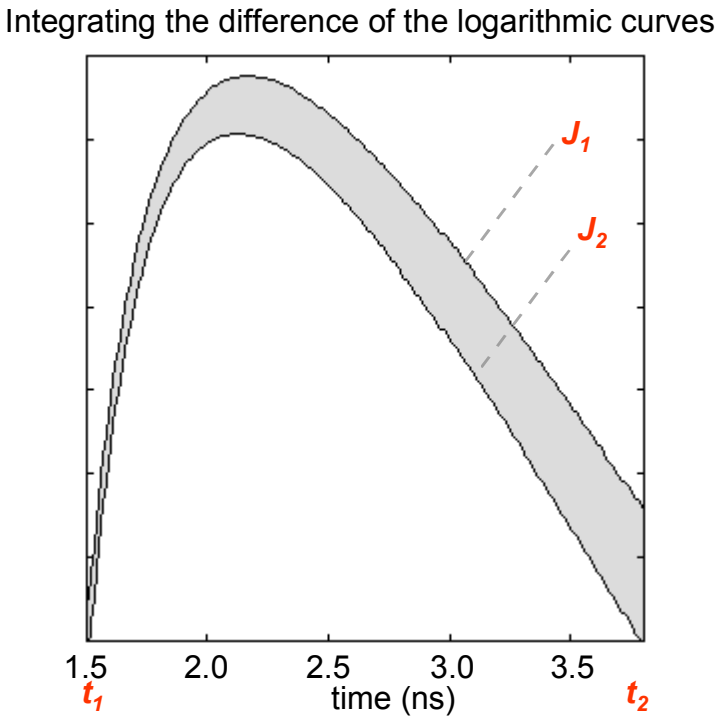

Figure 4-13. Schematic of the integration described by Eq.(4-18) or Eq.(4-20). Here J_1 is the curve before the absorption change and J_2 is the curve after an increase in the absorption coefficient.

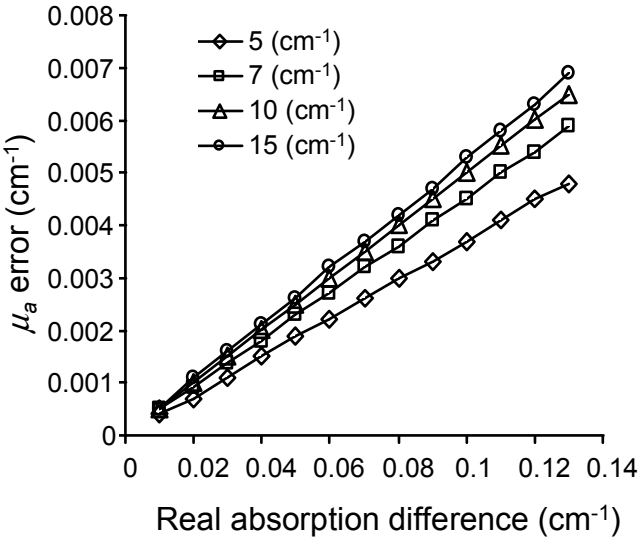

Figure 4-14: Quantification error of Eq.(4-18) as a function of the real absorption change.

This approach can be used as a very sensitive and accurate analysis method for measurement of absorption changes. An additional great advantage is that Eq.(4-18) and Eq.(4-20) are virtually independent of the boundary conditions for reflectance and transmittance geometries (as described in the previous section). The main limitation is the postulation of invariable diffusion coefficient for small absorption changes. The diffusion coefficient depends weakly on the absorption and therefore it will vary with absorption changes. We have investigated the error introduced due to this assumption. Figure 4-14 shows the error as a function of absorption changes for different values of background scattering coefficient. These simulated absorption changes were obtained using Eq.(3-28) and the error of the approximation was calculated by comparing the introduced absorption change with the absorption changes as calculated using Eq.(4-20). The error of the method is shown to be quite insensitive even if there is big uncertainty in the knowledge of the real background scattering coefficient. The error remains in most cases below 10^{-3} cm^{-1} for absorption coefficient changes of $\Delta\mu_a$<0.02 cm^{-1} and it scales approximately linearly with the absorption change. This could enable easy error correction if higher absorption changes are monitored.

5 Diffuse Optical Tomography.

Imaging with NIR photons has followed a development pattern somewhat similar to that of X-ray photons in that original developments using planar imaging were followed by to tomographic developments. Simple optical projection images have the inherent limitation of not providing three-dimensional information for the position of objects and not quantifying local optical properties. The combination of photon trajectories propagating at different angles (projections) contains information on the three dimensional distribution of optical heterogeneity. Tomographic techniques conveniently combine this information from projections to yield three-dimensional maps of optical properties.

Diffuse Optical Tomography, similarly to other tomographic schemes, is divided in two parts, the forward problem and the inverse problem. The forward problem describes the physical phenomenon of diffusive photon propagation. Practically it is a solution of the heterogeneous diffusion equation. Such solution can be obtained analytically as seen in Chapter 3 or numerically. The solution predicts the photon field propagating through an optically heterogeneous medium and the resulting field expected in the boundaries of the

measured system. The inverse problem uses the appropriate forward solution to construct an operator that is applied to the measured data from an unknown medium to yield the internal optical composition of this medium. This operator could be the direct inverse of a matrix, the numerically calculated inverse of a matrix or a minimization/data-fitting process.

Diffuse Optical Tomography can be performed in any of the domains discussed in the derivation of solutions in Chapter 3 and seen in the spectroscopic approaches of Chapter 4, namely the constant wave CW-domain, the frequency domain and the time-domain. In general the CW domain carries the lowest information content whereas the time domain carries the highest. Reconstruction performance depends on the information content of the domain used, the number of sources and detectors employed, their relative position and signal-to-noise ratio.

In this chapter, **Section 5.1** outlines a linear, analytical tomographic scheme, based on the perturbation solution derived in Chapter 3. This method is a classic approach, presented by Kak and Slaney [56] and adapted for diffuse optics by Arridge et. al.[90], O'Leary [55] and others. Although there are several more sophisticated techniques to perform DOT, the perturbation approach is a straightforward method to analytically examine and solve DOT problems and understand the reconstruction fundamentals. Personally I have also found it outstanding in quickly getting the right, reasonably quantified answer with simulated and real data from media with regular boundaries [88,91]. **Section 5.2** presents the algebraic reconstruction techniques that were primarily used for inverting simulated and experimental data used in this work. **Section 5.3** focuses on calibration issues for experimental measurements and demonstrates why under certain circumstances the Rytov perturbation approach is the method of choice. **Section 5.4** introduces an algorithm, based on the perturbative DOT, useful to image a diffuse medium with an increase in average absorption. This algorithm was applied to image the contrast-enhanced breast. The analysis exposes approximations leading to an intuitive and simplified inverse algorithm, shows explicitly why transmission geometries are less susceptible to error than the remission geometries, and why differential measurements are less susceptible to surface artifacts. These

ideas are not only applicable to tumor detection and characterization using contrast agents, but also to functional activation studies with or without contrast agents and multi-wavelength measurements. **Section 5.5** discusses upgrades of the linear tomographic method that improve the quantification accuracy using higher order solutions of the heterogeneous diffusion equation. Finally **section 5.6** presents the simplification of the tomographic scheme when a-priori structural information is available. This method was a key technique in the data analysis for the simultaneous DOT-MR examination and yields the image-guided localized spectroscopy approach (see Chapter 9).

5.1 Linear Diffuse Optical Tomography

In this section I review the linear analytical diffuse optical tomography problem in the frequency domain. Experimentally a time domain instrument was used and is described in Chapter 7. The description of the tomographic problem in the time domain however is more complicated than needed. Most derivations of diffraction tomography are done by considering only one temporal frequency [56]. This decomposition can be accomplished by finding the Fourier transform of the field with respect to time at each position of the volume of interest. Then the use of the information contained in the time-domain data can be also converted to the frequency domain via the Fourier transform. The information at multiple frequencies can be combined to yield superior reconstructions compared to reconstructions performed at a single frequency. The constant wave domain can be also represented by the frequency domain expressions by setting the frequency to zero.

In the following expressions I retain the dependence of the fluence rate on the modulation frequency ω to indicate the frequency-domain description. The scattered field for a medium where both the diffusion and absorption coefficients are spatially variant can be found under the Born approximation by combining Eq.(3-46) and Eq.(3-57), i.e.

$$\phi_{sc}(\vec{r}_d,\vec{r}_s,\omega) = -\int_V g(\vec{r}-\vec{r}_d,\omega)O(\vec{r})\phi_0(\vec{r},\vec{r}_s,\omega)d\vec{r} + \int_V \vec{\nabla} g(\vec{r}-\vec{r}_d,\omega)\cdot\vec{\nabla}\phi_0(\vec{r},\vec{r}_s,\omega)\frac{\delta D(\vec{r})}{D_0}d\vec{r}\,, \quad \textbf{(5-1)}$$

where $\phi_{sc}(\vec{r}_d,\vec{r}_s,\omega)$ here is the scattered field due to both the absorption and the scattering heterogeneity at modulation frequency ω. The field $\phi_0(\vec{r},\vec{r}_s,\omega)$ is the photon wave initiated at the source position $\vec{r}_s$ that hits the perturbation distribution $O(\vec{r})$ and $\delta D(\vec{r})$ at position $\vec{r}$ and $g(\vec{r}-\vec{r}_d,\omega)$ is the Greens function solution to the heterogeneous diffusion equation that propagates the field scattered from the heterogeneity to the detector position at $\vec{r}_d$ (see §3.5). Similarly the Rytov solution can be written as a superposition of Eq.(3-51) and Eq (3-58), i.e.,

$$\Phi_{sc}(\vec{r}_d,\vec{r}_s,\omega) = -\frac{1}{\phi_0(\vec{r}_d,\vec{r}_s,\omega)}\int_V g(\vec{r}-\vec{r}_d,\omega)O(\vec{r})\phi_0(\vec{r},\vec{r}_s,\omega)d\vec{r} + + \frac{1}{\phi_0(\vec{r}_d,\vec{r}_s,\omega)}\int_V \vec{\nabla} g(\vec{r}-\vec{r}_d,\omega)\vec{\nabla}\phi_0(\vec{r},\vec{r}_s,\omega)\frac{\delta D(\vec{r})}{D_0}d\vec{r}\,. \quad \textbf{(5-2)}$$

Eq.(5-1) and Eq.(5-2) can be solved analytically if the volume of integration V is discretized into a number of voxels N, with centers at the discrete positions $\vec{r}_n$, and the integral equations approximated as a sum of unknown perturbations multiplied by the appropriate coefficients (weights). The discrete Born solution, at cartesian coordinates $(\hat{x},\hat{y},\hat{z})$ can then be written as

$$\phi_{sc}(\vec{r}_d,\vec{r}_s,\omega) = -\sum_{n=1}^{N}\left(W_n^a\,\delta\mu_a(\vec{r}_n) + W_n^s\,\delta D(\vec{r}_n)\right), \quad \textbf{(5-3)}$$

where the absorption Born weight W_n^a at the discrete position $\vec{r}_n$ is

$$W_n^a = g(\vec{r}_n - \vec{r}_d, \omega)\phi_0(\vec{r}_n, \vec{r}_s, \omega)\frac{h_x h_y h_z}{D_0}, \quad \textbf{(5-4)}$$

the scattering Born weight is

$$W_n^s = \vec{\nabla} g(\vec{r}_n - \vec{r}_d, \omega) \cdot \vec{\nabla}\phi_0(\vec{r}_n, \vec{r}_s, \omega)\frac{h_x h_y h_z}{D_0}, \quad \textbf{(5-5)}$$

and h_x, h_y and h_z are the discretization steps along $\hat{x}, \hat{y}, \hat{z}$ respectively.

Similarly the discrete Rytov solution, at cartesian coordinates $(\hat{x}, \hat{y}, \hat{z})$ and for the same descretization steps (h_x, h_y h_z) can then be written as

$$\phi_{sc}(\vec{r}_d, \vec{r}_s, \omega) = -\sum_{n=1}^{N}\left(W_n^a \delta\mu_a(\vec{r}_n) + W_n^s \delta D(\vec{r}_n)\right), \quad \textbf{(5-6)}$$

where the absorption Rytov weight W_n^a at the discrete position $\vec{r}_n$ is

$$W_n^a = \frac{g(\vec{r}_n - \vec{r}_d, \omega)\phi_0(\vec{r}_n, \vec{r}_s, \omega)}{\phi_0(\vec{r}_d, \vec{r}, \omega_s)}\frac{h_x h_y h_z}{D_0}, \quad \textbf{(5-7)}$$

and the scattering Rytov weight is

$$W_n^s = \frac{\vec{\nabla} g(\vec{r}_n - \vec{r}_d, \omega) \cdot \vec{\nabla}\phi_0(\vec{r}_n, \vec{r}_s, \omega)}{\phi_0(\vec{r}_d, \vec{r}_s, \omega)}\frac{h_x h_y h_z}{D_0}. \quad \textbf{(5-8)}$$

Eq.(5-3) and Eq.(5-6) are written for a single measurement, for a source at position $\vec{r}_s$, a detector at position $\vec{r}_d$, and a frequency ω. For multiple measurements $m = o \times p \times q$, where o is the number of sources, p is the number of detectors and q is the number of frequencies employed, the discretization yields a set of coupled, linear equations which in matrix form are written as,

$$\begin{bmatrix} \phi_{sc}^{1}(\vec{r}_{s1},\vec{r}_{d1},\omega_1) \\ \vdots \\ \phi_{sc}^{m}(\vec{r}_{so},\vec{r}_{dp},\omega_q) \end{bmatrix} = \begin{bmatrix} W_{11}^{a} & \cdots & W_{1n}^{a} & W_{11}^{s} & \cdots & W_{1n}^{s} \\ \vdots & \ddots & \vdots & \vdots & \ddots & \vdots \\ W_{m1}^{a} & \cdots & W_{mn}^{a} & W_{m1}^{s} & \cdots & W_{mn}^{s} \end{bmatrix} \cdot \begin{bmatrix} \delta\mu_a(\vec{r}_1) \\ \vdots \\ \delta\mu_a(\vec{r}_n) \\ \delta D(\vec{r}_1) \\ \vdots \\ \delta D(\vec{r}_n) \end{bmatrix}. \qquad \textbf{(5-9)}$$

Eq.(5-9) can use either the Born or Rytov weights given by Eq.(5-5) and Eq.(5-8) respectively. It is implicit that the weights will be calculated for the appropriate geometry, as seen at the solutions for the fluence rate and Greens' function given in §3.4. Actually Eq.(5-9) can be used generically, since the calculation of the weights can be performed analytically and numerically, for homogeneous or inhomogeneous media. This issue will be discussed more analytically in §5.5.

Inverting Eq.(5-9) yields the map (image) of unknown absorption and scattering perturbations. This inversion is discussed in the next section.

5.2 Matrix Inversion

Solving (inverting) and evaluating inversions of a system of linear equations as in Eq.(5-9) has been the target of many decades of mathematical and engineering developments. As a result there is ample literature on many inversion approaches and their performance with general and specific problems.

The main solver selected for the inversions was a class of algorithms called algebraic reconstructions. This set of algorithms was originally applied to X-ray computed tomography reconstructions and has several logistical advantages. The techniques process the inversion problem line by line and do not require the creation or storage of any additional matrices. Therefore it is optimized towards minimum computer memory requirements, an important property for large tomographic problems.

Here I will describe briefly a technique called method of projections (MOP), which was the method of choice in this work. If *P* is the measurement vector for m measurements, *F* the vector of 2·n unknown perturbations from a volume discretized in n voxels and *W* is the Rytov or Born weight, then Eq.(5-9) can be written in a generalized form as:

$$P=W\cdot F. \qquad \textbf{(5-10)}$$

Since the weights used are generally complex numbers (except for zero modulation frequency), inverting Eq.(5-10) could be performed using only the real part, only the imaginary part or using both real and imaginary parts. When both real and imaginary parts are used the matrix equation can be written as

.

$$\begin{bmatrix} \phi_{sc}^{1}(\vec{r}_{s1},\vec{r}_{d1},\omega_1)^R \\ \vdots \\ \phi_{sc}^{m}(\vec{r}_{so},\vec{r}_{dp},\omega_q)^R \\ \phi_{sc}^{m}(\vec{r}_{so},\vec{r}_{dp},\omega_q)^I \\ \vdots \\ \phi_{sc}^{m}(\vec{r}_{so},\vec{r}_{dp},\omega_q)^I \end{bmatrix} = \begin{bmatrix} W_{11}^{aR} & \cdots & W_{1n}^{aR} & W_{11}^{sR} & \cdots & W_{1n}^{sR} \\ \vdots & \ddots & \vdots & \vdots & \ddots & \vdots \\ W_{m1}^{aR} & \cdots & W_{mn}^{aR} & W_{m1}^{sR} & \cdots & W_{mn}^{sR} \\ W_{11}^{aI} & \cdots & W_{1n}^{aI} & W_{11}^{sI} & \cdots & W_{1n}^{sI} \\ \vdots & \ddots & \vdots & \vdots & \ddots & \vdots \\ W_{m1}^{aI} & \cdots & W_{mn}^{aI} & W_{m1}^{sI} & \cdots & W_{mn}^{sI} \end{bmatrix} \cdot \begin{bmatrix} \delta\mu_a(\vec{r}_1) \\ \vdots \\ \delta\mu_a(\vec{r}_n) \\ \delta D(\vec{r}_1) \\ \vdots \\ \delta D(\vec{r}_n) \end{bmatrix}, \qquad \textbf{(5-11)}$$

where 'R' denotes "real" and 'I' denotes "imaginary". The weight matrix is of dimension 2m×2n. The use of three possible data combinations (real, imaginary or both) and of three unknown data combinations (absorption perturbation only, diffusion perturbations only or both) can create a total of 9 different schemes to be inverted, depending on the specific application. In the following we will generally examine an M×N problem.

Independently of the exact constitution of the matrix equation, the M×N problem creates N degrees of freedom. Therefore the image represented by the N-dimensional vector F may be considered to be a single point in the N-dimensional space. Each of the rows in W

then represents a hyperplane. The algebraic reconstruction technique begins with an arbitrary initial guess F_0, which represents a point in the N-dimensional space and projects from this initial point to the first hyperplane defined by the first row of the weight matrix W. From the point of intercept between the projection and the first hypeplane a new projection is performed to the hyperplane defined by the second row. Mathematically the process is written as

$$\vec{F}_i = \vec{F}_{i-1} + \frac{\left(P_i - \lambda \vec{F}_{i-1} \cdot \vec{W}_i\right)}{\vec{W}_i \cdot \vec{W}_i} \vec{W}_i , \qquad \textbf{(5-12)}$$

where i represents the i^{th} projection from hyperplane i-1 to hyperplane i, $\vec{W}_i$ is the i^{th} hyperplane (or i^{th} row of the weight matrix W), P_i is the i^{th} measurement and λ is a constant called the relaxation parameter. For λ=1, F_{i-1} is the projection point on hyperplane i-1 and F_I is the new projection point on hyperplane i. For $0< \lambda <1$, and if d is the projection distance between F_{I-1} and the i^{th} hyperplane, the new point F_i is located on the projection from F_{i-1} to hyperplane i but at a position which is λd. The relaxation parameter λ is introduced to minimize artifacts and inversion instability [92]. Typically in this work λ was set to 0.1.

A MOP iteration is defined here as one full projection circle through all hyperplanes, namely one MOP iteration equals N projections. Generally, repeating the number of projections in an iterative fashion improves the convergence of the reconstruction. When a unique solution exists then this sequential projection on hyperplanes leads to this point which is the common point of intersection for all these hyperplanes (for a proof see [56]). In the presence of noise and more generally when the system does not have a unique solution, either because it is overdetermined (M>N) or underdetermined (M>N), the solution reached represents a point of all possible solutions that is closer to the initial guess F_0.

The convergence speed of the solution depends on the size of the inverted problem and on the N-space orthogonality of the hyperplanes. Although optimization can be performed in order to increase the convergence speed, by appropriately selecting projections

between hyperplanes that are orthogonal or close to orthogonal, this generally requires additional computation or introduces complexity. In this work, unless otherwise indicated, the system of Eq.(5-12) was solved on a row to row projection and convergence was assumed when the change in the relative error

$$\Delta\varepsilon_i = \sum_{j=1}^{N} \frac{\left(F_i(j) - F_{i-1}(j)\right)^2}{F_i(j)^2} - \sum_{j=1}^{N} \frac{\left(F_{i-1}(j) - F_{i-2}(j)\right)^2}{F_{i-1}(j)^2}, \qquad \textbf{(5-13)}$$

became less than a preset value, normally ~10^{-5}.

5.3 Experimental calibration: Born vs. Rytov revisited

A comparison between the Rytov and a normalized Born approximation was discussed in §3.6. Generally it has been shown that the Rytov solution is equivalent to a normalized Born (and by extension to a standard Born) solution for weak scattered fields. For larger scattered fields it was found that the differences encountered between the two approximations it was not a result of the physics of the approximation per se but rather on the more efficient formulation of the Rytov scattered field.

Here I will discuss the experimental implementation of the Born and Rytov approximations and explain why many times it is preferable to use the Rytov approximation (or the equivalent normalized Born approximation for small scattered fields) over the standard Born approximation. In real measurements one needs to experimentally determine the scattered field in Eq.(5-1) and Eq.(5-2) . According to Eq.(3-41) the Born scattered field is

$$\phi_{sc}(\vec{r}_d, \vec{r}_s, \omega) = \phi(\vec{r}_d, \vec{r}_s, \omega) - \phi_0(\vec{r}_d, \vec{r}_s, \omega), \qquad \textbf{(5-14)}$$

where both the incident field $\phi_0(\vec{r}_d, \vec{r}_s, \omega)$ and the total field $\phi(\vec{r}_d, \vec{r}_s, \omega)$ depend on an experimental, multiplicative gain factor A. To denote that we can write Eq.(5-14) as

$$\phi_{sc}(\vec{r}_d,\vec{r}_s,\omega) = A\phi^1(\vec{r}_d,\vec{r}_s,\omega) - A\phi_0^1(\vec{r}_d,\vec{r}_s,\omega), \qquad \textbf{(5-15)}$$

where $\phi^1(\vec{r}_d,\vec{r}_s,\omega)$ is an assumed total field measured for a source term with unit amplitude and zero phase and similarly $\phi_0^1(\vec{r}_d,\vec{r}_s,\omega)$ is the incident field measured for the same source. Therefore the calculation of the Born scattered field requires the determination of the gain factor A and this generally has to be performed for every source detector pair independently, since individual gains may vary. Determination of A can be done experimentally on a medium with known optical properties and known geometry, i.e. a measurement where A is the only unknown. However the Rytov expression (or the normalized Born) gives a convenient way to cancel out the gain term in differential measurements, namely measurements where a baseline is obtained prior to a change in optical properties. This could be in situations where functional activation is monitored, when a contrast agent is administered, or simply when a measurement is performed in a calibration medium before or after the tissue measurement. The Rytov expression is written as (see Eqs. (3-47)-(3-49)):

$$\Phi_{sc}(\vec{r}_d,\vec{r}_s,\omega) = \ln\frac{A\phi^1(\vec{r}_d,\vec{r}_s,\omega)}{A\phi_0^1(\vec{r}_d,\vec{r}_s,\omega)} = \ln\frac{\phi^1(\vec{r}_d,\vec{r}_s,\omega)}{\phi_0^1(\vec{r}_d,\vec{r}_s,\omega)}, \qquad \textbf{(5-16)}$$

and obviously is independent of the gain factor A. Therefore there is no need to explicitly determine A if the experimental protocol is designed to allow for differential measurements. Taking the ratio of differential measurements also decreases the sensitivity on systematic errors under the premise that both the baseline and actual measurements "see" the same systematics (foe example fiber-medium boundary imperfect coupling) This issue will be revisited in the next section.

For the rest of this work, unless otherwise noted, all reconstructions will be performed using the Rytov approximation.

5.4 Differential DOT after contrast enhancement

There are certain implications for imaging a medium after the administration of a contrast agent. For simplicity we present this analysis for an infinite medium. This theory however can be easily extended to other simple geometries such as semi-infinite or slab, using weights derived with the method of image sources and the appropriate extrapolated boundary condition (see §3.4).

Let us assume a tissue where the contrast agent Indocyanine Green (ICG) is administered. The first order perturbation expansion divides the absorption ($\mu_a'(\vec{r})$) and diffusion ($D'(\vec{r})$) coefficients of the *pre-ICG* breast into spatially varying ($\delta\mu_a'(\vec{r}), \delta D'(\vec{r})$) and background components (μ_{a0}', D_0'), i.e. $\mu_a'(\vec{r}) = \mu_{a0}' + \delta\mu_a'(\vec{r})$ and $D'(\vec{r}) = D_0' + \delta D'(\vec{r})$. Throughout this section a single $'$ denotes pre-ICG tissue volumes. In the Rytov approximation the total photon density wave measured at position $\vec{r}_d$ due to a source at position $\vec{r}_s$ is written as the product of two components, (Eq.(3-47)- Eq.(3-49)) i.e.

$$\phi'(\vec{r}, \vec{r}_s, \omega) = \phi_0'(\vec{r}, \vec{r}_s, \omega) \exp[\Phi_{sc}'(\vec{r}, \vec{r}_s, \omega)], \qquad \textbf{(5-17)}$$

where the *scattered field* $\Phi_{sc}'(\vec{r}_s, \vec{r}_d, \omega)$, is produced by the heterogeneities ($\delta\mu_a'(\vec{r}), \delta D'(\vec{r})$) and the *incident field* $\phi_0'(\vec{r}_s, \vec{r}_d, \omega)$, is the field that would have been detected from the same medium if these heterogeneities were not present. The first order perturbative solution for the pre-ICG medium is given by Eq.(5-2). Here the dependence of the weights on the medium's optical properties is kept for reasons that will be shortly become apparent. Then the detected scattered field from the pre-ICG tissue is

$$\Phi_{sc}'(\vec{r}_s, \vec{r}_d, \omega) = \int_V [W_a'(\vec{r}_s, \vec{r}_d, \vec{r}, \mu_{a0}', D_0', \omega)\delta\mu_a'(\vec{r}) + W_s'(\vec{r}_s, \vec{r}_d, \vec{r}, \mu_{a0}', D_0', \omega)\delta D'(\vec{r})]d\vec{r}, \qquad \textbf{(5-18)}$$

where $W_a', (W_s')$ represents the absorption (scattering) weight of the voxel at position $\vec{r}$, due to a source at $\vec{r}_s$ and a detector at $\vec{r}_d$.

Following the administration of a contrast agent the background optical properties change. The new, *post-ICG,* total field can be written in a similar form:

$$\phi''(\vec{r},\vec{r}_s,\omega) = \phi_0''(\vec{r},\vec{r}_s,\omega)\exp[\Phi_{sc}''(\vec{r},\vec{r}_s,\omega)]. \qquad \textbf{(5-19)}$$

Here $\Phi_{sc}''(\vec{r}_s,\vec{r}_d,\omega)$ is the field component scattered from the post-ICG heterogeneities (i.e. $\delta\mu_a''(\vec{r}),\delta D''(\vec{r})$ with respect to the new background optical properties μ_{a0}'', D_0'') and $\phi_0''(\vec{r}_s,\vec{r}_d,\omega)$ is the incident field obtained from the homogeneous background medium with μ_{a0}'', D_0''. The first order perturbative solution of the heterogeneous diffusion equation yields

$$\Phi_{sc}''(\vec{r}_s,\vec{r}_d,\omega) = \int_V [W_a''(\vec{r}_s,\vec{r}_d,\vec{r},\mu_{a0}'',D_0'',\omega)\delta\mu_a''(\vec{r}) + W_s''(\vec{r}_s,\vec{r}_d,\vec{r},\mu_{a0}'',D_0'',\omega)\delta D''(\vec{r})]d\vec{r}, \qquad \textbf{(5-20)}$$

where W_a (W_s) represents the absorption (scattering) weight of voxels at position $\vec{r}$, due to a source at $\vec{r}_s$ and for a detector at $\vec{r}_d$.

Combining Eq.(5-17) with Eq.(5-19) we obtain the ***relative scattered field***, i.e

$$\Phi_{sc} = \Phi_{sc}'' - \Phi_{sc}' = \ln\left(\frac{\phi''}{\phi'}\cdot\frac{\phi_0'}{\phi_0''}\right). \qquad \textbf{(5-21)}$$

We will show that $\Phi_{sc}(\vec{r}_s,\vec{r}_d,\omega)$ can be attributed primarily to *perturbations created by the contrast agent injection*. $\phi'(\vec{r}_s,\vec{r}_d,\omega)$ and $\phi''(\vec{r}_s,\vec{r}_d,\omega)$ are the actual measurements on the pre- and post- ICG breast respectively, and $\phi_0'(\vec{r}_s,\vec{r}_d,\omega)$, $\phi_0''(\vec{r}_s,\vec{r}_d,\omega)$ can be determined from the average optical properties of the pre-and post- ICG breast (see Chapter 4 and Chapter 9).

During the administration of an absorption contrast agent the scattering properties of tissue are not expected to change. Therefore we assume $D_0' = D_0'' = D_0$ and $\delta D'(\vec{r}) = \delta D''(\vec{r})$. Substitution of Eq.(5-18) and Eq.(5-20) into Eq.(5-21) yields:

$$\Phi_{sc}(\vec{r}_s, \vec{r}_d, \omega) = \int_V [W_a''(\vec{r}_s, \vec{r}_d, \vec{r}, \mu_{a0}'', D_0'', \omega)\delta\mu_a''(\vec{r}) - W_a'(\vec{r}_s, \vec{r}_d, \vec{r}, \mu_{a0}', D_0', \omega)\delta\mu_a'(\vec{r})]d\vec{r} \ . \qquad \textbf{(5-22)}$$

Here we have also assumed $W_s''(\vec{r}_s, \vec{r}_d, \vec{r}, \mu_{a0}'', D_0, \omega) \approx W_s'(\vec{r}_s, \vec{r}_d, \vec{r}, \mu_{a0}', D_0, \omega)$. This is a very good approximation when the *average absorption change* due to the contrast agent is small or in the transmission geometry [93] .

Let $\delta\mu_a^{ICG}(\vec{r})$ be the total absorption perturbation due to the ICG injection that includes both position-independent and position-dependent contributions. Then $\mu_a''(\vec{r})$ can be written

$$\mu_a''(\vec{r}) = \mu_{a0}'' + \delta\mu_a''(\vec{r}) = \mu_{a0}' + \delta\mu_a'(\vec{r}) + \delta\mu_a^{ICG}(\vec{r}) , \qquad \textbf{(5-23)}$$

so that

$$\delta\mu_a''(\vec{r}) = \mu_{a0}' - \mu_{a0}'' + \delta\mu_a^{ICG}(\vec{r}) + \delta\mu_a'(\vec{r}) . \qquad \textbf{(5-24)}$$

The quantity $\delta\mu_a^{rel}(\vec{r}) = \mu_{a0}' - \mu_{a0}'' + \delta\mu_a^{ICG}(\vec{r})$ represents the position-dependent absorption heterogeneities induced by the contrast agent. The relative scattered field is computed by substitution of Eq.(5-24) into Eq.(5-22). It depends on contrast agent induced absorption heterogeneities and on pre-ICG tissue absorption heterogeneities.

$$\Phi_{sc}(\vec{r}_s, \vec{r}_d, \omega) = \int_V W_a''\delta\mu_a^{rel}(\vec{r})d\vec{r} + \int_V (W_a'' - W_a')\delta\mu_a'(\vec{r})d\vec{r} \ . \qquad \textbf{(5-25)}$$

The second integral in Eq.(5-25),

$$S = \int_V (W_a'' - W_a')\delta\mu_a'(\vec{r})d\vec{r}\,, \qquad \textbf{(5-26)}$$

describes the influence of the pre-existing (intrinsic) absorption heterogeneity of the breast on the relative scattered field. Since the intrinsic heterogeneity is weighted by the difference $W_a'' - W_a'$ the influence of this term can be quite small. Using the analytical forms for infinite absorption Rytov weights (Eq.(5-17)) for the pre- and post-ICG breast we can write out Eq.(5-26) explicitly, i.e.

$$S = \frac{c}{4\pi(D_0'')^2} \cdot \int_V W_a'' \cdot \frac{|\vec{r}_s - \vec{r}_d|}{|\vec{r}_d - \vec{r}| \cdot |\vec{r}_s - \vec{r}|} \cdot \left(1 - e^{i(k'-k'')R(\vec{r})}\right) \cdot \delta\mu_a'(\vec{r})d\vec{r}\,. \qquad \textbf{(5-27)}$$

where

$$R(\vec{r}) = |\vec{r}_d - \vec{r}| + |\vec{r}_s - \vec{r}| - |\vec{r}_s - \vec{r}_d|\,. \qquad \textbf{(5-28)}$$

The term $e^{i(k'-k'')R(\vec{r})}$ in Eq.(5-27) is approximately unity and S≈0 when the average absorption increase due to the ICG injection is very small (i.e. $k' \approx k''$). Usually however $k' \neq k''$. For example the recommended ICG dosage for humans (0.25mg/kg) introduces an average μ_a increase within the interval [0.005-0.015] cm^{-1} depending on breast vascularization. Figure 5-1a and b show the amplitude and phase of the term $e^{i(k'-k'')R(\vec{r})}$ respectively, for different $R(\vec{r})$, as a function of the post-ICG breast absorption coefficient for a source detector separation $|\vec{r}_d - \vec{r}_s|$=6cm, using the geometry of Figure 5-1c. The background μ_a=0.05 cm^{-1} and the background μ_s'=10cm^{-1}.

The deviation of $e^{i(k'-k'')R(\vec{r})}$ from unity increases for perturbations farther from the line adjoining source and detector (i.e. as $|\vec{r}_d - \vec{r}| + |\vec{r}_s - \vec{r}|$ grows larger than $|\vec{r}_d - \vec{r}_s|$ when α increases). However, the probability for photons to pass through these "distant" perturbations decreases exponentially via the weight W_a'' in the integrand of Eq.(5-27). Hence accumulated contributions of the heterogeneities at large α are small. Figure 5-2 plots the deviations introduced into $\Phi_{sc}(\vec{r}_s, \vec{r}_d, \omega)$ by taking S=0. Figure 5-2a depicts the

ratio of the amplitude detected with no approximation to the amplitude detected assuming S=0. Similarly Figure 5-2b depicts the phase shift between the phase detected with no approximation and the phase detected assuming S=0. The error is plotted for a single perturbation at different positions α for the geometry depicted in Figure 5-1c. The values assumed in Eq.(5-25) were $\delta\mu_a'(\vec{r})$ =0.05 cm^{-1}, $\delta\mu_a^{rel}(\vec{r})$ =0.05 cm^{-1} and the background optical properties μ_{a0}' =0.05cm^{-1}, μ_{a0}'' =0.05cm^{-1} and μ_s' =10cm^{-1}.

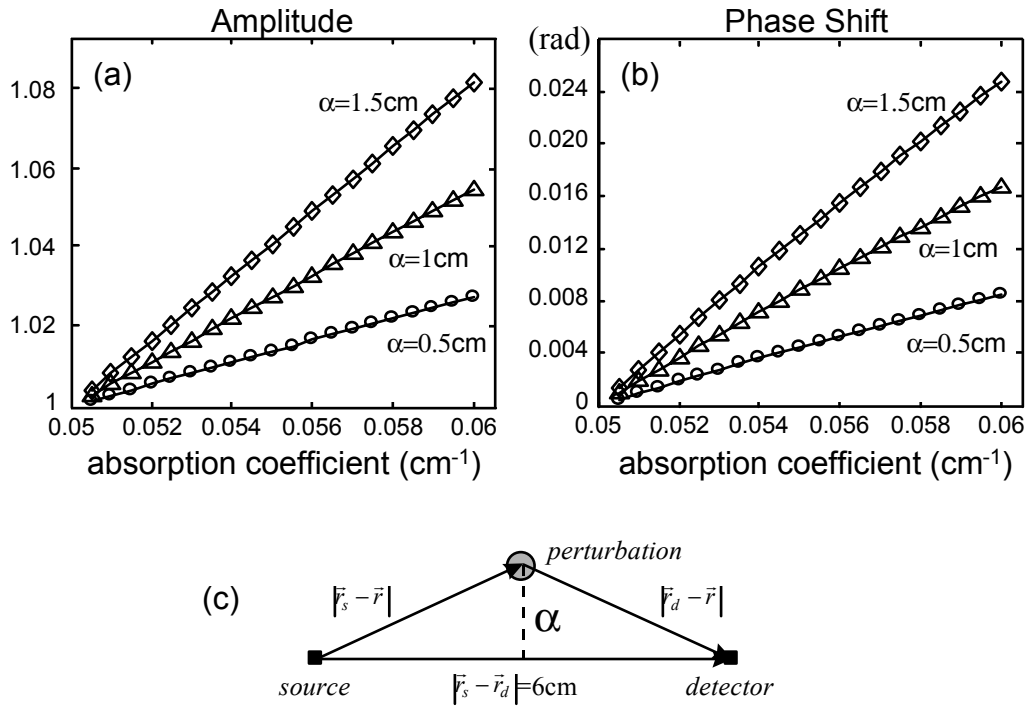

Figure 5-1: (a) Amplitude of the term $e^{i(k'-k'')R(\vec{r})}$ as a function of the average absorption coefficient of the post-ICG breast assuming pre-ICG optical properties of μ_a=0.05 cm^{-1} and μ_s'=10cm^{-1}., (b) Phase of the term $e^{i(k'-k'')R(\vec{r})}$ as a function of the average absorption coefficient of the post-ICG breast, (c) Test geometry for calculations in (a) and (b).

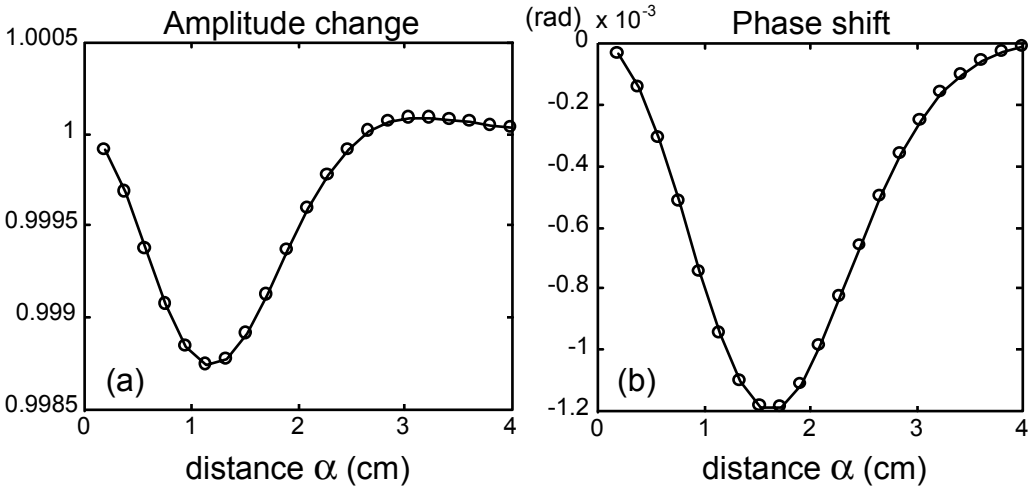

Figure 5-2: (a) Amplitude deviation and (b) Phase shift introduced in the field measured in Eq. (5-25) when S is assumed zero. The calculation is done as a function of the distance α, for the geometry shown in Figure 5-1, assuming 200MHz, background μ'_{a0}=0.05cm^{-1}, μ''_{a0}=0.05cm^{-1}, μ'_s=10 cm^{-1}, $\delta\mu_a^{rel}$=0.05 cm^{-1} and $\delta\mu'_a(\vec{r})$=0.01 cm^{-1}.

The simulation of Figure 5-2 explicitly shows that the errors introduced because of the approximation S=0 are very small for physiologically relevant optical properties (i.e. relatively small $\delta\mu'_a(\vec{r})$) provide the most probable photon paths. The same behavior is exhibited for the scattering weights as shown at the end of this section. Eq.(5-25) thus becomes

$$\Phi_{sc}(\vec{r}_s,\vec{r}_d,\omega)=\ln\left(\frac{\phi''}{\phi'}\cdot\frac{\phi'_0}{\phi''_0}\right)\cong\int_V W''_a\,\delta\mu_a^{rel}(\vec{r})d\vec{r}\ . \qquad \textbf{(5-29)}$$

Our conclusions do not change when image sources are invoked to satisfy more complex boundary conditions such as semi-infinite or slab geometries. In these cases

$e^{i(k'-k'')R(\vec{r})}$ will appear in all the terms corresponding to image sources. Note however that the assumption that S≈0 is best suited for slab geometry where $|\vec{r}_d - \vec{r}| + |\vec{r}_s - \vec{r}| \approx |\vec{r}_d - \vec{r}_s|$ for the most probable photon paths. This condition is not always true for reflectance geometry.

Notice that the differential measurements are insensitive to surface artifacts such as small skin absorbers and hair under a certain source or detector. The term $\delta\mu_a'(\vec{r})$ in Eq.(5-27) could be used to approximate surface heterogeneities by taking $\vec{r}$ to be close to medium surface, near to the corresponding source or detector. The influence of such terms is virtually zero since in such a geometry $R(\vec{r}) \cong 0$ and subsequently S=0.

For image reconstruction, Eq.(5-29) is discretized into a sum of voxels as seen in §5.2. Inverting the weights' matrix determines the spatial map of absorption due to contrast agent injection.

Discussion. Although Eq.(5-29) resembles the result of typical perturbation analyses, there are fundamental differences and constraints that must be considered when using it. First the parameter imaged is the synthetic perturbation term $\delta\mu_a^{rel}(\vec{r}) = \mu_{a0}' - \mu_{a0}'' + \delta\mu_a^{ICG}(\vec{r})$. Secondly, the relative scattered field ϕ_{sc} depends both on the ratio, U''/U', of the actual pre-ICG and post-ICG measurements, and the multiplicative term $U_0'/U_0'' = \exp(i(k'-k'')\cdot|\vec{r}_s - \vec{r}_d|)$. This term expresses the change in the incident field due to the average absorption coefficient increase of the post-ICG breast. Its use in Eq.(5-21) leads to significant reconstruction improvements. Note that the term U_0'/U_0'' depends on $|\vec{r}_s - \vec{r}|$ and not on $R(\vec{r})$. Therefore the arguments that led on the elimination of S from Eq.(5-25) cannot be applied to this term since $|\vec{r}_s - \vec{r}| >> R(\vec{r})$. The term U_0'/U_0'' can be analytically calculated for simple geometries such as infinite, semi-infinite or slab or calculated numerically for more complicated geometries if we know the average optical properties of the pre- and post- ICG breast.

5.5 Non-linear Diffuse Optical Tomography

The perturbative Diffuse Optical Tomography assumes a linear relationship between the scattered field detected and small perturbations of optical properties in a diffuse medium. Obviously for higher changes in optical properties the quantitative performance of the technique may deteriorate. Under these circumstances non-linear approaches may yield superior quantification accuracy.

The linear perturbation method can be upgraded to a non-linear approach. This can be accomplished by updating the weight functions, in an iterative fashion that employs the results of the previous iteration step to calculate more accurate, updated weight functions. To explain the process in the Born regime Eq.(5-1) can be written as an iteration step, i.e.

$$\phi_{sc}(\vec{r}_d,\vec{r}_s,\omega)=-\sum_{n=1}^{N}\left(W_n^a(s)\delta\mu_a(s,\vec{r}_n)+W_n^s(s)\delta D(s,\vec{r}_n)\right), \qquad \textbf{(5-30)}$$

where s∈[1..S], where s is the number of iteration step, $\delta\mu_a(s,\vec{r}_n)$, $\delta D(s,\vec{r}_n)$ are the optical perturbations reconstructed at the sth step and $W_n^a(s), W_n^s(s)$ are the weights calculated at the sth steps. The sth iteration absorption weight in the Born regime can be written as

$$W_n^a(s)=g(\vec{r}_n-\vec{r}_d,\omega)[\phi_0(\vec{r}_n,\vec{r}_s,\omega)+\phi_{sc}(s,\vec{r}_n,\vec{r}_s,\omega)]\frac{h_x h_y h_z}{D_0}, \qquad \textbf{(5-31)}$$

and the scattering weight as

$$W_n^s=\vec{\nabla}g(\vec{r}_n-\vec{r}_d,\omega)\cdot\vec{\nabla}[\phi_0(\vec{r}_n,\vec{r}_s,\omega)+\phi_{sc}(s,\vec{r}_n,\vec{r}_s,\omega)]\frac{h_x h_y h_z}{D_0}. \qquad \textbf{(5-32)}$$

The field $\phi_{sc}(s,\vec{r}_k,\vec{r}_s,\omega)$ at each discrete position $\vec{r}_k$ in the medium can be calculated as

$$\phi_{sc}(s,\vec{r}_k,\vec{r}_s,\omega) = -\sum_{n=1}^{N}\left(W_n^a(s-1)\delta\mu_a(s,\vec{r}_n) + W_n^s(s-1)\delta D(s,\vec{r}_n)\right). \quad \textbf{(5-33)}$$

Eq.(5-33) is not defined when $\vec{r}_k = \vec{r}_n$. In these positions one can retain the first order field or more accurately use a system of virtual sources [55, 94]. The s[th] iteration step is referred to as the s[th]-order Born solution. The scattered field $\phi_{sc}(\vec{r}_d,\vec{r}_s,\omega)$ in Eq.(5-30) is the measured scattered field and it does not change with the iteration steps. The scattered field $\phi_{sc}(s,\vec{r}_k,\vec{r}_s,\omega)$ however, in Eq.(5-33) is a theoretical prediction and it is updated in each iteration step to yield a better $\delta\mu_a(s+1,\vec{r}_n)$ and $\delta D(s+1,\vec{r}_n)$ solution.

The Rytov solution can be similarly treated but the result becomes too complicated for practical implementations. The non-linear Rytov solution can be practically implemented as a normalized Born solution (§3.6) Then the corresponding weights can be given by dividing Eq.(5-31) and Eq.(5-32) with $\phi_0(\vec{r}_n,\vec{r}_s,\omega)$. Also it can be argued that for media that contain multiple perturbations, the Greens function solution needs to be updated in a similar manner, since each heterogeneity can be seen as a new source creating a diffuse photon density wave propagating in the heterogeneous medium. Then the analytical approach quickly becomes very complicated to implement in practice, especially in the presence of complex boundaries. In this case it becomes necessary to numerically calculate the higher order $\phi_0(\vec{r}_n,\vec{r}_s,\omega)$ and $g(\vec{r}_n-\vec{r}_d,\omega)$. Numerical solutions also allow the easy implementation of arbitrary boundary conditions. In that respect, Eq.(5-9) can be seen as a generalized non-linear iterative equation that can be applied to more complex systems than the ones normally treated by the analytic linear forward solution. The iterative process will obtain a first-step solution assuming a homogeneous medium as an initial guess, similar to solutions obtained with the analytical approach. Then a numerical solution of the diffusion equation can be used to calculate the fluence rate distribution in the medium calculated in the first step. This yields a set of higher-order $\phi_0(\vec{r}_n,\vec{r}_s,\omega)$ and $g(\vec{r}_n-\vec{r}_d,\omega)$ terms that can be used to calculate a new set of higher order weights. These weights are then substituted in Eq.(5-9), which can be inverted again to yield a new solution of optical properties. The process can be repeated until convergence is reached.

5.6 Using a-priori information

An important contribution of the tomographic optical method is its ability to quantify the concentrations of physiologically important pigments such as oxygenated and deoxygenated hemoglobin, by providing absolute spatial quantification of scattering and absorption coefficients in the NIR region. Anatomical details derived from a conventional medical image, as the case of X-ray tomography or MRI can be taken into account, in order to improve the quantitative accuracy of the optical image.

Other researchers have considered the use of a priori structural information in numerical implementations of the diffusion equation to improve the reconstruction quantification [95,96]. In this section a method based on the perturbative solution of the diffusion equation is discussed. The method uses structural or functional information taken from another modality such as MRI and reduces the number of unknowns in the inversion problem, from the number of unknown voxel perturbations, to the number of tissue types. This significantly reduces the complexity of the inversion problem and generally converts it to a highly over-determined system that can be solved in principle more accurately than a standard inversion scheme that uses no a-priori information.

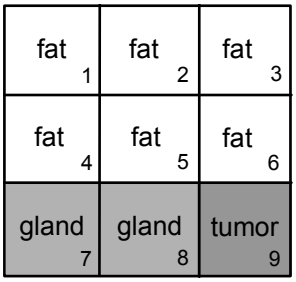

Figure 5-3: A simple breast model. This over-simplified model is used for describing the matrix reduction algorithm.

Let us consider an absorbing and scattering distribution in a region broken into n voxels. There is one unknown absorptive perturbation $\delta\mu_a$ and one unknown diffusive perturbation δD in each of the nine voxels ($\delta\mu_a^n$, δD^n are the perturbations in the nth voxel). For illustration reasons we assume n=9 as depicted in Figure 5-3. Then Eq.(5-9) can be written as an m×18 problem, i.e.,

$$\begin{bmatrix} \phi_{sc}^1(\vec{r}_{s1},\vec{r}_{d1},\omega_1)^R \\ \vdots \\ \phi_{sc}^m(\vec{r}_{so},\vec{r}_{dp},\omega_q)^R \\ \phi_{sc}^m(\vec{r}_{so},\vec{r}_{dp},\omega_q)^I \\ \vdots \\ \phi_{sc}^m(\vec{r}_{so},\vec{r}_{dp},\omega_q)^I \end{bmatrix} = \begin{bmatrix} W_{11}^{aR} & \cdots & W_{19}^{aR} & W_{11}^{sR} & \cdots & W_{19}^{sR} \\ \vdots & \ddots & \vdots & \vdots & \ddots & \vdots \\ W_{m1}^{aR} & \cdots & W_{m9}^{aR} & W_{m1}^{sR} & \cdots & W_{m9}^{sR} \\ W_{11}^{aI} & \cdots & W_{19}^{aI} & W_{11}^{sI} & \cdots & W_{19}^{sI} \\ \vdots & \ddots & \vdots & \vdots & \ddots & \vdots \\ W_{m1}^{aI} & \cdots & W_{m9}^{aI} & W_{m1}^{sI} & \cdots & W_{m9}^{sI} \end{bmatrix} \cdot \begin{bmatrix} \delta\mu_a^1(\vec{r}_1) \\ \vdots \\ \delta\mu_a^9(\vec{r}_9) \\ \delta D^1(\vec{r}_1) \\ \vdots \\ \delta D^9(\vec{r}_9) \end{bmatrix}. \qquad \textbf{(5-34)}$$

If the structural or functional distribution of the medium is known and we assume that each of the different structures or functional areas identified has uniform optical properties, then the problem dramatically simplifies. We need only to solve for the absorption and diffusion perturbations of each different type of inhomogeneity. For example, if the sample is composed of fat (background), glandular tissue (parenchyma) and tumor, then we only have two actual unknowns, (since the perturbation of the background fat is considered zero). We may then rewrite Eq.(5-34) as an m×4, i.e.,

$$\begin{bmatrix} \phi_{sc}^1(\vec{r}_{s1},\vec{r}_{d1},\omega_1)^R \\ \vdots \\ \phi_{sc}^m(\vec{r}_{so},\vec{r}_{dp},\omega_q)^R \\ \phi_{sc}^m(\vec{r}_{so},\vec{r}_{dp},\omega_q)^I \\ \vdots \\ \phi_{sc}^m(\vec{r}_{so},\vec{r}_{dp},\omega_q)^I \end{bmatrix} = \begin{bmatrix} W_{17}^{aR}+W_{18}^{aR} & W_{19}^{aR} & W_{17}^{sR}+W_{18}^{sR} & W_{19}^{sR} \\ \vdots & \vdots & \vdots & \vdots \\ W_{m7}^{aR}+W_{m8}^{aR} & W_{m9}^{aR} & W_{m7}^{sR}+W_{m8}^{sR} & W_{m9}^{sR} \\ W_{17}^{aI}+W_{18}^{aI} & W_{19}^{aI} & W_{17}^{sI}+W_{18}^{sI} & W_{19}^{sI} \\ \vdots & \vdots & \vdots & \vdots \\ W_{m7}^{aI}+W_{m8}^{aI} & W_{m9}^{aI} & W_{m7}^{sI}+W_{m8}^{sI} & W_{m9}^{sI} \end{bmatrix} \cdot \begin{bmatrix} \delta\mu_a^{gland} \\ \delta\mu_a^{tumor} \\ \delta D^{gland} \\ \delta D^{tumor} \end{bmatrix}. \qquad \textbf{(5-35)}$$

In this way we have reduced the number of linear equations to be solved from eighteen to four. This algorithm is easily extended for multiple voxels and tissue types. It is interesting to note that the sum of the weights in the above matrix represent our sensitivity

to each tissue type [55]. These totals can be used to design the experimental setup to maximize sensitivity to the tissue type of interest.

The simplification of Eq.(5-35) leads to an over-determined system since typically no more than 5 different tissue types are identified. Eq.(5-35) can be inverted using Eq.(5-12) but can also fitted to the measurements in a least squares sense. This leads to accurate determination of local optical properties, for the limited number of unknown tissue types *in vivo*. In §6.4 the implementation and evaluation of this method will be discussed. Additionally §8.2 describes tools developed to apply this technique for the analysis of the clinical data. The algorithm has been used with the clinical measurements to quantify intrinsic and extrinsic optical properties of selected breast lesions (see §9.4).

6 Performance of diffuse optical tomography.

The capability of diffuse optical tomography to resolve absorbing, fluorescing and scattering objects embedded in otherwise homogeneous media has been studied in the past with simulated and experimental data [97,98,99]. Although the technique has low spatial resolution, it offers high localization ability and quantification accuracy in the range of 10%-50% depending on the geometry, signal-to-noise ratio and inversion technique employed.

As DOT moves towards clinical applications however, it becomes important to evaluate its ability to image highly heterogeneous media. In this chapter I investigate the performance of the methods presented in the previous chapter using simulations on breast-like heterogeneity. Breast-like optical heterogeneity was modeled after the heterogeneous vascularity pattern that appears in Gadolinium enhanced MRI images. This work actually followed our initial experience with clinical data and was used to understand better the results and the original conclusions and to improve the reconstructions.

Section 6.1 describes the performance of the linear Diffuse Optical Tomography with heterogeneous diffuse media, as a function of the background heterogeneity. Reconstruction optimization schemes are also described. **Section 6.2** studies the performance of the tomographic method to image contrast-enhanced media and demonstrate certain improvements achieved when using Eq.(5-29). **Section 6.3** examines the combination of images at multiple wavelengths for producing images of hemoglobin concentration and hemoglobin saturation. Finally **section 6.4** evaluates the performance of the algorithm that uses a-priori information to simplify the inversion problem. This investigation employed experimental data from a breast-like phantom and the simulated data produced for the imaging purposes of Section 6.1.

6.1 DOT of highly heterogeneous media.

The study of simulated heterogeneous media has been performed in the past [96,100]. The simulations in these studies were based on segmentation of T_1-weighted Magnetic Resonance (MR) images of the brain and breast assuming that the variation of tissue optical properties coincides with tissue anatomy. Pogue et. al [96] have shown that heterogeneity distribution cannot be accurately reconstructed without using a-priori information. The study by Chang et. al [100]. showed that in the absence of a-priori knowledge on the background heterogeneity, diffuse optical tomography is unable to resolve objects that were simulating pathologies.

This section presents results from the study of breast-like media, segmented based on functional MR information, which more closely resembles the vasculature pattern. It is demonstrated that this heterogeneity is reconstructed as a specific artifact pattern that can be misinterpreted for actual structures. It is also shown that the use of an algorithm developed to reconstruct the contrast-enhanced breast (§5.4) can significantly improve the reconstruction of localized heterogeneities without using a-priori information.

The study was divided in two parts: The first studied the performance of DOT to reconstruct a breast like medium, containing a single 8mm lesion (the *tumor*) as a function of I) background heterogeneity, II) number of detectors employed. The second studied the performance of Eq.(5-29) to image the same media. Here, the capacity of Eq.(5-29) to image highly heterogeneous media in general is considered.

Absorption and scattering contrast for the tumor and the background heterogeneity are imaged either independently or concurrently. A finite-difference solution of the heterogeneous diffusion equation in the time-domain was employed to produce the forward measurements [101]. The assumed geometrical set-up is modeled after our clinical experiment (described in Chapter 7) and is described analytically in the methods section.

Our results indicate that background heterogeneity appears as *biological noise* leading to strong image artifacts. These artifacts are especially evident in the vicinity of the sources and detectors. The reconstruction of the tumor-structure also deteriorates as a function of background heterogeneity and the heterogeneous background cannot be imaged. An increase in the number of detectors used improves the reconstruction of the tumor structure but it does not remove the artifacts. On the other hand the correction algorithm employed, not only improves the tumor-structure reconstruction, but also eliminates the appearance of artifacts. The algorithm is found to be independent of the degree of background heterogeneity and is a good remedy when a-priori information is not available to the reconstruction.

6.1.1 Research design and methods

Inhomogeneity maps. The maps of optical heterogeneity employed have been modeled after Gadolinium (Gd) enhanced Magnetic Resonance images. The Gd-enhanced MR images depict the distribution of vasculature in breast tissue[102]. Since vascularization (hemoglobin concentration) is the main intrinsic contrast in breast imaging with light, it may be that breast heterogeneity, especially the absorption contrast, is better modeled using the function-revealing Gd-enhanced images than using the anatomy-revealing T_1-weighted images.

Although a weighted combination of the two could be an even better model for breast optical heterogeneity, the Gd based segmentation directly reflects the breast optical heterogeneity expected when NIR contrast agents are injected in the blood stream and for that was selected alone for this study.

The inhomogeneity maps employed have been constructed as random distributions using the Gd-enhancement pattern of coronal MRI images as a guiding model. Figure 6-1a depicts a coronal MR T_1-weighted anatomical image and Figure 6-1b depicts the same image superimposed with the signal enhancement due to Gd administration (in color). The Gd enhancement shown has been calculated by integrating the enhancement seen at all the coronal slices at ±0.5cm above and below the reference T_1-slice. Besides a major lesion enhancing at the upper left part of the image (in this case a fibroadenoma) there are patchy enhancements throughout the rest of the image, primarily within the parenchymal tissue regions. The pattern of this enhancement has virtually a random distribution.

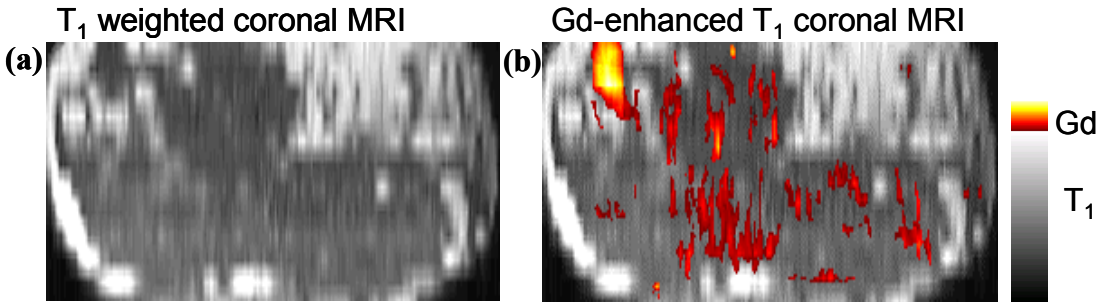

Figure 6-1 An MRI anatomical coronal slice (a) and the same coronal slice with superimposed enhancement due to Gd administration.

In order to model this distribution we have assumed a random 40x15 matrix with uniformly distributed entries in the range (0 1] as shown in Figure 6-2a. Figure 6-2b shows the histogram of Figure 6-2a. By applying a threshold, the degree of image heterogeneity is adjusted. Heterogeneity is characterized by the *volume fraction* (VF), i.e.,

$$VF = \frac{number\ \ of\ \ heterogeneous\ \ pixels}{total\ \ number\ \ of\ \ pixels}. \qquad (6\text{-}1)$$

For any selected VF the corresponding image was converted to binary and a 4-pixel rectangular structure, the *tumor* structure, was added as shown in Figure 6-2d. Therefore each image has three structures: (i) the *background*, (ii) the *heterogeneity* and (iii) the *tumor* structure.

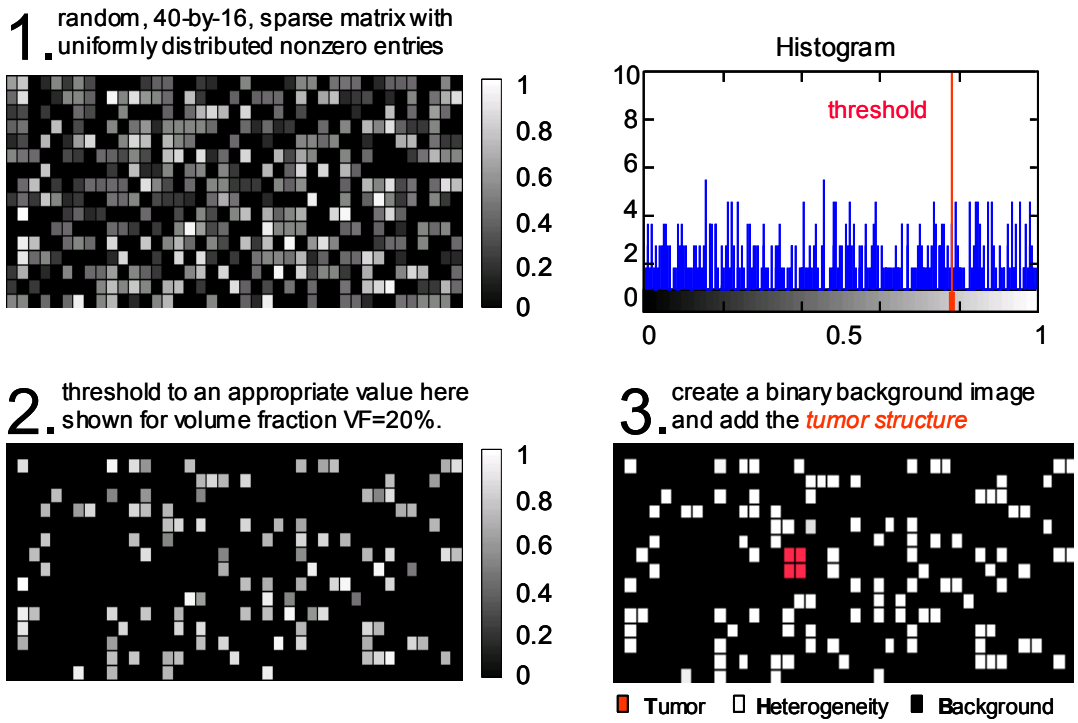

Figure 6-2: Creation of random maps for optical heterogeneity simulation.

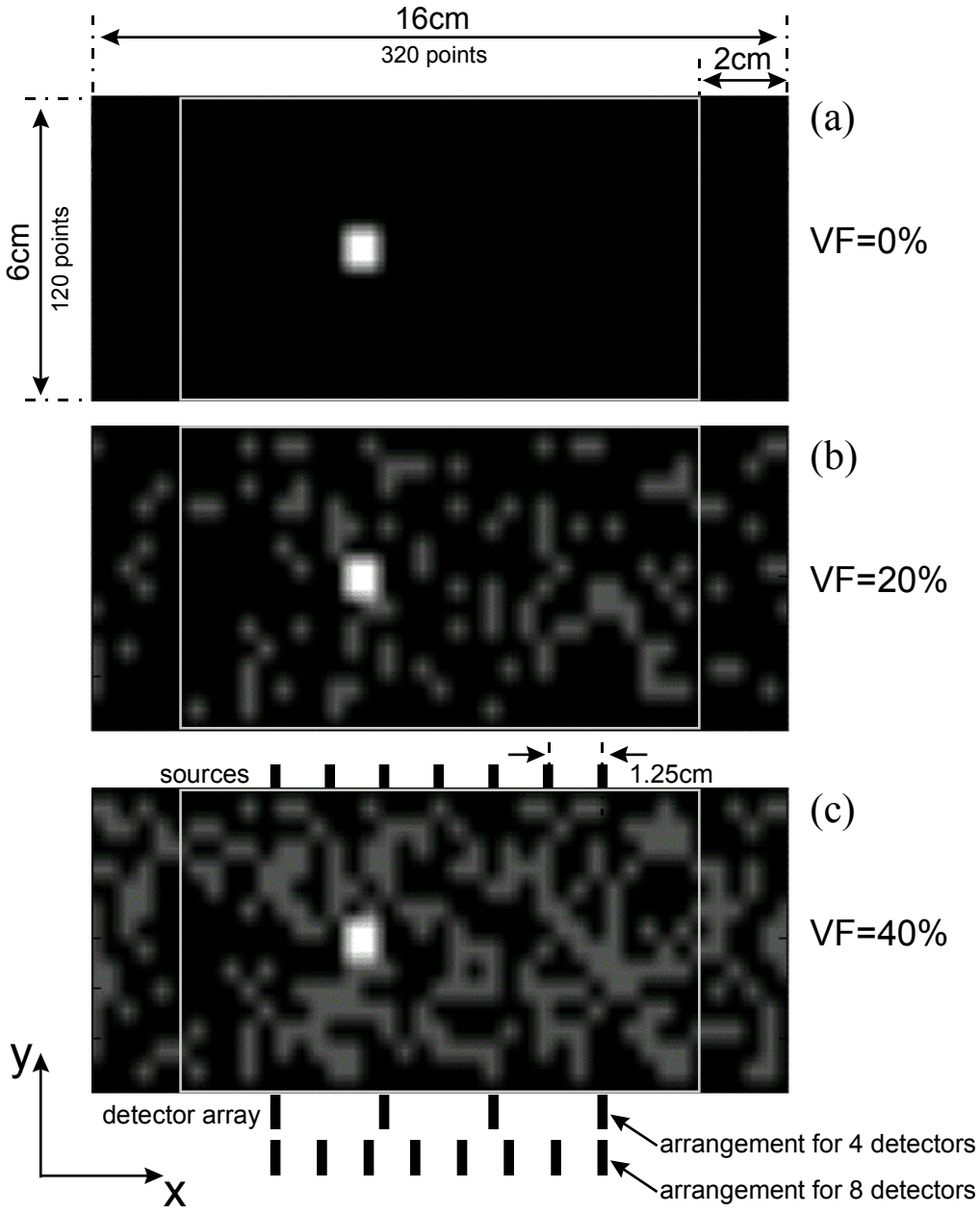

Figure 6-3: Final interpolation of optical maps and geometrical set-up.

Optical property maps For creating an optical map each of the three structures is assigned an absorption coefficient (μ_a) and a reduced scattering coefficient (μ_s'). The optical properties assigned were based on average breast optical properties (see §9.1). Each of the resulting 40x15 μ_a and μ_s' optical maps were interpolated on a 320x120 mesh. The final interpolated meshes are shown in Figure 6-3 for VF=0%, 20% and 40%. The meshes shown do not have units since they were used to create both absorbing and scattering maps. The exact μ_a and μ_s' assigned are described for each separate study in the results section.

Geometrical set-up Figure 6-3c depicts the transmittance geometry assumed for this study shown for the optical map produced for VF=40%. This geometry mimics the clinical set-up described in chapter 7. For this study we have employed 7 sources and a variable array of detectors (ranging from 4 to 32) in transmission geometry. The span of the detector array is also depicted in Figure 6-3. The exact number of detectors employed is explicitly described on a per case basis in the results section. The region of interest (ROI), namely the area that is reconstructed in the results section is indicated with a light-solid rectangle.

Numerical solution of the forward problem. Each set of μ_a – and μ_s' – maps produced (like the one shown in Figure 5.3 for VF=20%), served as an input to a finite-difference implementation of the time-domain diffusion equation. The finite differences problem was solved using an "*alternating directions implicit*" (ADI) method [103]. The spatial mesh step, was 0.05 x 0.05 cm^2 and the time resolution of the numerical simulation was 50 ps.

Perturbative Diffuse Optical Tomography. The tomographic scheme employed in this study is presented in § 5.1. Time resolved data are converted to the frequency domain via the Fourier Transform, yielding multiple modulation frequencies. The Rytov approximation was used to create a matrix similar to Eq.(5-9). Inverting the weights' matrix determines the spatial map of differences in absorption and diffusion coefficient. For matrix inversion the method of projections (MOP) was selected with relaxation parameter λ=0.1 and was applied only on the real part of the weight matrix for simplicity. The problem was simultaneously inverted at 80,160,240,320,400 MHz. The exact selection of frequencies is explicitly given for each

reconstruction in the results section. The voxel size for all reconstructions was 3 x 3 x 6 mm^3. The specific dimensions were selected so that an accurate quantitative reconstruction of the tumor structure was obtained for the absorption map with VF=0% and kept constant for all reconstructions. Convergence was assumed when an additional 100 iterations did not change the result more than 0.1% .

Correction algorithm. The correction algorithm employed was originally developed for differential measurements of the breast and has been analytically described [93] and in §5.4. The algorithm uses the *relative scattered field* $\phi_{sc}^{rel}(\vec{r}_s,\vec{r}_d,\omega)$ (see Eq.(5-21)), i.e.

$$\Phi_{sc}^{rel}(\vec{r}_s,\vec{r}_d,\omega)=\Phi_{sc}(\vec{r}_s,\vec{r}_d,\omega)+\ln\frac{\phi_0^c(\vec{r}_s,\vec{r}_d,\omega,\mu_a^{het},\mu_s'^{het})}{\phi_0^c(\vec{r}_s,\vec{r}_d,\omega,\mu_a^{base},\mu_s'^{base})}, \qquad (6\text{-}2)$$

where $\mu_a^{het},\mu_s'^{het}$ are the average optical properties of the heterogeneous medium, $\mu_a^{base},\mu_s'^{base}$ are the optical properties for VF=0% and ϕ_0^c is the incident field for transmittance geometry calculated theoretically in the frequency domain using the method of image sources. Practically the field $\Phi_{sc}(\vec{r}_s,\vec{r}_d,\omega)$ is the experimental measurement (in the Rytov approximation that would be the natural logarithm of the total field over the incident field) and the fields $\phi_0^c(\vec{r}_s,\vec{r}_d,\omega,\mu_a^{het},\mu_s'^{het})$, $\phi_0^c(\vec{r}_s,\vec{r}_d,\omega,\mu_a^{base},\mu_s'^{base})$ are theoretically calculated using the solutions developed in §3.4 for homogeneous media and the appropriate boundary conditions. Use of the $\Phi_{sc}(\vec{r}_s,\vec{r}_d,\omega)$ (the field without correction) reconstructs perturbations from the baseline optical properties ("baseline" being any measurement performed on another diffuse medium in order to calibrate the instrument or provide the incident field – see also discussion). On the other hand use of $\Phi_{sc}^{rel}(\vec{r}_s,\vec{r}_d,\omega)$ reconstructs the medium relative to its average optical properties, but retains the experimental simplifications of dividing the total field by the incident field described in §5.3. Eq. (6-2) offers certain advantages when imaging heterogeneous media as shown in the results section and explained in the discussion section. When the $\Phi_{sc}^{rel}(\vec{r}_s,\vec{r}_d,\omega)$ is used in Eq.(5-9), the weights W^a (W^s) are also calculated for the medium's average optical properties $\mu_a^{het},\mu_s'^{het}$.

6.1.2 Reconstruction results

The result section consists of three parts. The first part presents the reconstruction of simulated media with varying degree of background heterogeneity where a) only the absorption coefficient was spatially varying, b) only the reduced scattering coefficient was spatially varying and c) both absorption and reduced scattering coefficients were spatially varying. The second part shows the reconstruction performance as a function of detectors employed. In this second part we have focused only on imaging of absorption perturbations for simplicity. The third part presents imaging improvements when the correction algorithm (Eq.(6-2)) is applied to the measurement vector. No noise has been added to the measurement vector (besides the numerical simulation approximations) so that the performance of DOT in imaging heterogeneous media is decomposed from its sensitivity to random noise.

I. DOT as a function of background heterogeneity

a)Reconstruction of absorption. Figure 6-4 shows the reconstructed results when only the absorption coefficient was spatially varying, for VF=0%, 20% and 40%. The corresponding regions of interest (ROI), taken from the simulated absorption optical maps, are also shown to facilitate comparison between simulated and reconstructed results. The optical properties used for the simulation are tabulated in Table 6-1.

Table 6-1: Optical properties of absorption heterogeneity maps.

	Tumor	Heterogeneity	Background
μ_a (cm^{-1})	0.16	0.08	0.04
μ_s' (cm^{-1})	10	10	10

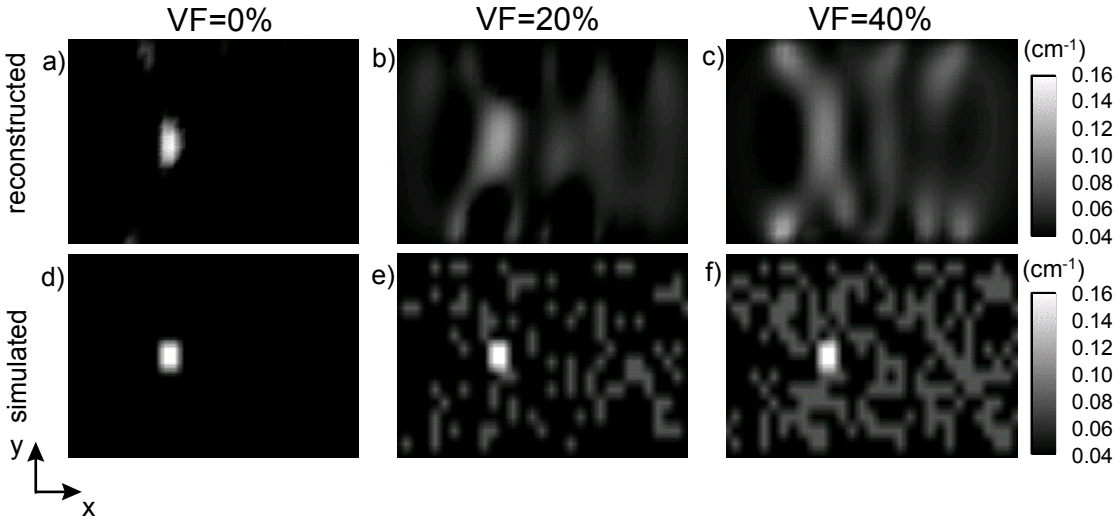

Figure 6-4: Reconstruction of absorption heterogeneity

The reconstructions shown employ 4 detectors spaced 2.5cm apart and 5 modulation frequencies (40, 80, 120, 160 and 200MHz). These results have been produced without using correction. Since scattering was homogeneous the diffusion coefficient perturbations $\delta D(\vec{r}_i), i \in [1..n]$ in Eq.(5-9) were assumed zero. This simplified the inversion problem by reducing the number of unknowns to half.

Figure 6-4a shows that when no background heterogeneity is present (VF=0%), the tumor structure is well resolved. The position is accurately resolved (within ~2mm which is the resolution allowed by the reconstruction mesh selected). The size is slightly overestimated, especially along y as is typical in such transmittance, underdetermined inversions. The voxel size selected allowed an accurate reconstruction of the magnitude as discussed in the "research design and methods" section. There is some minor random noise that appears close to the borders, which can be attributed to numerical and modeling noise.

For higher volume fraction VF the tumor structure is resolved with good positional accuracy but its size is significantly overestimated and the magnitude reconstructed is

underestimated. The reconstruction errors associated with the tumor structure amplify as the background heterogeneity increases.

A distributed background heterogeneity is also reconstructed for volume fractions higher than 0%. The reconstructed heterogeneity however appears to have a distribution that does not clearly correlate to the simulated background heterogeneity distribution. Moreover distinct "objects" appear close to the source and detector boundaries. These "objects" or "artifacts" are especially visible as the background heterogeneity increases (Figure 6-4c). The magnitude of the artifacts takes a value that is comparable or higher than the reconstructed tumor structure as is especially evident for VF=40%. The position of the artifacts correlates well with the position of a source or a detector.

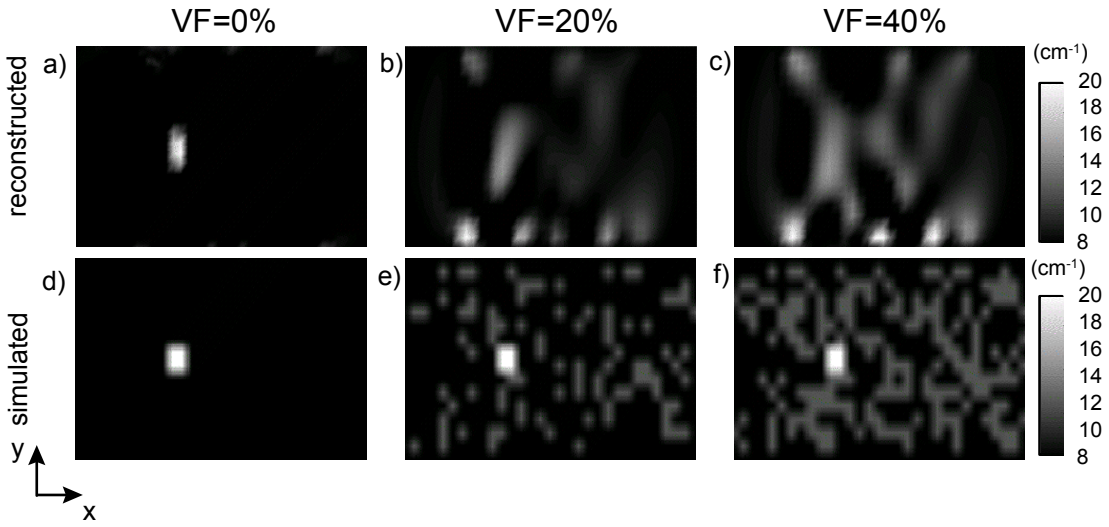

Figure 6-5: Reconstruction of scattering heterogeneity.

b)Reconstruction of scattering.

Figure 6-5 shows the reconstructed results when only the reduced scattering coefficient was spatially varying, for VF=0%, 20% and 40%. The corresponding regions of interest (ROI), taken from the simulated scattering optical maps, are also shown. The optical properties used for this simulation are tabulated in Table 6-2.

Table 6-2: Optical properties of scattering heterogeneity maps.

	Tumor	Heterogeneity	Background
μ_a (cm^{-1})	0.06	0.06	0.06
μ_s' (cm^{-1})	20	12	8

The reconstructions shown employ 4 detectors spaced 2.5cm apart and 5 modulation frequencies (40, 80, 120, 160 and 200MHz). These results have been produced without using correction. Since the absorption coefficient was constant, the absorption coefficient perturbations $\delta\mu_a(\vec{r}_i), i \in [1..n]$ in Eq.(5-9) were assumed zero. This again simplified the inversion problem by reducing the number of unknowns to half.

Figure 6-5a shows that when no background heterogeneity is present (VF=0%), the scattering tumor structure is well resolved. Similarly to the absorption reconstructions of Figure 6-4 the position of the tumor structure is accurately resolved (within ~2mm which is the resolution allowed by the reconstruction mesh selected). The size is slightly overestimated along the z axis and is slightly underestimated along the x axis.

As the background heterogeneity increases the tumor structure is overestimated in size and underestimated in magnitude. The background structures reconstructed appear "sharper" than the ones that appear on the absorption reconstructions (Figure 6-4) however there is little correlation between reconstructed and simulated background heterogeneity. The appearance of artifacts is stronger here. At VF=20% these "boundary" artifacts have already a magnitude higher than the tumor structure. For VF=40% more and stronger artifacts appear.

b) Simultaneous reconstruction of absorption and scattering. Figure 6-6 shows results from the reconstruction of simulated media for VF=0%, 20% and 40% where both the absorption

and the scattering were spatially varying. The absorption and scattering variations had the pattern shown in Figure 6-3. The exact optical properties used in the simulation are tabulated in Table 6-3. The reconstructions shown employ again 4 detectors spaced 2.5cm. However, since the number of unknowns was doubled from the previous cases, we employed 10 modulation frequencies (40MHz to 400MHz in steps of 40MHz). The reconstruction results shown were again produced by inverting Eq.(5-9) without correction.

Table 6-3: Optical properties of absorption & scattering heterogeneity maps.

	Tumor	Heterogeneity	Background
μ_a (cm^{-1})	0.16	0.08	0.04
μ_s' (cm^{-1})	20	12	8

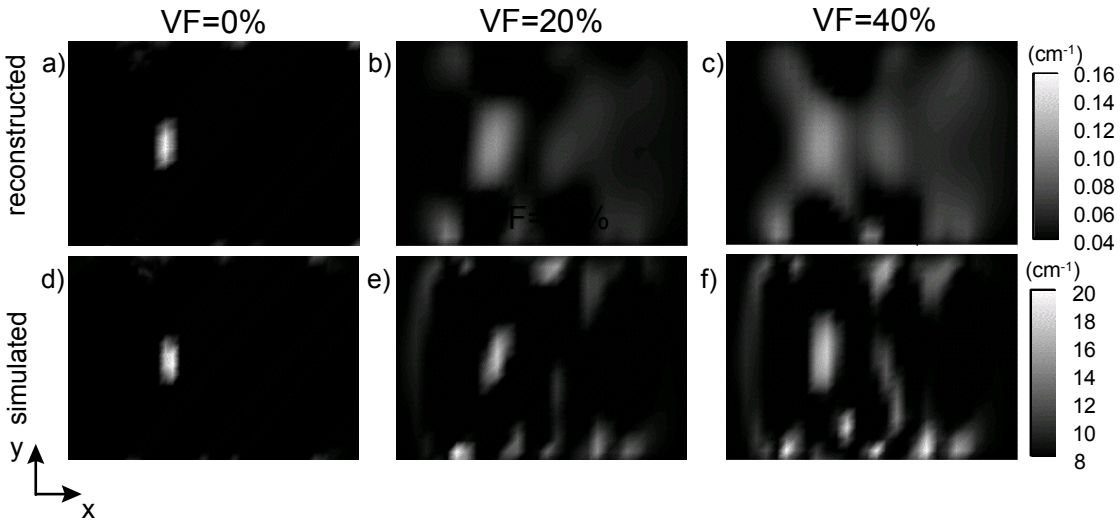

Figure 6-6 Reconstruction of absorption and scattering heterogeneity.

The simultaneously reconstructed μ_a and μ_s' images of Figure 6-6 are similar to the ones reconstructed independently in Figure 6-4 and Figure 6-5 respectively. The tumor structure is overestimated in size and underestimated in magnitude as the VF increases. Artifacts also appear close to the boundaries as the VF increases. The artifacts appear stronger on scattering image.

II. DOT as a function of detectors employed

As seen in Figure 6-4, Figure 6-5 and Figure 6-6 the imaging fidelity deteriorates as the VF increases. This can be attributed to the fact that an ill-posed system of linear equations is inverted. In this section we have increased the number of detectors employed, to investigate the effect of increased data-set to imaging quality. Specifically we investigate the reconstruction of absorption variations for VF=20% using 8, 16 and 32 detectors.

The results are shown in Figure 6-7. Figure 6-7a, b and c depict the reconstruction results with 8, 16 and 32 detectors respectively. Figure 6-7d shows the region of interest from the absorption optical map that was simulated. The optical properties are the ones shown in Table 6-1. Figure 6-7e is the result of 50 iterative convolutions of the simulated absorption map of Figure 6-7d with the 3x3 Gaussian kernel shown in Figure 6-7f. This low-resolution image has been provided for comparison reasons.

The increase of the number of detectors results in improvements in the reconstruction of the tumor structure. The magnitude of the tumor is more accurately reconstructed as the detectors used increase. The size is also more accurately resolved, especially along the x-axis but it does not reach the accuracy shown in Figure 6-4a when no background heterogeneity was present. The background structures appear more sharply resolved but they bear little correlation to the real background heterogeneity distribution (compare with Figure 6-7e). Artifacts appear again close to the boundary.

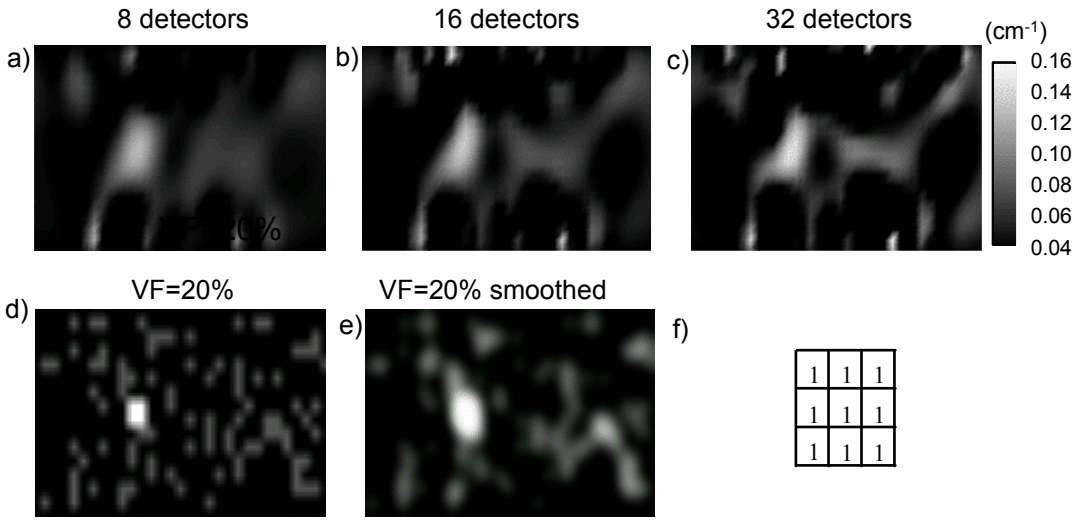

Figure 6-7 The effect of increasing the number of detectors in reconstructing highly absorptive heterogeneity (VF=20%).

III. DOT using the correction algorithm

Figure 6-8 shows a comparison between the reconstruction achieved using Eq.(5-9) without correction and the reconstruction achieved when Eq.(5-9) uses the corrected measurement vector (relative scattered field) in reconstructing the absorption maps. The weights employed when the correction is used are calculated for the average optical properties of the heterogeneous map, i.e. μ_a^{het} =0.048cm^{-1}, $\mu_s'^{het}$ =8 cm^{-1}. The optical properties used for the simulation are tabulated in Table 6-3. The reconstructions shown employ 4 detectors spaced 2.5cm apart and 5 modulation frequencies (40, 80, 120, 160 and 200MHz).

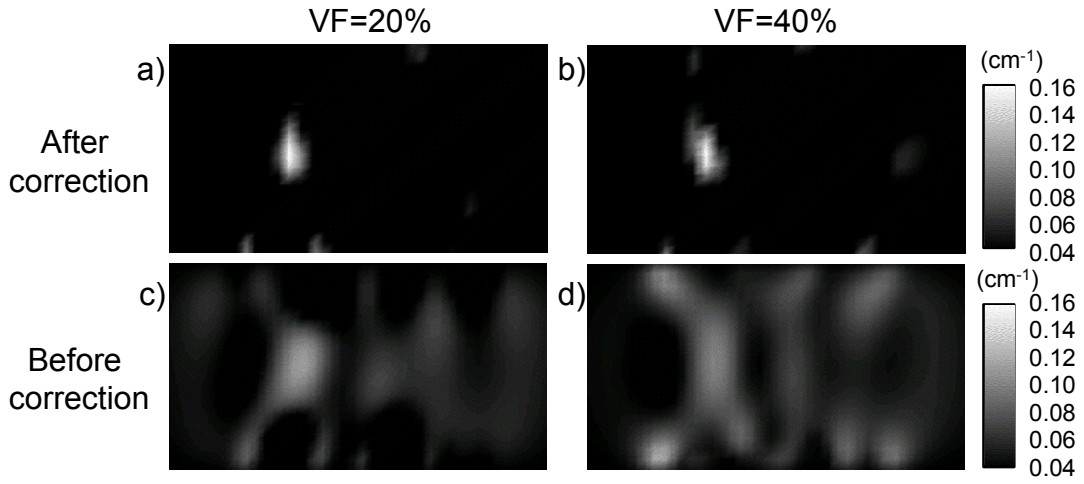

Figure 6-8: Absorption heterogeneity reconstruction before and after the correction of Eq.(6-2) for VF=20% and VF=40%.

The correction significantly suppresses the artifacts that appear close to the boundaries. Furthermore the tumor structure is reconstructed accurately in both size and magnitude. The effect of the correction is that by construction no background structure is reconstructed. This is further explained in the discussion section. The algorithm performs well independently of background heterogeneity since the reconstruction results are similar for both VF=20% and VF=40%.

6.1.3 Discussion

Diffuse Optical Tomography is found adequate to accurately retrieve the location of single objects embedded in *highly heterogeneous* diffuse media when sufficient contrast exists between the object above an average heterogeneous background. However, the reconstruction of size and magnitude becomes less accurate as the background heterogeneity increases. Obviously the detection capacity will depend on the size and relative optical

property of the object above the average background. In this work we did not attempt to probe "detection limits" but to investigate the effect of the background heterogeneity to the reconstruction of an ill-posed, underdetermined forward problem.

In the presence of background heterogeneity the single object will create "correlated" contrast (seen in many projections). This correlated contrast is correctly inverted. This would be also expected for a small number of objects distributed in the highly heterogeneous medium. On the other hand, the optical heterogeneity behaves as "biological noise" that appears uncorrelated in the underdetermined system, due to the absence of sufficient measurements. The technique therefore detects the presence of the background heterogeneity, since there is contrast reconstructed when the background heterogeneity increases, but it cannot correctly reveal its spatial distribution. The inversion of the ill-posed underdetermined system, in the presence of the "biological noise", does not converge to an accurate low-resolution spatial map (as reflected in Figure 6-7e) but in the reconstruction of artificial structures. The most significant artifacts appear close to the boundaries; preferentially in front of a source or a detector. These artifacts often have much higher contrast than the one expected for the background heterogeneity. Apparently the inversion erroneously concentrates the perturbation obtained from a distributed low contrast inhomogeneity to localized high contrast objects.

DOT is considered a modality that is not in need of high resolution since, similar to Positron Emission Tomography (PET) and Single Photon Emission Computed Tomography (SPECT), it targets function rather than structure. Therefore it is not the tissue architectural characteristics that are in pursue but functional characteristics of localized areas. Hence, the presence of strong artifacts is a major disadvantage since there is no other information (such as structural characteristics) that could enable the differentiation of these artifacts from real localized structures. Implementation of more orthogonal measurements (as in the case of a cylindrical geometry or two 90^0-rotated transmittance geometries) have been shown to improve imaging of simple heterogeneous systems [104, 105] and may be beneficial to better resolving the background distributed heterogeneity as well.

The correction algorithm proposed offers a practical solution to this problem. Let us assume that a calibration measurement is taken from a diffuse medium with optical properties $\mu_a^{base}, \mu_s'^{base}$. This calibration measurement can be used to provide the incident field or calibrate the gains of the source-detector pairs employed. The tissue measurement however is obtained from a different medium with optical properties $\mu_a^{het}, \mu_s'^{het}$. Therefore the two fields do not correspond to a "total" and an "incident" field in the way they were defined in §3.5. According to the definition in §3.5, the total and incident field differ slightly due to the weak perturbation distribution. In the case considered here, the two fields may be markedly different due to the change in the bulk optical properties ($\mu_a^{base}, \mu_s'^{base}$ vs. $\mu_a^{het}, \mu_s'^{het}$). The larger the change between the baseline and tissue optical properties, the stronger the scattered field $\Phi_{sc}(\vec{r}_s, \vec{r}_d, \omega)$ deviates form its definition and this results in artifacts as witnessed in this analysis. The algorithm proposed accounts for the change in optical properties and corrects the $\Phi_{sc}(\vec{r}_s, \vec{r}_d, \omega)$ to the new relative scattered field $\Phi_{sc}^{rel}(\vec{r}_s, \vec{r}_d, \omega)$. The latter corresponds to a measurement from the tissue of investigation relative to an incident field obtained from a medium with the average optical properties of the tissue and not relative to a baseline measurement. The effect of this correction is that it rejects the information that $\Phi_{sc}(\vec{r}_s, \vec{r}_d, \omega)$ contains on the difference between $\mu_a^{base}, \mu_s'^{base}$ and $\mu_a^{het}, \mu_s'^{het}$. Although the "biological noise" is retained its effect now diminishes. This results in great artifact suppression. Furthermore the size and magnitude of the tumor structure is more accurately resolved. The algorithm is found to be insensitive to the degree of background heterogeneity.

The use of this algorithm has been shown to be beneficial when performing differential measurements of tissue such as the pre- and post contrast enhanced breast [106]. Here we also demonstrate that this algorithm could also benefit the reconstruction of objects in highly heterogeneous systems even if no a-priori information is present.

The correction algorithm requires knowledge of the average optical properties of the heterogeneous medium. Here the average optical properties were easily calculated by simple averaging over the optical property map. In real measurements the average optical properties of the medium under investigation can be calculated by fitting the experimental measurements to the appropriate solution of the diffusion equation for the geometry used (see Chapter 4).

The tomographic scheme employed in this work was modeled after a clinical implementation of a breast DOT imager. Similarly the media simulated were modeled after the "typical" breast appearance although the anatomy and functional variability of the breast is large. Within these limitations the results allow insight on the expected performance of the technique in imaging the in-vivo breast although the conclusions may be extended to other tissue types.

6.2 DOT of contrast enhanced media.

In this section the DOT performance to image contrast enhanced tissue-like media is examined. This section evaluates the developments described in §5.4. Simulated data derived directly from baseline and Gd-enhanced MR images are used to model the pre- and post-ICG breast. The performance of three DOT formulations is examined in imaging tissue after contrast agent enhancement. The three formulations were:

A) Using Eq.(5-29), namely

$$\phi_{sc}(\vec{r}_s,\vec{r}_d,\omega)=\ln\frac{\phi''}{\phi'}\frac{\phi_0'}{\phi_0''}=\int_V W''_a\delta\mu_a^{rel}(\vec{r})d\vec{r}\,, \qquad (6\text{-}3)$$

This comparison investigates the effect of the correction algorithm as compared to the typical Rytov approximation.

B) The typical Rytov approximation which assumes $\Phi''_{sc}=\ln\left(\frac{\phi''}{\phi'}\right)$, namely

$$\Phi''_{sc}(\vec{r}_s,\vec{r}_d,\omega)=\ln\left(\frac{\phi''}{\phi'}\right)=\int_V W'_a\,\delta\mu_a^{ICG}(\vec{r})d\vec{r}\,, \qquad (6\text{-}4)$$

(see §5.1). This approach is similar to the one presented in the previous section (§6.1) but uses a baseline measurement that is on a heterogeneous medium (namely the pre-ICG) breast. This is the typical perturbation approach that does not consider the average absorption increase due to the extrinsic contrast.

C) Using Eq.(5-25) including the term S, namely

$$\phi_{sc}(\vec{r}_s,\vec{r}_d,\omega)-S=\ln\frac{\phi''}{\phi'}\frac{\phi'_0}{\phi''_0}-S=\int_V W''_a\,\delta\mu_a^{rel}(\vec{r})d\vec{r}\,, \qquad (6\text{-}5)$$

This comparison investigates the effect of the approximation S=0 assumed in Eq.(5-29).

A difference image was also produced by subtracting the post-ICG image from the pre-ICG image for comparison reasons. Both pre- and post- images were produced using Eq.(5-9), assuming a homogeneous medium as baseline. The optical properties of the homogeneous medium were μ'_{a0}=0.03cm^{-1} and μ'_{s0}=8cm^{-1}.

In order to perform the comparisons two MRI coronal slices of a human breast were obtained: one before and one after contrast enhancement. Figure 6-9a depicts the T1-weighted MR image. This image depicts structure. White regions correspond primarily to adipose (fatty) tissue while dark regions correspond to parenchymal (glandular) tissue. Figure 6-9 b depicts the signal enhancement of the same T1-weighted image due to injection of the MRI contrast agent Gd-DTPA. The Gd-DTPA enhancement is superimposed in color. An infiltrating ductal carcinoma (shown in yellow) demonstrated the highest signal enhancement. Gd-DTPA and ICG have similar distribution patterns. Here we assume that the Gd-DTPA distribution reflects the ICG distribution.

We converted the MR images to optical property maps, separating four structures based on the image intensity information (by applying appropriate thresholds). The cancer is assumed to have two states: pre- and post- ICG contrast. The structures selected and the corresponding absolute optical properties are shown in Table 6-4. The optical properties are chosen to simulate breast optical properties as obtained from our breast clinical measurements (§9.1 and §9.2).

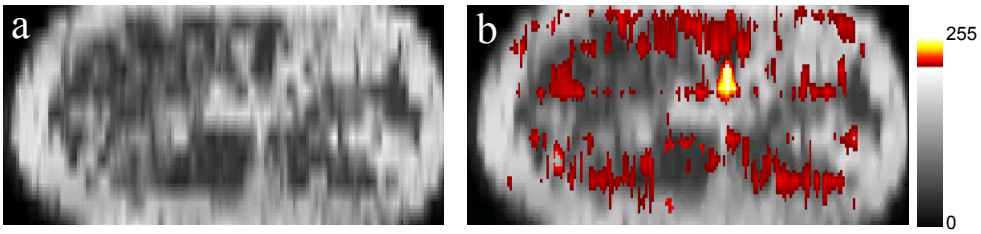

Figure 6-9. (a) T1-weighted MR coronal slice of a human breast, (b) Gd-DTPA distribution (in color) of the same coronal slice. A ductal carcinoma appears in yellow.

Table 6-4: Absolute optical properties of the different structures used for the simulations.

Structure	μ_a (cm^{-1})	μ_s' (cm^{-1})
Adipose	0.03	8
Parenchymal	0.06	8
ICG-background	0.09	8
Pre-ICG Cancer	0.09	8
Post ICG Cancer	0.16	8

Scattering has been assumed constant for all structures for simplicity. The resulting absorption maps are shown in Figure 6-10. The medium surrounding the breast was

arbitrarily simulated as a highly absorbing diffuse medium (μ_a =0.30cm^{-1} μ_s'= 8cm^{-1}). The average absorption of the pre- and post- ICG breast were found to be μ'_{a0} =0.0473 cm^{-1} and μ''_{a0} =0.0589 cm^{-1} so that average absorption increase due to the ICG is μ''_{a0} - μ'_{a0} =0.0116 cm^{-1}.

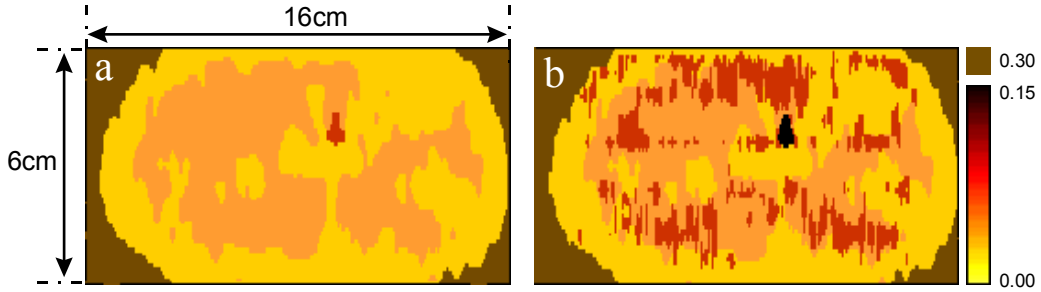

Figure 6-10: Absorption maps used for the simulation of the ICG effect. (a) pre-ICG breast (b) post-ICG breast.

The maps of Figure 6-10 served as an input to a finite-differences implementation of the frequency-domain diffusion equation. The simulation assumed 7 sources and 21 detectors as shown in Figure 6-11. The frequency employed was 200MHz. No noise was added in the forward data.

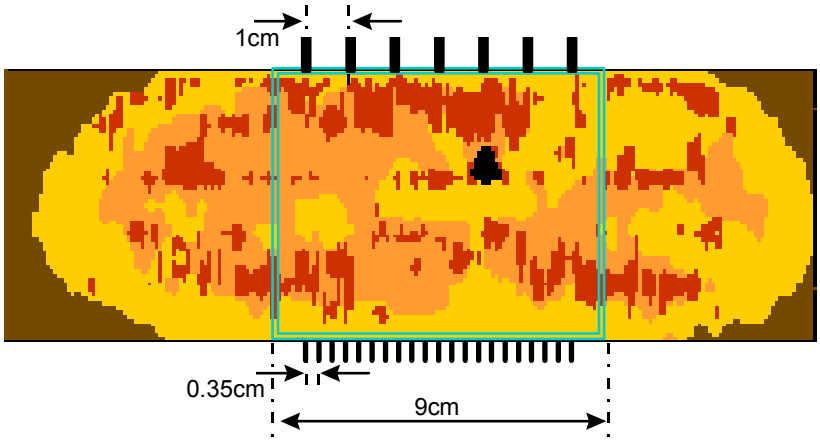

Figure 6-11: Sources and detector arrangement used for the simulation. The region reconstructed is outlined with a green double line.

For reconstruction purposes, the region of interest (indicated in Figure 6-11 as a green double line) was segmented into 35x25 voxels. The inversion was performed using the algebraic reconstruction technique of §5.2, with relaxation parameter λ=0.1. Convergence was assumed when an additional 100 iterations did not change the result more than 0.1%. The simulated image and the reconstructed $\delta\mu_a^{rel}(\vec{r})$ for the three cases examined are shown in Figure 6-12.

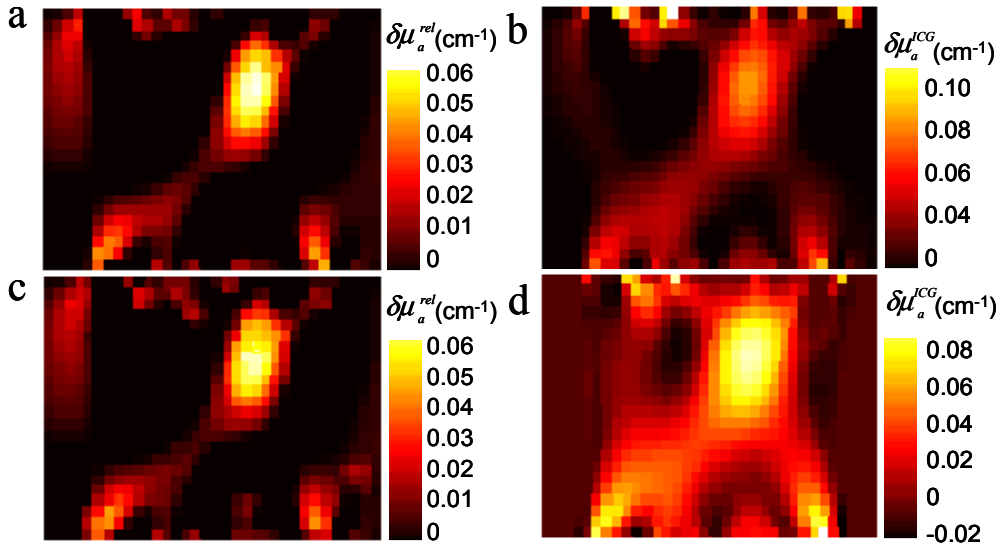

Figure 6-12: Reconstruction results of the region indicated with the green double line on Figure 6-11. a) Image using Eq.(6-3). b) Image using Eq.(6-4). c) Image using Eq(6-5). d) The result of subtracting an image of the post-ICG breast (reconstructed relative to a homogeneous baseline medium) from an image of the pre-ICG breast (reconstructed relatively to the same baseline medium). The optical properties of the homogeneous medium were μ'_{a0} =0.03cm^{-1} and μ'_s = 8cm^{-1}.

The superior performance of Eq.(6-3) compared to the typical perturbative formulation Eq.(6-4) can be evaluated by examining Figure 6-12 a and b. Although both methods resolve the cancerous lesion with comparable positional and size accuracy, the typical formulation (Figure 6-12b) yields several strong artifacts close to the boundaries. These artifacts illustrate that in the presence of distributed absorption, the perturbative method converges preferentially to localized regions of high absorption. This is often true when inverting underdetermined systems (see also §6.1). Eq.(6-3) on the other hand removes the "average absorption increase" from the measurement vector. Therefore Figure 6-12a images *weaker* perturbations introduced by the ICG injection, relative to the average absorption increase. Since by construction the perturbation method works especially well for weak perturbations [56], it is expected that the use of Eq.(6-3) will more accurately image the heterogeneous medium. The same behavior is expected for a Born-type perturbative formulation. We note that Figure 6-12b images the $\delta\mu_a^{ICG}(\vec{r})$ and not the $\delta\mu_a^{rel}(\vec{r})$ as in Figure 6-12a and Figure 6-12c. Therefore it is reasonable that the reconstructed value for cancer in Figure 6-12b is higher than the value reconstructed in Figure 6-12a and Figure 6-12c. The difference in reconstructed values equals approximately the average absorption increase in the post-ICG breast ($\mu''_{a0} - \mu'_{a0} = 0.0116$ cm^{-1}).

Figure 6-12c has been produced after correcting the measurement vector with S instead of setting it to zero as in Figure 6-12a. Only minor differences exist between the two images as had been predicted in Figure 5-1. In this simulation the pre-ICG cancer had a contrast of 2:1 to the average pre-ICG background value. This contribution has most likely resulted in the minor differences observed between the two images, especially in the structures close to the boundaries.

Figure 6-12d is the result of subtracting an image of the post-ICG breast from an image of the pre-ICG breast. Here the $\delta\mu_a^{ICG}(\vec{r})$ is imaged. The magnitude of the cancer is slightly overestimated and its size is significantly overestimated. Similarly to Figure 6-12b, strong artifacts appear close to the boundary. A distributed absorption is also reconstructed which does not correspond to the ICG distribution and is also an artifact. Compared to the other approaches the subtraction yields the most artifacts.

In these simulations the average optical properties were known by simple integration over the optical property map. In our clinical implementation (Chapter 7, 8, 9) the average optical properties of the pre-ICG breast are calculated by fitting the experimental time-domain data obtained to the appropriate solution of the diffusion equation for the geometry used as explained in Chapter 4. Furthermore, Eq.(5-29) calculates the difference $\mu'_{a0} - \mu''_{a0}$, (necessary to calculate both U'_0/U''_0 and $\delta\mu_a^{ICG}(\vec{r})$ with an accuracy of the order of 10^{-3} cm^{-1}.

To conclude the formulation of perturbation theory in Eq.(6-3) is particularly well suited for image reconstructions of differences in the absorption properties of tissues as a result of optical contrast agent administration. Importantly, these results enable the extraction of differential contrast agent absorption even within media that are heterogeneous in the absence of the contrast agent. The primary result is an intuitive equation, which is valid over a large range of conditions. It was shown explicitly what these corrections are and how these corrections can be included in more careful analyses. The results should be applicable for a broad range of other DOT applications wherein baseline and "stimulated" measurements are available, particularly functional imaging in brain and muscle.

6.3 Noise, hemoglobin concentration and saturation imaging.

The combination of spectral information is a fundamental part of DOT. "Spectroscopic" imaging can be easily performed by obtaining images at multiple wavelengths and utilizing Eq.(4-6) on a pixel to pixel basis (assuming two or more chromophore concentrations). In §4.1.4 the effect of systematic errors, namely errors that bias the calculation of the absorption coefficient at multiple wavelengths in the same manner was studied. Systematic errors were found to affect more the quantification of hemoglobin concentration [H] than hemoglobin saturation Y. Here the effect of random noise in [H] and Y calculations, as pertaining to spectroscopic imaging is investigated. Conversely to the findings for systematic errors, it is demonstrated that random noise affects more the saturation calculation.

6.3.1 Simulated [H] and Y maps.

To perform the investigation a two-dimensional medium was assumed, which contains only two absorbers, namely oxy- and deoxy- hemoglobin. The distribution of these absorbers was such, that they produce the [H] and Y maps shown in Figure 6-13. Using Eq.(4-6) the absorption coefficient in any wavelength can be calculated, given the extinction coefficients of oxy- and deoxy- hemoglobin at those wavelengths. Measurements at four wavelengths were assumed, i.e at λ=690nm, 750nm, 780nm and 830nm. Hence 4 absorption maps for each of the wavelengths were obtained (i.e Eq.(4-6) applied to each image pixel separately where [HbO2]=Y·[H] and [Hb]=[H]·(1-Y)). Then 5% random noise was added to each of the absorption maps.

The noise-added absorption coefficient maps were used to back calculate the [H] and Y maps and investigate the effect of noise. Two calculations were performed. The first used the data at 780nm and 830nm to retrieve the [H], Y maps by inverting a determined system of two equations (i.e. Eq.(4-6) written for the two wavelengths) and two unknowns (oxy- and deoxy-hemoglobin). The second used all available wavelengths to solve again for the two unknown concentrations of oxy- and deoxy- hemoglobin. The 4×2 over-determined system was solved by data fitting in the least square sense. The hypothesis behind using four wavelengths for two unknowns is that by using an over-determined problem, we will improve the noise statistics of the resulting image.

6.3.2 Noise effect on [H],Y imaging

Figure 6-13c and d depicts the result obtained after calculating the Y, [H] maps using only two wavelengths. The effect of the noise is more significant in the calculation of the Y map than the [H] map. This can be explained because the calculation of Y involves the division of the absorption coefficient in the two wavelengths [60] whereas the calculation of [H] implicates the addition of the two wavelengths. This behavior is similar to our observations with clinical results (see §9.3). The use of four wavelengths give superior performance compared to two wavelengths especially in reconstructing saturation. (Figure

6-13e and f). The reconstruction of blood volume is less affected by noise and therefore although improved when using 4 wavelengths, this improvement is less obvious. The use of four wavelengths to improve the calculation of Y and [H] is been considered as an alternative to improving quantification [107,108]

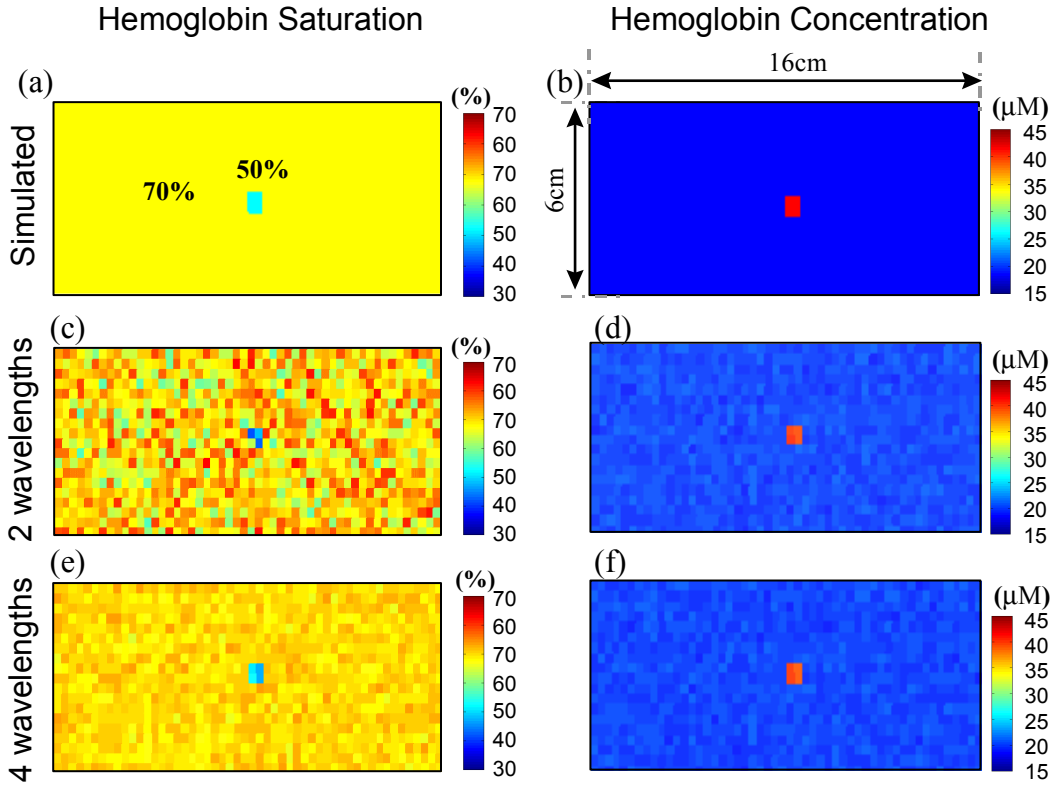

Figure 6-13: Simulated calculation of saturation (left column) and hemoglobin concentration (right column) images as a function of wavelengths employed in the presence of 5% percent noise. (a) and (b) Simulation maps employed. (c)-(d) images when using two wavelengths; (e)-(f) images when using four wavelengths; (a)-(c) is saturation.

6.4 Using a-priori information

In §5.6 an analytical way to implement *a-priori* geometrical information was discussed. In this section we examine the performance of this method with experimental measurements and with the heterogeneous media used in §6.1 to examine the performance of the tomographic approach.

An analytical merit function has been selected which assumes only two unknowns: an unknown absorptive lesion or lesions (the *lesion*) and an unknown background heterogeneity (the *background*). According to Eq.(5-35) this merit function is written as

$$\begin{bmatrix} \phi_{sc}^{1}(\vec{r}_{s1},\vec{r}_{d1},\omega_1) \\ \vdots \\ \phi_{sc}^{m}(\vec{r}_{so},\vec{r}_{dp},\omega_q) \end{bmatrix} = \begin{bmatrix} W_{11}^{a} & W_{12}^{a} \\ \vdots & \vdots \\ W_{m1}^{a} & W_{m2}^{a} \end{bmatrix} \begin{bmatrix} \delta\mu_a^{lesion} \\ \delta\mu_a^{back} \end{bmatrix}. \qquad (6\text{-}6)$$

Eq.(6-6) uses multiple modulation frequencies (derived experimentally from the Fourier transform of the time resolved measurements) Fitting only for absorptive heterogeneities is directed from the fact that fitting for both the absorption and scattering introduces cross talk. This cross-talk yields occasionally unexpected results. The reason for the presence of cross talk is illustrated in Figure 6-14 where the χ^2 is plotted for the lesion structure when it is minimized for both the absorption and the reduced scattering coefficient. As shown the minimum lies somewhere in the middle of a smooth valley. In the presence of noise the minimization process can converge anywhere in this valley and the solution becomes non robust.

When fitting extrinsic contrast, the absorptive dye does not introduce scattering changes, therefore Eq.(6-6) yields very accurate results. When fitting intrinsic contrast, scattering variations may introduce errors in the absorption coefficient. Eq.(6-6) then works efficiently under the assumption of small scattering contrast. The effect of scattering contrast can be however evaluated by repeating the fitting using different modulation frequencies. If

no scattering contrast exists the result should be virtually independent of the modulation frequency(ies) selected, otherwise scattering perturbation should be included in the fitting.

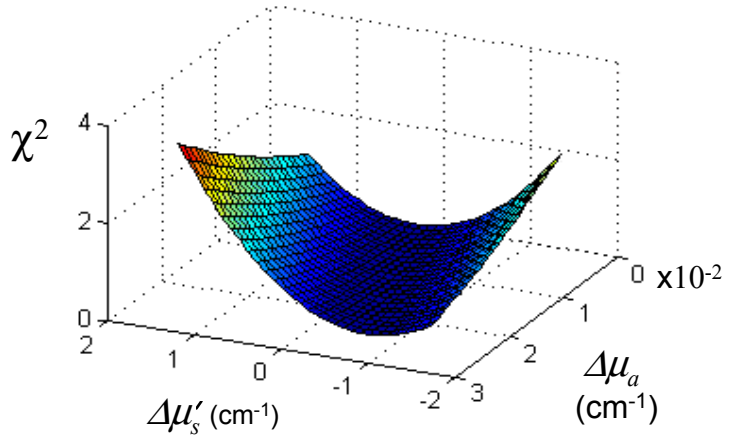

Figure 6-14: Minimization space for the optical properties of an unknown lesion using localized Diffuse Optical Spectroscopy with a two-unknown merit function.

In principle the method in §5.6 and Eq.(6-6) allows to solve for multiple structures, not only two. The selection of fitting for only two unknown structures however favors the robustness of the solution. Figure 6-15 depicts the expected error (standard deviation) of a three-unknown merit function versus a two-unknown merit function as a function of measurement noise (only absorptive heterogeneities were assumed). The result has been obtained by repeating the fit multiple times (under the presence of random noise at each noise level) and calculating the standard deviation of the result. Apparently the two-unknown merit function performs much better than the three-unknown merit function and for that was selected to fit the experimental data in Chapter 9.

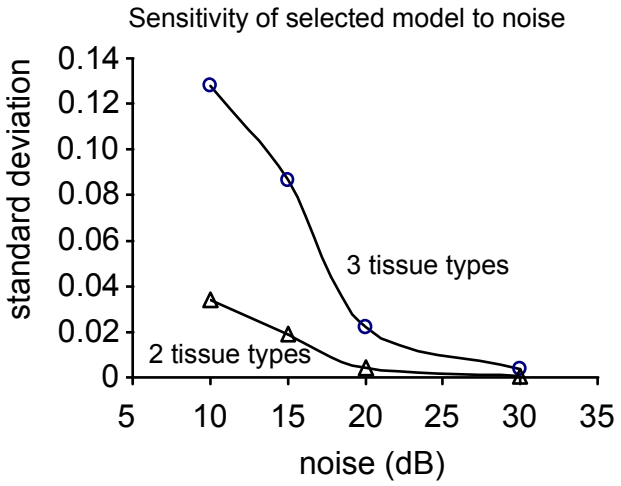

Figure 6-15: Sensitivity of the merit function for localized Diffuse Optical Spectroscopy using two or three unknown tissue types as a function of noise in the measurements.

The merit function minimization is performed using the Nelder-Mead simplex search [83], provided within the Matlab software package (MathWorks, MA USA). Experimentally the extraction of unknown tissue structures is performed with specific tools developed and described in §8.2. In the following, an evaluation of the selected two-uknown merit function with experimental data from a simple phantom and with simulated data of highly heterogeneous diffuse media outlines the performance of the technique.

6.4.1 Experimental measurements on a breast phantom.

The experiment described in this subsection was developed in collaboration with Maureen O'Leary and appears in [55, 109]. However the measurements and data analysis shown here have been obtained with the instrument and tools developed and presented in Chapter 5 and Chapter 7.

A solid resin model has been used that resembles the shape and the average optical properties of the human breast (μ_a=0.05cm^{-1}, μ_s'=8cm^{-1}). The model, shown in Figure 6-16,

has a cylindrical cavity that can be filled with combinations of absorbing and scattering liquids to simulate different kinds of inhomogeneities. In the sets of experiments performed here, the cavity was filled with 0.8% intralipid solution in order to match the scattering properties of the surrounding resin and different amounts of ink were added to induce local absorption differences.

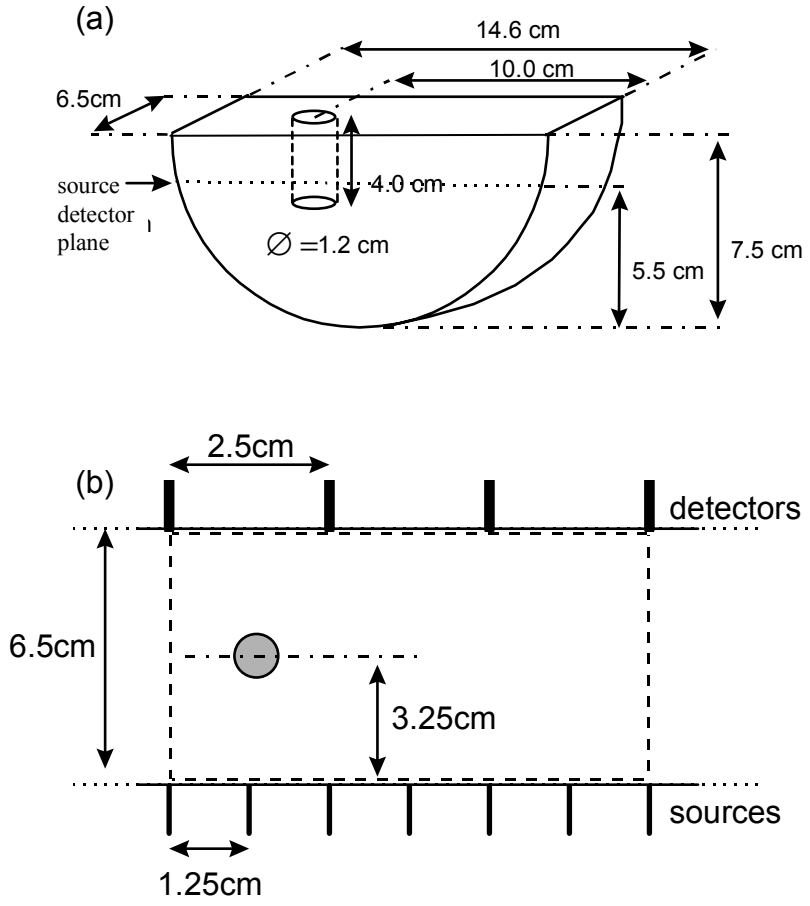

Figure 6-16. Breast resin model and experimental set-up used for the evaluation of localized Diffuse Optical Spectroscopy using the two-unknown merit function.

Transmittance geometry was realized using 7 sources and 4 detectors laying on the same plane but on opposite sides as shown in Figure 6-16b. Therefore 28 independent time-resolved curves were collected for all different source-detector pairs. The time-resolved data are transformed to the frequency domain and 5 frequencies were selected (80, 160, 240, 320, 400 Mhz). The dashed line indicates the volume reconstructed with dimensions $7.5 \times 6.5 \times 4$ cm^3. The selected mesh was $30 \times 26 \times 16$. The cavity was initially filled with a solution of intralipid and ink that matched the optical properties of the surrounding resin model and a baseline measurement was obtained. The baseline measurement was used to normalize all other measurements by providing the "*incident field*", similarly to the methodology described in §5.3. Subsequently, ink was diluted into the cavity to induce absorption perturbations indicated with a solid line in Figure 6-17a. The solver developed was used to fit those measurements assuming two unknowns namely the absorbing perturbation of the cavity and the background absorption of the surrounding medium. In this investigation the background and cavity scattering coefficients were assumed constant.

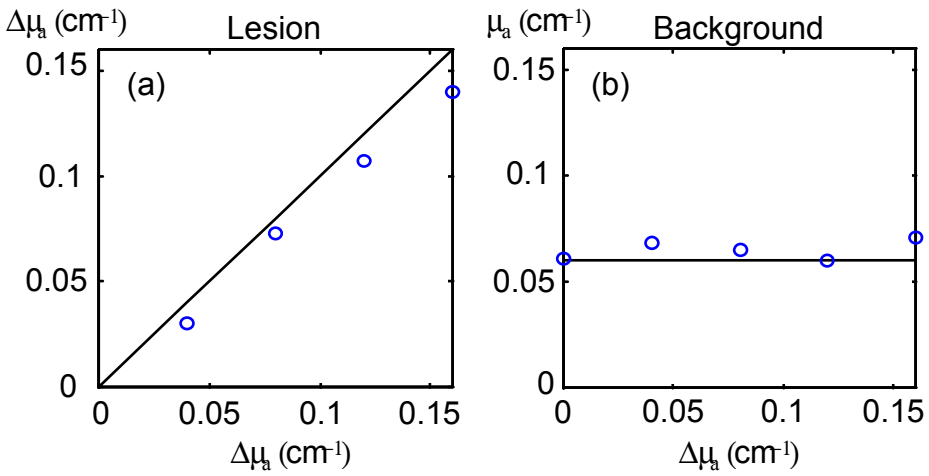

Figure 6-17. Result of the localized DOS fit employing the two-unknown merit function for varying lesion absorption coefficient.

The results of the fit are shown in Figure 6-17. Both the values for the perturbation and for the background are fitted well. The relative quantification error is ~7%. The result plotted for the background value is after addition to the absolute absorption coefficient value of the model. The deviation of the cavity reconstructed value from the real value can be attributed to experimental errors. The accuracy deterioration at the higher perturbation values is also characteristic of the linear perturbation model [55].

6.4.2 A-priori information and highly heterogeneous media.

Of particular interest for the clinical study, was the evaluation of the two-unknown merit function with heterogeneous, breast-like media. The two-unknown merit function allows two degrees of freedom: the "background" can measure the average background change and the "lesion" may quantify only the correlated information (information seen in all relevant projections), thus rejecting contrast from other lesions which will appear as noise and contribute to the average background optical property. To evaluate this hypothesis the simulated data from the heterogeneous maps of §6.1 were employed. Results from two volume fractions are used, namely for VF=10% and VF=30%. The same geometry and region of interest was selected as the one in Figure 6-3. Seven sources and four detectors were employed and the selected mesh was 50 × 25. The real part of five modulation frequencies at 80, 160, 240, 320 and 400 MHz was employed. Here the lesion or tumor structure remains constant and the background heterogeneity varies. The results are depicted in Figure 6-18 as a function of the volume fraction. The solid line indicates the actual value for the lesion (Figure 6-18a) and the average background absorption coefficient (Figure 6-18b). Since this is a two-dimensional forward model, the volume of the merit function voxel was selected so that the result for VF=0% is exact. Both lesion and background values are accurately predicted. The merit function selected calculates accurately the average background absorption increase due to the increase in heterogeneity and the lesion quantification is independent of the background heterogeneity.

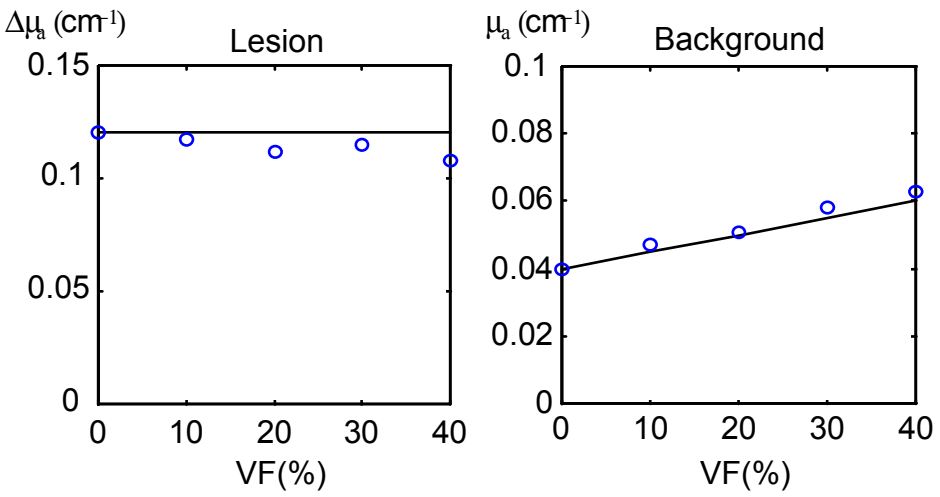

Figure 6-18. Result of the localized DOS fit employing the two-unknown merit function for varying the background heterogeneity of the absorption coefficient.

The great advantage of using the a-priori information is that it converts the typical DOT underdetermined system to an overdetermined one. The "availability" of more measurements for characterizing the same structures improves the noise statistics of the problem when random noise is considered, including both experimental and biological noise. As demonstrated in Figure 6-18, the two-unknown merit function selected is minimally affected by the random background heterogeneity and converges to the average value for the background structure. In the presence of systematic errors and noise however, the quantification result may be biased. For example if a highly heterogeneous structure existed only in the left part of the reconstructed area, the two-unknown merit function would have no capacity in producing a reasonable result since no provision is made for partial volume increases. In the clinical studies performed, a background check was always performed based on the Gd-enhancement of the MR images to verify the "randomness" of the breast vascularization. Then the volume of interest was appropriately selected to ensure a random background pattern and to avoid other systematic errors such as boundary effects. In general however, more complicated problems may require higher complexity merit functions.

In conclusion the two-unknown merit function has been found to perform very well in quantifying lesions embedded in homogeneous and random heterogeneous media and was selected as the function of choice for performing image-guided localized spectroscopy with the clinical examinations.

7 Experimental set-up

The clinical part of the present work was performed using a time-domain instrument designed to be coupled in the bore of a Magnetic Resonance scanner to perform simultaneous DOT and MRI examinations. In this chapter I describe the instrument and the experimental set-up for the in magnet application.

Section 7.1 describes the instrument and the performance of the individual components that comprised it. **Section 7.2** outlines the benchmark performance of the instrument and general time-resolved design considerations are discussed. **Section 7.3** investigates the tomographic performance of the instrument with tissue-like phantoms. **Section 7.4** describes the spectroscopic performance of the instrument. Finally **section 7.5** discusses the findings and gives a perspective on the clinical use of the apparatus presented.

7.1 Apparatus

Figure 7-1 depicts the block diagram of the instrument. The main components are: (i) the laser source consisting of two laser diodes at 780nm and 830nm (recently added 690nm as well), (ii) the wavelength coupler, (iii) the 95/5 beam splitter, (iv) the reference branch, (v)

the 1x24 DiCon FiberOptics optical switch, (vi) delivery source optic fibers, (vii) coupling plates that carry the optical fibers, radiofrequency coils for the MRI and are used for breast soft-compression, (viii) collection fiber optical bundles, (ix) light detectors, (x) amplification unit, (xi) router, (xii) photon counting unit with constant fraction discriminator (CFD), time-to-amplitude converter (TAC) and multi-channel pulse height analyzer (MCA) and finally (xiii) an Intel Pentium based personal computer for the control of the acquisition and data storage and analysis. Each of the components and its operation is described in detail in this section. Figure 7-2 depicts the placement of the patient and the compression plates in the magnet. The plates are mounted on an H-shaped holder designed to fit on the MR bed.

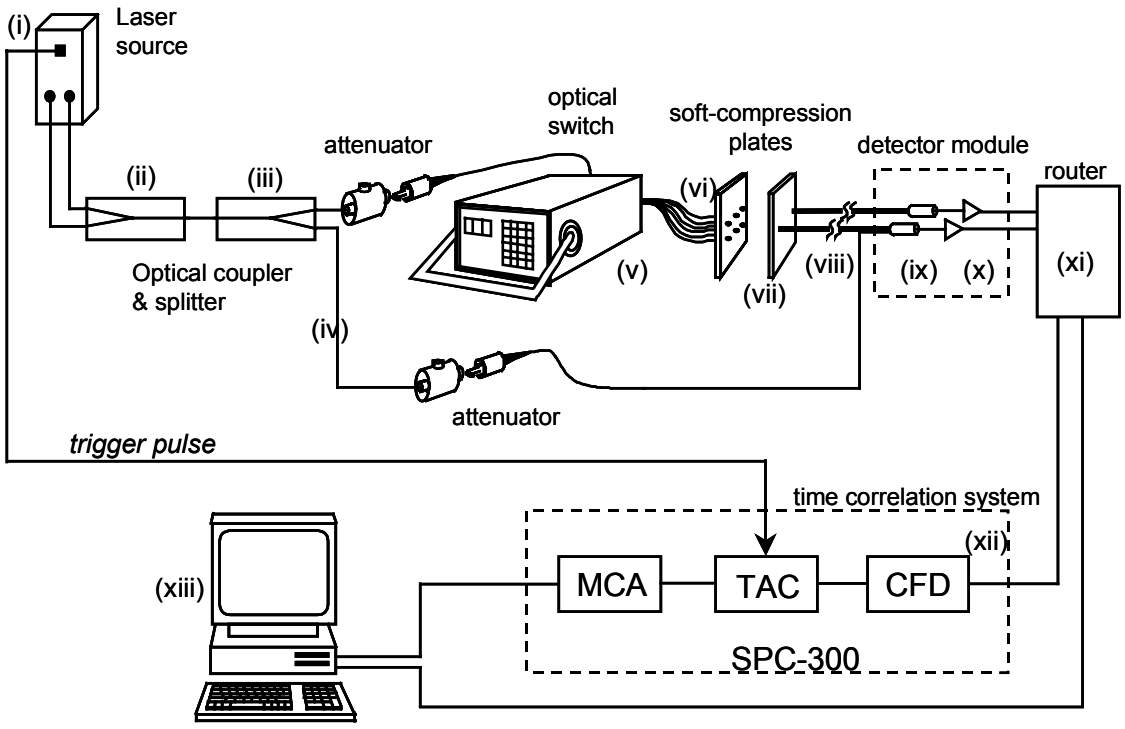

Figure 7-1. Time-resolved instrument used in the clinical examinations. (see text for component description).

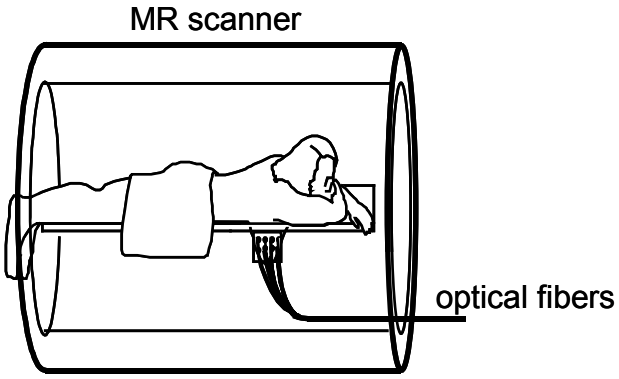

Figure 7-2: Patient placement in the MR scanner bore and the attachment of the compression plates holding the optical fibers.

7.1.1 Light source and delivery.

The Hamamatsu Picosecond Light Pulser (PLP) NIM module was used as the light source, having two laser diodes operating at 780 and 830 nm. The unit includes temperature feedback circuit for temperature drift compensation and a regulated drive circuit. The typical average power at the end of the delivery fiber was ~20μW for both the wavelengths used. The power employed is within the Food and Drug Administration (FDA) CLASS I classification and no special safety features were required for the operation of the instrument. The pulse repetition rate was 5Mhz and the output light pulse full width at half maximum (FWHM) for both diodes was ~50ps. The two wavelengths were time-multiplexed using an electrical delay line between the diode driving circuits (so that the laser trigger pulses were delayed 12 ns relatively to each other) and coupled together with a 50/50 fused coupler (OZ optics LTD, Ontario, Canada).

Time resolved measurements are very sensitive to the time t_0 that the pulse was launched into the sample under measurement. For this reason a 95%/5% 100/140μm core/clad silica fused coupler (OZ optics LTD, Ontario, Canada) is used, to introduce a reference branch as shown in Fig. 2a and monitor the t_0 simultaneously with any measurement. The reference channel can be either coupled alone to the 8th detector leaving 7

data channels available or simultaneously with the 8th fiber bundle. The reference fiber length was adjusted so the narrow peak does not interfere with the time-resolved curve in the time window. The 95% branch is connected to a DiCon Fiberoptics GP700 1x24 optical switch. The switch can be operated manually or through an IEEE 488.2 port. The switching time is ~0.5 s and the typical insertion loss is 0.6 dB. The 10m long multi-mode graded-index Spectran 100/140 fiber guides are coupled to the optical switch via FC connectors. At the other end of the fiber, thin rods made of Delrin® acetal resin were used to create connectors that mount the fiber on the compression plates.

7.1.2 Light detection.

Light was delivered to the detectors via eight 10m long fiber bundles (CeramOptec, MA). The bundles were made of 337 200/230 step index fibers (hard plastic clad, silica core Optran HWV), with a numerical aperture (NA) of 0.34. The active diameter was 5mm. The detector bundles were mounted on the compression plates as well. Fiber bundles were necessary to ensure delivery of sufficient light for detection. The bundles were attached to the detection module consisting of 8 detectors and 8 amplifiers each corresponding to one of the fiber bundles.

Three types of photo multiplier tubes (PMT) from Hamamatsu have been tested and used: the H5783-01, the R4110U-05MOD 8 channel MCP-PMT and the R5600U-50 GaAs.

H5783-01 PMT.

Being the most economical choice of the three, the H5783 PMT has the additional convenience of a built-in high voltage power supply making it ideal for a general-purpose photosensor. However in time-resolved applications the typical transient time spread (TTS) can be more than 200ps which results in a significant broadening of the input signal. The typical average current amplification is of the order of 10^6 at -950V (-1000V max). However significant variation in the plateau gain among different modules was found. Such variations reached ~10dB for the modules purchased making virtually impossible to operate all the channels in the same dynamic range conditions maintaining optimum photon amplification.

Similar variation was found for the TTS values. The multi-alkali photosensitive material used has a cut off wavelength at 810nm making the detector unsuitable for operation at 830nm where cathode radiant sensitivity reaches 0.5 mA/W.

R4110U-05MOD MCP-PMT

MCP-PMT detectors have very attractive characteristics for photon counting mainly due to the short transient and transient time-spread features. The 8-channel R4110U-05MOD module that was used has a typical TTS of 100ps per channel. The cross-talk between adjacent channels is of the order of 0.5%. Typical gain at -2700V (max -2800V) is also 10^6. The channel-to-channel gain variation is of the order of 4dB, therefore it is significantly lower than the H5783-01. The material of the photocathode is extended multialkali with radiant sensitivity (RS) of 15 mA/W at 780 nm and 7 mA/W at 830 nm.

R5600U-50 GaAs PMT

GaAs is a material with virtually flat quantum yield from 550nm to 850nm. The R5600U-50 detector yields a typical cathode radiant sensitivity (RS) of the order of 100 mA/W for this region. It is apparent that besides having an extended wavelength response this detector has also higher radiant sensitivity compared to the other two. Figure 7-3 depicts the photon count reflectance measurements on a solid model simulating the human breast optical properties, as a function of source-detector separation. In order to obtain comparable results the threshold is adjusted prior to the measurement so that the same dark current and background photon count is obtained from the sample. The R5600-50 GaAs demonstrates a significant higher gain compared to the other two detectors. The R5600U-50 uses a thick photosensitive layer, which is responsible for the high radiant sensitivity, but also results in high transient time spread (TTS) usually exceeding 300ps. The high TTS is the main disadvantage of the detector. Channel-to-channel gain variation is close to the MCP-PMT module.

Hence, the selection of detector is clear. When long separations or high absorbing samples are under investigation the R5600U-50 GaAs PMT is the only viable solution due to

the increased radiant sensitivity. Conversely, whereas the signal to noise ratio allows, the R4110U-05MOD MCP-PMT detector is a better choice for photon counting measurements due to the small TTS.

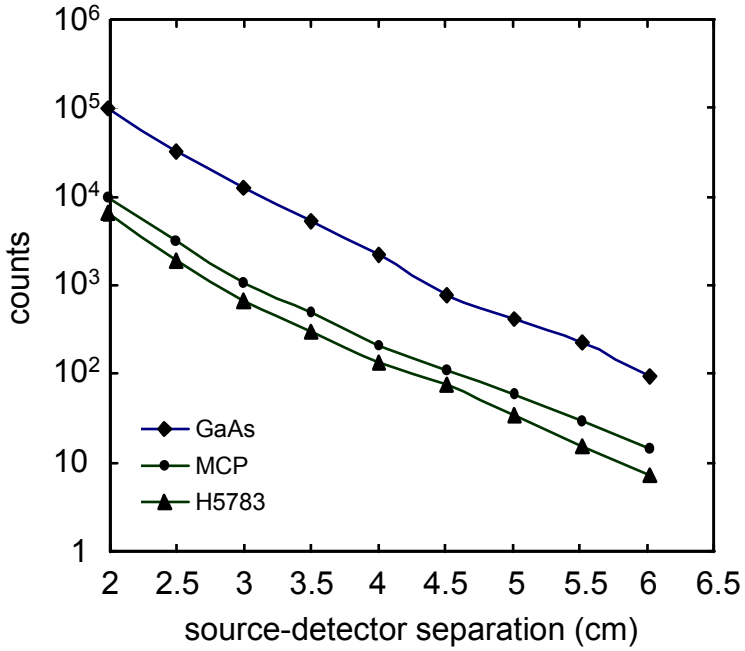

Figure 7-3 Amplitude versus separation for the three different detectors tested measured on a solid model. The absorption coefficient was μa=0.06 cm-1 and reduced scattering coefficient μs'=10 cm^{-1}. The laser intensity was adjusted to give ~100,000 counts for the GaAs detector at 2 cm and left unchanged thereon. In order to obtain comparable results the threshold is adjusted prior to the measurement so that the same photon count is obtained from the sample when no light source is on. The increased quantum efficiency of the GaAs detectors gives a significantly higher signal compared to the other two detectors.

7.1.3 Photon counting system

A typical time-correlated photon counting system is depicted as part of Figure 7-1 (component xii). A single photon, hitting on the detector photosensitive cathode, yields a negative electrical pulse at the anode, with a probability equal to the quantum efficiency of the photosensitive material. This pulse, after amplification, is directed to the constant fraction discriminator (CFD). The CFD sets a low threshold (low-level discriminator LLD) rejecting pulses with amplitude below this threshold, in order to increase the signal to noise ratio of the detected signal and establish single events for each accepted pulse. Signal to noise improvement can be explained if we consider that while the output pulse height distribution of the signal has a Poisson distribution, the output pulse height distribution of the dark current takes the form of an exponential function biased towards the region of low pulsed heights. This is evident by making a pulse height analysis of the photo-detector output with the light signal turned on and off respectively. Therefore setting an appropriate threshold will reject a significant number of dark current photons but only a small fraction of signal photons. The best way to set the threshold is by trial and error. Occasionally the CFD can also apply an upper threshold (upper level discriminator ULD) rejecting pulses higher than this upper level value. Pulses, within the levels set by the CFD, switch on the charging of a capacitor in the Time-to-Amplitude Converter (TAC). The charging is stopped and reset by a trigger signal from the PLP indicating the initiation of a new pulse. This is known as stop-start configuration and is necessary to ensure initialization of the charging capacitor in every cycle since the laser pulse is periodic and regular where the signal pulses are coming randomly. Therefore, time delays are converted to voltages, which are detected by an analog to digital converter (ADC). The time resolved curve is obtained by plotting the distribution of photons for separate time intervals.

For the time-correlated photon counting detection the SPC-300 photon counting card (Edinburgh Ltd, Edinburgh U.K.) was used. The SPC-300 integrates a complete photon counting system on a single AT-bus card. The system has a minimum time resolution of 18ps and can in principle count up to $\sim 10^6$ counts due to a fast flash ADC in combination with an error-correction technique, which allows a virtual 10-bit resolution (1024 time bins)

under such speeds. With the use of a router the card has the capability to detect signals from up to 128 different input channels and direct them to corresponding memory blocks. When a pulse appears to a channel, the router assigns to it a reference address indicating the channel number and in consequence the memory block that the incoming pulse should be stored to. Using 8-channels an average of $12 \cdot 10^4$ counts/sec per channel can be obtained. This is more than sufficient for typical measurements on human tissue for the laser power used. Since the system operates in a reversed start-stop mode, much lower count rates can be measured.

The LLD and ULD can be adjusted within the 5-80mV range in order to obtain optimum signal to noise ratio. Pulses above the ULD can still be detected if their duration is below 2ns due to the limited input circuitry bandwidth. The detectors described earlier give average pulse heights close to the minimum input requirement, especially the GaAs PMT. An amplification stage is necessary to ensure optimum interfacing of the photosensors to the SPC-300. We have used the C5594 Hamamatsu pre-amplifier with 36dB gain, 1.5 GHz typical upper cut-off frequency and an ACV 15D power supply (Astec America, Inc.Oceanside CA) with regulated output 15V/1.5A and $0.01\%/^0C$ temperature coefficient. The high gain gives the flexibility to interface the detection module to photon counting systems with different input pulse specifications. In order to interface properly the amplifier outputs to the SPC-300, SMA attenuators at 2GHz and 50 ohms (Pasternack Enterprises Irvine CA) have been employed. We use different attenuation values depending on the current gain of each individual detector in order to compensate for the current gain variation. In the case of the H5783 and MCP-PMT we use additional attenuators to couple the detector to the amplifier to avoid saturation of the amplifier.

7.1.4 Compression plates

The soft compression plates are shown in Figure 7-4 and are attached to the patient as shown in Figure 7-2. They are made of PVC material and bear both the MR coils [110,111] and the optical fiber holders. The medial plate can support up to 31 source fibers

and the lateral coil holds the 8 detector fiber bundles. Specially designed capillaries are filled with a solution of water and copper sulfate to mark the exact location of the plates on the MR 3D images. The plates apply soft compression on the both sides of the breast to ensure contact of the optical fibers onto the skin but without affecting the blood supply or blood volume of the breast. The medial plate is fixed and the lateral plate is mounted manually via a rail of preset positions. Special care is taken so that the medial and lateral plates are parallel when mounted.

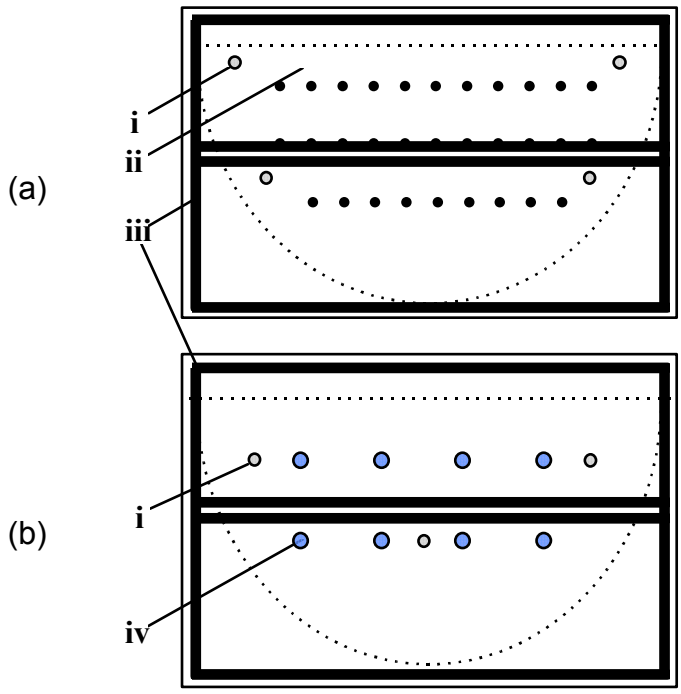

Figure 7-4: Soft compression plates. (a) medial plate with fiducial markers (i) source fiber holders (ii) and MR phased array coils(iii) (b) Lateral plate holding the detector fibers (iv), fiducials and MR coils.

7.2 COMPONENT PERFORMANCE

7.2.1 Impulse response

Figure 7-5 depicts instrument impulse responses for the two wavelengths and for the three detectors used. The measurements were obtained by abutting the source and detector fibers, the so called "instrument function" measurement. The full width at half maximum (FWHM) values vary depending on the detector used. Contributions to this pulse dispersion, besides the detectors, are the PLP (~50 ps), the step-index detection fiber bundles (~200ps) and the graded index source fibers, attenuator and photon counting system electronics jitter (~40 ps altogether).

7.2.2 Pulse dispersion

The large numerical aperture of the step-index detection fibers allows a large number of waveguide modes to be excited. Using a laser source with a low spectral width (~10 nm) the dominating dispersion will be the modal dispersion, a result of the differences in the group velocities of the modes [112].

With indexes of refraction n_{core}= 1.4533 and n_{clad}=1.4130 at 20^0C and 800nm and numerical aperture NA=0.34 the fractional refraction index change is

$$\Delta = \frac{n_1 - n_2}{n_1} = 0.0277 \text{ ,} \qquad \textbf{(7-1)}$$

and the expected time dispersion FWHM when all modes are excited is

$$\sigma_T = \frac{L}{c_n}\frac{\Delta}{4} \approx 300 ps \text{ ,} \qquad \textbf{(7-2)}$$

where $c_n=c_0/n_1$ is the speed of light into the core and L the fiber length.

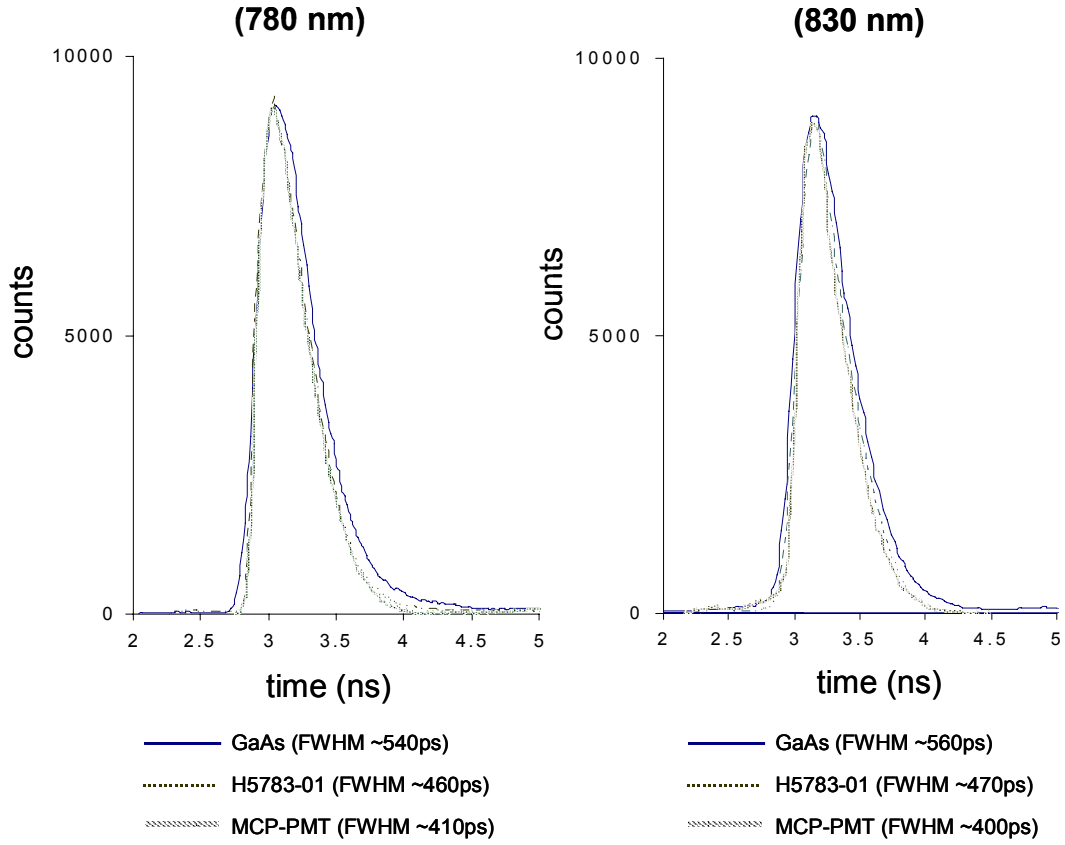

Figure 7-5: Instrument function measurement for the three detectors tested for the two wavelengths employed. The MCP-PMT demonstrates the lowest FWHM followed by the H5783-01 extended multi-alkali PMT and the GaAs PMT. The significant width of the instrument impulse response, unavoidable due to the necessary length of the detection step-index fiber bundles, is later corrected by performing deconvolution.

Experimental measurement of the fiber bundles' dispersion, however is 100ps lower than the theoretical calculation, indicating that not all the modes are typically excited. Shining laser light into the bundle from different angles (0 to 40 degrees range) results in a pulse shift or shape change of the order of 80ps as shown in Figure 7-6a verifying the above observation. Uncertainty of that order is undesirable for accurate measurements, as indicated in Chapter 4. Our homemade plastic fiber tips on the other hand do not guarantee exact positioning and shining angle when repeating a measurement, leading to time and amplitude shifts. To reduce such uncertainties light collimation is performed using MgF_2 coated, Plano-Convex lenses, 12mm diameter and 9.76mm back focal length (Edmund Scientific) encased in a special instrument-function measurement holder, as shown in Figure 7-6c. Light collimation, besides eliminating dispersed-pulse shifts and shape changes, also results in excitation of a lower number modes and reduction of overall pulse dispersion in the detection fiber bundles. Figure 7-6 b depicts the instrument function measurement when using the lens and demonstrates the narrowing effect at the pulse width of the instrument function. Practically, the lens holders are used for evaluation or calibration (i.e. warm up or jitter) measurements when narrow pulses are required for accurate time shift determination.

7.2.3 Calibration

There is a significant amplitude and time delay variation among the channels due to detector gain and fiber guide length variation. Such variations are recorded by measuring the instrument function for all source-detectors combinations. The measurements are made in the presence of the reference channel. All future measurements are being done using the same reference channel in order to be able to correct for laser drift and jitter. Curve fitting the reference channels of the instrument function and data files, with respect to amplitude and time delay, recovers the t_0 at the time of measurement.

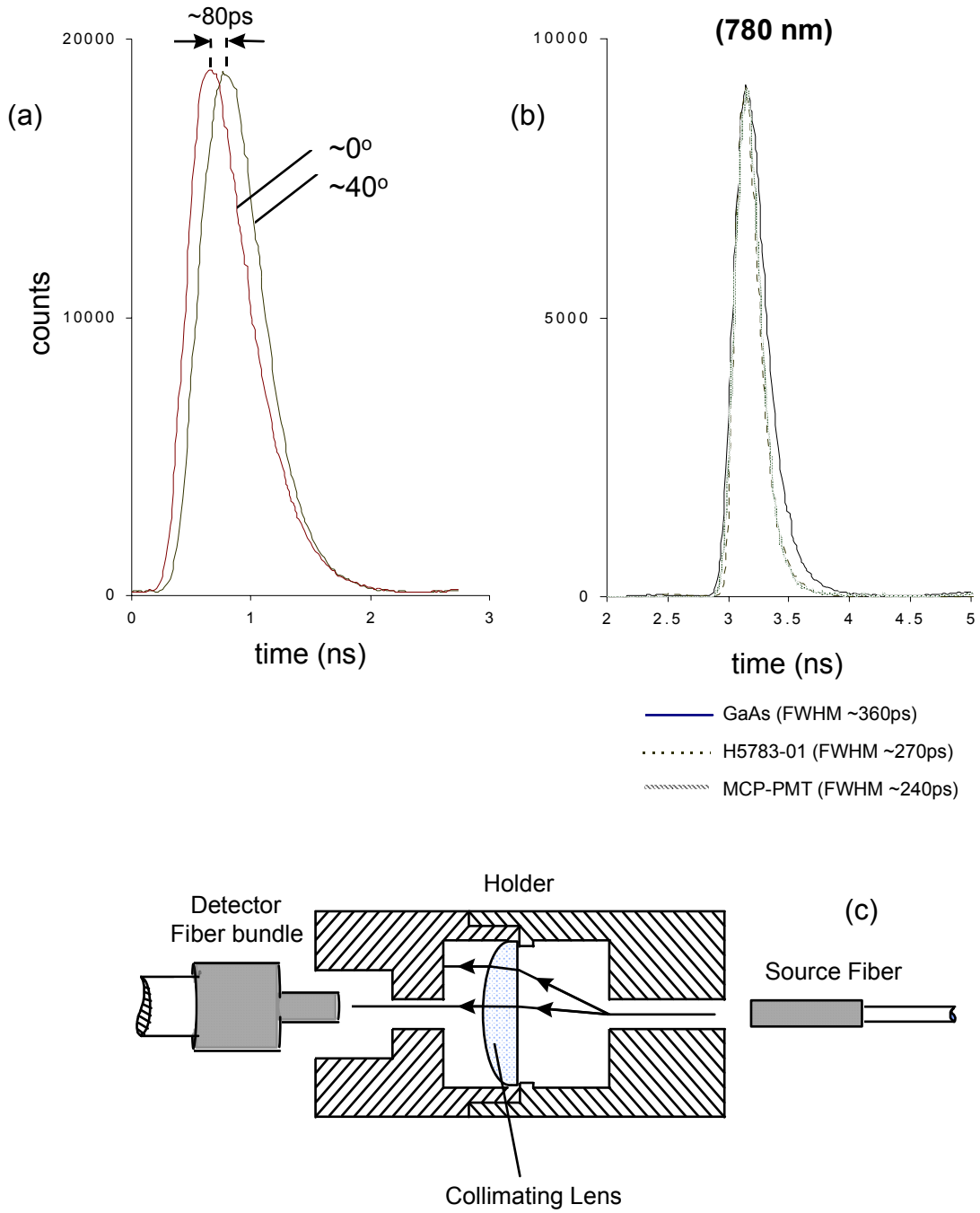

Figure 7-6: Effect on the instrument function measurement due to fiber bundle illumination at different angles. (b) Light collimation eliminates the effect and reduces the dispersion of the pulse in the detector fiber bundles. The decrease of the time dispersion is around 180ps for all detectors. (c) holder used for light collimation.

7.2.4 Instrument noise

The main parameters that may affect the accuracy of the spectroscopy and tomography are time uncertainties and amplitude uncertainties as was described in chapter 4. Time uncertainties include the pulse launch-time drift and the random launch-time fluctuation or *jitter* which translate to timing differences of the trigger pulse and propagation uncertainties in the photodetector and electrical and electronic components. These time-differences result in temporal noise between the data measurements and the instrument function recording or between the data measurements obtained at different times as when performing differential measurements. Allowing for 60 min of warm-up may significantly reduce laser drift problems. Laser drift can be further accounted for by using the reference measurement. However the jitter, which is determined after the warm-up period by monitoring the time position of the time-resolved curves' maximum as a function of time, is always present. Typical drift and jitter of the instrument function and reference curve vs. time, observed at room temperature, is plotted in Figure 7-7. Jitter is determined after the warm-up period by monitoring the time position of the time-resolved curves' maximum as a function of time. Instrument function measurements are made using the holder with the collimating lens to ensure a narrow, well-defined peak maximum. The average jitter of the instrument was ~25ps and it did not generally correlate with the reference fiber branch, therefore it cannot be accounted for and it practically defines the time-uncertainty of the instrument.

Other instrument uncertainties that affect spectroscopic and tomographic performance are the light intensity fluctuations. Amplitude stability was characterized by repeating the impulse response measurement and monitoring the fluctuation of the time-resolved curve maximum (after median-filtering to reduce shot noise) at an average of 10,000 counts at room temperature. The fluctuation was found to be ~1.5% at 10sec of integration time.

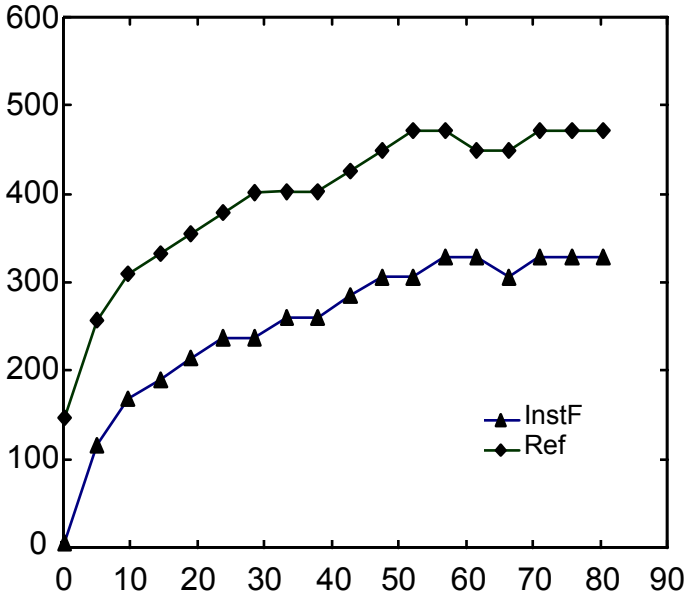

Figure 7-7: Warm-up drift and jitter of the instrument function and reference channel measurement for the 780 nm PLP. The warm-up period lasts almost an hour. Typical jitter is around 25ps and is determined after the warm up period.

7.2.5 Time versus frequency domain

Time domain methods yield data with much greater information content than single frequency or continuous wave (CW) measurements, which is necessary especially for absolute quantification measurements. The equivalent in the frequency domain would be multiple frequency laser modulation by using a frequency sweeper. In principle time-domain and frequency-domain at multiple frequencies are equivalent. Although greatly dependent on the specific instrument characteristics, generally, t_0 calibration issues become initial phase ϕ_0 determination (see Chapter 3 and 4) with similar practical limitations and accuracy considerations [113]. Acquisition time is practically also equivalent. A time-resolved system

needs averaging time to yield satisfactory signal to noise ratio where a phase instrument needs time to scan a range of frequencies.

However a great advantage of the time domain instrument is that it operates with only a small fraction of the laser power that phase instruments use [114]. This allows time domain instruments to operate in the FDA CLASS I limit of 20-40μW [115] category where no additional safety features are required, which simplifies the design and eases the acceptance of the instrument in a clinical environment.

7.3 Tomographic performance

This section evaluates the tomographic performance of the instrument with appropriately selected diffuse models that mimic the average optical properties of the breast.

7.3.1 Methods

The model employed was a 25 × 15 × 7 cm^3 black PVC fish tank, filled with Intralipid (Kabi Pharmacia , Clayton NC) emulsion. Intralipid is a polydisperse suspension of fat particles ranging in diameter from .1μm to 1.1 μm and serves as the scattering background medium. Nine sources and five detectors were attached through the material on the two opposite sides of the fish-tank as shown in Figure 7-8. Both source and detector fibers come in face with the inner surface of the fish tank walls. Baseline measurements from the intralipid suspension, for all source-detector pairs were obtained prior to introducing local inhomogeneities. Subsequently, absorbing and scattering cylinders were submerged into the solution and the same source scanning was performed. Data acquisition was 10 sec for each selected source.

The perturbative analysis presented in §5.1 using the Rytov approximation was used to formulate the forward problem for five selected frequencies at 80, 160, 240, 320 and 400 Mhz. The 12.5 × 7 × 1 cm^3 mesh selected for the reconstructions is also shown in Figure 7-8. The voxel size was 0.41 × 0.50 × 1.0 cm^3. Reconstruction was performed for a single plane

perpendicular to the z-axis. Matrix inversion was performed using the simultaneous iterative reconstruction technique (SIRT) [56]. Only the real part of the measurements was used, since the imaginary part (corresponding to a phase measurement) is greatly affected by instrumental time-uncertainties. For all images produced, median filtering (kernel size 3 x 3) followed by cubic spline interpolation was performed to improve the presentation.

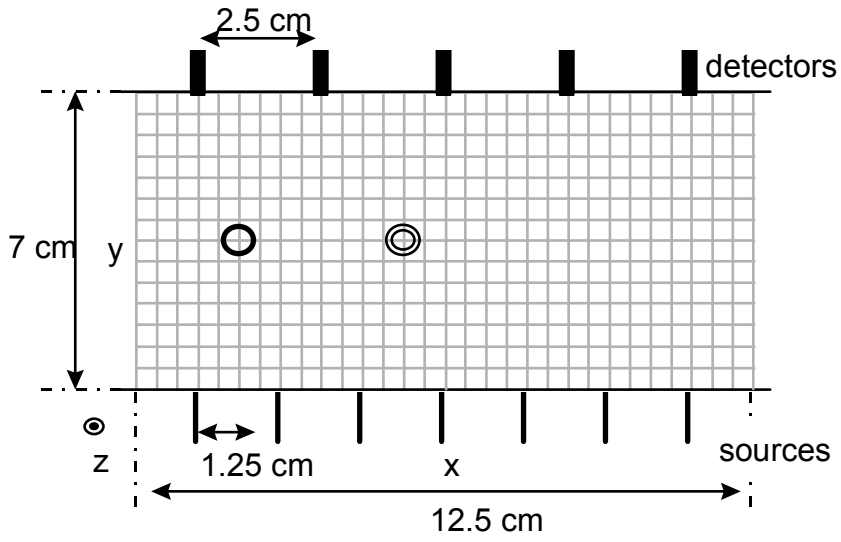

Figure 7-8: Top view of the experimental set-up and mesh used for the reconstructions. The background absorption and scattering coefficients were 0.025cm^{-1} and 5 cm^{-1} respectively. The thick line circle represents a cylindrical 0.8 mm diameter absorber (μ_a=0.1 cm^{-1} and μ_s'=5cm^{-1}) permanently fixed in the position shown, where the double thin line object indicates a second, similar absorber that was moved along x to investigate resolution limits. The voxel size was 0.41 x 0.50 x 1.0 cm^3.

7.3.2 Absorption objects

Absorption objects were constructed using 8mm diameter transparent thin-plastic cylinders. The cylinders were filled with 0.5% intralipid solutions matching the background scattering medium and 21μl/l of India Ink (3080-4 KOH-I-NOOR Inc. Bloomsbury NJ08804) to induce an absorption coefficient of 0.1 cm^{-1}. A single cylinder was initially

submerged into the intralipid solution. The cylinder was placed at a plane parallel to the fish tank walls that hold the sources and detectors, and passing through the center of the slab as shown in Figure 7-8. The depth was selected so that the cylinder was passing through the source detector plane.

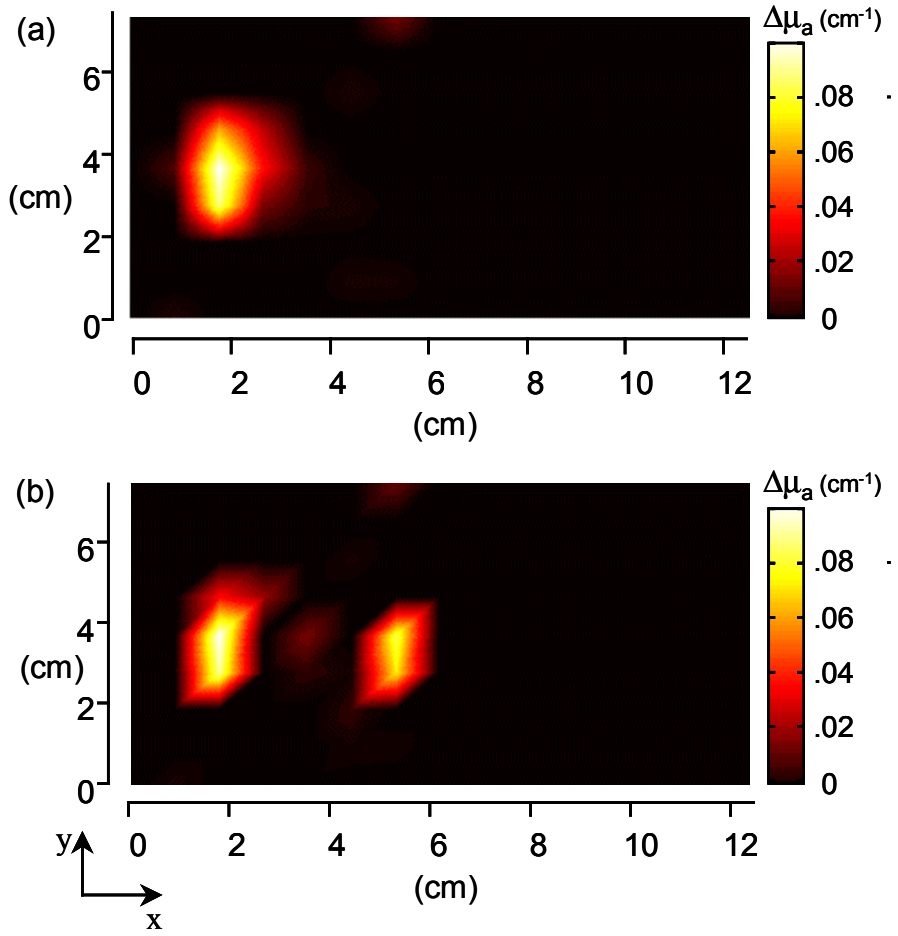

Figure 7-9: Experimental imaging of the absorption coefficient. (a) Resolving the permanently fixed absorber with no other object present. (b) Resolving two similar 0.8 mm diameter absorbers 3 cm apart

The image, obtained after 5000 iterations of the algebraic reconstruction, is shown in Figure 7-9a. The position of the object is reconstructed with excellent accuracy since the mesh selected favors the constructed geometry. The size along x, measured as the FWHM of

the reconstructed object is within 20% of the real object size. The size along y however (measured again as the FWHM of the object), is almost two times the size of the real object. This is typical for this type of "transmittance" geometry reconstructions. The wrong estimation along y is expected to improve as the object moves towards the center of the reconstruction mesh. Finally assuming that after 5000 SIRT iterations convergence has been achieved, the quantification of the objects' absorption coefficient is within 20% of the expected value as demonstrated here (taking under consideration volumetric uncertainties as well).

A second cylinder, identical to the first one, was subsequently immersed into the same set-up at 1cm, 2 cm and 3 cm away from the original object at the middle plane of the fish-tank, along the x-axis. The reconstruction configuration used to image the single object was also employed to image the two absorbing cylinders. The same inversion scheme was applied as for the single cylinder case. Figure 7-9b depicts the reconstructed result for the two objects for 3 cm separation. The 3-dimensional view of this reconstruction result is plotted in Figure 7-10a. Again the position of the original object is accurately reconstructed, however the position of the second object has an offset of 2 mm since there are "discrete position" cells forced by the selected mesh. Quantification lies within the same accuracy limits as in the single object case.

Figure 7-10b demonstrates the profiles of the reconstruction for the cylinders at different separations. The profiles are drawn along the x-axis passing through the center of the image as shown in Figure 7-10a. The cylinders are clearly distinguishable for separations 2 and 3 cm. At 1 cm separation, the reconstruction resolves only one object with a wider FWHM. In this last case the clear separation between the two 0.8 mm dia. cylinders is only 2mm, which is apparently not resolved by the imager. The diffusion equation predicts a banana shape photon distribution pattern [116], clearly indicating that the maximum diffusion occurs at a position that is farthest from both the source and detector location. Therefore the resolution limit for transmittance geometry is going to be set by the differentiation ability of the technique along an equidistant layer, parallel to source and detector planes and is not constant for all positions. The experiment performed here is a worst resolution case.

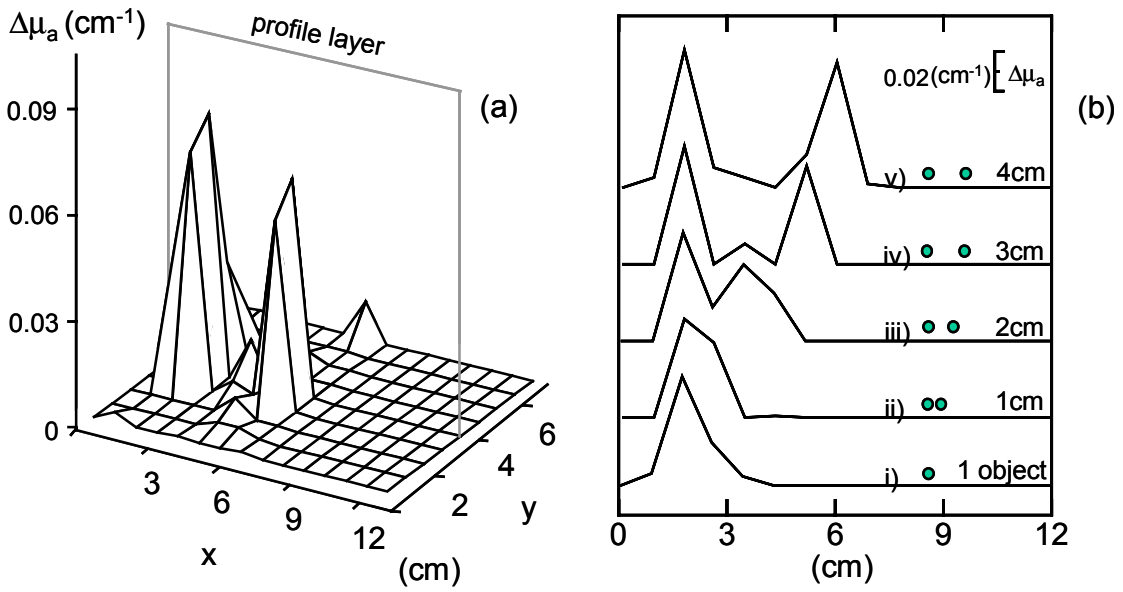

Figure 7-10: Three-dimensional view of Figure 7-9b. (a)The result is depicted with half the resolution of the reconstruction grid for rendering clarity (b) Image profiles along the layer indicated in (a). Curve (i) depicts the profile for one absorber in the medium, curve (ii) is for a second absorber immersed into the medium 1 cm apart and curves (iii), (iv) and (v) for the absorber moved 2 cm, 3 cm and 4 cm apart respectively.

7.3.3 Scattering objects

The same intralipid model and experimental set-up used for the absorbing objects, was employed to investigate the ability of the instrument to resolve scattering objects. Two plastic cylinders, similar to the ones used to simulate absorption objects, were filled with 0.2% solution of intralipid (μ_s'=20cm^{-1}) and immersed into the intralipid medium at the same position as in the absorbing object case. The reconstructed image obtained for two objects at 3 cm separation, and the profiles along the x-axis for all positions, are depicted in Figure 7-11a and Figure 7-11b respectively after 7000 iteration steps. The resolution performance is similar as in the absorption case. The quantification typically achieved was within 30% of the expected value.

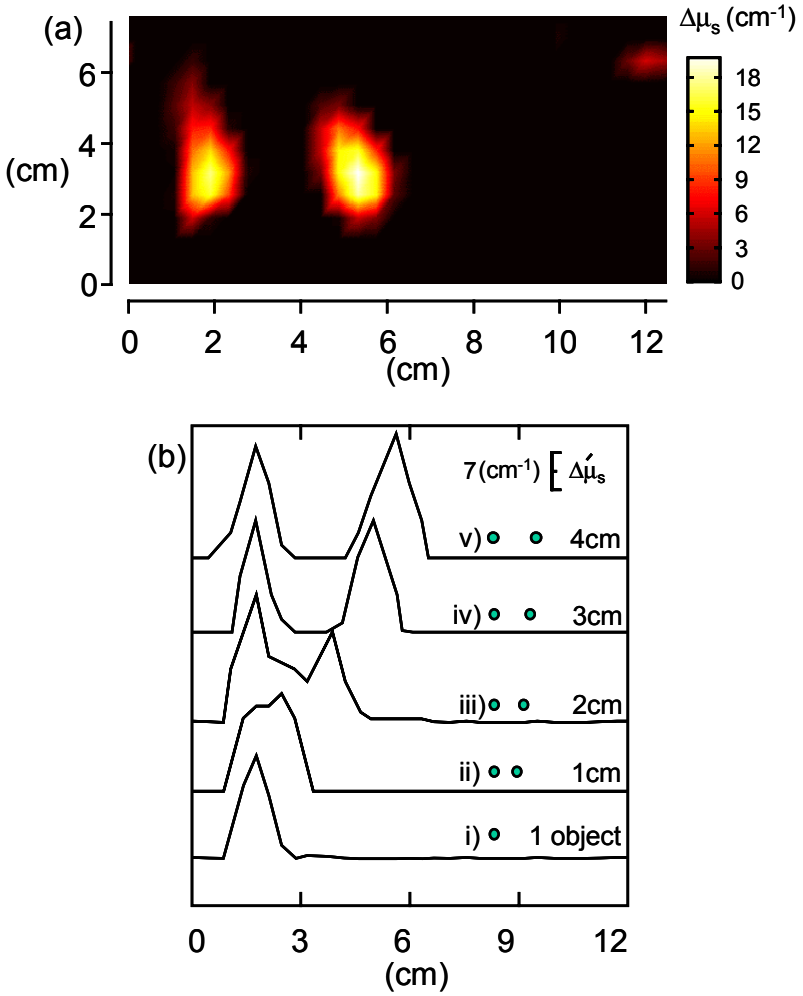

Figure 7-11: Imaging the reduced scattering coefficient for the set-up depicted in Figure 7-8. (a) Resolving two similar 0.8 mm dia. scatterers 3 cm apart. The optical properties of the scatterers were μ_a=0.025 cm^{-1} and μ_s'= 20cm^{-1}. (b) Image profiles along the profile layer indicated in Fig 6.13a. Curve (i) depicts the profile for one scatterer in the medium, curve (ii) is for a second scatterer immersed into the medium 1 cm apart and curves (iii), (iv) and (v) for the scatterer moved 2 cm, 3 cm and 4 cm apart respectively.

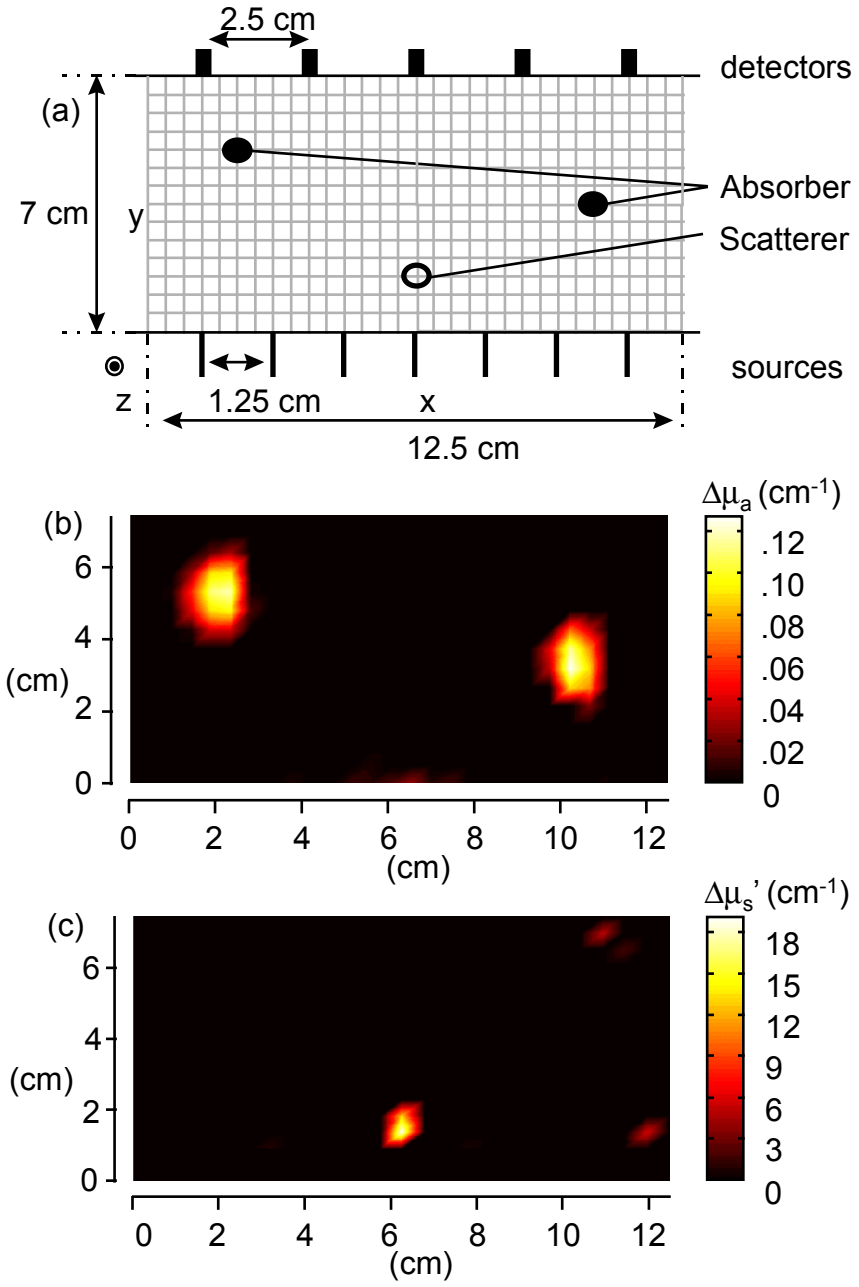

Figure 7-12: Simultaneous reconstruction of absorption and scattering objects. (a) Experimental set-up and mesh used for the reconstructions. The optical properties of the absorbers are μ_a=0.1cm^{-1}, μ_s'=5cm^{-1}, of the scatterer μ_a=0.025 cm^{-1} μ_s'=20cm^{-1} and of the background μ_a =0.025 cm^{-1}, μs'=20 cm^{-1}. (b) Reconstructed absorption image. (c) Reconstructed scattering image.

7.3.4 Absorbing and scattering objects

A measurement was performed with the same tank filled with IL and containing two absorbing objects (μ_a=0.1cm^{-1}) and one scattering object (μ_s'=20cm^{-1}) immersed into the medium at positions shown in Figure 7-12a. The values of the objects were selected so they are four times higher than the background medium values (μ_a= 0.025cm^{-1}, μ_s'= 5 cm^{-1}). Using the same reconstruction parameters as previously, 15,000 iterations were needed to simultaneously reconstruct the absorption and scattering images shown in Figure 7-12b and c respectively. The absorbing and scattering components are virtually completely separated. The increased number of iterations required to obtain this result has also produced objects with smaller dimensions and higher reconstructed values than in the single perturbation case of Figure 7-9 and Figure 7-11, which is an anticipated result due to the nature of the algebraic reconstruction algorithms.

7.3.5 Signal to noise performance on volunteers.

Measurements were performed on 4 volunteers, to investigate the signal to noise ratio (SNR) obtained and instrument compatibility issues with the MR scanner. The volunteers were from the Caucasian and African race and the age varied from 23 to 71 yrs old. The selection of volunteers was done so denser breast tissue as in the case of the young volunteers and dark skin was included in the study. All scans were performed using the GaAs detectors.

SNR values vs. separation are shown in Figure 7-13, for all volunteers. The signal to noise ratio in photon counting mode is calculated by [87]

$$SNR = \frac{Ns\sqrt{T}}{\sqrt{Ns + 2(Nb + Nd)}}, \qquad \textbf{(7-3)}$$

where Ns is the number of counts per second resulting from incident light per second, Nb is the number of counts resulting from background light per second, Nd is the number of counts resulting from dark current per second and T is the measurement time (sec). The measures Nb, Nd can be experimentally measured when no "real" signal is impinging upon the photocathode. The number Ns can be calculated as the subtraction of Nb+Nd from the total number of counts.

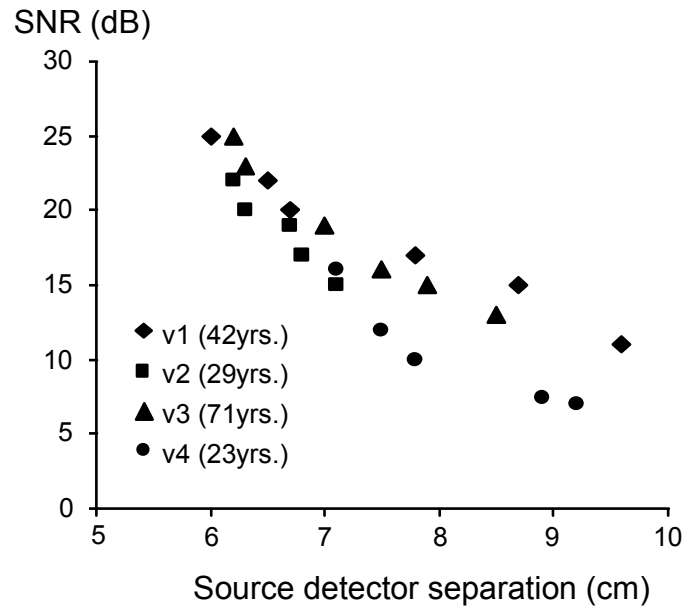

Figure 7-13: Signal to noise measurements from 4 volunteers as a function of separation. The results depicted here are for 1 sec acquisition time. Averaging increases the signal to noise ratio by the square root of the acquisition time. Volunteer 1 was African American and volunteers 2,3 and 4 were Caucasian.

The results demonstrate satisfactory signal to noise ratios even for separations up to 10 cm, especially considering that these results can improve by increasing the acquisition time. Furthermore the measurements did not show significant variation for the different ages

or skin color in terms of the SNR achieved. Neither the MR nor on the DOT scan encountered interference problems during the 4 trials.

7.4 Spectroscopic performance

We demonstrate the spectroscopic sensitivity, accuracy and inter-channel variations of the instrument using model measurements. Two types of models were used:

Similarly to the models used for tomography, the first type utilizes suspensions of Intralipid (Kabi Pharmacia , Clayton NC) emulsion and India Ink (3080-4 KOH-I-NOOR Inc. Bloomsbury NJ08804) diluted in water in a $40 \times 50 \times 60$ cm^3 "fish-tank". By diluting Intralipid the scattering properties (reduced scattering coefficient) of the model are controlled. Addition of India Ink changes the model absorption. For all measurements the sources and detectors were submerged into the solution using special holders in order to simulate infinite media.

The second model employed was a solid mold made of clear casting polyester resin (ETI Fields Landing CA). Titanium Oxide TiO_2 particles (SIGMA St. Louis MO) were suspended in the resin before the addition of catalyst. The particles furnish scattering properties to the model, while the addition of India ink adjusts the absorption. Thus appropriate molds can be constructed resembling specific tissue optical properties.

Figure 7-14 depicts a typical time-resolved curve through 0.5% intralipid solution for source-detector separation of 7 cm in transmittance geometry and the associated instrument function measurement. The high signal to noise ratio obtained in measurements like this allows very good fitting results that render the fitted curve and the real measurement virtually indistinguishable. The inset depicts the residual between the real measurement and the result of the fitting procedure.

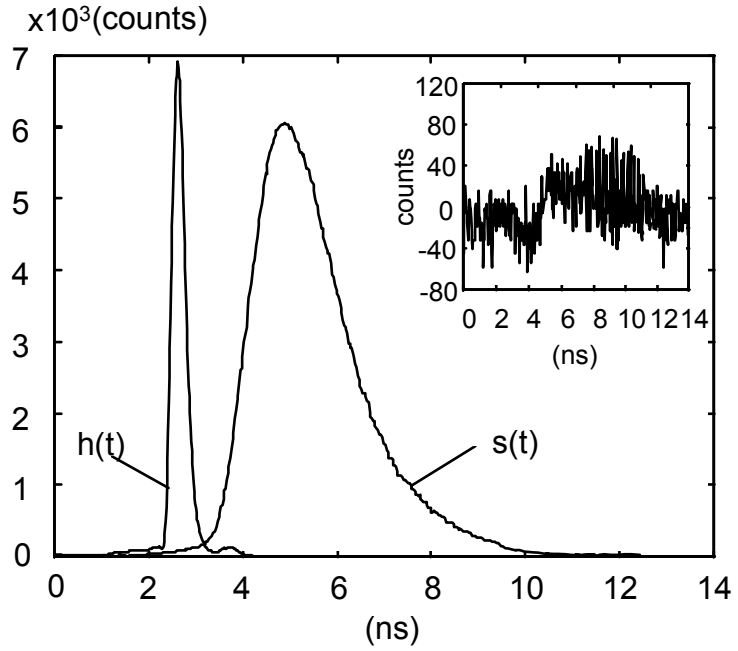

Figure 7-14: Time resolved curve s(t) aqcuired for a source detector separation of 7cm through 0.5% intralipid solution and the associated instrument function h(t). The inset shows the residual between the measured curve and the result of the fitting process.

7.4.1 Absolute absorption measurements

Figure 7-15a shows fitted μ_a and μ_s' values of a single source detector pair submerged into a 0.5% IL solution. The medium absorption changes are induced by adding 2.11μl of India Ink in every liter of 0.5% intralipid solution for every step. The extinction coefficient of the ink was measured in a photospectrometer (Hitachi U2000) and absorption coefficient values were calculated and plotted in the same figure. Both the calculated and fitted absorption values were due to water and ink absorption combined. The range of absorption values was selected to represent absorption properties found in human tissue

[117]. The deviation of absolute μ_a values from the theoretically calculated ones, especially in the higher absorption range, arises when the time resolved-curve FWHM becomes narrower and hence comparable to the instrument function width. Then the fitting procedure becomes more sensitive to convolution, time drift and jitter errors (see chapter 4). The reduced scattering coefficient is also plotted to demonstrate the observed cross talk of absorption changes to scattering changes. The observed cross-talk may be due to fitting errors.

7.4.2 Absolute scattering measurements

Figure 7-15b depicts experimental determination of changes of μ_s' as a function of scatterer concentration. In this experiment concentrated IL (20%) was added incrementally to a 0.5% IL solution in order to vary the scattering properties of the medium from 5 cm^{-1} to 13 cm^{-1}. No ink was added. The range of reduced scattering coefficients was similarly selected to be close to the typical values of human breast. Absorption coefficient values are plotted to demonstrate $\mu_a - \mu_s'$ cross-talk in the case of scattering changes. Again the observed cross-talk may be due to fitting error.

7.4.3 Quantification of absorption changes

Intralipid solution was used again to simulate the scattering background at $\mu_s' \sim 5$ cm^{-1}. A measurement obtained from the solution with no ink added constituted the baseline measurement. Subsequently small quantities of India ink (0.211 μL/L) were added to induce absorption increments of $\Delta\mu_a = 10^{-3}$ cm^{-1}. Absorption differences between the baseline and the subsequent measurements were calculated using Eq.(4-20) and the result is shown in

Figure 7-16 as a function of ink concentration. The experimental data verify the simulated data of Figure 4-14. The error of the experimental measurement is approximately double that of the simulation due to issues related with the amplitude stability of the laser.

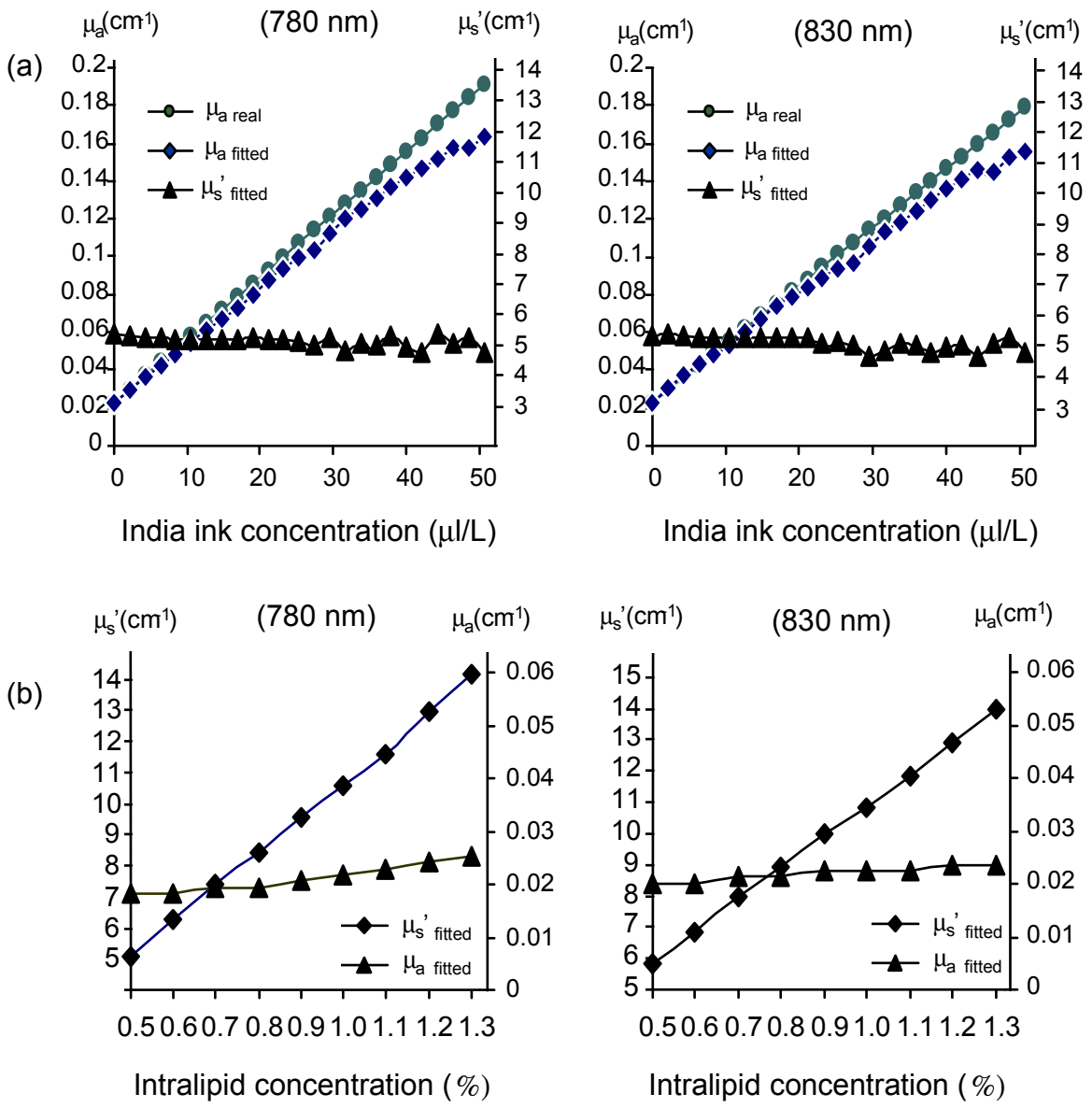

Figure 7-15: Experimental spectroscopic data on phantoms. (a) Measurement of absorption and scattering coefficient as a function of ink concentration in a .5% Intralipid- India Ink solution at 780 nm and 830 nm. (b) Measurement of scattering coefficient as a function of IL concentration. The background absorption is due to water. Absorption-scattering coefficient cross talk is probably due to fitting error.

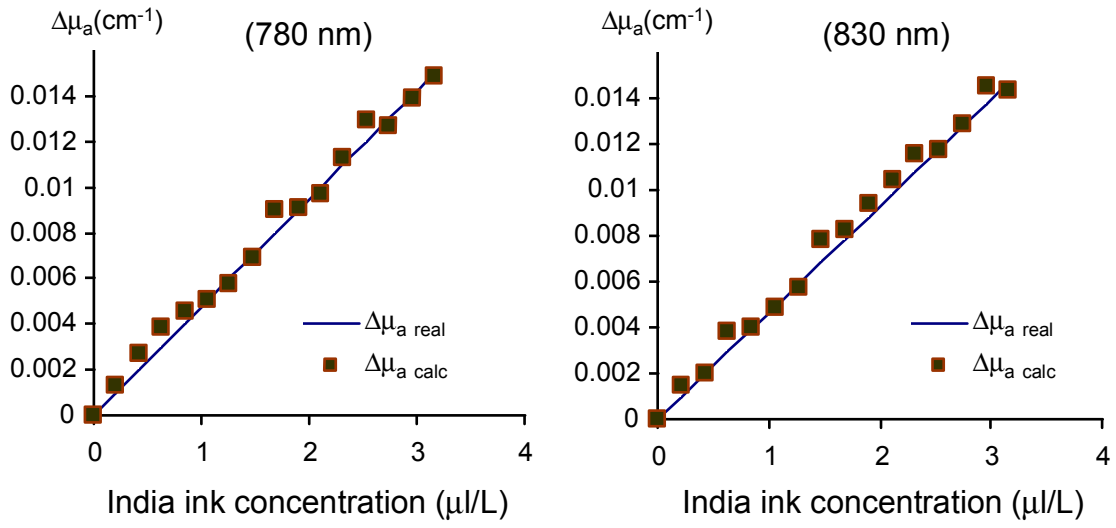

Figure 7-16: Measurement of absorption changes using Eq.(4-20) induced in a 0.5% Intralipid solution, by adding India Ink at 780 nm and 830 nm. Real absorption change values are derived theoretically from the ink extinction coefficient measured with a spectrophotometer.

7.4.4 Inter-channel variation

In order to examine the inter-channel variation we have performed measurements on a homogeneous resin model with μ_a=.05 cm^{-1} and μ_s'=8 cm^{-1} using reflectance geometry, using 7 sources and 4 detectors. Figure 7-17 depicts the scattering and absorption coefficient distribution calculated for all source-detector pairs used for the 780nm. Similar behavior is observed for the 830nm. Inter-channel variation is within ±5% of the mean calculated value for all channels, and within ±3% if only the short separation (and therefore good signal to noise ratio) pairs are considered.

Inter-channel variation was also examined when absorption differences were calculated using Eq.(4-20). In this case 7 sources and 4 detectors were employed in

transmittance geometry. The scattering medium was 0.5% Intralipid solution and 0.01cm^{-1} absorption changes were induced by adding India Ink as before. The absorption differences at 780nm, calculated for different channel, are plotted as a histogram in Figure 7-17c. Inter-channel variation in this case is below ±2%, which can be attributed solely to laser amplitude variations and signal to noise ratio.

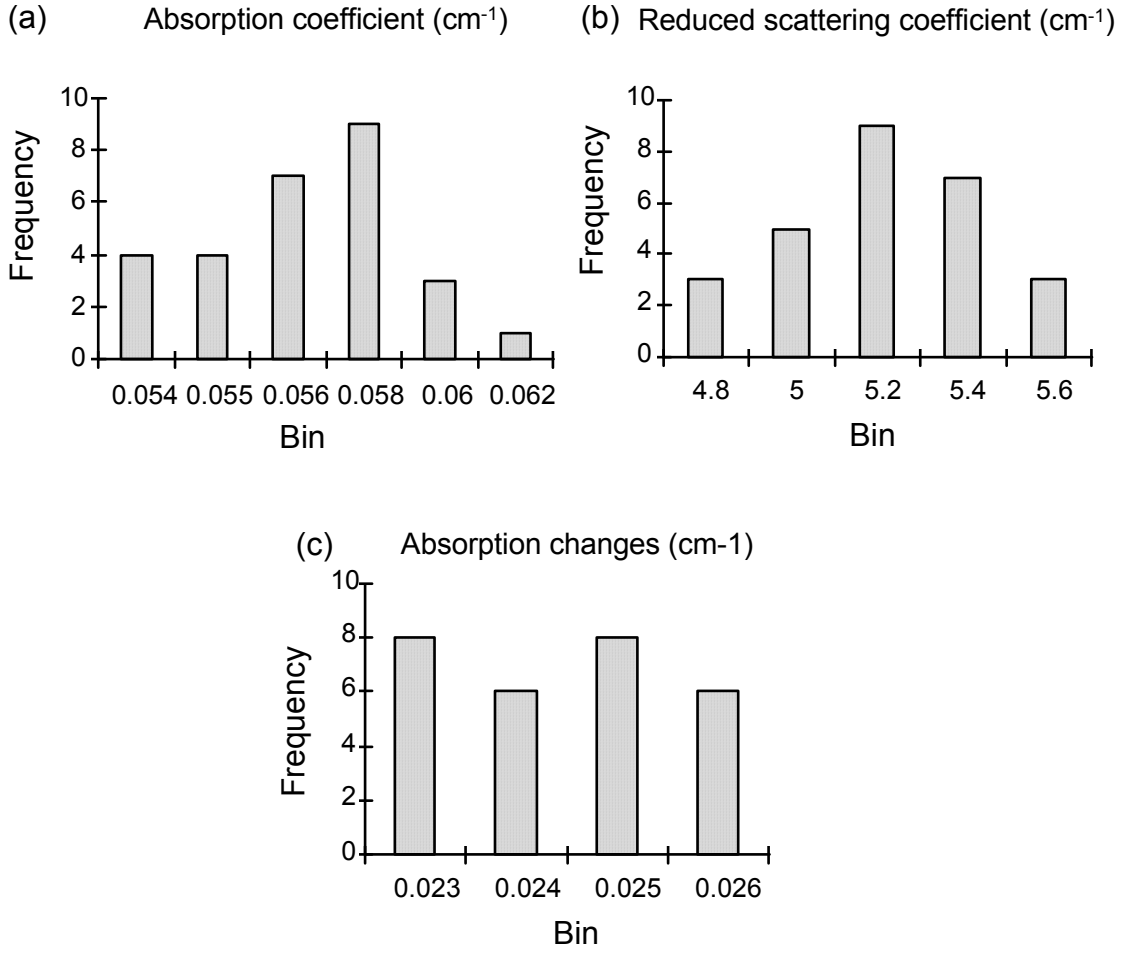

Figure 7-17: Inter-channel instrument variation in spectroscopic measurements. (a) Variation of absorption coefficient. (b) Variation of the scattering coefficient (c) Inter-channel variation in calculating absorption differences from an IL model.

7.5 Discussion

The diagnostic utility of a modality is often directly related to the resolution it can achieve. The imager developed has poor resolution compared to other modalities used in the radiological arena due to the diffuse nature of light, the experimental uncertainties and noise and the limited number of sources and detectors. However one has to consider the source of the contrast for the specific modality. In the case of cancer diagnosis the differentiating signatures are the increased blood volume, the hypoxic state of the lesion or the induced contrast due to the injection of a contrast agents [118]. Therefore there are novel distinguishing criteria that introduce new information to cancer diagnosis. It is not the anatomical and structural detail that is in pursuit but rather local functional characteristics of the volume under investigation. And the optical method seems quite sensitive in this role.

Clinical measurements induce impediments not present in the laboratory tests. Baseline measurements are a necessity in diffuse optical tomography (see §5.3). Measurements on models and phantoms provide an easy way to obtain baseline measurements as described above, because of the availability of a "background" medium. However breast measurements impel a difficulty. The easiest case is the one of extrinsic contrast since the measurement before the injection may be considered as the incident field. For imaging the oxygenation and vascularization state, measurements on a solid resin model with known optical properties, after the breast examination, is a possible method to obtain the reference signal. In this case the baseline may be obtained from a medium with different optical properties than the breast measured and potentially different geometry. Correction for the background optical properties and geometry differences may be required similarly to the method proposed in §5.4. (The method in §5.4 corrects only for absorption coefficient changes, but its modification to account for scattering and geometrical differences is straightforward as seen in §6.1.1). Such corrections however could introduce additional errors due to experimental uncertainties in the measurement of the properties required for the correction. Other methods where adjacent source detector pairs are used to obtain the incident field and self-calibrate the approach have also been proposed [55].

This chapter discussed the specifics of a time-resolved optical tomographer, developed for detection and calculation of local optical variations. The sensitivity of the instrument has been shown to be suitable for small optical signals expected from breast lesions. Localization accuracy within the geometrical limits of the selected reconstruction grid has also been demonstrated. Quantification of absolute absorption and scattering coefficients exhibits linear response for the range encountered in biological applications. The error of the absolute quantification has been found to be ± 5% and is attributed to laser jitter, photon dispersion in the detection system, experimental uncertainty and theoretical approximations. Quantification of absorption *changes*, under the assumption of invariable scattering background, has been shown to attain accuracy of the order of 10^{-3} cm^{-1}. The limitations here were mainly due to laser instabilities.

8 Clinical Implementation

This chapter serves as the link between the theory and instrumentation presented in the previous chapters and the simultaneous DOT-MR clinical study. Since 1997 the time-resolved imager developed (see Chapter 7) was coupled to the 1.5T HUP5 Magnetic Resonance Scanner of the Hospital of the University of Pennsylvania and studied 4 volunteers and 20 patients that had a suspicious X-ray finding. Some of the specific issues that made this study possible are presented in this chapter. **Section 8.1** describes the experimental protocol and its relevance to the theory of chapter 5 and chapter 6. **Section 8.2** describes the MR image retrieval and MR image processing and the specific software tools developed to obtain the MR-DOT coregistration.

8.1 Examination protocol

The simultaneous MR and DOT study and informed consent form were approved by the institutional review board, and the investigation was conducted in full compliance with the accepted standards for research involving humans. Except for control cases, patients entering the study had a previous suspicious mammogram or palpable lesion and

were scheduled for excisional biopsy or surgery. Written informed consent was obtained from all participants.

8.1.1 Magnetic Resonance Imaging

The MR studies were performed in a 1.5 T imager (Signa; GE Medical Systems, Milwaukee, Wis), version 5.4 software. The body coil was used as the transmitter and a custom-built multicoil consisting of four coils constructed on the two soft compression plates [111] served as a receiver.

Patient placement followed standard procedures used for the MR examination. The patient assumed the prone position (see Figure 7-2) with the breasts falling away from the chest wall and into an H-shaped coil holder as described in §7.1 . The two compression plates were positioned parallel to the sagittal plane and ensured contact of the optical fibers onto the tissue.

The simultaneous examination protocol is depicted in Figure 8-1. The MR imaging protocol consisted of i) an axial T1 spin-echo sequence SE (TR/TE 500/14 FOV 24) localizer, ii) a sagittal T1-weighted spin-echo sequence SE (TR/TE 500/14 FOV 16), iii) a sagittal T2-weighted, fat saturated fast spin-echo sequence FSE (TR/TE 5000/120 FOV 16) and iv) a sagittal 3-D, fat saturated gradient echo GRE sequence (TR/TI/TE 9.3/27/2.2, acquisition matrix 512x512 FOV 16 slice thickness 2.5-3). The last sequence (iv) acquired one pre-Gd and three post-Gd sets of images to investigate the Gd enhancement and kinetics. Gadolinium was administered intravenously at 0.1 mmol/kg.

The DOT examination protocol had two parts. The first part ran simultaneously with the MR protocol. First a measurement with the laser light off was performed to obtain dark current and background light noise. Then the light power was adjusted and all sources were scanned to obtain the breast baseline (SET I). During the post-Gd period the DOT protocol selected 6 sources close to the suspicious region and scanned them during SET II. This measurement acquired the *total field* $\phi'(\vec{r},\vec{r}_s,\omega)$ of Eq.(5-17). The selection of the

sources was based on the information for suspicious lesions produced by the post-gadolinium MR images. At the end of the MRI protocol, the first optical source of the chosen six was selected to continuously acquire data at ~10 sec intervals (SET III). Then a bolus of sterile ICG (SERB, France) was injected intravenously at 0.25 mg/kg. Three minutes after injection, a scan of the remaining 5 sources was performed (SET IV). Finally the input light was directed again to the first source for an additional 1 minute of data acquisition at ~10 sec intervals (SET V). The measurements of SET IV and the first measurement of SET V acquired the total field $\phi''(\vec{r},\vec{r}_s,\omega)$ of Eq.(5-19). The overall examination lasted 25 min (20 min for MRI/DOT and 5 min for ICG-enhanced DOT). At the end of the examination protocol a calibration optical measurement was acquired for all sources on a specially constructed resin model with typical optical properties and dimensions of a human breast (SET VI) that can be used in combination with SET I to image intrinsic breast optical properties.

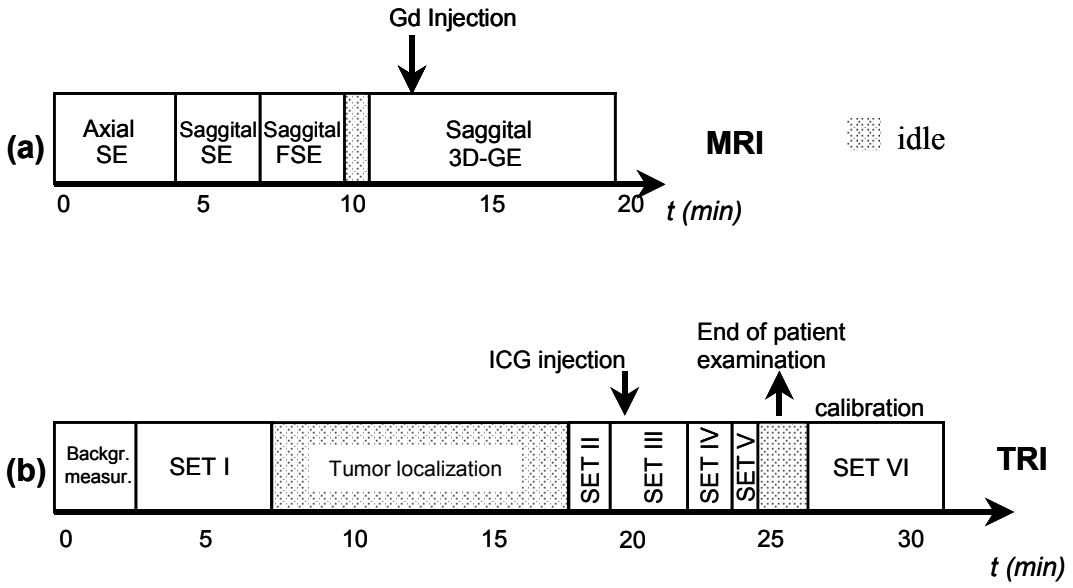

Figure 8-1: Examination Protocol for the simultaneous DOT-MRI study.

8.1.2 MR Image Retrieval

MRI images were retrieved from the research MRI scanner HUP-5 of the Hospital of the University of Pennsylvania using the General Electric GINX X-windows software tool. The images were transferred in accordance with the privacy and security guidelines suggested by the department of Radiology of the Hospital of the University of Pennsylvania and stored for processing on a Windows NT based workstation.

According to the MR protocol described above and in Figure 8-1, four sets of images are obtained from the MR examination as follows:

a) One set of 256 x 256 axial localization T1-weighted Spin Echo multi-slice images with ~5mm slice thickness

b) One set of 256 x 256 sagittal anatomical T1-weighted Spin Echo images with ~3 mm slice thickness.

c) One set of 256 x 256 sagittal fat-suppression T2-weighted Fast Spin Echo multi-slice images with ~ 4mm slice thickness

d) One set of 512 x 512 sagittal 3-D gradient echo images with ~3mm slice thickness before Gd injection and three similar sets following Gd injection.

8.2 Coregistration

Coregistration with the MRI images was a key feature of the aims of this study. DOT needed to be validated with the underlying structure, pathology and functional activity of the tissue under investigation. The simultaneous examination allowed for the direct comparison of NIR and MR contrast under the exact same geometry and physiological conditions. Furthermore image coregistration was by definition needed for the use of the MR a-priori information according to the theory described in §5.6. Breast is an organ of high plasticity and it is very likely that non-simultaneous examinations will not be geometrically accurate for such an approach.

Coregistration is based on the H_2O-$CuSO_4$ filled fiducials mounted on the compression plates as described in §7.1. Those fiducials appear on the MR images as bright spots, shown in Figure 8-2. The center of the fiducials is retrieved via image post-processing, usually on the GRE images that offer the highest resolution of the study. To perform the coregistration, specific software tools were developed. The code was programmed in C and C++. The program can load a clinical examination and allows the user to interactively identify the fiducials on the MR images and define the reconstruction mesh, lesions of interest and perform simple image processing tasks. Some of the features are more analytically described below.

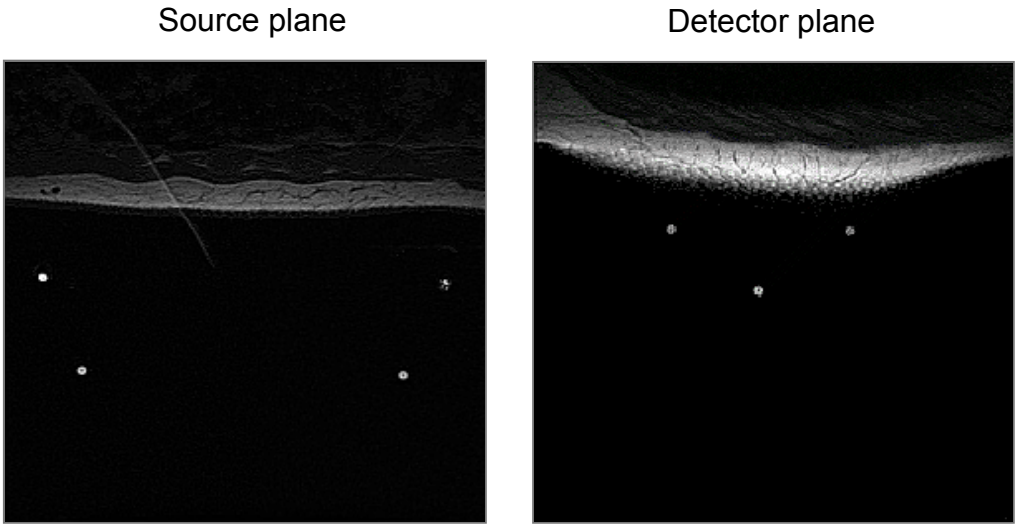

Figure 8-2: Appearance of the compression plates' fiducial markers on MR images.

8.2.1 Geometry Assignment.

Figure 8-3 shows the appearance of the software with a clinical examination loaded and the main control panel called " Image Analysis ". The image here is shown negated: the $CuSO_2$-H_2O fiducials appear as dark spots. The user can select these spots with the mouse in order to input their position in the 3-dimensional space. The process is performed for the

source and detector plane. The software automatically then calculates the position of the sources and detectors relative to the breast.

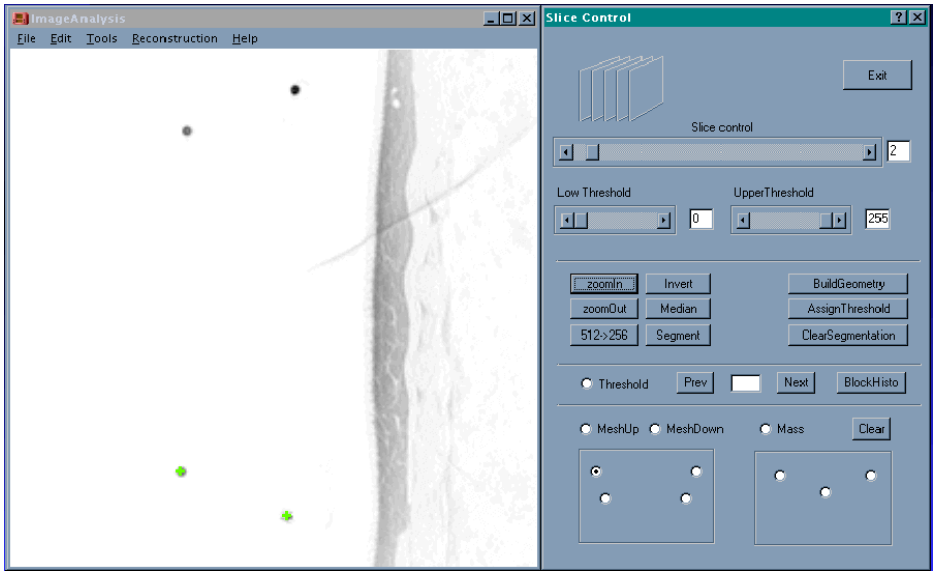

Figure 8-3: Image analysis software tool used for geometry retrieval and for constructing the DOT, DOS and localized DOS forward problem (screen 1).

Figure 8-4 shows a slice taken from the middle of the breast. The position of the sources and detectors has been calculated and is superimposed on the image (the triangles indicate sources and the circles indicate detectors). The user can also interactively define the volume to be reconstructed and the mesh parameters. Although semi-automatic segmentation can be performed, as will be described in the next paragraph, the user can also manually identify lesions of interest that are stored as special structures and can be later fitted for optical property retrieval (when the MR-apriori information is used). Therefore all the geometrical parameters are calculated and can be stored.

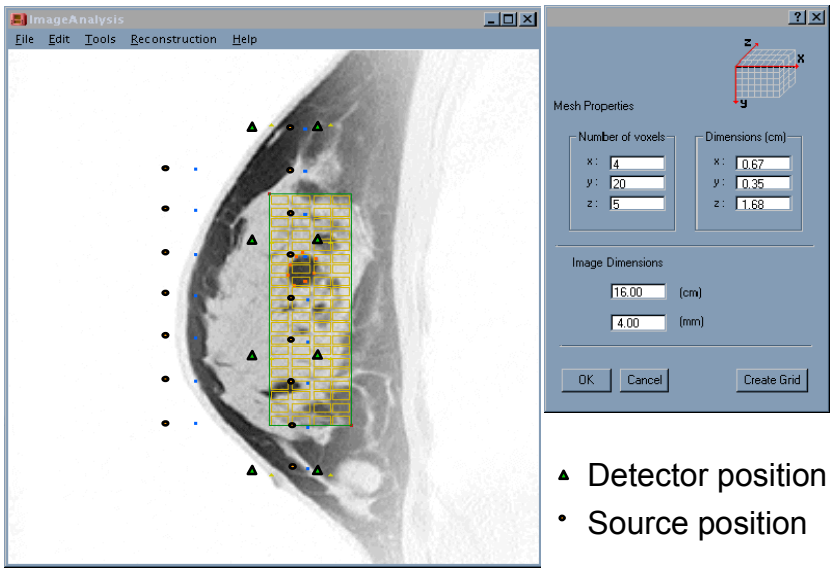

Figure 8-4: Image Analysis Tool (screen 2). The mesh properties and suspicious lesions can be manually chosen by the user.

8.2.2 Segmentation.

MR image segmentation or feature extraction is needed for the purposes of using the MR a-priori information as described in §5.6. The software developed can aid in segmenting basic breast tissue structures, such as skin, adipose, glandular and parenchymal tissue based on intensity information. Smaller, more specific tissue structures, such as suspicious masses or veins can be assigned manually.

Feature extraction, based on the anatomical information of the MR images, is performed under the assumption that same types of tissue will have brightness (intensity) levels very close to each other. This assumption works reliably when the MR field and the radio-frequency excitation and detection are fairly homogeneous so that the MR images do not have *intensity variations*. However it is common that intensity variations along the image

arise, especially due to radio-frequency field inhomogeneity. When this occurs the images are treated with an algorithm that is described in the following subsection. We note that multilevel thresholding is quite rudimentary for high-resolution highly specific segmentation, but quite efficient for the DOT a-priori use requirements.

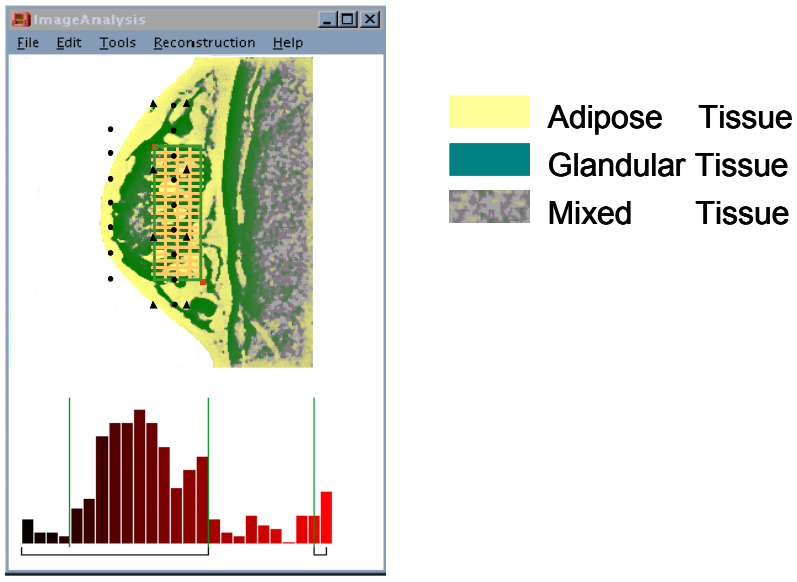

Figure 8-5: Automatic segmentation result using the Image Analysis Tool. Segmentation was performed based on MR-image intensity information after any intensity variations along the image are treated using image processing tools (see next subsection).

Multi-level thresholding is employed for tissue differentiation on the sagittal spin-echo images (MR set 2). Analysis of the FSE images can provide more detailed information about the underlying structure since fat suppression usually reveals in more detail the glandular infrastructure but were not used in this work. Finally with the aid of the GRE sets the suspicious lesions can be identified based on their Gd-enhancement and introduced to the segmentation process manually. The user has the ability to identify certain areas of choice to be treated as different tissue types. This gives the flexibility to manually interfere

and indicate areas where it is postulated that special care should be taken as in the case of veins, or areas that look suspicious but were not retrieved by the automatic segmentation process. In practical terms the code groups together all the MR image voxels that belong to the same DOT mesh voxel and creates a histogram of the average intensity of each group. Obviously the total number of incidences in the histogram equals the number of DOT voxels. Then thresholding is assigned by indicating cut-off points on the histogram, as shown in Figure 8-5 where the segmentation result for one case is presented as it appears on the computer screen. The x-axis of the histogram is intensity value (0 to 255). The histogram is calculated for the whole volume, not just the slice shown. In this example three structures have been segmented: adipose tissue, parencymal tissue and mixed-type tissue, which indicates voxels that contained both tissue types. The right most part of the histogram corresponds to noise.

Segmentation is combined with the results of the geometry assignment process to create the geometrical description of the volume of interest, the underlying structures and the tomographic arrangement. This information can be used for tomography or localized MR-guided spectroscopy as described in the following chapter.

8.2.3 Intensity Correction

Intensity correction is a very important process to ensure that the multi-level thresholding, which was described in the previous paragraph, will work efficiently. Intensity correction procedures have been employed to treat MR images that appear to have slice to slice or interslice intensity variations. Two types of intensity correction are performed on the MR images using routines developed under the Matlab environment (Mathworks MA).

The first intensity correction occurs at the single slice level and accounts for intensity variations along the slice. The intensity correction is applied on median filtered images (to reduce shot noise) and uses the rank leveling procedure [119]. After this step has been completed for all slices, the second intensity correction is performed in the inter-slice level where all slices of the set are corrected to the same average intensity level based on the

histogram properties. This second intensity correction is also applied on median filtered images, followed by noise level subtraction for each individual slice and finally by aligning the peaks of the intensity histograms between all slices. Finally histogram equalization is applied to the 3D image-set to enhance the contrast between adipose and parenchymal tissue. An example of the effect of the correction process is shown for a single slice in Figure 8-6.

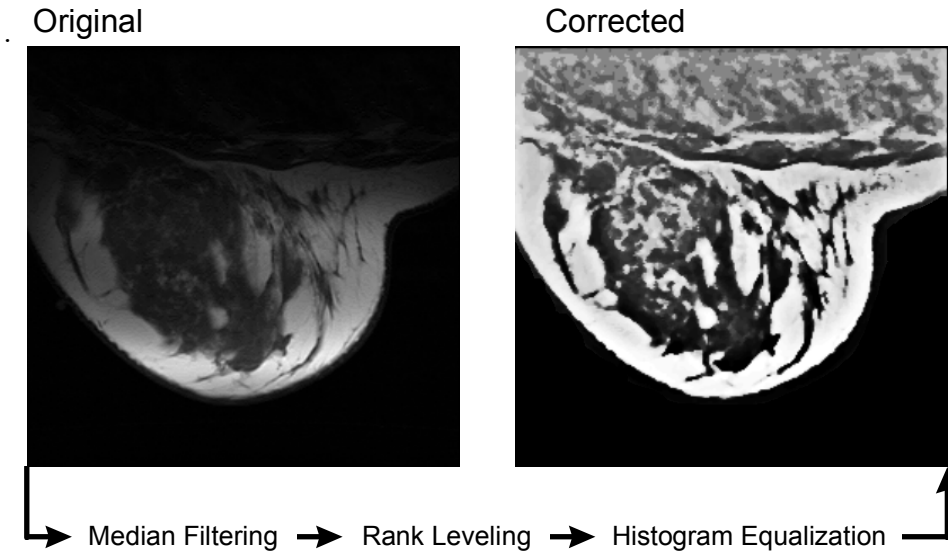

Figure 8-6: An example of correcting intensity variations along an MR sagittal image of the breast.

9 Clinical Results

This chapter presents the results of the concurrent MRI-DOT study. The purpose of this study was two-fold. The first goal was to examine the feasibility of DOT to image the breast. Since the accurate coregistration of images was implicit (see chapter 8) an exact validation of the spatial occurrence of lesions could be performed. The use of vascular contrast agents for both modalities guaranteed that a physiological validation could be performed as well. The second goal was to create a hybrid modality. The structural and physiological information from the MRI could be implemented in the DOT inversion problem to simplify it and increase its quantification accuracy. Therefore the simultaneous examination could provide supplementary information to the MRI readings for lesion characterization.

This chapter is divided in four sections. **Section 9.1** presents average optical properties of the intrinsic and ICG-enhanced breast and average hemoglobin concentration and saturation are obtained. These optical properties are plotted as a function of age and may serve as the baseline or typical sample of the normal breast. **Section 9.2** shows coregistered DOT and MRI images of the same volume and demonstrates the feasibility of

DOT to image the ICG-enhanced breast. Images of intrinsic contrast are also shown. **Section 9.3** demonstrates the results obtained by implementing the a-priori MR information in the DOT inversion problem to obtain optical properties of intrinsic and extrinsic contrast of specific lesions. Finally **section 9.4** presents some specific cases of particular interest and gives an insight for the use of ICG for breast cancer detection.

9.1 Spectroscopic measurements

This section focuses on the average optical properties of the breast with and without indocyanine green enhancement. These measurements have been collected from patients and volunteers that participated in the clinical study. Most of the measurements have been performed at 780nm and 830nm wavelengths. A recent addition of a third wavelength in the summer of 1999 made some measurements in the 690nm possible as well. The average optical properties of intrinsic contrast in two or three wavelengths are converted to hemoglobin concentration and saturation values.

In general the average optical properties are an integral part of the tomographic approach. This issue was described in chapter 5. Additionally, the presentation of average optical properties and of hemoglobin volume and saturation aims in identifying the baseline or "typical" NIR properties of the breast for later comparison with diseased tissue. In general, average optical properties are minimally affected by the optical contrast of a localized tumor. This is because diffuse photons sample a large volume of healthy breast tissue; the localized tumor, if present, constitutes only a small fraction of this volume. Here, particular care was taken so that the measurements used for the calculation of average optical properties were not in the vicinity of diseased regions so that the influence of diseased tissue in the calculation of average optical properties was further reduced. Therefore these measurements describe the average properties of the healthy breast tissue

9.1.1 Intrinsic contrast

The absorption and reduced scattering coefficient of intrinsic contrast are calculated by fitting the time-resolved curves to the time-domain solution of the diffusion equation for transmittance geometry. This methodology was analytically described in Chapter 4. The time parameters K1 and K2 of the fit used in this data analysis were selected as shown in Figure 9-1. The fitting process includes only the later parts of the time-resolved curves because this was found to reduce time uncertainty errors (see §4.4.5).

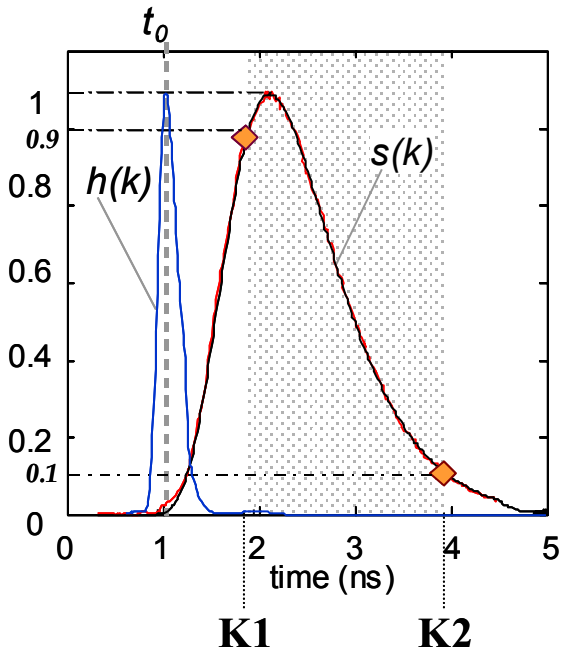

Figure 9-1: Fitting scheme selected for the spectroscopic analysis of the breast time-resolved measurements. Only the latter parts of the time-resolved curve were fitted because this offers higher quantification accuracy.

In order to calculate the average optical properties of each breast scanned, measurements from different locations of the breast (different source-detector pairs) were fit independently. Then the optical properties found were averaged to yield a single absorption coefficient and single reduced scattering coefficient per breast and per wavelength. Typically

10 to 15 different time-resolved curves per wavelength were fit for each breast. The absorption coefficients calculated from 21 patients and volunteers (for the 780nm and 830 nm) are shown in Figure 9-2 and the reduced scattering coefficient from the same examinations in Figure 9-3. The 690nm wavelength was added and used only in the last four examinations.

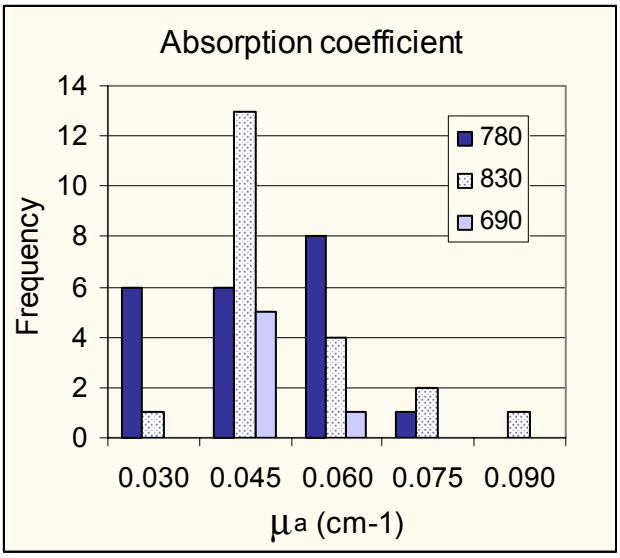

Figure 9-2. Histogram of the absorption coefficients at 780nm and 830 nm obtained from 21 patients and volunteers examined by the simultaneous MRI-DOT. Measurements of the absorption coefficient at 690nm were obtained from four patients.

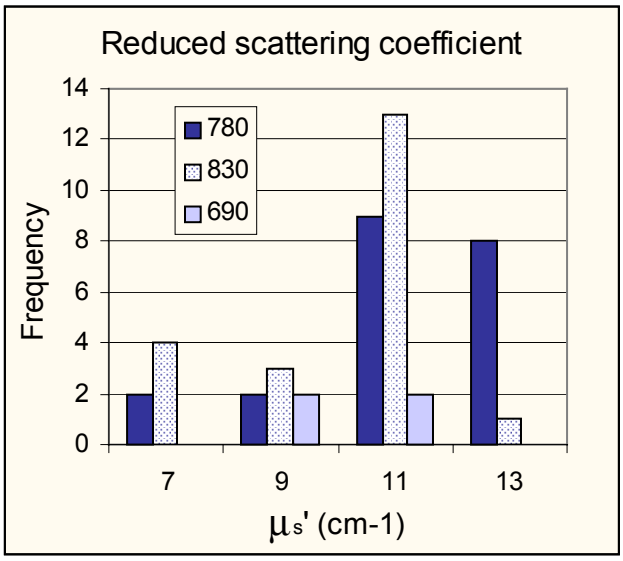

Figure 9-3: Histogram of the reduced scattering coefficients at 780nm and 830 nm obtained from 21 patients and volunteers examined by the simultaneous MRI-DOT. Measurements of the reduced scattering coefficient at 690nm ware obtained from four patients.

The mean and standard deviation of the μ_a at each wavelength for the 21 patients and volunteers examined are tabulated in Table 9-1 and for the μ_s' in Table 9-2. Generally the absorption coefficient of all wavelengths is around 0.04cm^{-1} and the reduced scattering coefficient around 10cm^{-1}. This result offers a practical advantage. Since the optical properties of the healthy breast have similar values in 690nm, 780nm and 830nm, the signal attenuation is also similar in all wavelengths. Hence the dynamic range of the instrument is not compromised while sensitivity to deoxy-hemoglobin is enhanced due to the 690nm light.

Table 9-1: Mean and standard deviation of the breast absorption coefficient (21 subjects).

μ_a	Mean (cm^{-1})	Standard Deviation (cm^{-1})
690 nm (only 4 patients)	0.041	0.005
780 nm	0.041	0.012
830 nm	0.043	0.014

Table 9-2: Mean and standard deviation of the reduced-scattering coefficient (21 subjects).

μ_s'	Mean (cm^{-1})	Standard Deviation (cm^{-1})
690 nm (only 4 patients)	10.25	0.54
780 nm	11.02	1.77
830 nm	9.96	1.47

9.1.2 Average Hemoglobin Concentration and Saturation

In order to calculate the hemoglobin concentration and saturation from the absorption coefficient calculations that were presented in the previous sub-section, we use the relationship

$$\mu_a^\lambda = \varepsilon_{HB}^\lambda \cdot [HB] + \varepsilon_{HB02}^\lambda [HBO_2] + \mu_{a,back}^\lambda , \qquad \textbf{(9-1)}$$

where μ_a^λ is the absorption coefficient at wavelength λ, [HB] is the concentration of deoxy-hemoglobin, [HBO_2] the concentration of oxy-hemoglobin and $\mu_{a,back}^\lambda$ is the absorption coefficient of water and lipids at wavelength λ. Obviously, Eq.(9-1) assumes that other chromophores besides the HBO_2, HB and H_2O have insignificant contributions to the overall absorption coefficient. The absorption coefficient of water and lipids can be generally obtained from the literature or measured experimentally on phantom measurements [77,121] and is used as a constant. For L number of wavelengths one can construct a system of L equations with two unknowns (the concentrations of oxy- and deoxy- hemoglobin) that can be inverted (for L=2) or fitted (for L>2). In principle, for L number of wavelengths one can solve for L unknown chromophore concentrations. For example for L=3 the water absorption coefficient could also be solved for. However, similarly to the results presented in §6.3 the utilization of three wavelengths to fit for two unknown chromophore concentrations reduces the influence of random noise in experimental uncertainties. This is the reason that Eq.(9-1) was used as is, even when 3 wavelengths were available.

Figure 9-4 depicts the hemoglobin concentration [H]=[HB]+[HBO2] and Figure 9-5 the hemoglobin saturation Y=[HBO2]/[H] calculations for the patients and volunteers examined as a function of age. Both [H] and Y have a weak, inverse dependence on age shown with the straight line fitted through the measurements (linear regression). This is consistent with the fact that the aging breast substitutes glandular tissue with adipose tissue, thus reducing the vascularization and evidently also its oxygenation. Saturation and hemoglobin concentration may be affected by the patient placement on the experimental set-up. Although care was taken to ensure minimal breast compression, (only to obtain fiber contact with the tissue), it is possible that patient placement against the bed could obstruct blood vessels and have an effect on hemoglobin concentration and saturation. This could explain that one of the measurements yielded a very low saturation value. This measurement was excluded from the regression and other aggregate calculations. Table 9-3 tabulates the mean and standard deviation of the hemoglobin concentration and hemoglobin saturation calculated from the cases examined.

Table 9-3: Mean and standard deviation of the Hemoglobin Saturation and concentration (21 patients).

	Mean	Standard deviation
Saturation Y	0.69	0.06
Hemoglobin Concentration (mM)	0.017	0.053

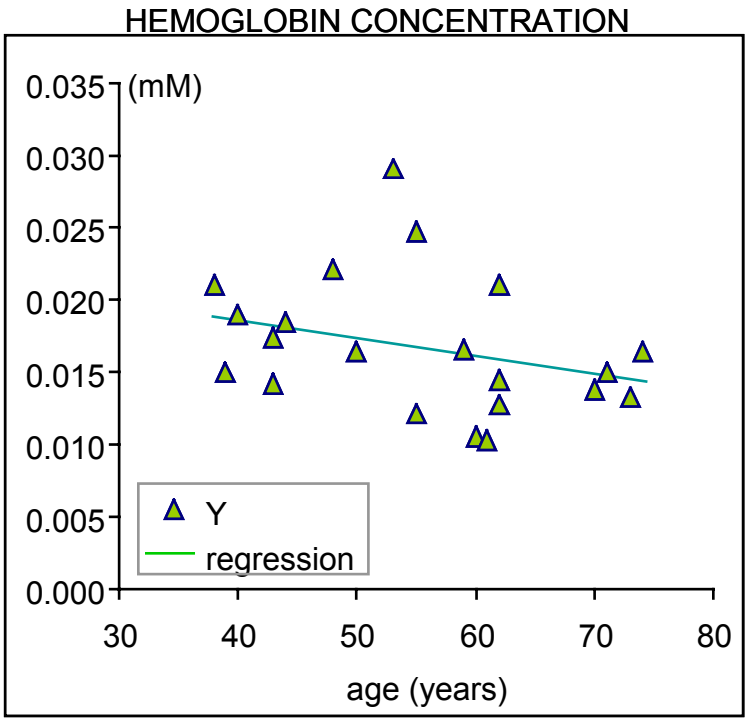

Figure 9-4: Breast hemoglobin concentration from 21 subjects as a function of age.

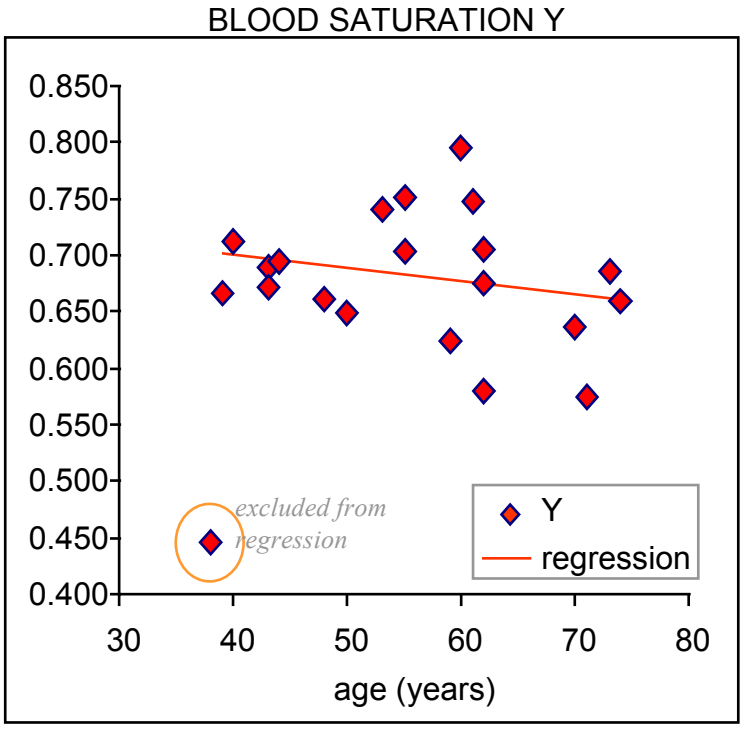

Figure 9-5: Breast hemoglobin saturation from 21 subjects as a function of age.

9.1.3 Extrinsic contrast

The absorption coefficient increase after contrast agent enhancement was obtained using the methodology of §4.5, which allows the quantification of absorption changes in diffuse media with an accuracy of 10^{-3} cm^{-1}.

Figure 9-6 depicts the typical absorption coefficient increase of the breast due to the intravenous administration of 0.25mg of ICG per kg of body weight as a function of time. Shortly after the administration of the contrast agent, a rapid absorption increase is measured in the breast due to the distribution of the dye intravascularly. In less than a

minute the absorption coefficient reaches a maximum. After this point the ICG concentration in the intravascular compartment is cleared exponentially via the hepatobiliary pathway [120].

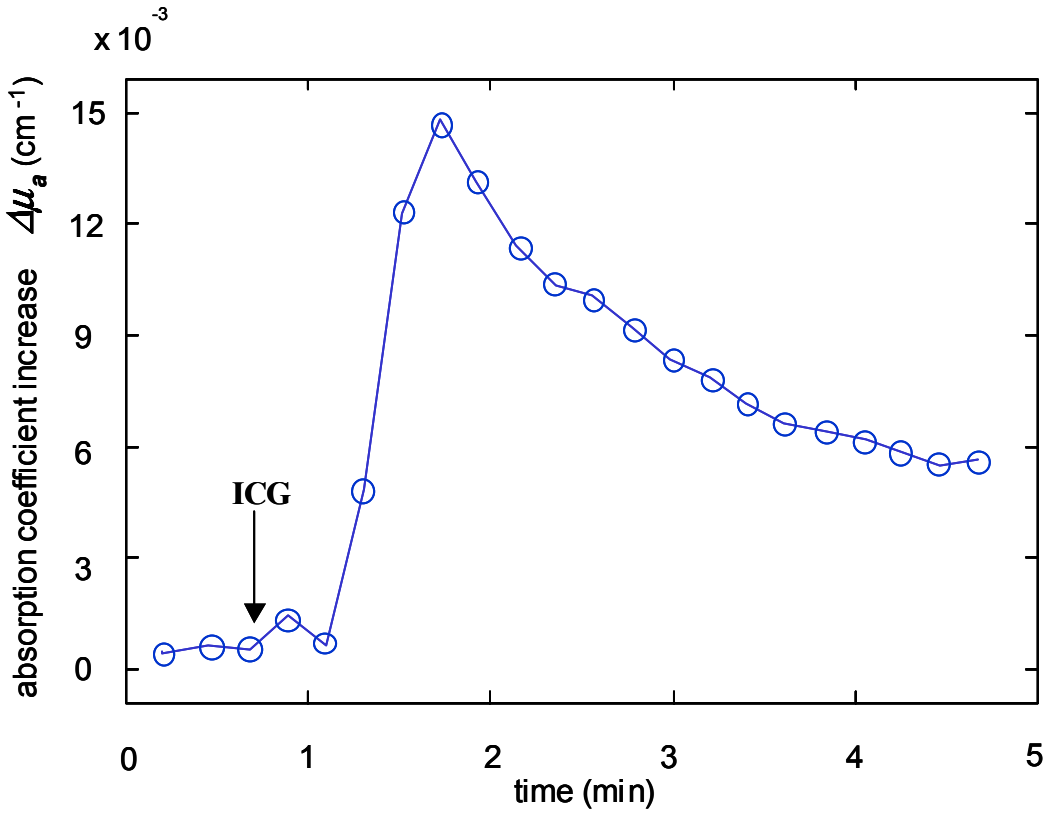

Figure 9-6: Typical breast absorption increase as a function of time due to the administration of Indocyanine Green (ICG).

The ICG-induced average absorption increase per breast studied was obtained similarly to the approach used to yield average measurements of intrinsic contrast. Specifically for each breast, 10-15 calculations were performed for different source-detector pairs using Eq.(4-20) and the results were averaged to yield a single mean absorption coefficient change measurement as a function of time. Figure 9-7 shows the histogram of the

maximum average absorption increase for the cases studied. The average absorption increase obtained was 0.012 cm^{-1}. The standard deviation of these measurements was 0.009cm^{-1}.

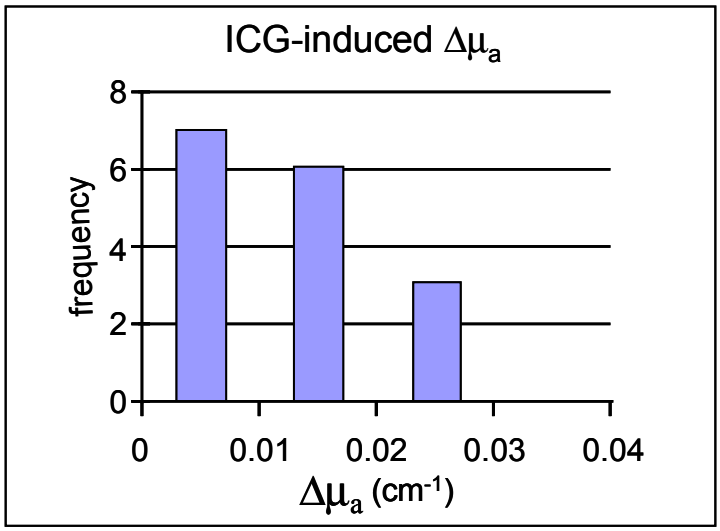

Figure 9-7: Histogram of the absorption coefficient increase due to ICG injection obtained from 16 patients.

Figure 9-8 depicts the maximum average absorption increase due to the ICG administration as a function of age for the cases studied. Similar to Figure 9-4 and Figure 9-5, there is an inverse dependence of absorption increase on age. A first hypothesis would be that since ICG is an intravascular contrast agent, it is expected that it will distribute less in the aging breast, which appears less vascular. However the ICG measurement samples the breast vascularization in a relative and not in an absolute manner as in the case of hemoglobin concentration calculations (assuming fairly constant hematocrit). The ICG is injected in a vascular pool that naturally varies in different women. Although the ICG dose administered scales with body weight to compensate for the varying total blood volume with body size, the exact blood volume of each patient or volunteer is not known. Hence the average ICG concentration measurement (via the absorption coefficient measurement) depends on the ratio of the breast blood volume to the total blood volume of the body and

not only on the absolute breast vascularization. Therefore the measurements in Figure 9-8 are indicative of a combined effect of changes in breast vascularization and of the ratio of breast volume to total body blood. Figure 9-9 depicts the correlation of the hemoglobin concentration measurement with the ICG-induced absorption increase measurement. As expected no perfect correlation is observed. The correlation coefficient between the two measurements is a=0.73. Obviously this correlation coefficient value is also affected from hematocrit fluctuations and experimental noise. If we could determine some of the unknown parameters (total blood volume or hematocrit), the composite ICG - hemoglobin concentration measurement from the same breast can be used to determine an additional parameter of interest.

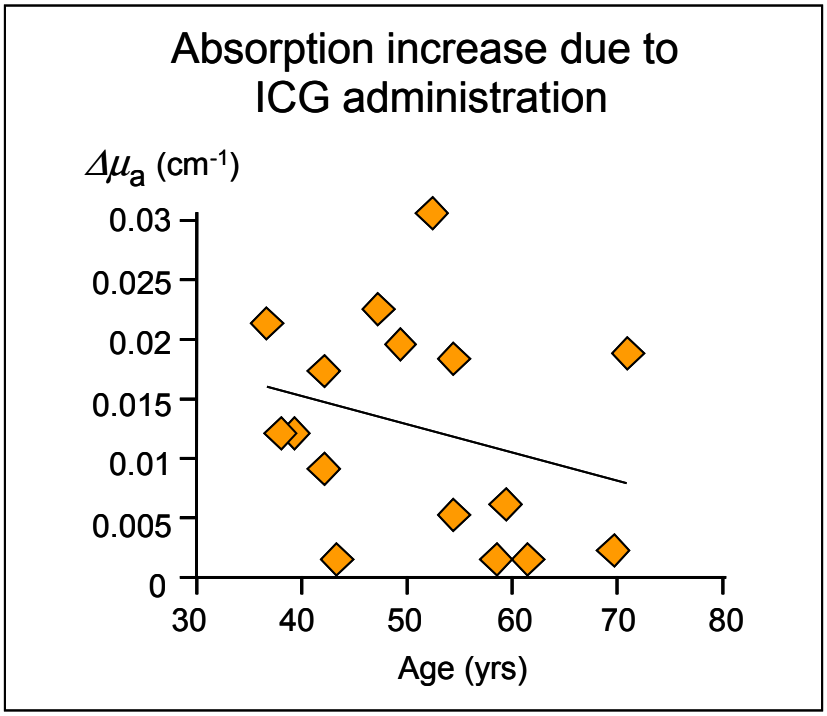

Figure 9-8: Breast absorption increase due to ICG administration as a function of age.

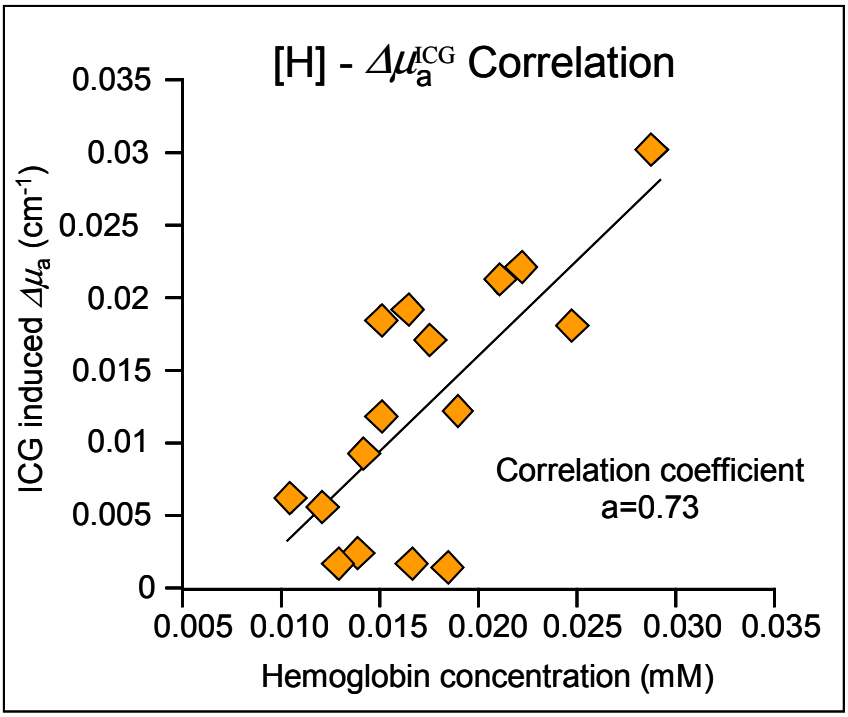

Figure 9-9: Correlation between the ICG-induced absorption coefficient increase and the hemoglobin concentration of the same breast calculated for 16 patients (each point corresponds to one patient)

9.2 Concurrent MRI and Diffuse Optical Tomography of Breast following Indocyanine Green enhancement.

Quantitative optical images of human breast in-vivo are presented. The images were obtained using diffuse optical tomography (DOT) following the administration of Indocyanine Green (ICG) for contrast enhancement. The results are compared with the concurrently obtained Magnetic Resonance images of the same breast. Histo-pathological

information of the suspicious lesions was available since the patients that participated in the study were scheduled for biopsy.

Three cases are shown: a ductal carcinoma, a fibroadenoma and a control study with no suspicious enhancement. The aim was to validate the efficiency of DOT for imaging breast and breast cancer and to demonstrate features of contrast enhanced DOT. The ICG enhanced images reveal good congruence with the Gd-enhanced MR images. Contrast agent uptake exhibited differentiation between disease and other structures. In contrast to simple transillumination, it is shown that DOT provides for localization and quantification of exogenous tissue chromophore concentrations. Thus the capacity to use DOT with existing vascular contrast agents or engineered contrast agents that target cancer or probe specific functionality was demonstrated in-vivo.

9.2.1 Reconstructions

The tomographic approach used is based on the analysis of §5.4 where correction for the average absorption increase of the breast due to the ICG injection is performed. This method was shown in §6.1 and §6.2 to produce more accurate images of diffuse media. The reconstructions performed in this study use five frequencies (80, 160, 240, 320 and 400 MHz) and the real part of the matrix of Eq.(5-9). The real part is an amplitude measurement and is affected by laser amplitude variations. The imaginary part is a phase measurement and is affected by time uncertainty. In the system used, amplitude variations were significantly lower than time-uncertainties compared to the corresponding amplitude and phase contrast expected from breast structures. Therefore the real part had superior signal-to-noise ratio characteristics compared to the imaginary part and for that was selected alone for the reconstructions.

Matrix inversion is based on the method of projections with relaxation parameter λ=0.1 and 500 iteration steps. In this case the number of iterations was chosen after calibrating the algorithm with phantom measurements and was kept constant for all cases. Since minimal change in the scattering properties of the breast is expected following ICG

injection, the diffusion coefficient differential perturbations were set to zero. Furthermore to facilitate quantitative comparisons between the DOT images obtained from different patients, similar volumes were reconstructed and the voxel size was kept constant, i.e. 0.3 × 0.4 × 1 cm^3. All reconstructions shown are done for a 1cm thick slice, perpendicular to the compression plates (coronal plane), passing through the suspicious lesion.

9.2.2 NIR data pre-processing

Data pre-processing consisted of three steps:

1) During the first step standard median filtering was applied to all time resolved curves, followed by subtraction of the dark current and ambient light photon count (obtained prior to SET I).

2) In the second step a *correction* was effectively applied to the *total field* $\phi''(\vec{r}_s, \vec{r}_d, \omega)$ to account for the μ''_{a0} change as a function of time, due to the clearance of ICG from the plasma. This normalization is critical because different sources are "on" at different times, while ICG is clearing. Figure 9-10 shows the average change in μ''_{a0} from a 50-year-old patient after ICG administration. The measurement is obtained during SET III and SET V for a single source-detector pair. The μ''_{a0} change calculation is based on an algorithm [121] developed specifically to monitor absorption changes with an accuracy of 10^{-3} cm^{-1} (see §4.5). The area in gray indicates the time allocated to SET IV. The *correction* normalizes all data acquired during SET IV to correspond to the absorption level of the first point of SET V. For this purpose the absorption coefficient $\mu''_{a0}(i)$ $(i = 1..5)$ was calculated at each of the five time points during SET IV (i.e. the open circles in Figure 9-10) using linear interpolation between the last points of SET III and the first points of SET V. Each circle defines the temporal midpoint of the acquisition period allocated to a particular source. Although the ICG clearance from the plasma follows an exponential decay, linear interpolation suffices to predict the μ_a values for the small time interval of SET IV. The $\mu_a(i)$ at each of the points was used to derive a signal intensity $T_i = T_i(t, \mu''_{a0}(i), D''_0, |\vec{r}_s - \vec{r}_d|)$ using the time-domain

diffusion equation solution for slab geometry. Then letting T_6 be the calculated intensity for the first point of SET V with absorption coefficient $\mu''_{a0}(6)$, five correction factors a_i were calculated; $a_i = max(T_6)/max(T_i)$. The a_i were multiplied with the amplitude of the time-resolved curves T_i acquired at each point i. The calculation was done for each patient separately by constructing a graph like the one of Figure 9-10.

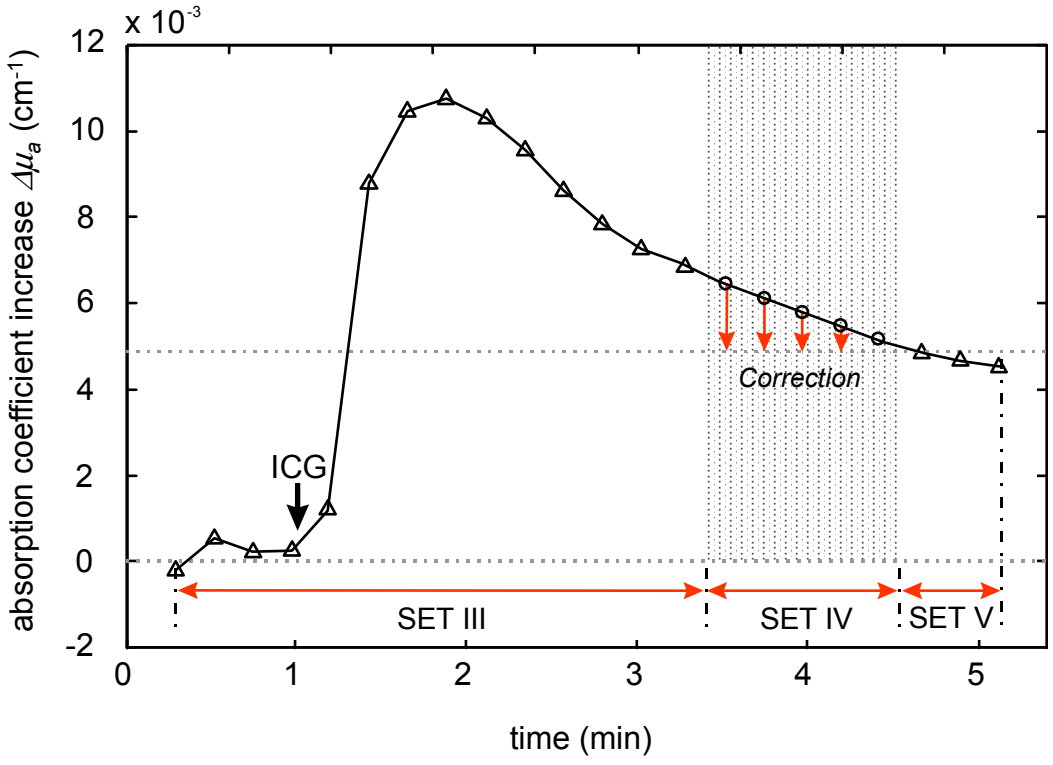

Figure 9-10: Absorption coefficient change in breast due to ICG administration and corresponding scans used for imaging and localized DOS purposes.

3) The third step calculated the relative scattered field Φ_{sc} in Eq.(5-21), at each frequency ω. The total fields $U''(\vec{r}_s,\vec{r}_d,\omega)$ and $U'(\vec{r}_s,\vec{r}_d,\omega)$ were obtained at each frequency ω by Fourier transforming the time resolved curves of SET II and the corrected time-resolved

curves of SET IV respectively. The incident fields $U_0''(\vec{r}_s,\vec{r}_d,\omega)$, $U_0'(\vec{r}_s,\vec{r}_d,\omega)$ were theoretically obtained using the frequency-dependent solution of the diffusion equation (Eq.(3-36)) for an infinite slab using the post-ICG (μ_{a0}'', D_0'') and pre-ICG (μ_{a0}', D_0') background optical properties. The values μ_{a0}'', D_0'' and μ_{a0}', D_0' were calculated by averaging the optical properties obtained after fitting (see §9.1) the time-resolved curves acquired during SET IV and SET II respectively to the time-domain diffusion equation for an infinite slab. The measurements included in the fit were obtained from source-detector pairs that were away from the lateral breast boundaries to satisfy the assumption of an infinite slab.

9.2.3 Results

The three cases presented are a malignant tumor, a benign tumor and a control measurement from a patient with no disease. Average background optical properties and the average absorption increase three minutes after the administration of the contrast agent are tabulated in TABLE I for the three cases.

Table 9-4: Average optical properties for three breast cases presented (830nm).

	μ_a (cm^{-1}) pre-ICG	$\Delta\mu_a$ (cm^{-1}) due to ICG	μ_s' (cm^{-1})
CASE I	0.031 ± 0.002	0.007 ± 0.001	11.1 ± 0.7
CASE II	0.046 ± 0.003	0.004 ± 0.001	11.9 ± 0.7
CASE III	0.052 ± 0.003	0.005 ± 0.001	9.3 ± 0.6

Case I: Infiltrating ductal carcinoma

Figure 9-11 depicts the results from a 70 years old patient with an infiltrating ductal carcinoma of ~1cm. Figure 3a depicts the pre-Gd sagittal MR slice passing through the carcinoma in grayscale and the relative signal increase due to Gd superimposed in color. The

color image is obtained by subtracting the corresponding pre-Gd from the post-Gd slice and thresholding the resulting image to 40% of the maximum. All the MR images were median-filtered to reduce shot noise. The rectangle surrounding the carcinoma indicates the sagittal cut of the *volume of interest* (VOI) imaged under the NIR protocol examination following ICG administration (SET II and SET IV). Figure 9-11b shows the DOT image obtained from the VOI, along the coronal plane. Figure 9-11c depicts a pre-Gd GRE coronal slice (in grayscale) passing through the center of the VOI, superimposed with the distribution of Gd (in color) from the entire VOI projected on this coronal plane. The Gd distribution is calculated as $Gd_{VOI} = \sum_{i \in VOI} [Gd_i^{post} - Gd_i^{pre}]$, where Gd_i^{post} is the i^{th} post-Gd coronal slice that is included in the VOI and Gd_i^{pre} the corresponding pre-Gd slice. The final Gd_{VOI} image seen superimposed in color on Fig. 3c is thresholded to 40% of the maximum. All post-Gd images used are from the MR set obtained immediately after Gd-chelate injection.

Figure 9-11b exhibits a marked absorption increase in the upper right of the image, congruent with the position that the carcinoma appears in Figure 9-11c. The local absorption coefficient increase of this lesion is ~0.05 cm^{-1} at 830nm, corresponding to an ICG concentration of ~0.1 mg/L. There is another lesion shown in the left part of the NIR image, congruent with enhancements seen on the MR images, albeit with a different size and shape than the MRI lesions. In its current implementation the low resolution of DOT is not sufficient to separately resolve such small lesions. Furthermore a characteristic feature of DOT is that there are no clear borders of the structures imaged. Therefore characterization of a lesion size depends on a selected threshold. The full width at half maximum of the DOT-resolved carcinoma is comparable with the carcinoma size seen on the MRI image. There is fair comparison between the full-width at half-maximum size of the secondary lesion on the DOT image and the corresponding enhancement distribution seen on the MR image. The cancerous lesion however shows marked enhancement relative to the secondary structure on the DOT image. One other small absorbing lesion appears on the border of the DOT image. This lesion could be due to a superficial blood vessel just in front of the corresponding source, but is most likely an artifact due to experimental noise since it does not appear on the Gd image.

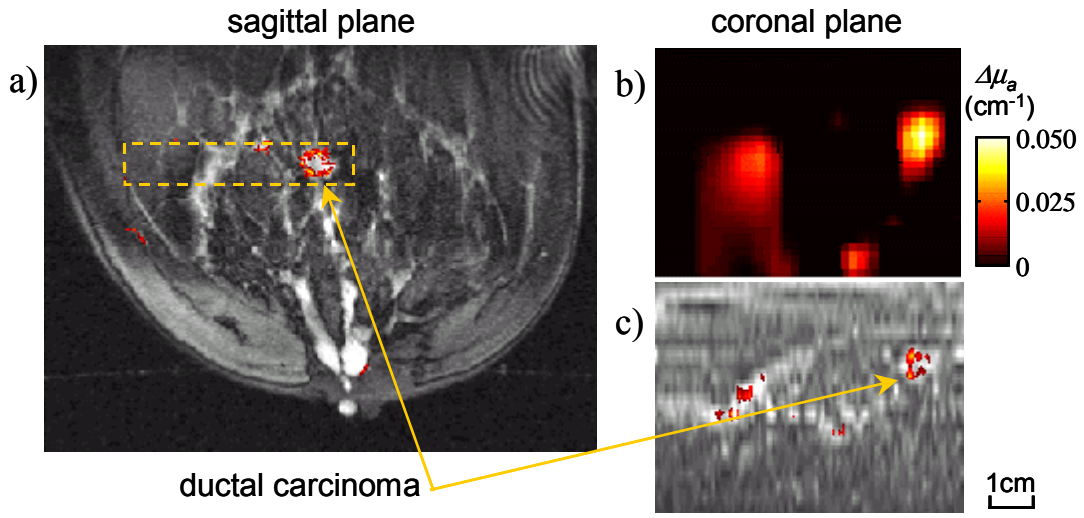

Figure 9-11: Ductal carcinoma (case I). *a)* Functional sagittal MR image after Gd contrast enhancement passing through the center of the cancerous lesion. *b)* Coronal DOT image, perpendicular to the plane of the MRI image in (a), for the *volume of interest* (VOI) indicated on (a) with the interrupted line box. *c)* Functional MR coronal re-slicing of the VOI with the same dimensions as (b).

Case II: Fibroadenoma

Figure 9-12 depicts results from a patient diagnosed with a fibroadenoma. The fibroadenoma was 1.5 cm in diameter and was close to one of the two compression plates. The lesion is clearly shown enhanced on the functional MR images of Figure 9-12a and Figure 9-12c (produced like Figure 9-11a and Figure 9-11c respectively). Figure 9-12b depicts the result obtained with DOT for the VOI. There is a lesion that appears mildly enhanced after ICG injection congruent with the appearance of the fibroadenoma on Figure 9-12c. The $\Delta\mu_a$ value reconstructed for the fibroadenoma is ~0.03 cm^{-1} at 830nm, corresponding to an ICG concentration of ~0.06 mg/L. The full-width at half-maximum size of the lesion appears underestimated. Such differences may be partly attributed to the different distribution mechanisms of ICG and Gd-DTPA, as explained in the discussion

section, and partly to the low DOT resolution. No other structure significantly enhances in this image. The DOT image is printed in scale with Figure 9-11b for direct comparison between the DOT images.

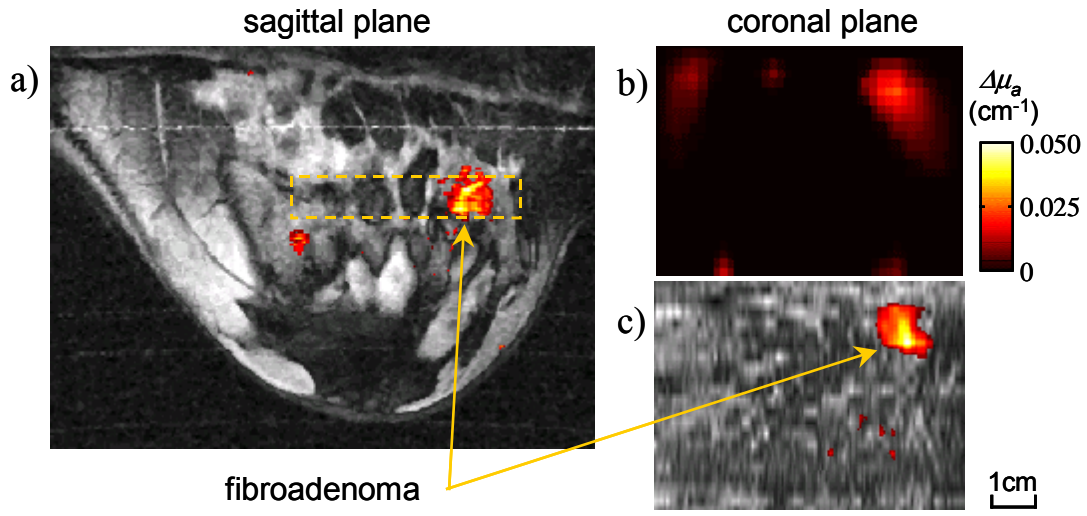

Figure 9-12: Fibroadenoma. (case II) *a)* Functional sagittal MR image after Gd contrast enhancement passing through the fibroadenoma. *b)* Coronal DOT image, perpendicular to the plane of the MRI image in (a), for the *volume of interest* (VOI) indicated on (a) with the interrupted line box. *c)* Functional MR coronal re-slicing of the VOI with the same dimensions as (b).

Case III: Control case

Figure 9-13 depicts the results from the control case, namely a patient that demonstrated no suspicious enhancement in the post-Gd images. Figure 9-13a shows an arbitrarily selected sagittal functional image passing from the middle of the breast. Minor signal enhancement due to Gd appears (in color) scattered in a random manner throughout the breast (color superposition is also thresholded to 40% of the maximum). Figure 9-13b shows the result of DOT for the selected volume of interest, in scale with the results of Figure 9-11b and between the DOT images. Figure 9-13 depicts the functional coronal MR

image produced similarly to Figure 9-11c. The optical image shows moderate enhancements (~0.025 cm^{-1}) in the left and right sides of the image, which coincide with increased number of enhanced structures seen on the MR coronal slice.

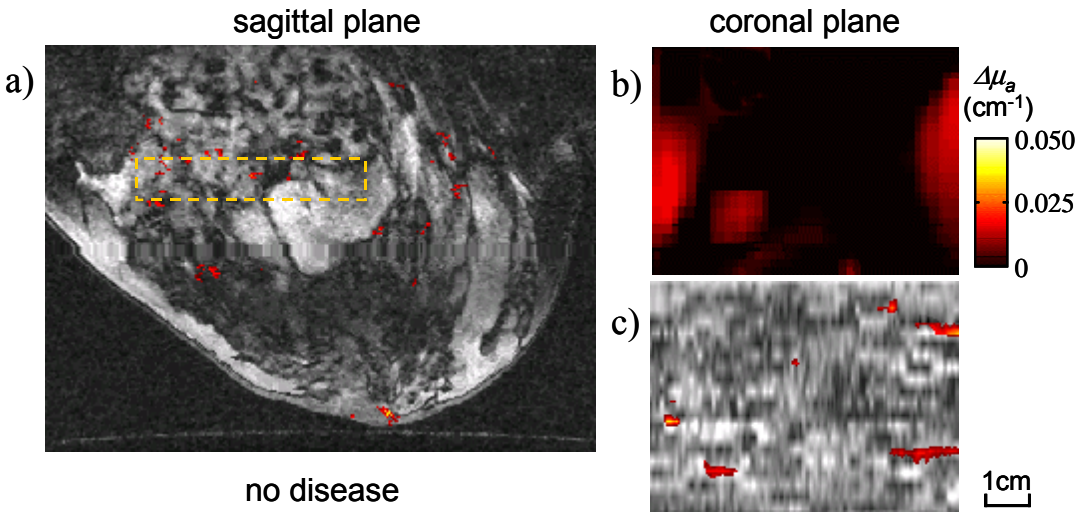

Figure 9-13: No disease. (case III) *a)* Functional sagittal MR image after Gd contrast enhancement passing through the middle plane of the breast. *b)* Coronal DOT image, perpendicular to the plane of the MRI image in (a), for the *volume of interest* (VOI) indicated on (a) with the interrupted line box. *c)* Functional MR coronal re-slicing of the VOI with the same dimensions as (b).

9.2.4 Discussion

In this section we have investigated the fidelity of DOT for imaging the in-vivo distribution of ICG in human breast by comparing it with MRI. The Gd-enhanced MR images provide insight on the functional characteristics of lesions and supported by the histopathological findings serve as our "Gold Standard".

In the case of the carcinoma (case I) the optical method resolves two lesions that are congruent with the two primary areas that enhance after Gd administration. The accuracy of this localization is within the resolution limits allowed by the reconstruction mesh (±4mm). A good correlation is also seen between the contrast of the imaged lesions: the enhancement intensity of the carcinoma relatively to the secondary lesion is approximately 2:1 for the two modalities. This contrast consistency can be attributed to the fact that both ICG and Gd are expected to be probes of hypervascularization in this study, even though they have different distribution patterns. Gd are known as *extracellular agents* that quickly distribute in the intravascular space and the whole body interstitial space (except in the central nervous system [122]). Hence cancer differentiation due to Gd is mainly attributed to the hypervascularity of cancers [123]. On the other hand, when ICG is injected in the blood stream, it binds immediately and totally to blood proteins, primarily albumin by 95%, but also alpha-1-lipoproteins and beta-1-lipoproteins [124]. Therefore it is likely that ICG does not significantly extravasate except for incidences of abnormal blood capillaries with high permeability as in the case of tumor hypervascularity [125]. This extravasation would be a slow process as has been suggested by studies of similar *macromolecular contrast agents* such as the albumin-bound-Gd molecule [126]. Under this premise only minimum ICG extravasation should occur three minutes after injection (when the optical images were acquired). The coronal slices of Figure 9-11b and Figure 9-11c could then be seen approximately as vascularization maps with the carcinoma in this case being two times more vascular compared to the secondary benign lesion.

In the case of the fibroadenoma (Case II) the moderate ICG enhancement similarly indicates lower vascularization. The MR diagnosis in this protocol does not use quantified information; the characterization of the lesion is based on morphological features, such as lobulated borders and internal septations. Therefore MRI enhancements seen in different patients are not compared to each other on an intensity basis. The use of quantified information however seems to be an important feature for DOT diagnosis, which by construction produces quantitative images of the absorption coefficient in this study.

Finally in the normal case, the several minor enhancements shown on the MR coronal slice (Figure 9-13c) are due to distributed small vascular structures. Healthy breast demonstrates a heterogeneous ICG distribution probably similar to the Gd enhancement pattern seen in this measurement. Hence the reconstruction of the large absorbing lesions at the sides of Figure 9-13b reflects an average absorption increase due to many small-localized centers that cannot be adequately resolved independently, as was also observed in the reconstruction of the secondary benign lesion in Figure 9-11b.

Although it is not feasible in this study to validate the accuracy of the reconstructed μ_a, by keeping the reconstruction parameters similar in the three cases examined, it is shown that quantification could be used diagnostically or as a probe of functionality. This is a significant advantage over transillumination. The evaluation of ICG as a contrast agent of high diagnostic potential requires a larger patient study. Our findings suggest that ICG, although not developed as a cancer targeting dye, could find applications in DOT mammography. Additionally it should be pointed out that the study of macromolecular contrast agent kinetics enables the independent estimation of vascularization and permeability [127,128,129]. Such differentiation has been demonstrated by MRI using albumin-bound-Gd and is examined by the MR community as a surrogate to increasing specificity [127,130,131]. In this study the time-limitations of our protocol did not allow imaging at longer times after ICG injection. However images taken at later times could study localized ICG kinetics, and thus quantify permeability as well, offering an additional feature for cancer differentiation.

Independent of the ICG performance in breast cancer detection however, DOT has been shown to be capable of localizing and quantifying enhancing lesions in-vivo. Hence it could be used to investigate the clinical utility of different contrast agents and use the best of them for optical mammography. In support of this view is the fact that the diagnostic mechanisms of DOT do not focus on high-resolution structural details but rather on local functional characteristics. Furthermore the resolution and sensitivity of DOT is expected to increase by increasing the source-detector pairs employed and the signal to noise ratio.

Finally the use of appropriate NIR markers developed to target specific biological or molecular properties of tissue may expand the potential applications of DOT in probing functionality.

9.3 Imaging of intrinsic contrast

As can be seen in §8.1, the DOT clinical protocol aims at imaging both the intrinsic and extrinsic breast optical contrast. Tomography of intrinsic contrast imposes experimental difficulties associated with obtaining the baseline measurement as described in §7.5. This baseline measurement is not specific to the perturbation method that has been followed here but is necessary for the reconstructions because it is equivalent to an instrument calibration measurement (determination of source-detector gain and coupling). In the Rytov regime this calibration is transparent since it is cancelled out by taking the ratio of the total to the incident field. In other reconstruction approaches, the instrument calibration has to occur at an earlier stage. The fact remains that in imaging the intrinsic contrast one has to devise a convenient calibration measurement. In our case the simultaneous examination required the patient to leave the experimental set-up so that a resin model of similar optical properties and geometry substituted the breast. However this substitution changed the experimental set-up and required corrections for the change in optical properties and in geometry between the breast and the model (see §6.1). Stand-alone instruments may use a bath of intralipid where the breast is immersed in, so that the geometry does not change during the calibration measurement [132]. Additionally, self-calibrated reconstruction schemes may be devised when large data-sets are available, by employing a data-set subset to divide out gain factors and other unknown parameters. Nevertheless, the calibration measurements induce additional experimental errors compared to the differential measurements of the contrast agent distribution and the self-calibrated methods are usually more sensitive to random noise.

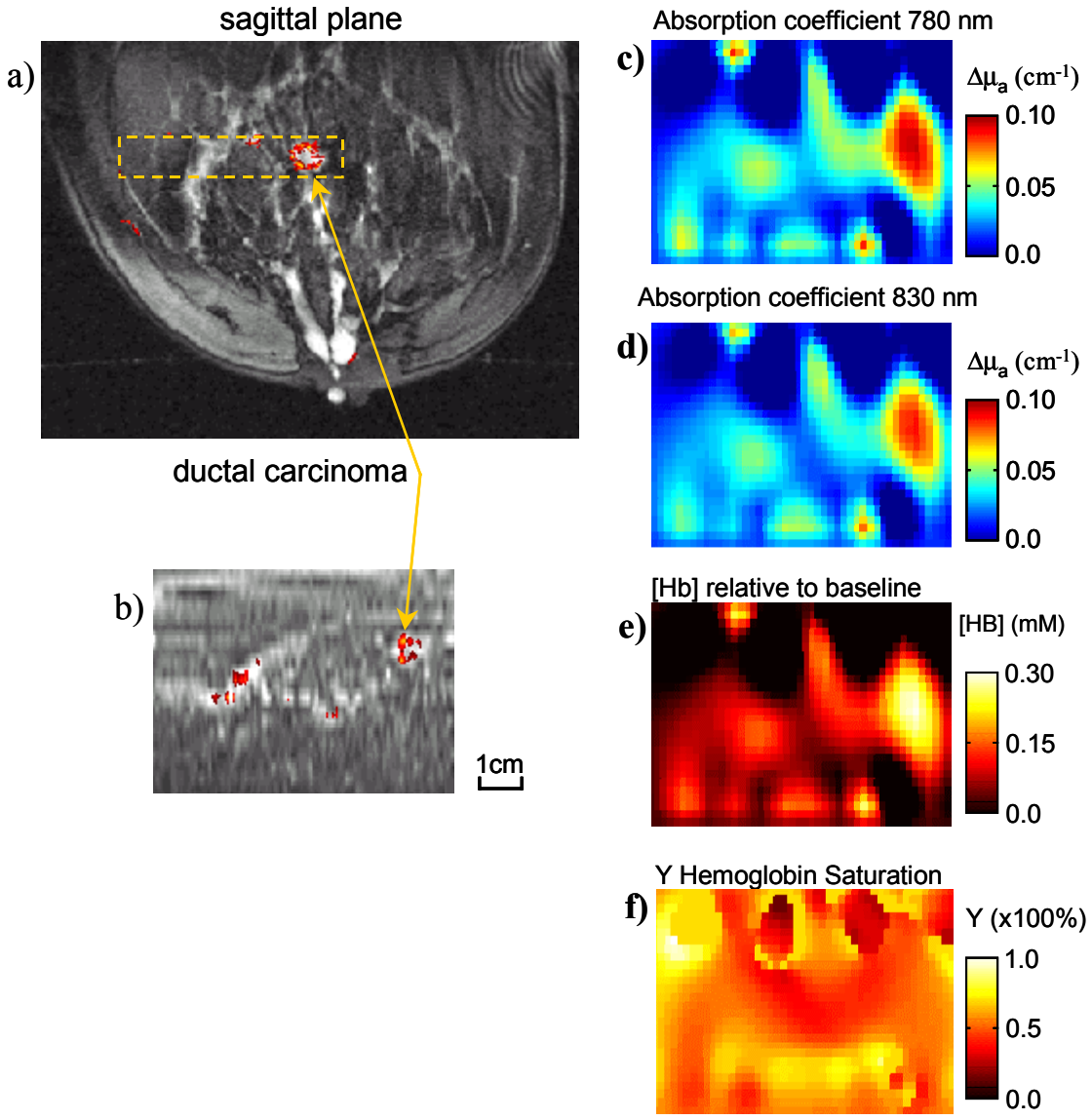

Figure 9-14: Imaging of intrinsic contrast. (case I) *a)* Functional Gd-enhanced sagittal MR image passing through the center of the cancerous lesion. *b)* Coronal DOT image, perpendicular to the plane of the MRI image in (a), for the *volume of interest* (VOI) indicated on (a) with the interrupted line box. c), d) absorption coefficient images at 780nm and 830 nm respectively. e) Hemoglobin concentration image, f) hemoglobin saturation image.

Figure 9-14 depicts the reconstruction of intrinsic contrast for the ductal carcinoma seen in Figure 9-11. Figure 9-14c shows the reconstructed image at 780nm and Figure 9-14d the reconstructed image at 830 nm. Six sources, four detectors and five frequencies (80Mhz – 400MHz in steps of 80MHz) were employed for the reconstruction of these images. The measured data were pre-processed by correcting the scattered field for the change in optical properties between the resin model and the breast and for the changes in source-detector separation using the methodology described in §5.4 and §6.1 (see Eq.(6-2) - the correction for source-detector distance changes between the breast and baseline measurements can be easily added). In this case ϕ_0'' was calculated for the optical properties and geometry of the breast and ϕ_0' was calculated for the optical properties and geometry of the resin block.

Both absorption coefficient images (Figure 9-14c and Figure 9-14d) demonstrate an absorption increase congruent with the appearance of the DCIS on the MR coronal image in Figure 9-14 Combining the image in Figure 9-14c with the image in Figure 9-14d using Eq.(9-1) on a pixel to pixel basis we can obtain an image of the hemoglobin concentration (Figure 9-14e). The image depicts several other objects that do not appear on the extrinsic contrast image of the same volume shown in Figure 9-11b. It is possible that for the reasons explained in the previous paragraphs and according to the results of section §6.1, these additional structures represent artifacts due to experimental noise. The saturation image is depicted in Figure 9-14f. This image is governed by artifacts. The explanation for that was given is §6.3. Saturation images are generally more sensitive to random noise than hemoglobin concentration images. An increased data set with more source-detector pairs and wavelengths has been shown to better the saturation images (§6.3).

9.4 MR-guided Localized diffuse optical spectroscopy

In this section the MRI anatomical and primarily functional information is implemented in the DOT inversion problem according to the methodology described in §5.6, §6.4, and §8.2. When the method is applied to measurements at multiple wavelengths, it

can be thought as an image guided localized spectroscopy technique, similarly to the notation used within the MR community (see [133] and references therein). As was described in §5.6 this technique significantly simplifies the inversion problem and consequently offers superior accuracy by converting the underdetermined tomographic problem to highly over-determined. Inversion of the overdetermined system can better the robustness of the technique to experimental and biological random noise (see §6.4).

Here we have used the two-parameter model, developed and examined in §6.4, to extract the absorption coefficient at two or three wavelengths of diseased and healthy lesions with and without ICG administration. The first part of this section presents the method for lesion selection, which is based on the functional MR information. The second part demonstrates the experimental findings of the MR-DOT study.

9.4.1 Lesion extraction.

NIR absorption contrast in the breast is primarily due to the distribution of oxy- and deoxy-hemoglobin. Therefore similarly to the argumentation used in §6.1.1 the T1 or T2 weighted MR images may not offer sufficient information that is directly related to NIR contrast. The Gd enhancement of the MR images was used to guide the selection of suspicious lesions for the DOT problem since Gd is an extravascular contrast agent, which concentrates more at areas with high vascularization and available extracellular space. Let us examine two examples, one of a cancer and one of a fibroadenoma that will illustrate some of the issues pertaining to lesion extraction. Figure 9-15 shows the Gd enhancement pattern of a cancer that is seen approximately in the center of an MR sagittal image seen in Figure 9-15a. The image in Figure 9-15b is the magnification of the lesion outlined with a solid line on Figure 9-15a. An assumed DOT voxel segmentation is superimposed on the magnified MR image of the cancer. The grayscale image depicts the Gd-enhanced contrast (structural information) while the color segments indicate the regions that where enhanced after the Gd administration. Figure 9-16 shows a fibroadenoma and its Gd-enhancement taken from the MR sagittal slice seen in Figure 9-12. Figure 9-16 b is the magnification of the region

outlined in Figure 9-16a with a solid line. An indicative voxelization pattern is superimposed on the magnified lesion.

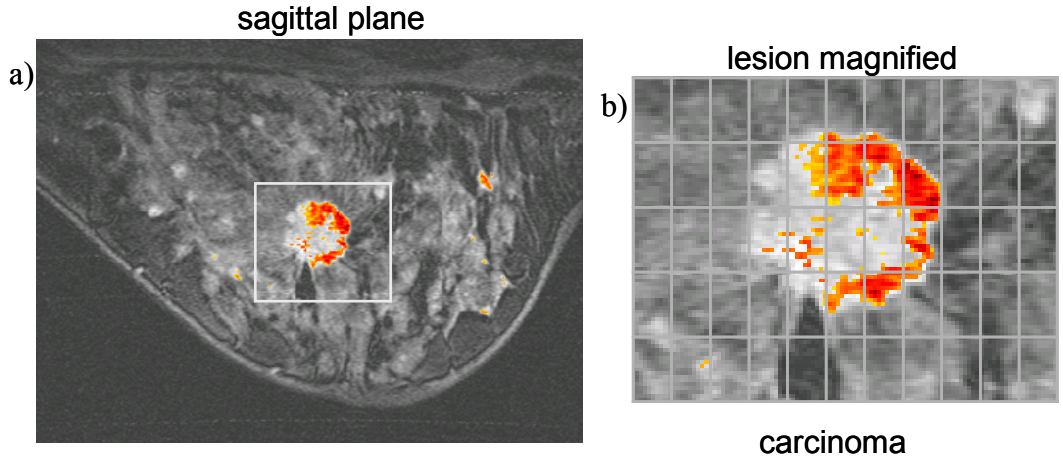

Figure 9-15: Carcinoma enhancement pattern

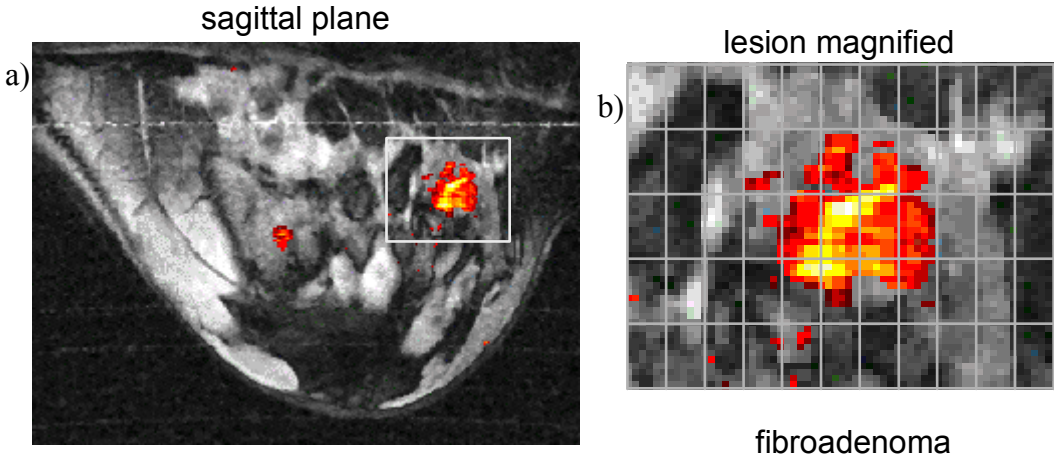

Figure 9-16: Fibroadenoma enhancement pattern

The enhancement patterns in these two cases are markedly different; while Gd-enhancement appears almost homogeneous in the fibroadenoma, the cancer exhibits a characteristic rim enhancement shown in color. We should note that the Gd enhancement is not printed in scale.

It is expected that NIR contrast will more closely resemble the Gd-enhancement pattern since areas that do not demonstrate significant Gd contrast should be of low vascularization assuming flow is not obstructed. When the Gd enhancement is used, the selection of "a suspicious lesion" and subsequently of the volume that this suspicious lesion occupies will be very different between the cancer and the fibroadenoma. Specifically the cancer lesion based on the functional Gd information will occupy a much smaller volume than the fibroadenoma. Therefore the results obtained when using the a-priori information, especially the quantification, are expected to be markedly different compared to when performing DOT as stand-alone, since different partial volumes are implicated.

9.4.2 Results and discussion

Figure 9-17 plots the hemoglobin saturation of selected lesions as a function of their hemoglobin concentration. The filled circles correspond to the five cancerous lesions encountered. The clear circles indicate benign tumors. The triangles are arbitrary lesions selected within normal tissue to serve as controls and the diamonds are some of the baseline (average) measurements presented in §9.1.2. The exact pathologies of malignant and benign tumors are given in Table 9-5. In general the cancerous lesions appear more hypoxic and higher in hemoglobin concentration. Higher hemoglobin concentration is characteristic of angiogenesis. Lower hemoglobin saturation asserts higher metabolic activity and insufficient and irregular blood supply to the different lesions within the malignant mass. However it would need a much higher statistical sample in order to extract the sensitivity/specificity of the NIR results and of the combination of the NIR results with the MRI features.

Table 9-5: MRI and histpathological diagnosis of the cases studied with localized Diffuse Optical Spectroscopy.

Case #	MRI diagnosis	Histopathological Diagnosis
1	Carcinoma	In-situ and infiltrating ductal carcinoma
2	Diffuse carcinoma	Invasive carcinoma
3	Diffuse carcinoma	Invasive lobular carcinoma
4	Invasive carcinoma	Invasive and situ ductal carcinoma
5	Carcinoma	In-situ and infiltrating ductal carcinoma
6	Fibroadenoma	Fibroadenoma and benign breast tissue with fibrosis and focal duct hyperplasia without atypia
7	Fibroadenoma	Benign breast tissue with fibrocystic change and ductal hyperplasia
8	Multiple cysts	-
9	No suspicious enhancement	Fibrocystic changes with extensive stromal fibrosis
10	Ductal hyperplasia	Focal ductal hyperplasia without atypia

Another issue to be considered here is the experimental error of the calculated results. As was discussed in §6.4 the sensitivity to random uncertainties and noise is significantly lower in localized DOS than in stand-alone DOT, since the problem inverted is highly over-determined. The merit function constructed and used here (Eq.(6-6)) does not account for geometrical irregularities (tilted compression plate, non-parallel compression etc) but experimental parameters like the exact geometry were implemented in the construction of the weight matrix. Additionally measurements that were close to boundaries were not included in the calculation to avoid systematic errors. It is difficult however to fully determine the presence of systematic errors and therefore their propagation in the results may not be completely overruled. Simulations have determined that the error bars in the

results shown in Figure 9-17, due to expected systematic errors would be ±5% for the saturation calculation and ±15% for the hemoglobin concentration calculation. Systematic errors affect more the hemoglobin concentration calculation as was described in §4.1.4. The influence of random noise should not affect the results significantly as indicated in §6.4. The use of increased data sets can better the performance of the fit. Also alternative fitting methods have been suggested recently [134], that account for the tissue-fiber coupling irregularities. Such approaches may cope better with instrument-induced systematic errors and should be investigated in the future.

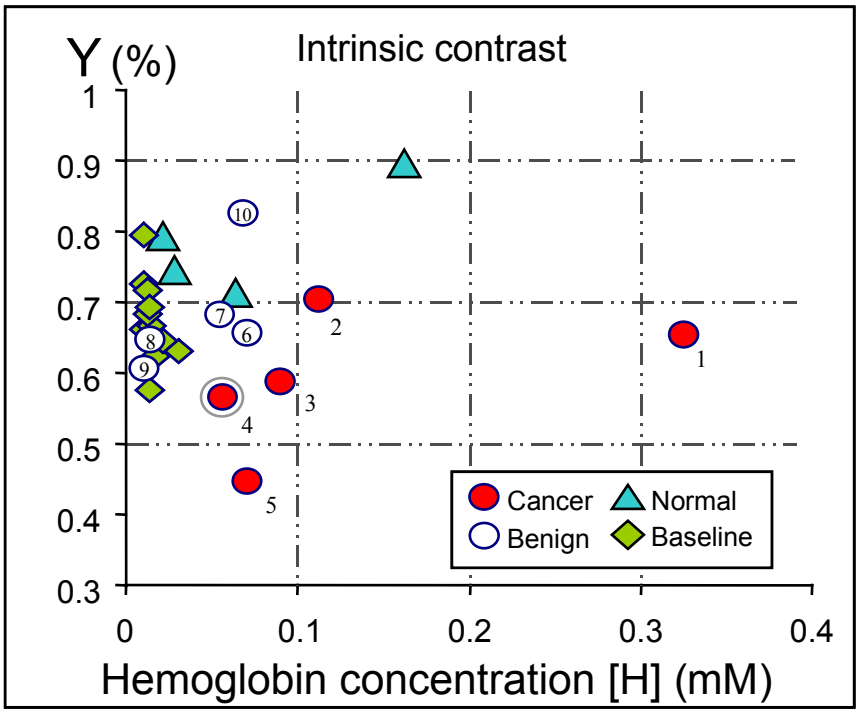

Figure 9-17: Intrinsic contrast (Hemoglobin Saturation vs. Hemoglobin concentration) of selected lesions using MR-guided localized Diffuse Optical Spectroscopy.

Figure 9-18 demonstrates the absorption increase of the same lesions due to ICG enhancement, 3 minutes after ICG injection. The exact same segmentation as in the intrinsic

contrast case was used. The results indicate that the cancers had higher ICG uptake except one that demonstrated zero contrast. This case has special interest and is described in detail in the following subsection. The benign diseases showed markedly smaller contrast agent uptake with the fibroadenomas exhibiting the highest and the cysts demonstrate practically zero ICG uptake. Normal lesions can also demonstrate significant absorption change after the ICG administration depending on how vascular they are.

The experimental errors introduced in the calculation of extrinsic contrast are significantly lower than the ones in the calculation of intrinsic contrast because of the accurate calibration as explained in §5.4.

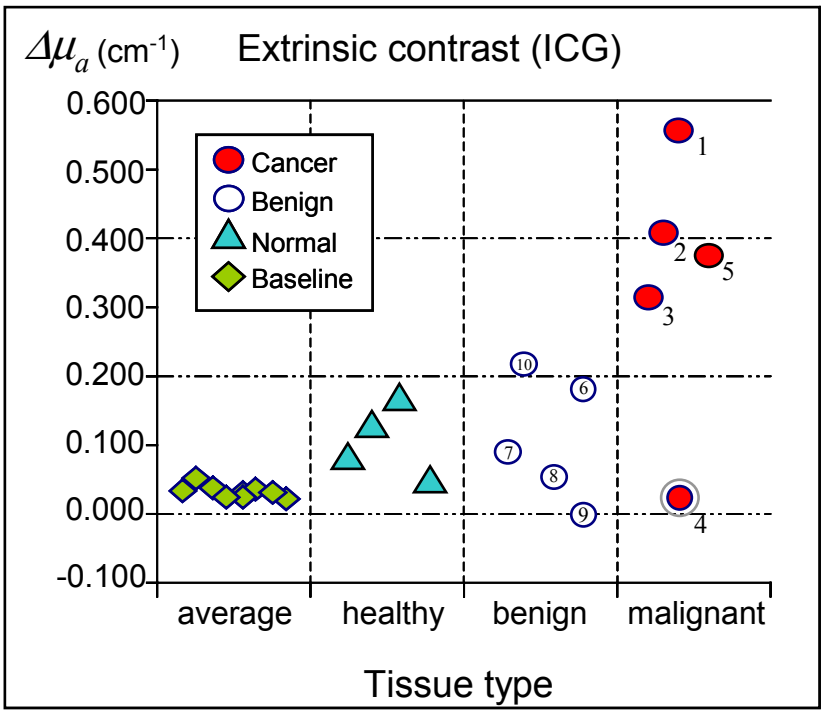

Figure 9-18. Absorption increase due to ICG uptake of selected lesions using MR-guided localized Diffuse Optical Spectroscopy

9.4.3 **The Hybrid modality**

The concurrent MR-DOT examination is in practice a hybrid modality in which both the high resolution and Gd-enhancement pattern can be studied with MRI but also quantified information on hemoglobin concentration, saturation and contrast agent uptake is obtained.

DOT is a complementary technique to MRI. MRI targets primarily structure whilst DOT targets function. MRI can also target deoxy- hemoglobin, but only indirectly via the BOLD effect, and vascularization and tissue function via the study of contrast agent kinetics. But the addition of DOT, which resolves oxy- and deoxy-hemoglobin with high sensitivity, can significantly augment or validate measurements of functional activation or hemodynamics, without compromising the resolution. Similarly, the resolution of DOT as a stand-alone modality is limited to the millimeter range (currently ~5 mm) in large organs due to the nature of photon diffusion. Hence the use of MRI can aid the optical study in providing geometrical certainty that cannot be achieved with DOT alone. The implementation of multiple wavelengths and of higher DOT data set may be potentially used to study additional tissue absorbers of functional, pathological or biochemical importance and tissue scattering.

The interplay between MRI and contrast-enhanced DOT, combined in a hybrid modality, is a more complicated approach, since the tissue property that is examined depends on the contrast agent used. In this study, both the MR contrast agent Gd and the DOT contrast agent ICG probe mainly vascularization. When both techniques use these vascular contrast agents they yield significantly correlated information that was used here to validate the DOT performance. Nevertheless, there are differences in the distribution of the two contrast agents as was described in section §9.2.4. These differences may be used to extract different tissue functional properties, for example extracellular and intracellular volume and tissue permeability when kinetics are included in the calculation. For the study of such parameters however it would probably be more efficient to use the same modality

with different contrast agents, for example MRI with Gd and albumin-bound Gd so a high-resolution study could be obtained.

There are however advantages in using contrast enhancement with both modalities. First, the combined MR-DOT modality allows the study of ICG uptake in tumors with high certainty. Therefore the concentrations of various contrast agents can be studied. This is very important to evaluate existing and emerging contrast agents [44, 135] in-vivo. Thus the hybrid MRI-DOT modality is rendered as an invaluable tool in studying fundamental properties very useful to the development of contrast-enhanced stand-alone DOT as a clinical modality. Second and most importantly the use of specific sets of molecular contrast agents [44] can yield a hybrid modality where high-resolution structural and functional information can be extracted with MRI and biochemical and molecular signatures can be studied with DOT.

9.5 **Special cases**

Measurements from each patient represented a challenging DOT problem. The interaction of theory, experiment and disease presented a delicate balance between the actual performance of the tool and the true contribution of disease that had to be understood in these first clinical steps. There are two cases that have special interest as they allow an insight on more complicated issues in ICG contrast enhancement and I will present them here in more detail. Those two cases should be considered as anecdotal studies and not used necessarily to outline general results. However they could be used for cross-reference with other studies and help in understanding better the complexity of the problem studied.

9.5.1 Ductal carcinoma.

This case is the carcinoma that demonstrated zero absorption increase after ICG administration (see Figure 9-18). This was the largest carcinoma encountered in the study

measuring 1.5cm in diameter and was diagnosed by histopathology as an "invasive and in-situ ductal carcinoma with associated microcalcifications". Figure 9-19a depicts a sagittal MR image passing through the carcinoma, which is clearly seen after Gd enhancement in the middle of the breast.

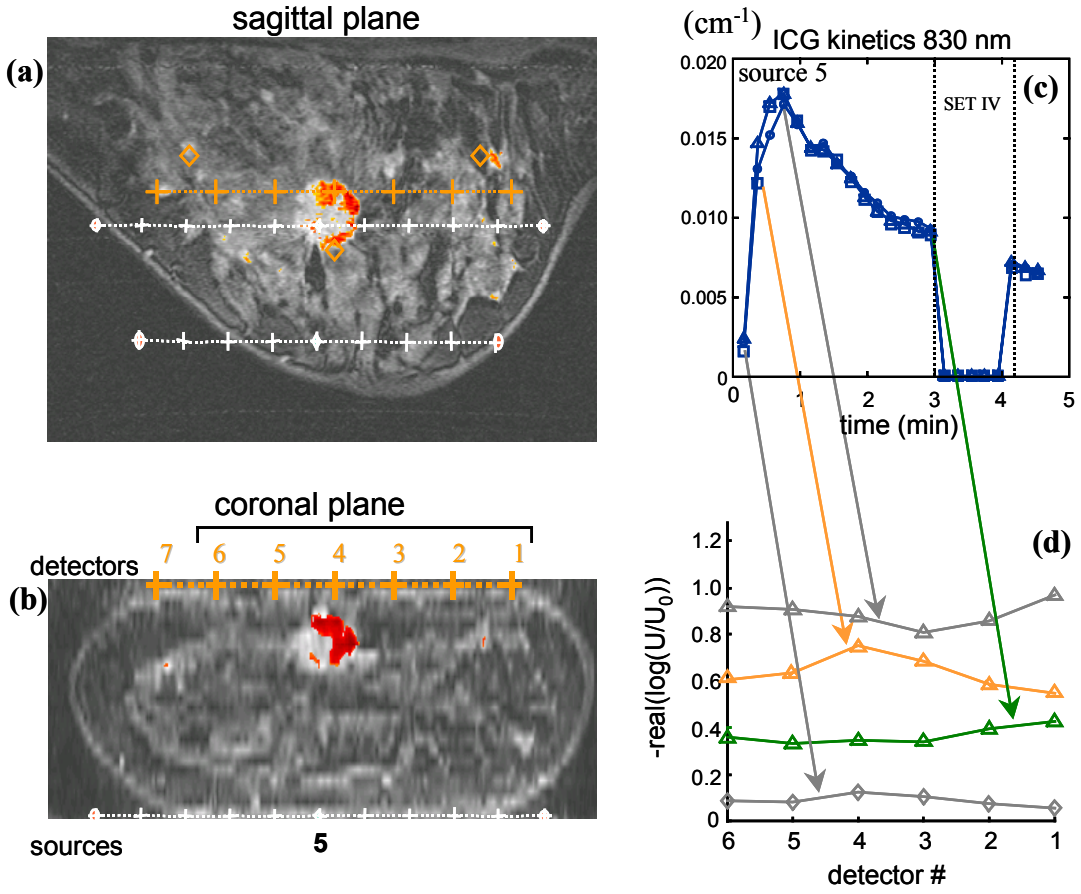

Figure 9-19: Gd and ICG enhancement of special case 1: an in-situ and invasive ductal carcinoma

The position of the optical sources and detectors is also marked on the figure with crosses. Figure 9-19b depicts a coronal MR slice passing through the carcinoma. The position of the sources and detectors projected onto this plane is also shown on this figure with crosses. Detector number 4 was very close to the carcinoma and instrument operation

was stable as was verified by the reference channel measurements. Figure 9-19c depicts the average absorption kinetics through the breast after ICG injection. Figure 9-19d depicts the $real(\ln \phi/\phi_0)$ measurement for source #5 and six of the detectors at four different times. An increase of the quantity $real(\ln \phi/\phi_0)$ indicates a decrease in signal intensity compared to baseline. Immediately after the ICG injection a high intensity decrease is observed for detector 4 relative to the other detectors. This change is very likely to be due to a higher ICG uptake by the carcinoma. At later times however this contrast disappears. It is as the surrounding tissue "catches up" in absorption. Therefore 3 minutes after the ICG injection where imaging or localized spectroscopy is performed there is no contrast from virtually anywhere in the breast and both imaging and localized spectroscopy completely "miss" the cancer.

The reason for this result is not apparent. Although necrotic tissue could be assumed, the tumor depicts a marked Gd uptake and does demonstrate an initial ICG uptake as well. This behavior could also be attributed to differences in blood flow and higher ICG uptake at earlier times, or high permeability differences between malignant and surrounding tissue. However before a complete discussion is given on this result let us also consider the next case of a multifocal carcinoma.

9.5.2 Multifocal carcinoma.

Figure 9-20a depicts the sagittal MR slice of a patient with an invasive lobular carcinoma. The disease was spread throughout the breast and occupied a significant part of its volume. This patient had on a different day a PET scan (Positron Emission Tomography), where the ^{19}FDG uptake (and thus the metabolic activity) was imaged. Figure 9-20b depicts a sagittal PET slice of the same breast where it is shown that the whole volume "lights up", indicative of a distributed disease. Since DOT and PET resolution are of the same order, the NIR photons are also "seeing" a large cancerous volume. Therefore spectroscopic measurements of this breast would reflect measurements on a "diluted" cancer. The average absorption coefficient kinetics due to ICG injection of this breast is

plotted in Figure 9-20c, simultaneously with four other cases taken from normal breasts. The line with squares is the measurement from the breast with the multifocal carcinoma. The four other lines with circles include the lower and highest absorption case seen amongst all breasts studied and are characteristic of the variation in absorption kinetics of the normal breast (see §9.1.3).

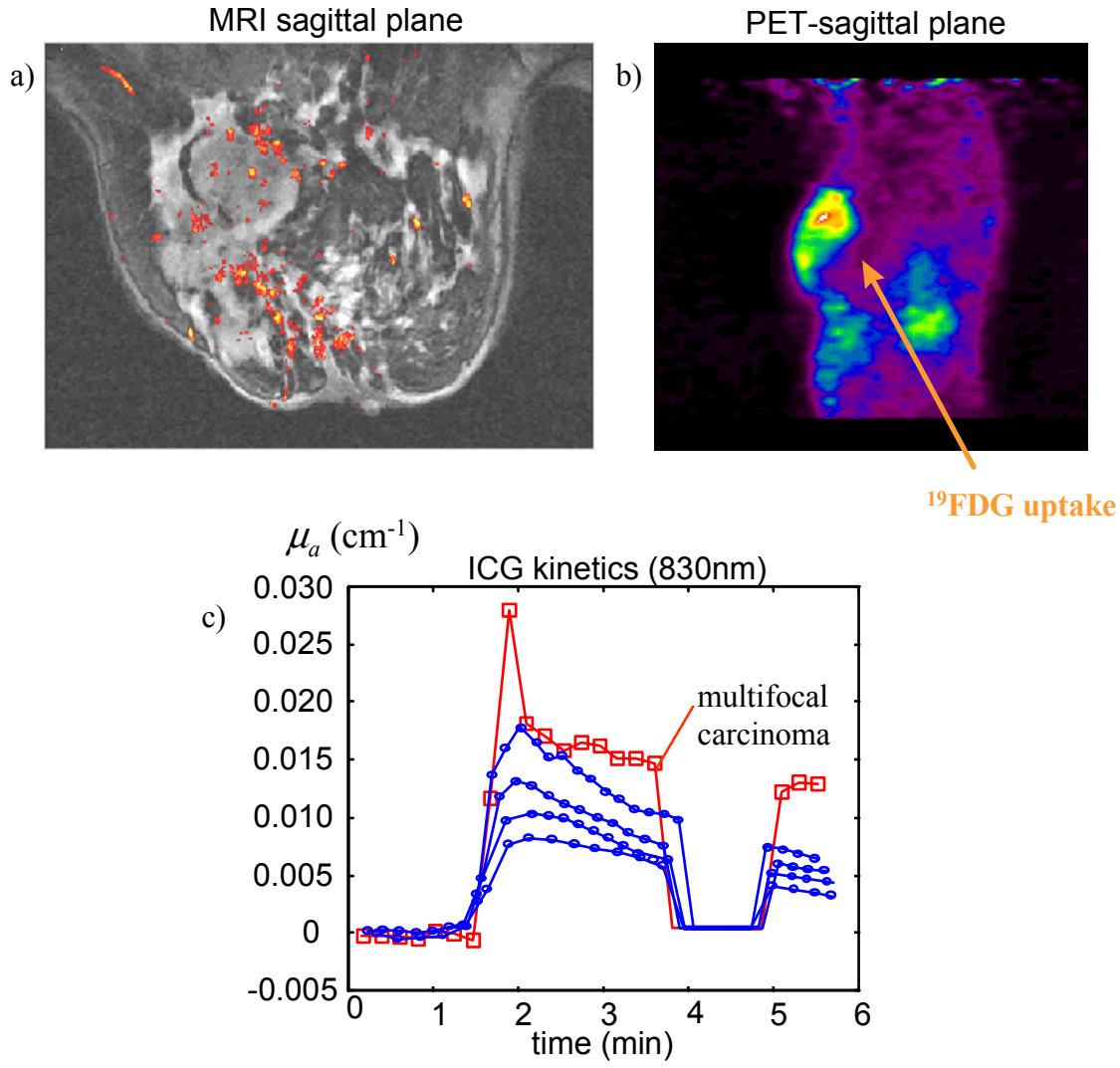

Figure 9-20: Gd and ICG enhancement and 19FDG uptake of a multi-focal carcinoma.

There is a characteristic initial high absorption that is not seen in the "typical sample", namely the kinetics obtained from healthy breasts. Laser operation was stable during the measurement as verified by the reference channel measurement and minimum breast compression was applied, so it is unlikely that this pattern is an experimental artifact. This response is similar to the pattern seen in the previous case of the 1.5 cm carcinoma, where an apparent initial ICG uptake was also seen. It is possible that high vascularization due to angiogenesis, combined with the unregulated blood flow of cancerous vessels (due to the absence of smooth muscle) could be a reason for this result. Figure 9-20c conveys another interesting issue. Approximately 0.5 min after the initial absorption increase, the average absorption increase of the cancer falls at absorption levels that are comparable with the ones encountered in the highly vascular normal breast shown in the kinetic of the first line with circles. However at later times (>2 min) the absorption increase of the mulifocal carcinoma breast depict significant contrast again compared with the typical sample. Although this phenomenon was not seen in the previous case of Figure 9-19, it could be characteristic of cancer with high permeable vessels. The circulating ICG would extravasate in the intravascular space and its kinetics may differ compared to normal vascular structures where extravasation is not significant for macromolecular contrast agents.

The cases presented could lead to some insight regarding the behavior of ICG in various cancers. Although the primary contrast is vascularization as seen in §9.2.3 and discussed in §9.2.4, additional mechanisms seen in dynamic studies seem to exist that may be used to characterize tissue. For the two cases presented in this section, ICG demonstrated an initial high uptake in the cancerous structures, probably due to the higher angiogenesis and unregulated blood flow. Permeability differences could also be a reason for this initial high ICG uptake. The clearance differences observed at later times could also be indicative of differences in the permeability of the blood vessels. It was argued in §9.2.4 that similarly to MRI studies with macromolecular contrast agents, ICG is not expected to significantly extravasate in the first minutes after injection (assuming similar dissociation behavior). However this may be not true for tumors with very permeable vessels. Therefore it could be hypothesized that the multifocal carcinoma exhibited abnormally high permeability

compared to the 1.5 cm carcinoma and healthy structures. In general, it is possible that different cancers (in terms of type, size, growth rate etc) will demonstrate different vascularization/permeability patterns, and dynamic phenomena could therefore use to characterize them.

It would be advantageous to allow longer examination times so that images are obtained as a function of time. This could study the ICG kinetics and resolve vessel permeability. Permeability could be an important feature for cancer detection. The examination protocol applied for the present study performed imaging at 3 minutes after ICG injection. This selection was directed by practical issues. Since administration of ICG was performed at the end of a 20 minute stay in the magnet, patient convenience directed a maximum of an additional 5 minutes for the optical protocol. It should be noted however that this may not be an optimal scan time. The measurement of ICG kinetics could be used to optimize the time that imaging should be performed relative to the time ICG was injected. For example it may be that contrast between malignant and benign or healthy lesions is much higher at later times. Additionally, imaging at times shortly after ICG injection was avoided. This was because the transient phenomena that occur at early times can complicate the reconstructions, which require a constant background absorption level (see §9.2.2). However the results presented indicate that there may be significant diagnostic information in the early kinetics as well. If ICG is to be used for cancer detection it would be beneficial to design fast scanners that with the aid of correction methods such as the one described in §9.2.2 can obtain images at earlier times.

9.5.3 Optimal feature selection

The results presented demonstrated that if a single feature is to be selected for breast cancer detection with stand-alone DOT that would be the use of contrast agents. Even if one of the cancers was missed it is evident that the optimization of imaging at appropriate times and even more the use of appropriately engineered contrast agents can yield significant and accurate diagnostic information. Nevertheless the importance of intrinsic contrast is

fundamental and can be used to characterize lesions. For example the blood saturation level of malignant lesion may be a correlate of the metastatic potential since lower saturation levels may indicate metabolically active tumors. Most importantly it was demonstrated in this chapter that the optical method, either in the form of stand-alone Diffuse Optical Tomography or as image-guided localized Diffuse Optical Spectroscopy can be used clinically. These results and the overall assessment of the technique are summarized in the next chapter.

10 Conclusion and future outlook

In the present work diffuse photons were employed either in the form of Diffuse Optical Tomography or in the form of MR-guided localized Diffuse Optical Spectroscopy to probe breast cancer. Both intrinsic contrast and ICG uptake were studied.

Diffuse Optical Tomography resolved ICG-enhanced lesions that showed congruence with Gd-enhanced lesions seen on the MR images. The comparison was performed on the basis that both ICG and Gd are vascular contrast agents, and although they have somewhat different distribution, they in essence probe angiogenesis. Thus the capacity for the clinical use of DOT was demonstrated. Images of intrinsic contrast, especially those of hemoglobin concentration also demonstrated congruence with the Gd-enhanced images, however they appeared to be noisier than the extrinsic contrast NIR images. DOT performance depends on the information content and the signal-to-noise ratio of the measurements. In this implementation a small number of sources and detectors were employed. However the use of a larger number of sources, detectors, wavelengths and

projections can improve the reconstruction performance as it effectively improves the information content and signal-to-noise ratio. The study of data-set information content can play a vital role in DOT optimization and the design of second-generation DOT systems. We have recently looked into analytical ways to connect the DOT resolution and image fidelity with the data-set employed [136, 137] by performing singular value analysis of the forward problem or looking into the degree of correlation between adjacent measurements. The data set optimization, and technological advances in parallel detection (low noise CCD cameras, high channel capacity frequency and time-resolved systems) as well as more stable sources can increase the detection capacity and DOT performance. The topic may receive further attention especially pertaining to image fidelity, i.e. what is the certainty that the image reconstructed does not contain artifacts but accurately reflect tissue function. In this work we took a first step to study this issue. We have demonstrated that highly heterogeneous media such as tissue yield image artifacts if proper care is not taken. We also presented methodologies to minimize the reconstruction artifacts. This leads now to asking more specific questions, such as what is the DOT fidelity in reconstructing the background heterogeneity as well and what is the capacity to construct determined and over-determined systems and the benefit in using grids with varying discretization step.

The use of a-priori information in the inverse DOT problem relaxes the high inversion requirements of the stand-alone problem. However the same questions and optimization can be applied here. Nevertheless this venue offers truly exciting opportunities. The use of the anatomical and functional information can yield highly accurate merit functions and therefore improve the quantification of optical properties. We have calculated the intrinsic contrast and the absorption increase due to ICG enhancement in selected breast lesions. Breast cancers generally demonstrated higher vascularization and ICG uptake and lower oxygen saturation than normal lesions and benign diseases. This information can be combined with the MR features to enhance the specificity or to predict metastatic potential.

Besides the use of DOT as a research or "add-on" tool, the present work allowed an insight on the potential to use DOT or localized DOS to detect breast cancer. The problem

is two-dimensional. The first issue is whether the features probed by DOT can yield appropriate specificity to use DOT diagnostically. The second issue is if there exists adequate contrast that can be detected with realistically feasible technology. Early detection of small primary tumors remains the basis for improved survival rates and early detection of breast cancers still represents a diagnostic challenge. It may be that even if angiogenesis and hypoxia prove to be highly specific of breast cancers, they will require a well-formed malignancy (larger than a few millimeters) to yield adequate contrast. The smaller cancer detected in this study was 8mm. No smaller cancer was available in the clinical examinations performed to investigate the clinical detection limits.

Similarly to other clinical imaging modalities, contrast agents will play an important role for breast cancer detection with DOT. Vascular contrast agents may yield significant differentiation characteristics, especially if the acquisition protocol and the distribution mechanisms of the contrast agent are optimized as discussed in Chapter 9. It can be argued that since vascular contrast agents can be imaged with high-resolution MRI as well, it is futile to pursue their imaging with DOT. There are many advantages however in the optical method to make it attractive for clinical applications. Besides being economical and portable, photon technology can detect vascular optical contrast agents with high sensitivity. Most importantly however, there are many biologic processes that cannot be easily or directly monitored by existing imaging techniques, because key molecules in these processes are not distinguishable from each other with the existing technologies. New classes of contrast agents, may be used to target highly specific cancer signatures at the molecular level. The high sensitivity of the optical method can then allow the detection and localization of disease before anatomic changes become apparent. Advancement in optical imaging and contrast agent developments is mutually beneficial. Furthermore, the combination of absorbing or fluorescent probes with appropriate imaging systems and techniques may create a powerful modality for the detection of early cancers and push the detection limits of the current state of the art.

11 References

[1] Chance B, "The optical method", Ann Rev Biophys Biophys Chem **20**:1-28 (1991).

[2] National Institutes of Health Consensus Development Conference Statement: Treatment of Early Breast Cancer. (June 18-21,1990) Bethesda, MD.

[3] American Cancer Society:Cancer Facts & Figures – 1992. Atlanda, Anerican Cancer Society, 1992 (publication no. 5008.920LE).

[4] O'Maley M, Fletcher S, Morrison B, "Does Screening for Breast Cancer Save Lives? Effectiveness of Treatment After Breast Cancer Detection Following Screening by Clinical Breast Examination, Mammography and Breast Self-examination", New York, NY: Springer-Verlag New York Inc; (1990).

[5] Andersson I, Aspegren K, Janzon L, Landberg T, Lindholm K, Linell F, Ljungberg O, Ranstam J, Sigfusson B, "Mammographic screening and mortality from breast cancer:

the Malmo mammographic screening trial", BMJ. **297**(6654): 943-8 (1988).

[6] Roberts MM, Alexander FE, Anderson TJ, Chetty U, Donnan PT, Forrest P, Hepburn W, Huggins A, Kirkpatrick AE, Lamb J, "Edinburgh trial of screening for breast cancer: mortality at seven years", Lancet. **335**(8684): 241-6 (1990).

[7] Frisell J, Eklund G, Hellstrom L, Lidbrink E, Rutqvist LE, Somell A, "Randomized study of mammography screening: preliminary report on mortality in the Stockholm trial", Breast Cancer Res. Treat. **18**:49-56 (1991).

[8] Shapiro S, Venet W, Strax P, Venet L, Roeser R, "Ten- to fourteen-year effect of screening on breast cancer mortality", J Natl Cancer Inst **69**(2): 349-355 (1982).

[9] Tabar L, Fagerberg CJ, Gad A, Baldetorp L, Holmberg LH, Grontoft O, Ljungquist U, Lundstrom B, Manson JC, Eklund G, "Reduction in mortality from breast cancer after mass screening with mammography. Randomized trial from the Breast Cancer Screening Working Group of the Swedish National Board of Health and Welfare", Lancet. **1**(8433): 829-32 (1985).

[10] Verbeek AL, Hendriks JH, Holland R, Mravunac M, Sturmans F, Day NE, "Reduction of breast cancer mortality through mass screening with modern mammography. First results of the Nijmegen project, 1975-1981", Lancet. **1**(8388):1222-1224 (1984).

[11] Adair F, Berg J, Joubert L, Robbins GF, "Long-term followup of breast cancer patients: the 30-year report", Cancer. **33**(4):1145-1150 (1974).

[12] Carter CL, Allen C, Henson DE, "Relation of tumor size, lymph node status, and survival in 24,740 breast cancer cases", Cancer **63**:181-186 (1989).

[13] Kerlikowske K. Grady D. Barclay J. Sickles EA. Ernster V. "Likelihood ratios for

modern screening mammography. Risk of breast cancer based on age and mammographic interpretation", JAMA. **276** (1): 39-43 (1996).

[14] Kerlikowske K, Grady D, Barclay J, Sickles EA, Eaton A, Ernster V, "Positive predictive value of screening mammography by age and family history of breast cancer", JAMA. **270**(20): 2444-2450 (1993).

[15] Sickles EA, "Periodic mammographic follow-up of probably benign lesions: results in 3,184 consecutive cases", Radiology **179**:463-468 (1991).

[16] Cyrlak D, "Induced costs of low-cost screening mammography", Radiology **168**:661-663, (1988).

[17] Gabrielli M, Martella E, Maccarini PA, Piazza N, Conti GM, Pilato FP, Corcione L, Caruana P, Piccolo P, Paolucci R, "Stereotactic fine-needle aspiration biopsy (FNAB) of nonpalpable breast lesions: cyto-histological correlations", Acta Bio-Medica de l Ateneo Parmense. **65** (1-2): 5-15 (1994).

[18] Okamoto H, Ogawara T, Inoue S, Kobayashi K, Sekikawa T, Matsumoto Y, "Clinical management of nonpalpable or small breast masses by fine-needle aspiration biopsy (FNAB) under ultrasound guidance", Journal of Surgical Oncology. **67**(4): 246-250 (1998).

[19] Cristallini EG, Padalino D, Bolis GB, "Role of FNAB in the follow-up of cancer patients", Applied Pathology. **7**(4): 219-224 (1989).

[20] Arisio R, Cuccorese C, Accinelli G, Mano MP, Bordon R, Fessia L, "Role of fine-needle aspiration biopsy in breast lesions: analysis of a series of 4,110 cases", Diagnostic Cytopathology. **18**(6):462-467 (1998).

[21] Parker SH, Lovin JD, Jobe WE, Luethke JM, Hopper KD, Yakes WF, Burke BJ, "Stereotactic breast biopsy with a biopsy gun", Radiology. **176**(3):741-7 (1990).

[22] Parker SH, Burbank F, Jackman RJ, Aucreman CJ, Cardenosa G, Cink TM, Coscia JL, Eklund GW, Evans WP, Garver PR, Gramm HF, Haas DK, Jacob KM, Kelly KM, Killebrew LK, Lechner MC, Perlman SJ, Smid AP, Tabar L, Taber FE, Wynn RT, "Percutaneous large-core breast biopsy: a multi-institutional study", Radiology. **193**(2):359-364 (1994).

[23] Seoudi H, Mortier J, Basile R, Curletti E, "Stereotactic core needle biopsy of nonpalpable breast lesions: initial experience with a promising technique", Archives of Surgery. **133**(4):366-372 (1998).

[24] Homer MJ, "Nonpalpable breast microcalcifications: frequency management and results of incisional biopsy", Radiology. **185**:411-413 (1992).

[25] Kopans DB, "Breast Imaging", Philadelphia: J.B. Lippincott Company (1989).

[26] Kramer S, Schulz-Wendtland R, Hagedorn K, Bautz W, Lang N, "Magnetic resonance imaging and its role in the diagnosis of multicentric breast cancer", Anticancer Research. **18**(3C):2163-4 (1998).

[27] Liu PF, Debatin JF, Caduff RF, Kacl G, Garzoli E, Krestin GP, "Improved diagnostic accuracy in dynamic contrast enhanced MRI of the breast by combined quantitative and qualitative analysis", British J. Radiology. **71**(845): 501-509 (1998).

[28] Friedrich M, "MRI of the breast: state of the art", European Radiology. **8** (5): 707-725 (1998).

[29] Orel SG, Mendonca MH, Reynolds C, Schnall MD, Solin LJ, Sullivan DC, "MR imaging

of ductal carcinoma in situ", Radiology. **202**(2):413-420 (1997).

[30] Nunes LW, Schnall MD, Siegelman ES, Langlotz CP, Orel SG, Sullivan D, Muenz LA, Reynolds CA, Torosian MH, "Diagnostic performance characteristics of architectural features revealed by high spatial-resolution MR imaging of the breast", AJR. American Journal of Roentgenology. **169**(2):409-415 (1997).

[31] Nunes LW, Schnall MD, Orel SG, Hochman MG, Langlotz CP, Reynolds CA, Torosian MH, "Breast MR imaging: interpretation model", Radiology. **202**(3):833-841 (1997).

[32] Orel SG, Hochman MG, Schnall MD, Reynolds C, Sullivan DC, "High-resolution MR imaging of the breast: clinical context", Radiographics. **16**(6):1385-1401 (1996).

[33] Degani H, Gusis V, Weinstein D, Fields S, Strano S, "Mapping pathophysiological features of breast tumors by MRI at high spatial resolution", Nature Medicine. **3**(7):780-782 (1997).

[34] Ting YL, Sherr D, Degani H, "Variations in energy and phospholipid metabolism in normal and cancer human mammary epithelial cells", Anticancer Research. **16**(3B):1381-1388 (1996).

[35] Ronen SM, Rushkin E, Degani H, "Lipid metabolism in large T47D human breast cancer spheroids: 31P- and 13C-NMR studies of choline and ethanolamine uptake", Biochimica et Biophysica Acta. **1138**(3):203-212 (1992).

[36] Kristensen CA, Kristjansen PE, Brunner N, Clarke R, Spang-Thomsen M, Quistorff B,"Effect of estrogen withdrawal on energy-rich phosphates and prediction of estrogen dependence monitored by in vivo 31P magnetic resonance spectroscopy of four human breast cancer xenografts", Cancer Research. **55**(8):1664-1669 (1995).

[37] Daly PF, Cohen JS, "Magnetic resonance spectroscopy of tumors and potential in vivo clinical applications: a review", Cancer Research. **49**(4):770-779 (1989).

[38] Roebuck JR, Cecil KM, Schnall MD, Lenkinski RE, "Human breast lesions: Characterization with proton MR spectroscopy", Radiology **209**(1): 269-275 (1998).

[39] Folkman J, "Angiogenesis and angiogenesis inhibition: an overview", EXS. **79**:1-8 (1997).

[40] Folkman J, "Angiogenesis and breast cancer", Journal of Clinical Oncology. **12**(3): 441-443 (1994).

[41] Vaupel, P, 'Vascularization, blood flow, oxygenation, tissue pH, and bioenergetic status of human cancer", Adv. Exp. Med. Biol. **411**:243-254 (1997).

[42] Dvorak HF, Nagy JA, Dvorak JT, Dvorak AM, "Identification and characterization of the blood vessels of solid tumors that are leaky to circulating macromolecules", American Journal of Pathology. **133**(1): 95-109 (1988).

[43] Garbett PK, Gibbins JR, "Experimental neovascularization in vivo: the early changes in a stable adult vasculature responding to angiogenic stimulation by a syngeneic neoplasm", British Journal of Experimental Pathology. **68**(5): 625-635 (1987).

[44] Weissleder R., Tung CH., Mahmood U, Bogdanov A Jr., "In vivo imaging of tumors with protease-activated near-infrared fluorescent probes", Nat. Biotechnology **17**: 375-378 (1999).

[45] Mahmood U, Tung CH, Bogdanov A, Weissleder R, "Near-infrared optical imaging of protease activity for tumor detection", Radiology **213**: 866-870 (1999).

[46] Boas D, "Diffuse photon probes of structural and dynamical properties of turbid media" Theory and biomedical applications", Dissertation in Physics, University of Pennsylvania (1996).

[47] Keijzer M, Star WM, Storchi PRM, "Optical diffusion in layered media", Appl. Opt. **27:** 1820-1827 (1988).

[48] Zhu JX, Pine DJ, Weitz DA, "Internal-reflection of diffusive light in random-media", Phys. Rev. A **44**(6): 3948-3959 (1991)

[49] Lagendijk A, Vreeker R, Devries P, "Influence of internal-reflection on diffusive transport in strongly scattering media", Phys. Lett. A **136**(1-2): 81-88 (1989).

[50] Patterson MS, Chance B, Wilson BC, "Time Resolved Reflectance and Transmittance for the Noninvasive Measurement of Tissue Optical Properties", J. Appl. Opt. **28**: 2331-2336 (1989).

[51] Farrrell TJ, Patterson MS, Wilson BC, "A diffusion theory model of spatially resolved, steady-state diffuse reflectance for the non-invasive determination of tissue optical properties in vivo", Med. Phys. **19**: 879-888 (1992).

[52] Aronson R, "Boundary conditions for diffusion light", J. Opt. Soc. Am. A **12**(11): 2532-2539 (1995).

[53] Haskell RC, Svaasand LO, Tsay TT, Feng TC, Mcadams MS, Tromberg BJ, "Boundary-conditions for the diffusion equation in radiative-transfer", J. Opt. Soc. Am. A **11**(10): 2727-2741 (1994).

[54] Kienle A, Patterson MS, "Improved solutions of the steady-state and the time-resolved diffusion equations for reflectance from a semi-infinite turbid medium", J. Opt. Soc.

Am. A **14**(1): 246-254 (1997).

[55] O'Leary M, "Imaging with diffuse photon density waves", Dissertation in Physics, University of Pennsylvania (1996).

[56] Kak AC, Slaney M, "Principles of Computerized Tomographic Imaging", IEEE Press, New York (1988).

[57] Li XD, OLeary MA, Boas DA, Chance B, Yodh AG, "Fluorescent diffuse photon: density waves in homogeneous and heterogeneous turbid media: Analytic solutions and applications", Appl. Opt. **35** (19): 3746-3758 (1996).

[58] Optical Tomography and Spectroscopy of Tissue III, Chance B, Alfano RA, Tromberg BJ, eds. Proceedings of SPIE vol. 3597, San Jose, CA (1999).

[59] OSA Trends in optics and Photonics, vol. 22, Biomedical Optical Spectroscopy and Diagnostics/Therapeutic Laser Applications Sevick-Muraca EM, Izatt JA, Ediger MN, eds., Orlando, FL (1998).

[60] Sevick EM, Chance B, Leigh JC, Nioka S, Maris M, "Quantitation of time-resolved and frequency-resolved optical-spectra for the determination of tissue oxygenation", Anal. Biochem. **195** (2): 330-351 (1991).

[61] Cooper CE, Elwell CE, Meek JH, Matcher SJ, Wyatt JS, Cope M, Delpy DT, "The noninvasive measurement of absolute cerebral deoxyhemoglobin concentration and mean optical path length in the neonatal brain by second derivative near infrared spectroscopy", Pediatric Research. **39**(1): 32-38 (1996.).

[62] Hayden RE, Tavill MA, Nioka S, Kitai T, Chance B, "Oxygenation and blood volume changes in flaps according to near-infrared spectrophotometry", Archives of

Otolaryngology - Head & Neck Surgery. **122**(12): 1347-1351 (1996).

[63] Peebles DM, Edwards AD, Wyatt JS, Cope M, Delpy DT, Reynold EO, "Changes in human fetal cerebral oxygenation and blood-volume during delivery", Am. J. Obst. & Gyn. **167**(6): 1916-1917 (1992).

[64] Villringer A, Chance B, "Non-invasive optical spectroscopy and imaging of human brain function", Trends Neurosci. **20**(10): 435-442 (1997).

[65] Binzoni T, Cerretelli P, Ferrari M, Delpy D, "Metabolic studies of human skeletal muscle by near infrared spectroscopy: Possible applications in space research", Int. J. Sports Med.. **18** (4): 312-314 (1997).

[66] Arakaki LSL, Kushmerick MJ, Burns DH, "Myoglobin oxygen saturation measured independently of hemoglobin in scattering media by optical reflectance spectroscopy", Appl. Spectrosc., **50**(6): 697-707 (1996).

[67] Cooper CE, Cope M, Quaresima V, Ferrari M, Nemoto E, Springett R, Matcher S, Amess P, Penrice J, Tyszczuk L, Wyatt J, Delpy DT, "Measurement of cytochrome oxidase redox state by near infrared spectroscopy", Adv. Exp. Med. & Biol. **413:** 63-73 (1997).

[68] Kohl M, Essenpreis M, Cope M, "The influence of glucose-concentration upon the transport of light in tissue-simulating phantoms", Phys.Med.Biol. **40**(7): 1267-1287 (1995).

[69] Chance B, Cope M, Gratton E, Ramanujam N, Tromberg B, "Phase measurement of light absorption and scatter in human tissue", Rev. Sci. Instrum. **69**(10): 3457-3481 (1998).

[70] Tromberg BJ, Coquoz O, Fishkin JB, Pham T, Anderson ER, Butler J, Cahn M, Gross JD, Venugopalan V, Pham D. "Non-invasive measurements of breast tissue optical properties using frequency-domain photon migration", Phil. Trans. Royal Soc. London Series B: Biological Sciences. **352**(1354): 661-668 (1997).

[71] Gratton E, Fantini S, Franceschini MA, Gratton G, Fabiani M, "Measurements of scattering and absorption changes in muscle and brain", Phil. Trans. Royal Soc. London - Series B: BiologicalSciences. **352**(1354): 727-735 (1997).

[72] Fishkin JB, Gratton E, "Propagation of photon-density waves in strongly scattering media containing an absorbing semi-infinite plane bounded by a straight edge", J. Opt. Soc. Am. A**10:** 127-140 (1993).

[73] Patterson MS, Moulton JD, Wilson BC, Berndt KW, Lakowicz JR, "Frequency-domain reflectance for the determination of the scattering and absorption properties of tissue", Appl. Opt. **30:** 4474 - 4476 (1991).

[74] Pogue BW, Patterson MS, "Frequency-domain optical absorption spectroscopy of finite tissue volumes using diffusion theory", Phys. Med. Biol. **39:** 1157 - 1180 (1994).

[75] Arridge S, Cope M, Delpy DT, "The theoretical basis for the determination of optical pathlengths in tissue: temporal and frequency analysis", Phys. Med. Biol. **37:** 1531 - 1560 (1992).

[76] Tromberg BJ, Svaasand LO, Tsay TT, Haskell RC, "Properties of photon density waves in multiple-scattering media", Appl. Opt. **32:** 607 - 616 (1993).

[77] Ntziachristos V, Kohl M, Ma H, Chance B, "Oximetry based on diffuse photon density wave differentials", Med. Phys. **27**(2): 410-421 (2000).

[78] Ramanujam N, Du C, Ma HY, Chance B, "Sources of phase noise in homodyne and heterodyne phase modulation devices for tissue oximetry studies", Rev. Sci. Instr. **69**(8): 3042-3054 (1998).

[79] Fantini F, Franceschini MA, Fishkin JB, Barbieri B, Gratton E, "Quantitative determination of the absorption spectra of chromophores in strongly scattering media: a light-emitting-diode based technique", Appl. Opt. **33**: 5205-5213 (1994).

[80] Fantini S, Franceschini-Fantini MA, Maier JS, Walker SA, Barbieri B, Gratton E, "Frequency domain multichannel optical detector for non-invasive tissue spectroscopy and oximetry", Opt. Eng. **34**: 32-42 (1995).

[81] Kohl M, Watson R, Cope M, "New method for the absolute determination of absorption coefficients in highly scattering media in frequency domain", Optics Letters **21**: 1519-1521 (1996).

[82] Kohl M, Watson R, Cope M, "Optical properties of highly scattering media determined from changes in attenuation, phase and modulation depth", Applied Optics **36:** 105-115 (1997).

[83] Nelder JA, Mead R, "A Simplex Method for Function Minimization", Computer Journal **7**: 308-313 (1964).

[84] Nichols MG, Hull EL, Foster TH, "Design and testing of a white light, steady-state diffuse optical spectrometer for determination of optical properties of highly scattering systems", Appl. Opt. **36**: 93-104 (1997).

[85] Jannson PA, "Deconvolution with applications in spectroscopy", Academic Press Inc. Orlando (1984).

[86] Frieden BR, "Probability, Statistical Optics and Data Testing", Springer Verlang, New York. (1983).

[87] Hamamatsu Photonics K.K., "Photomultiplier Tube", 1st edition, Chief Editor Kume H., Hamamatsu Photonics K.K. JP (1994).

[88] Ntziachristos V, Ma XH, Chance B, "Time-correlated single photon counting imager for simultaneous magnetic resonance and near-infrared mammography", Rev. Sci. Instr. **69**(12): 4221-4233 (1998).

[89] Chance B, Nioka S, Kent J, McCully K, Fountain M, Greenfield R, Holtom M., "Time-resolved spectroscopy of Hemoglobin and Myoglobin in resting and ischemic muscle", Anal. Biochem. **174**: 698-707 (1988).

[90] Arridge SR, "Photon-measurement density-functions .1. Analytical forms", Appl.Opt. **34** (31): 7395-7409 (1995).

[91] Ntziachristos V, Hielscher A, Yodh AG, Chance B, "Diffuse Optical Tomography of highly heterogeneous media.", accepted IEEE transactions on Medical Imaging.

[92] Zair Censor personal communication.

[93] Ntziachristos V, Chance B, Yodh AG, "Differential diffuse optical tomography", Optics Express **5**(10): 230-242 (1999).

[94] Jacques SL, Ostermeyer MR, Wang L, Hielscher AH, "Effects of sources, boundaries and heterogenbeities on photon migration", in Advances in Optical Imaging and Photon Migration (Opt, Soc. Am., Washington DC) Vol **21:** 83-87 (1994).

[95] Barbour RL, Graber HL, Chang JW, Barbour SLS, Koo PC, Aronson R, "MRI-guided optical tomography: Prospects and computation for a new imaging method", IEEE Comp. Sci. & Eng. **2**(4): 63-77 (1995).

[96] Pogue BW, Paulsen KD, "High-resolution near-infrared tomographic imaging simulations of the rat cranium by use of apriori magnetic resonance imaging structural information", Opt. Lett. **23**(21): 1716-1718 (1998).

[97] O'Leary MA, Boas DA, Chance B, Yodh AG, "Experimental images of heterogeneous turbid media by frequency-domain diffusing-photon tomography", Opt. Lett., **20**(5): 426-428 (1995).

[98] Jiang HB, Paulsen KD, Osterberg UL, Patterson MS "Improved continuous light diffusion imaging in single- and multi-target tissue-like phantoms", Phys. Med. Biol. **43** (3): 675-693 (1998).

[99] Hebden JC, Schmidt FEW, Fry ME, Schweiger M, Hillman EMC, Delpy DT, Arridge SR, "Simultaneous reconstruction of absorption and scattering images by multichannel measurement of purely temporal data", Opt. Lett. **24**(8): 534-536 (1999).

[100] Chang JW, Graber HL, Koo PC, Aronson R, Barbour SLS, Barbour RL, "Optical imaging of anatomical maps derived from magnetic resonance images using time-independent optical sources", IEEE Trans. Med. Imag. **16**(1): 68-77 (1997).

[101] Hielscher AH, Alcouffe RE, Barbour RL, "Comparison of finite-difference transport and diffusion calculations for photon migration in homogeneous and heterogeneous tissues", Phys. Med. Biol. **43**(5): 1285-1302 (1998).

[102] Wikstrom MG, Modeley ME, White DL, Dupon JW, Winkelhake JL, Kopllin J, Brasch RC, "Contrast enhanced MRI of tumors: comparison of Gd-DTPA and a

macromolecular contrast agent", Inv. Radiol. **24**(8): 609-615 (1989).

[103] Hielscher AH, Klose A, Catarious Jr. DM, Hanson KM, "Tomographic imaging of biological tissue by time-resolved, model-based, iterative, image reconstruction", OSA Trends in Optics and Photonics: Advances in Optical Imaging and Photon Migration II, Vol. 21, R.R Alfano and J.G. Fujimoto, eds., Optical Society of America, Washington, DC, 156-161 (1998).

[104] Pogue BW, McBride TO, Osterberg UL, Paulsen KD, "Comparison of imaging geometries for diffuse optical tomography of tissue", Opt. Exp. **4**(8): 270-286 (1999).

[105] Yao YQ, Wang Y, Pei YL, Zhu WW, Barbour RL, "Frequency-domain optical imaging of absorption and scattering distributions by a Born iterative method", J. Opt. Soc. Am.A-**14**(1): 325-342 (1997).

[106] Ntziachristos V, Yodh AG, Schnall M, Chance B, "Concurrent MRI and Diffuse Optical Tomography of Breast following Indocyanine Green enhancement", Proceedings of the National Academy of Sciences, USA. **97**(6): 2767-2772, (2000).

[107] McBride T, Pogue B, Osterberg U, Paulsen K, "Image of reconstruction varying objects and simulated breast cancer lesions", SPIE Vol. **3597**: 514-525 (1999).

[108] Cheng X, and Boas D, "Diffuse optical tomography errors resulting from uncertainty in the background optical properties", SPIE Vol. **3597**: 213-220 (1999).

[109] Ntziachristos V, O'Leary M, Chance B, Yodh AG, "Coregistration of images from diffusive wave with other imaging modalities to enhance specificity", OSA TOPS on Advances in Optical Imaging and Photon Migration, **2**: 164-168. (1996).

[110] Roberts DA, Insko EK, Bolinger L, Leigh JSJ, "Biplanar radiofrequency coil design",

Magn. Reson. Series A; **102**(1): 34-41 (1993).

[111] Insko EK, Connick TJ, Schnall MD, Orel SG, "Multicoil array for high resolution imaging of the breast", Magn. Reson. Med. **37**(5): 778-784 (1997).

[112] Saleh BEA, Teich MC, "Fundamentals of Photonics", J. Wiley & sons Inc. New York. (1991).

[113] Yang Y, Liu H, Li X, Chance B, "Low-cost frequency-domain photon migration instrument for tissue spectroscopy, oximetry, and imaging", Opt. Eng. **36**(5): 1562-1569 (1997).

[114] Chance B, Cope M, Gratton E, Ramanujam N, Tromberg BJ, "Phase measurement of light absorption and scatter in human tissue", Rev. Sci. Instr. **69**(10): 3457-3481 (1998).

[115] Compliance Guide for Laser Products. HHS Publication FDA86-8260,. U.S. Department of Health and Human Services, FDA, MD 1985.

[116] Feng SC, Zeng FA, Chance B, "Photon migration in the presence of a single defect - a perturbation analysis", Appl. Opt. **34**(19), 3826-3837 (1995).

[117] Cheong, W.F., Prahl, S.A., and Welch, A.J., "A review of the optical-properties of biological tissues", IEEE J. Quantum electronics **26** (12): 2166-2185 (1990).

[118] Henschen S, Busse MW, Zisowski S, Panning B, "Determination of plasma-volume and total blood-volume using indocyanine green - a short review", J. Med. **24**(1): 10-27 (1993).

[119] Russ JC, "The Image Processing Handbook", CRC Press, Boca Raton, (1995).

[120] Meijer DKF, Weert B, Vermeer GA, "Pharmacokinetics of Biliary Excretion in Man. VI. Indocyanine Green", Eur. J. Clin. Pharmacol. **35**: 295-303 (1988).

[121] Ntziachristos V, Ma XH, Yodh AG, Chance B, "A multi-channel photon counting instrument for spatially resolved NIR spectroscopy", Rev. Sci. Instr. **70**(1): 193-201 (1999).

[122] Rosen BR, Belliveau JW, Buchbinder BR, Mckinstry RC, Porkka LM, Kennedy DN, Neuder MS, Fisel CR, Aronen HJ, Kwong KK, Weisskoff RM, Cohen MS, Brady TJ, "Contrast agents and cerebral hemodynamics", Magn. Res. Med. **19**(2): 285-292 (1991).

[123] Buadu LD, Murakami J, Murayama S, Hashiguchi N, Sakai S, Masuda K, Toyoshima S, Kuroki S, Ohno S, "Breast lesions: Correlation of contrast medium enhancement patterns on MR images with histopathologic findings and tumor angiogenesis", Radiology 200(3), 639-649 (1996).

[124] Leevy CM, Smith F, Longueville J, Paumgartner G, Howard MM, "Indocyanine green clearance as a test for hepatic function. Evaluation by dichromatic ear densitometry", JAMA. **200**(3): 236-240 (1967).

[125] Hansen DA, Spence AM, Carski T, Berger MS, "Indocyanine green (ICG) staining and demarcation of tumor margins in a rat glioma model", Surg. Neurol **40:** 451-456 (1993).

[126] Su MY, Najafi AA, Nalcioglu O, "Regional comparison of tumor vascularity and permeability parameters measured by albumin-GD-DTPA and GD-DTPA", Magn. Res. Med. **34**(3): 402-411 (1995).

[127] van Dijke CF, Brasch RC, Roberts TP, Weidner N, Mathur A, Shames DM, Mann JS,

Demsar F, Lang P, Schwickert HC, "Mammary carcinoma model: Correlation of macromolecular contrast-enhanced MR imaging characterizations of tumor microvasculature and histologic capillary density", Radiology **198**(3): 813-818 (1996).

[128] Schwickert HC, Stiskal M, van Dijke CF, Roberts TP, Mann JS, Demsar F, Brasch RC, "Tumor-angiography using high-resolution, 3-dimensional magnetic-resonance-imaging - comparison of gadopentetate dimeglumine and a macromolecular blood-pool contrast agent", Academic Radiology **2**(10): 851-858 (1995).

[129] Demsar F, Roberts TPL, Schwickert HC, Shames DM., vanDijke CF, Mann JS, Saeed M, Brasch RC, "A MRI spatial mapping technique for microvascular permeability and tissue blood volume based on macromolecular contrast agent distribution", Magn. Res. Med. **37**(2): 236-242. (1997).

[130] Daldrup H, Shames DM, Wendland M, Okuhata Y, Link TM, Rosenau W, Lu Y, Brasch, RC, "Correlation of dynamic contrast-enhanced MR imaging with histologic tumor grade: Comparison of macromolecular and small-molecular contrast media", American Journal of Roentgenology. **171**(4): 941-949 (1998).

[131] Adam G, Muhler A, Spuntrup E, Neuerburg JM, Kilbinger M, Bauer H, Fucezi L, Kupper W, Gunther RW, "Differentiation of spontaneous canine breast tumors using dynamic magnetic resonance imaging with 24-gadolinium-DTPA-cascade-polymer, a new blood-pool agent - Preliminary experience", Inv. Radiol. **31**(5): 267-274 (1996).

[132] Colak SB, van der Mark MB, Hooft GW, Hoogenraad JH, van der Linden ES, Kuijpers FA "Clinical optical tomography and NIR spectroscopy for breast cancer detection", IEEE J.of Selected Topics in Quantum Electronics **5**(4): 1143-1158 (1999).

[133] Ntziachristos V, Kreis R, Boesch C, and Quistorff B, "Dipolar resonance frequency shifts in ^{1}H MRS spectra of skeletal muscle: Confirmation in rats at 4.7T in-vivo and

observation of changes postmortem", Magnetic Resonance in Medicine **38**(1): 33-39 (1997).

[134] David Boas personal communication.

[135] Licha K, Riefke B, Ntziachristos V, Becker A., Chance B, Semmler W, " Hydrophilic cyanine dyes as contrast agents for near-infrared tumor imaging: synthesis, photophysical properties and spectroscopic in vivo characterization", accepted J. Photochem. Photobiol.

[136] Culver J, Ntziachristos V, Zubkov L, Durduran T, Pattanayak DN, Yodh AG, Holboke M, Yodh AG, "Data set size and image quality in diffuse optical mammography: evaluation of a clinical prototype", in Advances in Optical Imaging and Photon Migration, OSA Technical Digest (Optical Society of America, Washington DC) 392-394 (2000).

[137] Ntziachristos V, Culver J, Holboke M, Yodh AG, Chance B, "Optimal selection of frequencies for Diffuse Optical Tomography", in Advances in Optical Imaging and Photon Migration, OSA Technical Digest (Optical Society of America, Washington DC) 475-477 (2000).